Reconstruction of the Σ^0 baryon in Ag+Ag collisions at $\sqrt{s_{\mathrm{NN}}}$ =2.55 GeV with HADES

Dissertation zur Erlangung des Doktorgrades der Naturwissenschaften (Dr. rer. nat.)

vorgelegt beim Fachbereich
Mathematik und Informatik, Physik, Geographie
der Justus-Liebig-Universität Giessen

Marten Becker

Giessen, 2025

JUSTUS-LIEBIG-
UNIVERSITÄT
GIESSEN

Dekan:	**Prof. Dr. Christian Heiliger**
Gutachter:	**Prof. Dr. Claudia Höhne**
Gutachter:	**PD Dr. Manuel Lorenz**

Declaration

I declare that I have completed this dissertation single-handedly without the unauthorized help of a second party and only with the assistance acknowledged therein. I have appropriately acknowledged and cited all text passages that are derived verbatim from or are based on the content of published work of others, and all information relating to verbal communications. I consent to the use of an anti-plagiarism software to check my thesis. I have abided by the principles of good scientific conduct laid down in the charter of the Justus Liebig University Giessen „Satzung der Justus-Liebig-Universität Gießen zur Sicherung guter wissenschaftlicher Praxis“ in carrying out the investigations described in the dissertation.

Statement about the use of Artificial Intelligence (AI) based aids like ChatGPT or SchulKI by OpenAI, or Gemini by Google in the creation of my thesis (marked as applicable):

- ☐ I have not used any AI tool in preparing this text
- ☐ I used an Al tool in the following areas (multiple answers possible):
  - ☐ Finding ideas, stimulating my creativity
  - ☐ Understanding concepts, researching facts and definitions
  - ☐ Optimizing a text that I drafted myself
  - ☐ Creating entire text passages following my prompts

I used the following AI tools to improve the given passages of the text in the manner stated:

Date

Signature

Abstract

This work presents the experimental reconstruction of the Σ^0 baryon in – with respect to NN interactions – subthreshold Ag+Ag collisions at 1.58 AGeV kinetic beam energy measured with the HADES experiment.

At the HADES experiment, which is located at GSI in Darmstadt, Germany, heavy ion collisions at moderate freeze-out temperatures and high baryon chemical potential are measured, analyzed, and evaluated in comparison with the existing data as well as theoretical predictions. This kinetic beam energy corresponds to a center of mass energy of $\sqrt{s_{NN}}$ =2.55 GeV, which is the Λ baryon production threshold in NN collisions. With only a small mass difference of Σ^0 to the Λ baryon of 77 MeV/c^2, Σ and Λ baryons are the lightest strangeness containing baryons. Since all quantum numbers of the Σ^0 and the Λ baryon are identical, their production mechanisms are expected to be very similar. Due to a different spin configuration of the valence quarks inside the Σ^0, the Σ^0 is slightly more heavy and decays with nearly 100 $\%$ branching ratio into $\Lambda\gamma$. However, the reconstruction of the low-energy γ is challenging for most detectors, particularly when attempting to concurrently satisfy the requirements of Λ reconstruction.

For the beamtime of the analyzed Ag+Ag collisions, 15 billion events were recorded. The newly installed electromagnetic calorimeter enables photon reconstruction for HADES for the first time without relying on the previously used conversion method. Within the 0-40 $\%$ most central events, around 8000 Σ^0 baryons were reconstructed in the $\Lambda\gamma$ channel with a significance of approximately 10. In addition to the newly installed electromagnetic calorimeter, the RICH was upgraded with new multi-anode photomultipliers which strongly enhance reconstruction efficiency as well as lepton purity. These advantages were used for feasibility studies in the Λe^+e^- decay channel. Hints for a signal were found that are consistent with the extracted signal from the $\Lambda\gamma$ channel, but due to the small statistics, only a significance level of less than 3 was achieved.

A full efficiency and acceptance correction was performed with a resulting multiplicity of $0.014 \pm 0.002_{\text{stat.}} \pm 0.004_{\text{sys.}}$ produced Σ^0 per event which corresponds to a Λ/Σ^0 ratio at freeze-out of $3.2 \pm 0.3_{\text{stat.}} \pm 0.6_{\text{sys.}}$. This represents the first measurement of this ratio for a subthreshold Σ^0 production in nucleus nucleus collisions.

Comparing to the available world data of p+p collisions close to the Σ^0 production threshold, this ratio increases in p+p to values of 30 and higher. Even more, the measured ratio compares well to measurements in p+p far from threshold. This indicates that the NN threshold has no influence on the Σ^0 production for this energy.

The $\Lambda\gamma$ channel result is compared to statistical hadronization model fit as well as to several transport model predictions. The statistical model calculations are in good agreement to our measurement which endorses the possibility of hyperon production in a thermally equilibrated medium. In this case, the freeze-out ratio is directly connected to the mass difference of two states with the same quantum numbers, resulting in a temperature estimation of the created matter by only measuring Λ and Σ^0. From these measurements T=66 MeV is extracted, which compares well with fits of all hadrons with a statistical model.

Zusammenfassung

Diese Arbeit präsentiert die Ergebnisse der experimentellen Rekonstruktion von Σ^0 Baryonen in Ag+Ag Kollisionen bei 1,58 AGeV kinetischer Strahlenergie, die mit dem HADES Experiment gemessen wurden. Bei dieser Energie liegt die Produktion von Σ^0 Baryonen unterhalb der Produktionsschwelle in Nukleon-Nukleon Kollisionen.

Das HADES Experiment, welches sich an der GSI bei Darmstadt in Deutschland befindet, misst Schwerionenkollisionen bei moderaten Freeze-Out Temperaturen und hohem baryochemischen Potential, analysiert diese und wertet sie im Bezug zu existierenden Daten und theoretischen Vorhersagen aus. Die kinetische Strahlenergie entspricht einer Schwerpunktsenergie von $\sqrt{s_{NN}}$ =2,55 GeV, wobei dieser Wert exakt dem Schwellenwert zur Produktion von Λ Baryon in freien Nukleon-Nukleon Kollisionen gleicht. Durch die kleine Massendifferenz vom Σ^0 Baryon zum Λ Baryon von nur 77 MeV/c^2 sind die Σ und Λ Baryonen die leichtesten Baryonen mit Seltsamkeit. Da alle Quantenzahlen von Σ^0 und Λ Baryon identisch sind, werden sehr ähnliche Produktionsmechanismen erwartet. Wegen einer unterschiedlichen Spin Konfiguration der Valenzquarks im Σ^0 ist das Σ^0 etwas schwerer und zerfällt zu nahezu 100 % in $\Lambda\gamma$. Die Rekonstruktion des niederenergetischem γ erweist sich allerdings als herausfordernd, im Speziellen wenn gleichzeitig alle Voraussetzungen für die Λ Rekonstruktion erfüllt sein müssen.

Während der hier analysierten Strahlzeit wurden 15 Milliarden Ag+Ag Ereignisse aufgenommen. Das hierbei neu integrierte elektromagnetische Kalorimeter erlaubt HADES nun zum ersten Mal Photonen zu rekonstruieren, ohne sich auf die Konversionsmethode verlassen zu müssen. Für die zentralsten 0-40 % der Ereignisse wurden ca. 8000 Σ^0 Baryonen im $\Lambda\gamma$ Zerfallskanal rekonstruiert, wobei eine Signifikanz von 10 erreicht wurde. Zusätzlich zu dem neu integrierten elektromagnetischem Kalorimeter wurde der RICH mit Multi-Anoden-Photomultipliern aufgerüstet, wodurch sowohl die Rekonstruktionseffizienz der Leptonen, als auch deren Reinheit deutlich gesteigert wurde. Diese Vorteile wurden für Machbarkeitsstudien im Λe^+e^- Kanal verwendet. Hinweise auf ein Signal wurden extrahiert, die konsistent zu dem Signal im $\Lambda\gamma$ Kanal sind. Leider wurde hierbei anhand der geringen Statistik nur eine Signifikanz von unter 3 erreicht.

Nach Effizienz- und Akzeptanzkorrektur wurde insgesamt eine Multiplizität von $M_{\Sigma^0} = 0,014 \pm 0,002_{\text{stat.}} \pm 0,004_{\text{sys.}}$ gemessen, was einem Λ/Σ^0 Verhältnis von $3,2 \pm 0,3_{\text{stat.}} \pm 0,6_{\text{sys.}}$ beim Freeze-Out entspricht. Dies ist die erste Messung des Λ/Σ^0 Verhältnis in Kern-Kern Kollisionen unterhalb des Schwellenwerts in Nukleus-Nukleus Kollisionen.

Verglichen damit steigt dieses Verhältnis in den weltweit vorhandenen p+p Daten nahe der Σ^0 Produktionsschwelle auf Werte über 30 an. Des Weiteren ist das gemessene Verhältnis sehr ähnlich mit Messungen in p+p Kollisionen weit über dem Schwellenwert. Dies lässt darauf schließen, dass der NN Schwellenwert keinen Einfluss auf die Σ^0 Produktion in A+A Kollisionen bei dieser Energie hat.

Das Ergebnis aus dem $\Lambda\gamma$ Zerfallskanal wird mit dem statistischen Hadronisierungsmodell sowie Vorhersagen aus verschiedenen Transportmodellen verglichen. Der Vergleich mit dem statistischen Hadronisierungsmodell ergibt eine gute Übereinstimmung mit unserer Messung, was eine Hyperon Produktion in einem thermischen Medium nahelegt. In diesem Fall ist die Freeze-Out Temperatur direkt mit dem Massenunterschied von zwei Zuständen mit gleichen Quantenzahlen verbunden, was eine Temperaturabschätzung ausschließlich über die Messungen von Λ und Σ^0 erlaubt. Über diese Messung wird eine Temperatur von T=66 MeV extrahiert, was gut mit dem Fit aller Hadronen im statistischen Hadronisierungsmodell übereinstimmt.

Table of Contents

List of Figures

List of Tables

CHAPTER 1

Introduction

1.1 Motivation

The success of humanity in evolutionary history is closely tied to its intelligence. We collate and utilize knowledge in order to generate advantageous predictions. As a logical consequence, different scientific research areas have been examining our environment to improve predictive capabilities. While biologists are primarily concerned with the study of plants, humans, and life in general, physicists are primarily interested in the interactions of matter. The initial focus from over 2000 years ago was conceptualizing matter in four fundamental elements: water, air, fire, and earth. However, the question remains as to what maintains the fundamental cohesion of these latter states of matter.

The exploration of the subatomic scale, initiated with the discovery of the electron by J.J. Thomson in 1897, represents a significant milestone in the history of scientific inquiry [1]. In the subsequent decades, the decomposition of our known matter was specified in increasingly analytical approaches. Notable contributions to the understanding of matter were achieved by Rutherford with his discovery of the inner structure of atoms [2], and by Chadwick in 1932 with the discovery of the neutron [3]. During this time Stern discovered the magnetic moment of a proton, which already was hinting to an inner structure of the proton [4]. Furthermore, the experimental conclusion of the 1940s/1950s demonstrated that protons and neutrons are insufficient to describe so called V-particles, which were subsequently referred to as strangeness-containing particles. The particle zoo was filled with various hadrons until mid 1960s which lead to the quark model description.

All know particle behaviours are put in context within the state of the art model of subatomic particle physics: the Standard Model.

1.2 Standard Model of Particle Physics

The most successful model of subatomic particle physics is the standard model of particle physics. It contains all so far known elementary particles and describes

their fundamental interactions via the strong, electromagnetic and weak interaction. It was continuously developed since the 1950s when it started with the proposal of quarks by Gell-Mann and Zweig [5][6], to describe the pure amount of new particles discovered earlier that century. Zweig himself mentioned [7] the idea of Fermi and Yang from 1949 [8], that the newly discovered pions may not be elementary particles. The experimental evidence for the theory of quarks as fundamental particles was given in inelastic proton-electron scattering at SLAC in 1968 [9][10].

The elementary particles are categorized in fermions which carry spin $\frac{1}{2}$ and form matter, and the bosons with integer spin which are exchange particles of the fundamental forces. This assertion is not applicable for the Higgs boson, whose particular properties are described in section 1.2.3. Besides the spin, the elementary particles are characterized by mass and charges, namely color, electric and weak charge.

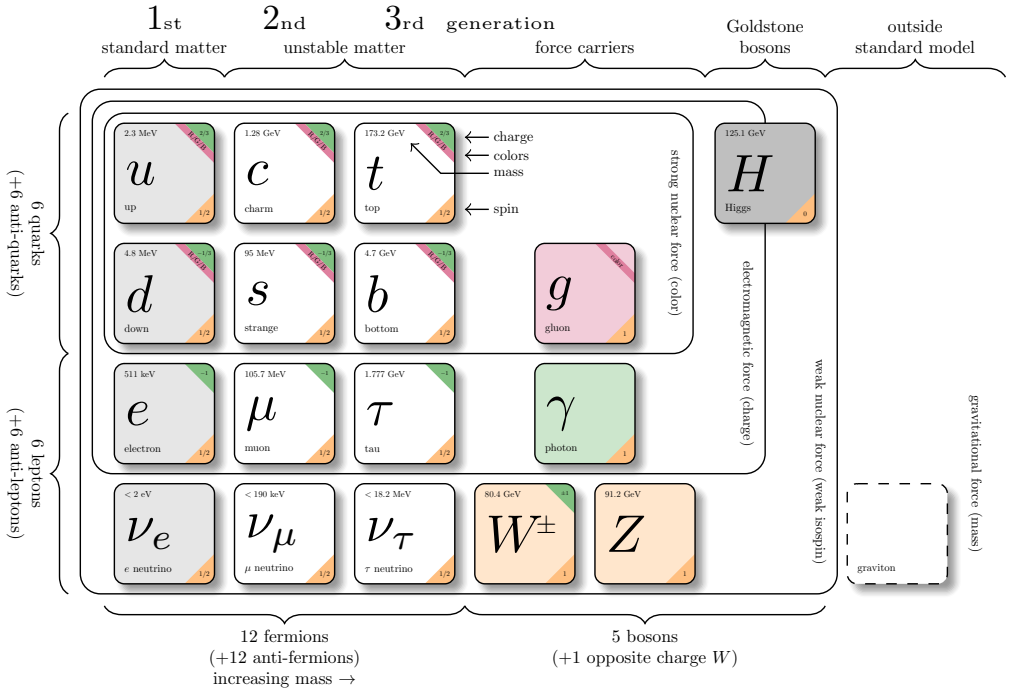

Figure 1.1: Characterization of all known elementary particles included in the standard model. Figure taken from [11].

The fermions are divided up into strongly interacting quarks and the leptons which do not interact strongly. Leptons and quarks are divided into 3 families each, where a family consists of 2 partners building a pair as shown in figure 1.1 resulting in 6 different flavors for leptons and quarks. For the quarks, the electromagnetic charges are $+\frac{2}{3}$ and $-\frac{1}{3}$ respectively while the leptons carry -1 or 0 electric charge. While quarks also carry color charge and thus interact via all

three fundamental forces within the standard model, none of the leptons carries color charge and will not interact strongly. As previously mentioned, there are 3 lepton flavors which carry electromagnetic charge. These e^-, μ^- and τ^- and their anti-particles e^+, μ^+ and τ^+ can interact electromagnetically and weak while the neutrinos which are electrically neutral do only interact weakly. In total, the standard model is mathematically represented as

$$SU(3)_C \times SU(2)_L \times U(1)_Y \tag{1.1}$$

symmetry where the first term accounts for the color symmetry of the strong interaction while the combination of the latter two terms describe the symmetry of the electro weak unification. Those theories are briefly summarized in the following sections.

1.2.1 Strong Interaction

The strong interaction is described by the theory of **Q**uantum **C**hromo**D**ynamics (QCD). This quantum field theory is mathematically described as a non-abelian gauge symmetry with the symmetry group SU(3), which is determined by the combination of three different color charges in QCD and the self interaction of the gauge bosons of QCD, namely the gluons [12][13]. Only quarks, anti-quarks and the gluons have non vanishing color quantum numbers and participate in the strong interaction. While all quarks carry color, all anti-quarks carry anti-color. The gluon is carrying net color charge as combination of a color and an anti-color, which leads to an anti-symmetric color/anti-color octet in nature, while the symmetric singlet state does not exist since it would be color neutral. In nature we can only observe color neutral objects, which are described as “white”.

The Lagrangian density of QCD is given by

$$\mathcal{L}_{QCD} = \sum_f \overline{q}_f (i\gamma^\mu D_\mu - m_f) q_f - \frac{1}{4} G^a_{\mu\nu} G^{a,\mu\nu} \tag{1.2}$$

where $D_\mu = \partial_\mu - igA^a_\mu(x)\frac{1}{2}\lambda_a$ is the covariant derivative which introduces the 8 gluon fields $A^a_\mu(x)$ and the corresponding field strength $G^a_{\mu\nu} = \partial_\mu A^a_\nu - \delta_\nu A^a_\mu + gf^{abc}A^b_\mu A^c_\nu$. Hence the latest term is vastly different to QED, and involves the gluon-gluon self interaction. The density functional in equation 1.2 allows the calculation of Feynman diagrams in perturbation theory which generalize the calculation of interaction probabilities [14].

The non-abelian structure of QCD leads to an energy dependency of the coupling constant α_s which is precisely measured from several experiments in a wide range of momentum transfer Q. The coupling constant is often precisely stated at the Z mass with the most recent value of $\alpha_s(m_Z^2) = 0.1179 \pm 0.0009$ [15]. Various observables like hadronic τ decays, multi/inclusive jet probabilities and deep inelastic scattering were used to cover a large momentum transfer range. A summary of the results is depicted in figure 1.2.

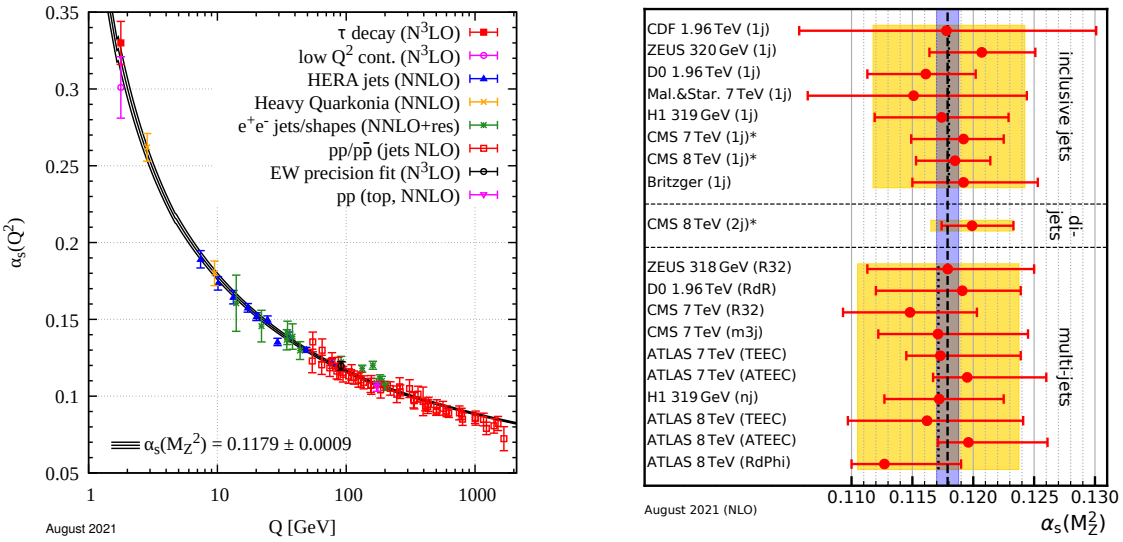

(a) World data which is currently used for describing the running of α_s

(b) Extrapolation towards $\alpha_s(m_Z^2)$ of the available jet analysis

Figure 1.2: Summary of the most recent measurements of α_s [15].

The decrease of α_s at large momentum transfer is phenomenological described as asymptotic freedom. As result the quarks would not interact for a vanishing distance. On the other hand the steep rise in α_s at small Q^2 binds the quarks. This behaviors leads to the so called confinement, leading to an attractive force in between quarks which results in hadron formation. This behavior of rising α_s for rising small momentum transfer is contrary to the behavior of the quantum electrodynamics. On the other hand, for large temperatures α_s is declining, which leads to a deconfined hadronic matter at high energy density where no hadrons exist. This phase condition with quasi free quarks and gluons was predicted already 1973 [16] and later was called **Q**uark**Q**luon**P**lasma (QGP).

Chiral symmetry

Compared to the proton mass of $M_p = 938\,\mathrm{MeV/c^2}$, its constituent quarks (uud) have only masses of $m_u = 2.2\,\mathrm{MeV/c^2}$ and $m_d = 4.7\,\mathrm{MeV/c^2}$ [17]. Considering vanishing quark masses, the QCD Lagrangian would conserve chirality [1]. With $\frac{m_u}{m_p} < 1\,\%$ this assumption is much more exact than for the s quark with an estimated mass of $m_s \approx 100\,\mathrm{MeV/c^2}$.

In a world without quark masses, the decoupling of the Lagrangian into its chiral components of the form $q_f = q_f^L + q_f^R$ can be performed as

$$q_f^L = \frac{1}{2}(1+\gamma_5)q_f \qquad q_f^L = \frac{1}{2}(1-\gamma_5)q_f \tag{1.3}$$

[1] Chirality is the more general approach of conserving the left and right handed symmetry in the massless limit, where no reference frame of flipped handedness exists

However, the symmetry is broken dynamically by the non vanishing quark condensate as well as explicitly by the masses of the quarks. Those effects result in the known mass hierarchy of our hadrons, where as example the pseudoscalar mesons are shown in figure 1.3.

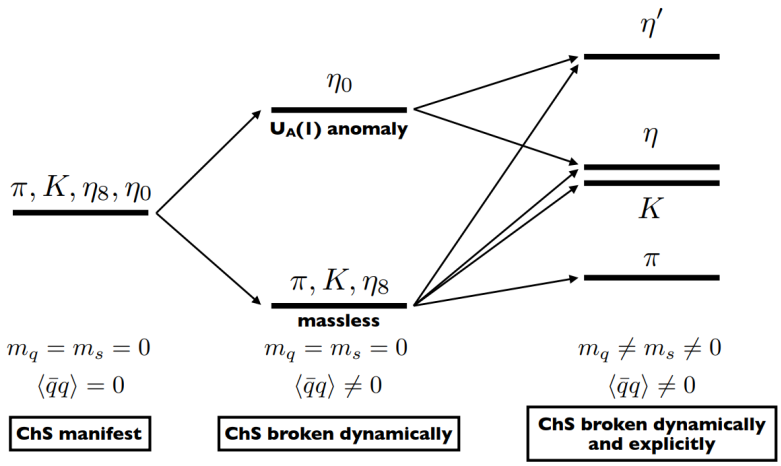

Figure 1.3: Scheme of meson masses and the origin of the mass hierarchy of the experimentally accessible spin zero meson nonett [18].

Chiral partners have the same spin, but different parity. This leads to an experimental observable for the chiral symmetry. So in experiment, the explicitly broken chiral symmetry is observed when comparing the invariant masses of chiral partners, for example as shown in the hadronic decay of τ leptons [19].

1.2.2 Electroweak Theory

From the fundamental forces which are included in the Standard Model, the electromagnetic force was described first by Maxwell in 1873 [20]. In 1926 it was also the first interaction which quantum field theory was successfully applied to [21], and is in the following referred to as **Q**uantum **E**lectro **D**ynamics (QED).

The Lagrangian density of QED is given by

$$\mathcal{L}_{QED} = \overline{\psi}(i\gamma^\mu D_\mu - m)\psi - \frac{1}{4}F_{\mu\nu}F^{\mu\nu} \tag{1.4}$$

with the covariant partial derivative $D_\mu = \partial_\mu + iqA_\mu$ and the field strength $iqF_{\mu\nu} = [D_\mu, D_\nu]$ [14]. Mathematically, the electromagnetic force is described by an abelian gauge symmetry with the symmetry group U(1).

The massive Z^0, W^+ and W^- gauge bosons of the weak interaction are either neutral or carry electromagnetic charge. The weak force is described by a SU(2) symmetry group.

The weak interaction only couples to left handed particles and right handed anti-particles and thus shows the maximum possible parity violation.

Experiments show that Z and W bosons do couple differently to the known fermions, in particular Z bosons couple not only to the weak but also to the electromagnetic charge. The unification of QED and the weak interaction resolves this specialty and results in the electroweak theory.

It was proposed in the late 1960s by Weinberg and Salam [22] as a minimal gauge theory which only needs four gauge fields, namely the fields of the electromagnetically charged W^+, W^- as well as the neutral γ and an additionally electromagnetically neutral vector boson, the Z^0.

Technically, a weak isospin I_w is introduced, as well as the weak hypercharge Y. Both newly introduced quantities are connected to the electromagnetic charge Q, where the hypercharge is calculated as $Y = 2Q - I_w^3$. While the left handed chiral feminons are assigned to $I_w = 1/2$ doublets, the right handed particles form $I_w = 0$ singlets.

Therefore the $SU(2) \times U(1)$ gauge group is satisfying all constrains. Fermionic flavours are introduced as well as a separation of left and right handed fermions. The resulting massless gauge bosons are the isotriplet W_i and the B_0 singlet. The mixture of W_3 and B_0 creates the Z^0 and γ bosons, while the mixing of W_1 and W_2 result in the W^+ and W^- states.

$$\begin{pmatrix} W_1 \\ W_2 \\ W_3 \end{pmatrix}, B_0 \qquad \rightarrow \qquad \begin{pmatrix} W^+ \\ Z \\ W^- \end{pmatrix}, \gamma \tag{1.5}$$

From the spontaneous symmetry breaking of the Higgs field, the Z^0, W^+ and W^- obtain mass, while the γ stays massless. Due to the large masses of the Z and $W^\pm$ bosons, the weak interaction will be highly suppressed compared to the strong or electromagnetic interaction and thus leads to long lifetimes, when a particles decays weakly due to conservation laws.

1.2.3 Higgs Mechanism

In 1963 F. Englert and R. Brout published the idea of a massive gauge boson which gains its mass by interaction [23]. The Higgs boson was defined as excitation of the Higgs-field which itself is responsible to provide all fundamental particles a mass [24]. Especially for the gauge bosons of the weak interaction this mechanism is needed to understand their masses which occur from symmetry breaking.

By coupling to the SU(2) weak interaction, the Higgs has a weak charge, building a doublet of complex Higgs fields

$$\phi = \begin{pmatrix} \phi_1 \\ \phi_2 \end{pmatrix} \tag{1.6}$$

The potential of the Higgs field, schematically shown in figure 1.4 and often referred to as “Mexican hat” potential, leads to the effect of the so called symmetry breaking. With a potential of the free Higgs field in the form of

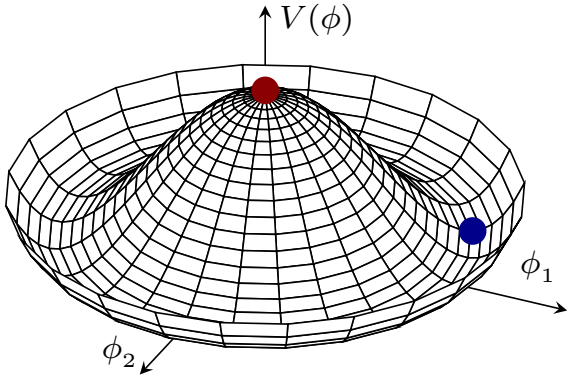

Figure 1.4: Schematic view of the Higgs field potential with its typical "Mexican hat" structure.

$$V = -\mu^2\phi^\dagger\phi + \lambda(\phi^\dagger\phi)^2 \tag{1.7}$$

the Higgs field has an expectation value $V(\phi = 0) \neq 0$ shown as red dot in figure 1.4. This expectation value can only be accessed by experimentally measured quantities [25]. However, this value is not the minimum value, it will be chosen spontaneously, since $\sqrt{\phi_1^2 + \phi_2^2}$ will break the symmetry, as indicated by the blue point.

In 2012 the Higgs boson was experimentally measured by the two collaborations ATLAS [26] and CMS [27] [28]. The measurement of the predicted Higgs provided an additional confirmation of the standard model and thus the Higgs was added as the last elementary particle.

1.2.4 Limits of the Standard Model

While the standard model has been tested to very high precision and is consistent in itself, there are several experimental observations, e.g. in astrophysics, that are incompatible and require physics beyond it.

Most obviously, the gravitation is missing. Up to now no theory is able to successfully combine gravity and quantum field theory to quantum gravity [29]. This arises by the difference in strength of these interactions, leading to the so called "hierarchy problem". The "hierarchy problem" occurs due to the large differences in energy scales for the 3 fundamental forces within the standard model. This hierarchy is highly sensitive to the Higgs mass where the bare mass theoretically strongly differ from the effective mass [30]. Another key observable is the magnetic moment of the muon, where measurements throughout the last decades showed enhanced deviations to theoretical standard model calculations [31][32]. This tension might be resolved recently by precise experimental reference measurements which influence the theoretical predictions [33]. The universality of leptons which claims all interactions of the different leptons are the same besides their different masses in still under debate [34]. Combined with cosmology and

observations from astrophysics, the lack of knowledge about the structure of our universe gets obvious when looking on rotation curves of spiral galaxies which are currently attempted to be explained by dark matter [35][36]. Additional evidence for dark matter is given by gravitational lensing effect and the anisotropy of the cosmic microwave background [37]. Finally, asymmetry between matter and anti-matter in our universe and thus our origin is still not understood and might hint to a CP violation in the strong interaction [38].

1.2.5 Grand Unified Theory

With these open questions and limitations, needless to say physicists are not satisfied. Thus the Grand Unified Theory (GUT) was developed as theoretical model where all three forces of the standard model are unified at an energy scale of $10^{16}\,GeV$, which in the most simple form is described by a SU(5) gauge symmetry group [39]. Being located close to the Planck scale, quantum gravity is not vanishing any longer. With the state of the art knowledge, the interactions do not converge to one point, which can be tuned via missing particles like it is done in various SUSY models were a symmetry between bosons and fermions is introduced [40][41].

1.3 QCD Phase Diagram

The different phases of the strongly interacting matter are commonly described as function of the temperature T and the baryochemical potential μ_B. The baryochemical potential is utilized to quantify the net baryon density. For vanishing μ_B the ratio of matter and anti-matter is equal to unity, whereas at increasing μ_B finite net baryon density rises.

Figure 1.5 shows a sketch of the QCD phase diagram, our surrounding nuclear matter is located at low temperatures close to zero and $\mu_B \approx 930\,\text{MeV}$. While the hadron gas consists of bound hadrons, extreme conditions lead to a change of the phase and thus result in the QGP.

This phase transition is widely studied by theorists where the lattice QCD calculations can describe the area of vanishing baryochemical potential. The transition is shown to be a cross over [42]. The transition temperature is accurately estimated using five different observables and results in a temperature of $T_C = 156.5 \pm 1.5\,\text{MeV}$ [43]. This is consistent with measurements from the ALICE collaboration [44]. This cross over describes the phase transition with the same abundance of quarks and anti-quarks $(\mu_B = 0)$ which was the case for the early stages of the universe. This is not the case for the QCD phase diagram at non-vanishing baryochemical potential.

Several theoretical calculations with different approaches are predicting a first-order phase transition at larger μ_B, including for example methods of functional renormalization groups [46] or Dyson-Schwinger equations [47].

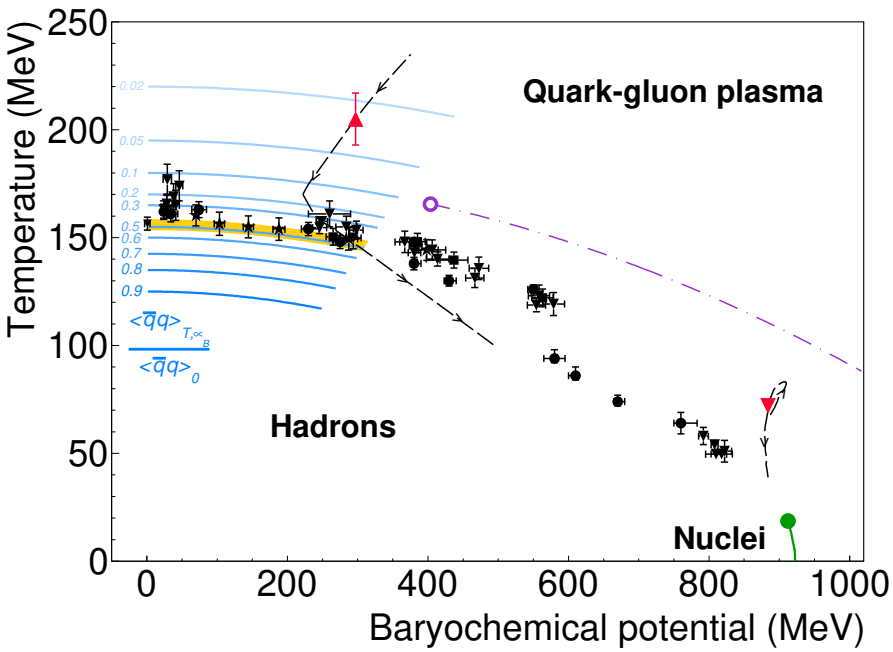

Figure 1.5: Schematic view of the $T - \mu_B$ plane of the QCD phase diagram with theoretical calculations and experimental accessed regions [45].

Thus a critical point is expected in between the crossover at small μ_B and this first order phase transition. Not only the critical point is discussed as one of the most interesting topics in heavy ion physics, but also the overall structure of dense nuclear matter at high baryochemical potential μ_B.

The area of dense nuclear matter at high μ_B is of particular interest for its analogous behaviour to neutron stars and neutron star mergers. In dependence on the equation of state and its composition the neutron star density is estimated in the regime of a factor $3 - 12$ larger than nuclear ground state density [48]. In this context, the interplay of hyperons (Y) and nucleons (N), shortly written as YN interactions at high densities is discussed theoretically, while additional experimental results of separated production rates of Σ and Λ baryons would enable a more precise comparison with theoretical predictions of the equation of state [49]. Especially the merger of neutron stars, so called binary neutron star merger events seem to take place under very similar thermodynamical conditions as heavy ion collisions at SIS energies [50]. Investigating dense nuclear matter at SIS thus can constrain parameters for astrophysics. Figure 1.6 compares simulations of the time evolution of dense matter in astrophysics and in the laboratory.

The similarities are obvious, even though there is a large discrepancy of the scale in time and space. Most importantly, the calculated densities, which are represented in the color code, are very similar. This visualizes the capability of reproducing neutron star merger densities in the laboratory for periods of a few fm/c. The abundance of hyperons in neutron stars and their influence on the formation process of neutron stars is widely discussed in astrophysics [51].

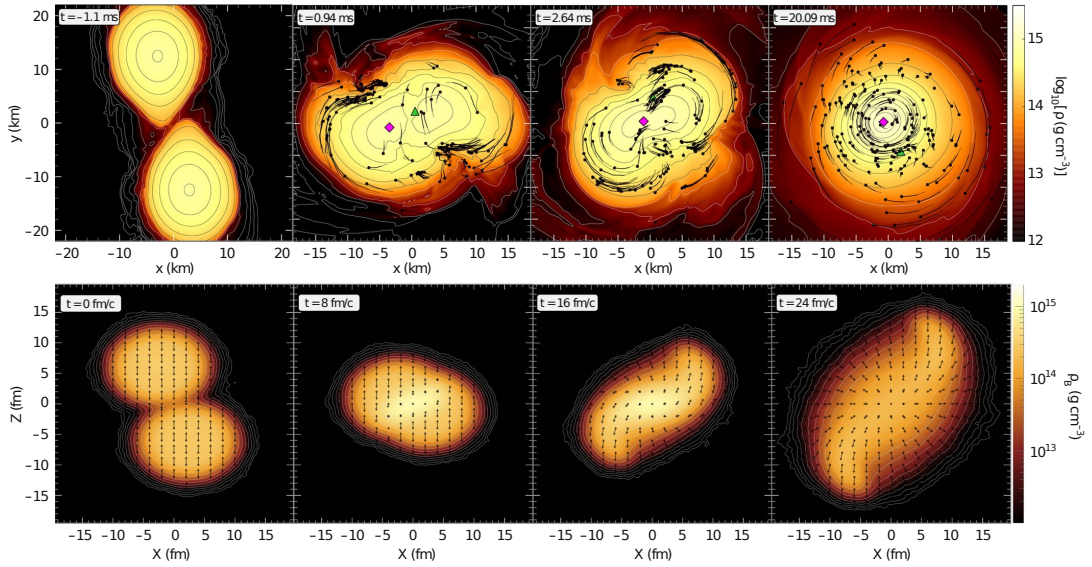

Figure 1.6: Time evolution of the collision of nuclear matter which forms extreme densities in neutron star merger events in the top row and heavy ion collisions in the bottom row [45].

In the region of the highest μ_B and low temperatures a phase of color superconductivity is predicted [52]. In this phase, the Fermi gas produces a condensate of Cooper pairs in the vicinity of the Fermi surface. The feasibility of experimental accessibility of this region is under strong debate [53] [54].

1.4 Heavy Ion Collisions as Diagnostic Tool

The following sections will shortly summarize a few approaches of experimentalists to contribute to the quest of understanding the QCD phase diagram with heavy ion collisions as diagnostic tool.

Heavy ion collisions are the unique tool to create extreme conditions of high temperatures and pressures which are needed to study the phase diagram of strongly interacting matter. A deconfined state of matter is only produced at high temperatures and energy densities, which are generated in the laboratory via heavy nuclei collisions at high collision energy. For collisions in the LHC energy regime, the formation of quark-gluon plasma is observed and studied, where as the medium at GSI SIS18 energies will not be fully deconfined.

An evolution of heavy ion collisions is depicted schematically in figure 1.7. In the very left picture, the two Lorentz contracted nuclei in their initial state are approaching each other until the collision in the second most left picture. Dependent on the energy of the system, a quark gluon plasma can be created in the third step, or for smaller energies a fireball with medium properties of interest is created without QGP formation by converting the available center of mass energy provided by the nuclei and breaking up hadron structures. The upcoming expansion of the fireball leads to a decrease of the energy density and possibly

a thermalization with a following chemical freeze-out, from which on particle yields of each species are constant and only elastic interactions take place up to the kinematic freeze-out [55].

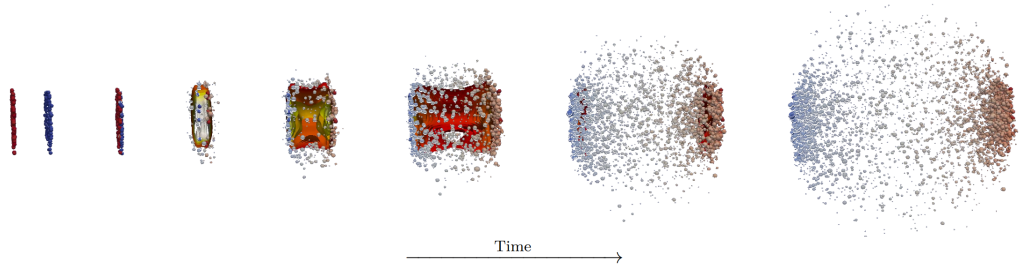

Figure 1.7: Evolution of a heavy ion collision. Figure taken from [56].

For a systematic exploration of the entire QCD phase diagram, results from experiments at accelerators all over the world are combined, each experiment being dedicated to a certain region. LHC at CERN provides the highest energies, reaching up to a few TeV, in heavy-ion collisions at the center of mass [57] [58]. RHIC is the second largest collider with up to $\sqrt{s_{NN}} = 200\,\text{GeV}$ in Au+Au collisions, but also providing access to energies down to $7.7\,\text{GeV}$ in collider mode and $3\,\text{GeV}$ in the fixed target mode [59] [60]. In the intermediate energy regime, NA61/SHINE at CERN SPS is measuring various heavy ion system collisions, covering the region of $\sqrt{s_{NN}} = 5.1 - 16.8\,\text{GeV}$ [61] [62]. The low energy regime with large baryochemical potential is or will be studied at the facilities of J-Parc [63], NICA [64] and GSI/FAIR, covering the lowest center of mass energies up to $\sqrt{s_{NN}} = 5\,\text{GeV}$.

1.4.1 Flow

Flow is one of the most intuitive observables to study collectivity of the emitted particles from the interaction. It was predicted, that nuclear matter under extreme conditions behaves like a fluid and thus is modeled in fluid dynamical models. A similar behaviour of nuclear matter under extreme conditions and fluid dynamical models was predicted [65][66]. Flow is connecting the particle emission distribution with the pressure gradient of the created hot and dense matter [67]. The anisotropic flow is commonly described as Fourier expansion of the Lorentz invariant particle momentum distributions of emitted particles [68] [69]:

$$E\frac{d^3N}{d^3p} = \frac{1}{2\pi}\frac{d^2N}{p_t dp_t d_y}\left(1 + \sum_{n=1}^{\infty} 2v_n cos\big(n[\phi - \psi_r]\big)\right) \tag{1.8}$$

The true reaction plane is denoted as Ψ_r, ϕ is the azimuth angle of the particle and a sin term is vanishing due to the symmetry with respect to the reaction plane. By averaging all particles in the event and accordingly correcting for acceptance, the flow coefficients v_n are calculated.

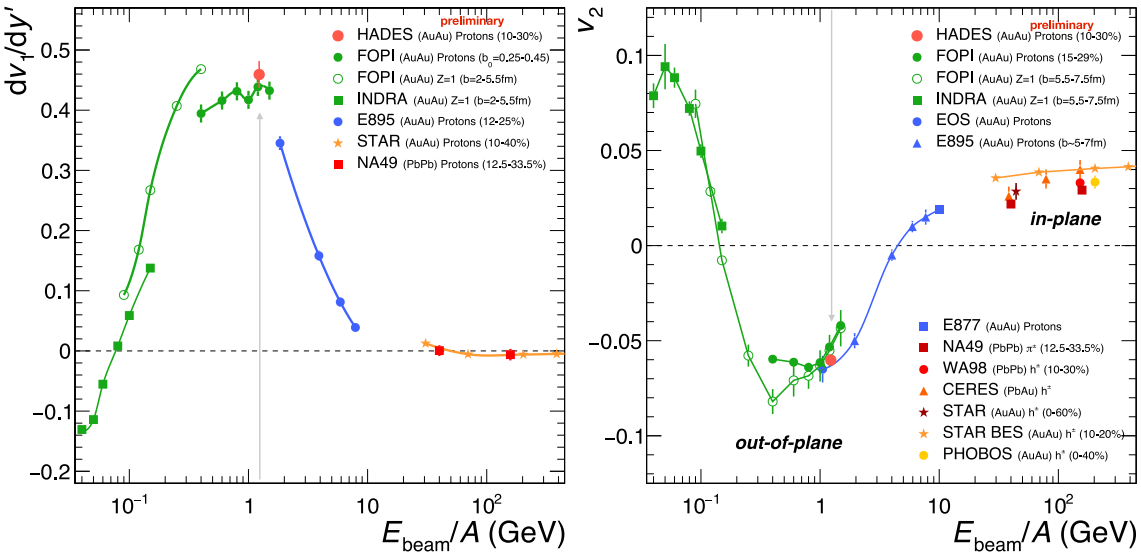

Figure 1.8: The so called direct flow v_1 dependency on the kinetic beam energy for existing world data is shown on the left, and the elliptic flow v_2 on the right hand side [70].

The spatial anisotropy is used a hadronic observable of the full evolution of the fire ball, since it is most pronounced at the early stage of the fire ball evolution [71]. In experiments, the flow coefficients of various particles from mesons up to hyperons and light nuclei are measured and analyzed, as shown in [72] and references therein. Especially higher order flow coefficients are sensitive to the bulk properties of the dense nuclear matter and can help disentangling various contributions. Due to its direct connection to the equation of state, theoretical models can be adjusted by tuning the density dependent potentials, to describe the flow.

1.4.2 Electromagnetic Probes

In heavy ion collisions, the created dense matter emits dileptons during the whole evolution. Since the dileptons do not interact via the strong interaction, they are utilized to probe all stages of the collision without additional modification. Therefore, dielectrons as penetrating rare probes provide information about the initial NN collisions, possible medium modifications of hadrons, as well as the temporal evolution and fireball lifetime [73]. Starting in the 1990s the CERES [74] and DLS [75] collaborations, both being designed for high precision dielectron measurements, published their first results. They both observed an enhanced excess yield in the low invariant mass region [76] which is dominated by the decay of vector mesons and sensitivity to medium modifications.

Following these pioneering experiments, HADES [77] and NA60 [78], but also PHENIX [79] were designed and built, dedicated to measure dileptons with highest precision. However, also ALICE [80] and STAR [81] could contribute to this

subject. Thus, finally a wide energy range is accessible from LHC energies of a few TeV down to SIS18 energies of less than one AGeV.

While ALICE, STAR and HADES are currently measuring, additional experiments are currently build, like the CBM experiment which will cover the beam energy regime of $\approx 4.5 - 15$ AGeV [82].

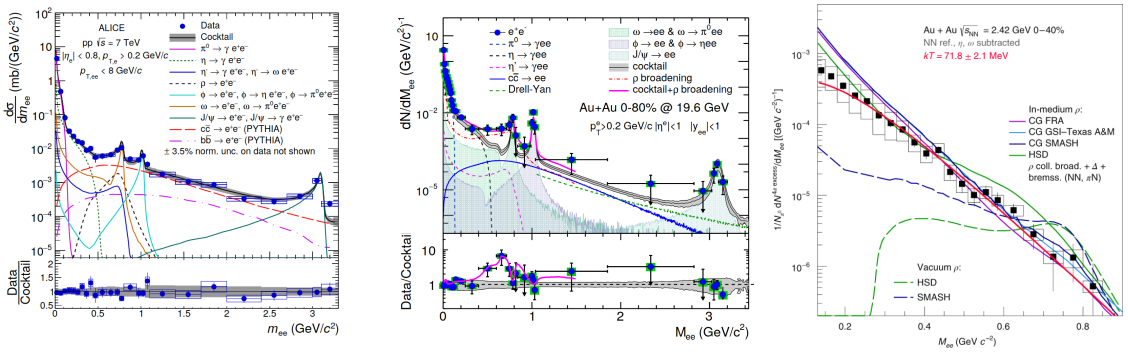

(a) ALICE (b) STAR (c) HADES

Figure 1.9: Available dielectron spectra for a wide range of energies from the very largest energy of 7 TeV measured by ALICE in p+p collisions [83] on the left, an intermediate beam energy measured by STAR [84] and the very lowest beam energy of 1.23 AGeV beam energy which was measured by HADES [45], where the two latter spectra both show Au+Au collisions.

The different experiments provide consistent information about a broadening of the ρ meson, which is seen as in medium effect. In case of high energies, also radiation from the quark-gluon plasma is seen. Furthermore, spectra allow for temperature estimations.

1.4.3 Event-by-Event Fluctuations

Measuring the critical point of the QCD phase diagram is emphasized as one of the main goals in heavy ion collisions, for which event-by-event fluctuations would be a promising observable. Any fluctuations of a conserved quantity, like for example proton or even better baryon number, strangeness or net electromagnetic charge is predicted to be sensitive to a near by critical point by a non-monotonic behavior or the control parameters [85][86].

Measured cumulants k_n provide insight in the multi-particle correlators as well as being directly connected to the equation of state by

$$\frac{1}{VT^3}k_n = \frac{\partial^n \hat{p}}{\partial \hat{\mu}^n} \tag{1.9}$$

where $\hat{\mu} = \frac{\mu}{T}$ represents the reduced chemical potential and $\hat{p} = \frac{p}{T^4}$ is the reduced pressure [87].

The cumulants itself can be accessed as shape parameters of measured distribution, The first cumulant is defined as the mean of the distribution, and the

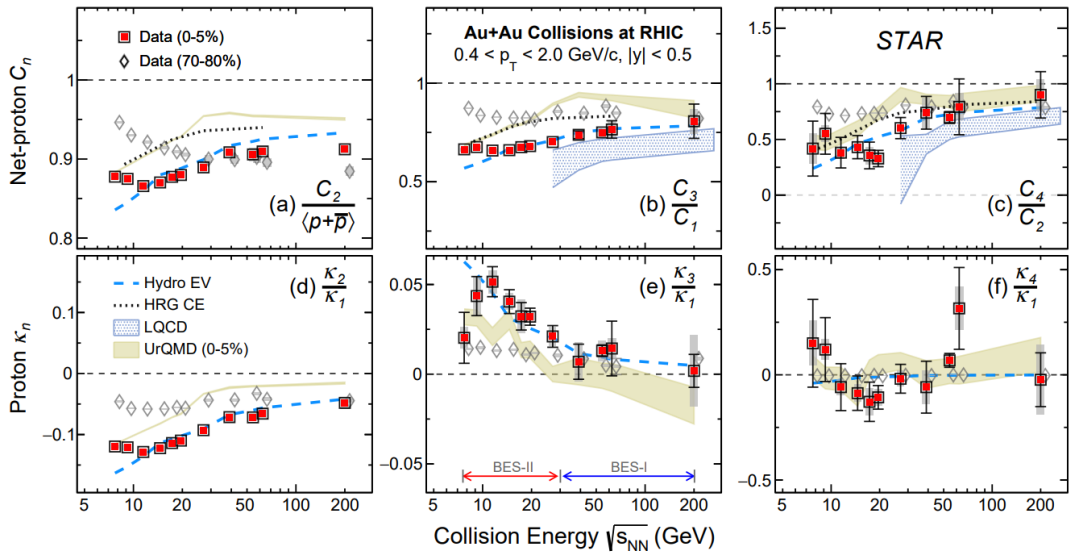

Figure 1.10: Experimental measurement of net proton cumulants for the beam energy scans of the STAR experiment [91]. Overlayed are theoretical model calculations.

higher order cumulants represent the standard deviation, skweness $S = \langle(\delta N)^3\rangle/\sigma^3$ and kurtosis $\kappa = [\langle(\delta N)^4\rangle/\sigma^4] - 3$ and their interplay [2].

In near vicinity of the critical point, the baryon number is related to thermodynamic derivatives via

$$-\frac{\partial^3\omega}{\partial\mu_B^3} = \frac{\partial\chi_B}{\partial\mu_B} \tag{1.10}$$

where ω is the density of thermodynamic states while χ_B is the baryon number susceptibility which itself is defined as

$$\chi_B = -\frac{\partial^2\omega}{\partial\mu_B^2} = \frac{(\delta N_B^2)}{VT} \tag{1.11}$$

the susceptibility diverges [88]. This implication originates in the diverging correlation length. A non-monotonic behaviour of the moments would thus imply a critical behaviour, assuming the time and spatial evolution survived and can still be accessed [89]. The effect of a diverging correlation length is influencing especially the higher moments as pointed out in [90].

In experimental data, ratios of the cumulants are used in order to cancel to at least first order volume effects as shown in figure 1.10. The measured data is compared to theoretical calculations without critical point, which leads to deviations. Especially in $C_4/C_2 = \kappa\sigma^2$, the model calculations show unexpected behaviour for energies of $\sqrt{s_{NN}} \approx 20$ GeV which is currently under debate.

[2] $\delta N = N - \mu$ with μ being the mean of the distribution, σ is the standard deviation

1.5 Strangeness Production

Strangeness is widely used as diagnostic tool to describe the properties of the produced bulk matter [92][93]. The initial state of the reaction can be accessed and thus strangeness measurements provide direct inside to the thermodynamics of the medium. Since our ordinary matter consists only of protons and neutrons which together form all known nuclei, there is no net strangeness available. By quantum fluctuations, virtual $s\bar{s}$ pairs can be created and contribute to the virtual soup of sea quarks within the nucleus [94].

For the production of real strange quarks, the following processes displayed in figure 1.11 are contributing:

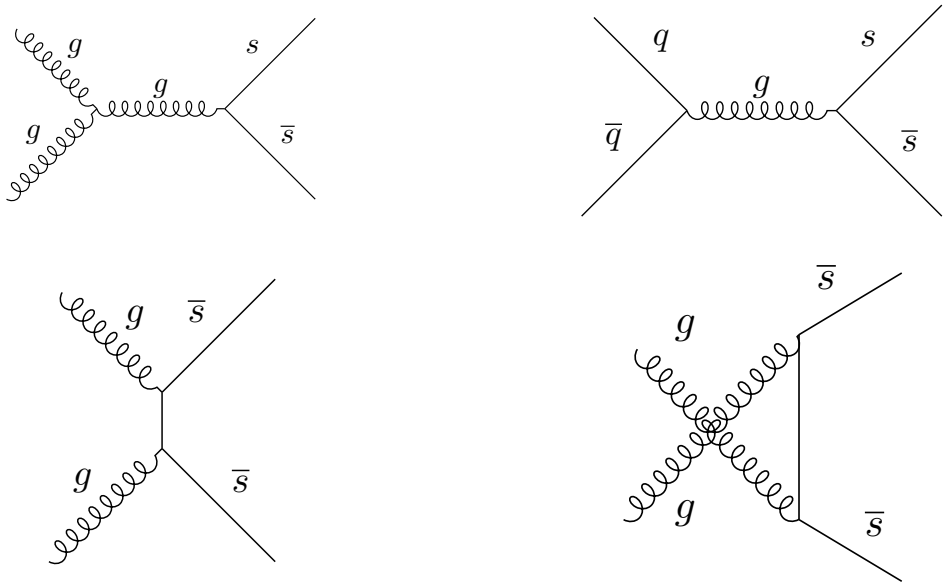

Figure 1.11: Fundamental processes of strangeness production in heavy ion collisions.

For all Feynman diagrams, the time axis goes from the left to the right with an arbitrary y axis. While in the upper right picture, the pair of $s\bar{s}$ is created by an annihilation of a pair of light $u\bar{u}$ or $d\bar{d}$ quarks, the remaining diagrams show the strangeness production by gluon fusion, where always several gluons are involved for color conservation purposes. Thus strangeness is created by fundamental principles of the QCD, with the fundamental processes of partonic flavor creation

$$gg \rightarrow s\bar{s}, q\bar{q} \rightarrow s\bar{s} \tag{1.12}$$

Additionally excitations via partonic qs as well as gs scattering can occur [95].

Due to energy conservation, there must be enough energy in the system to produce new hadrons. Heavy ion collisions can be described as multiple simultaneous nucleon nucleon collisions. The available energy for each single NN collision is denoted as $\sqrt{s_{NN}}$, which needs to exceed the production threshold of a desired particle.

At SIS18, the provided energies are of the same order of magnitude as the threshold energy for strangeness production which differs for the various hadron species, as summarized in table 1.1.

Production channel	$\sqrt{s_{NN}}\,[GeV]$
$NN \rightarrow N\Lambda K$	2.55
$NN \rightarrow N\Sigma^0 K$	2.63
$NN \rightarrow N\Sigma^* K$	2.82
$NN \rightarrow N\Lambda^* K$	2.84
$NN \rightarrow NNK\overline{K}$	2.86
$NN \rightarrow NN\Phi$	2.89
$NN \rightarrow N\Xi^- KK$	3.25
$NN \rightarrow N\Omega KKK$	4.10

Table 1.1: Strangeness production thresholds for various production channels in nucleon nucleon collisions.

In this table, N is either a proton or neutron while the kaons K represent either a K^0 or a K^+ while the anti-kaons $\overline{K}$ are a $\overline{K}^0$ or a K^-, dependent on the electromagnetic change which is always conserved. Even without reaching the threshold energy from a free NN collision, sub threshold particle production can occur in AA collisions. This had been measured in several experiments, e.g. shown in [96], as well as those examining deep sub-threshold production of $\sqrt{s_{NN}} - \sqrt{s_{Thr}} = -640$ MeV [97]. Several physics mechanisms are contributing to these cases. The most obvious difference between AA and NN collisions is the additionally available Fermi momentum of $p_F \approx 300$ MeV/c, which slightly increases with the size of the nuclei [98]. This additional momentum smears out the overall available energy and allows the sub threshold production with respect to free NN collisions. In addition to in-medium effects, such as the modification of spectral functions of the strange hadrons and their modified momentum distributions, two or multi step processes within the collision influence the measured results [99]. In AA collisions, sequential NN collisions can occur forming intermediate resonances such as Δ or N^*s. These particles may subsequently collide, thereby accumulating energy over the course of multiple collisions. Besides Fermi momentum and multi step energy accumulation, so called strangeness exchange reactions can take place. For those a light strangeness containing hadron is produced in first interactions. This hadron later on exchanges its strange quark with surrounding hadrons to form resonances with larger threshold. Especially for the K^- this process is crucial at lowest energies since strange quarks are energetically always favored to be bound in baryons. However, with a $\pi^-\Lambda \rightarrow K^- n$ reaction, the K^- is produced without reaching the K^- production

threshold. These so called final state interactions take place in the time between chemical freeze-out and kinetic freeze-out taking place at even lower densities [100].

The multiplicity of strange hadrons and especially their abundance in comparison to non strange hadrons is providing information on their production process. Different yields are expected for production in a hadron gas and a QGP. In addition, for low energies such as at SIS18, medium effects on interactions and multi-step processes can be studied.

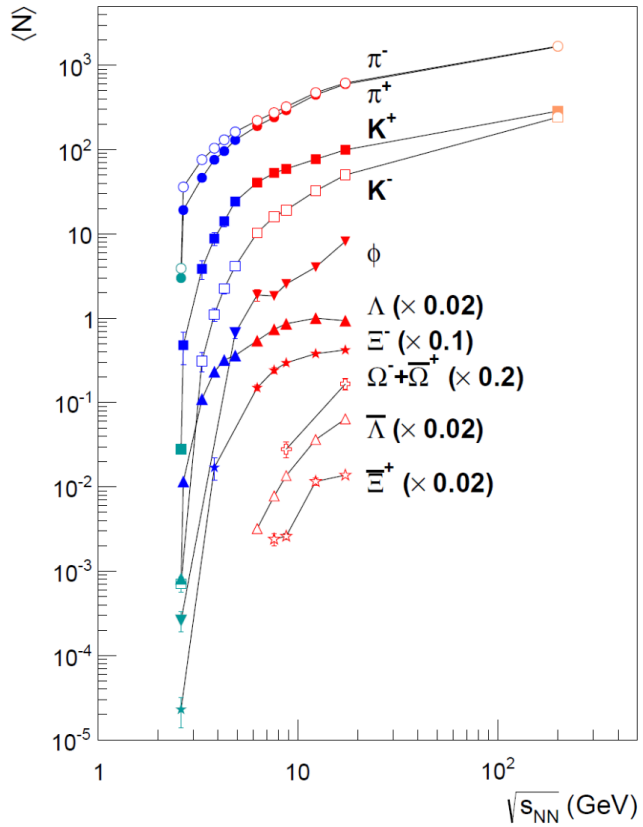

Figure 1.12: Measured strangeness containing particle yields in comparison to the charged pion yields in dependency of the available center of mass energy. Figure taken from [101]. More details are written in the text.

The measured strangeness production within a large range of center of mass energies in heavy ion collisions is summarized in figure 1.12, where the baryons are scaled down arbitrarily for better visualization. The orange data points are measured at RHIC [102], the red data points are from SPS [103][104] [105][106], AGS data is shown in blue [107][108][109][110][111][112] and HADES data from SIS18 in green [113][97]. This thesis aims at providing additional information on hyperon production at the steep decline for low center of mass energies.

Figure 1.13 shows the energy dependent relative strangeness production either as K^+/π^+ ratio or as E_s. E_s combines results of strange hadrons as $E_s =$

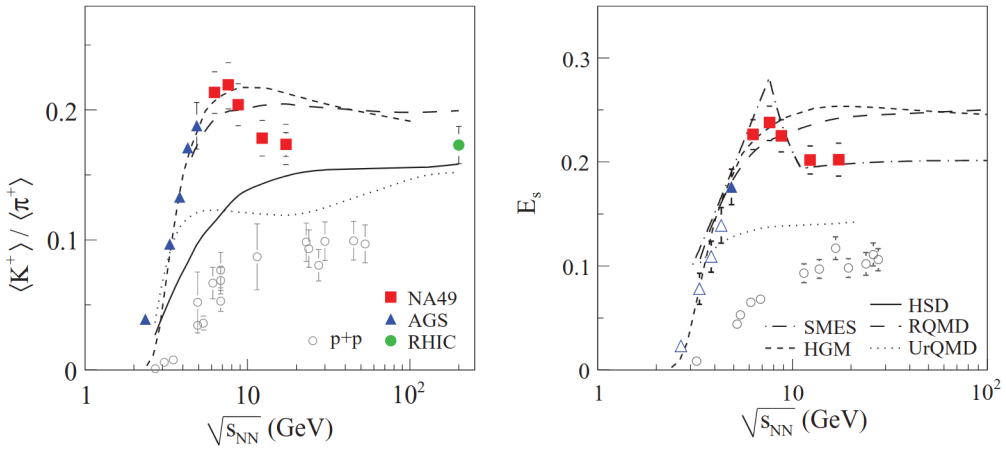

Figure 1.13: Experimental measurement of the K^+/π^+ and E_s ratio with a clear "horn" structure [114]. More details are written in the text.

$\langle\langle\Lambda\rangle + \langle K + \overline{K}\rangle\rangle/\langle\pi\rangle$. A maximum is visible around $\sqrt{s_{NN}} \approx 7$ GeV for both distributions measured by the NA49 Collaboration. This so called "horn" structure was validated with high precision [115] indicating the region from where on with rising energy, a deconfined state is created in AA collisions. This maximum of relative strangeness production is located at around 7.7 GeV and marks the region where a baryon dominated system changes to a meson dominated system [116].

As already states, SIS18 energies correspond to center of mass energies which are close to the production threshold of all various strangeness containing hadrons. Thus, the multiplicity measurements in AA collisions provide insight in the production mechanisms which differ from the free nucleon nucleon collisions.

1.6 The Σ^0 Baryon

As described in section 1.2.1, quarks are forming hadrons, namely mesons and baryons. The Σ^0 contains 3 quarks (uds) which characterizes it as baryon. The comparison in table 1.2 between Σ^0 and the Λ baryon clearly show the similarity of those two states. The Σ^0 baryon ground state is characterized by the following attributes:

The identical quark content leads to a very similar mass with a small difference of only $\Delta M = m_\Sigma - m_\Lambda \approx 77\,\mathrm{MeV/c^2}$. This mass difference exists since the two states are members of different isospin multipletts. Since the Λ has I=0, no charged Λ ground state exists, while the charged Σ ground states exist with I=1 and I_z= -1 for the Σ^- and I_z=1 for the Σ^+ respectively. The distinction between Σ^0 and Λ is attributed to the spin-spin coupling of the u and d quark. In case of identical spin orientations, a Σ^0 is formed while an opposite spin orientation results

	Σ^0	Λ
Mass $[MeV/c^2]$	1192.6	1115.7
Lifetime $[s]$	$7.4 \cdot 10^{-20}$	$2.6 \cdot 10^{-10}$
Quark content	uds	uds
Baryon number	1	1
Isospin (I_z)	+1 (+0)	0 (+0)
Strangeness	-1	-1
Spin	1/2	1/2
Parity	+1	+1

Table 1.2: Comparison of the quantum numbers of the Σ^0 and the Λ baryons.

in a Λ [117]. A more detailed description of the influence of the spin composition and di-quark coupling within hyperons is described in [118].

Because of the small mass difference between the two participating baryons, the decay can only occur via the electromagnetic force to conserve the 4-vector momentum. Emitting a particle would not be possible as even for pions their mass exceeds the mass difference $m_\pi > \Delta M(\Lambda, \Sigma)$. In addition, a decay via the strong interaction can not take place due to isospin conservation which is not conserved in the electromagnetic force. In general, the Σ decay via a virtual photon was never measured before and is only estimated by QED to be in the order of $5 \cdot 10^{-3}$ [119].

The Λ itself is the lightest baryon containing strangeness and thus will only be able to decay via the weak force into a nucleon and a π. The branching ratio of the Λ in proton and π^- is $63.9\,\%$ and $35.8\,\%$ for the nπ^0 channel [119]. The differences in the branching ratio result from the isospin selection rules within the weak interaction, which are accessible by the Clebsch-Gordon coefficients.

Since the Σ^0 and the Λ are that similar, their production mechanisms are expected to be the same with the only slight difference being the required production energy which is calculated in section 1.5. Due to the short Σ^0 lifetime of $7.4 \cdot 10^{-20}$ s, no separation between directly produced Λ, and those which stem from Σ^0decays is possible without using additional information about the γ. The indistinguishable behavior in experiment leads to missing information when comparing to theoretical models which will be discussed in chapter 8. As example, single particle potentials of the Λ and Σ^0 hyperons in dense baryonic matter are discussed, lacking precise experimental constrains [120].

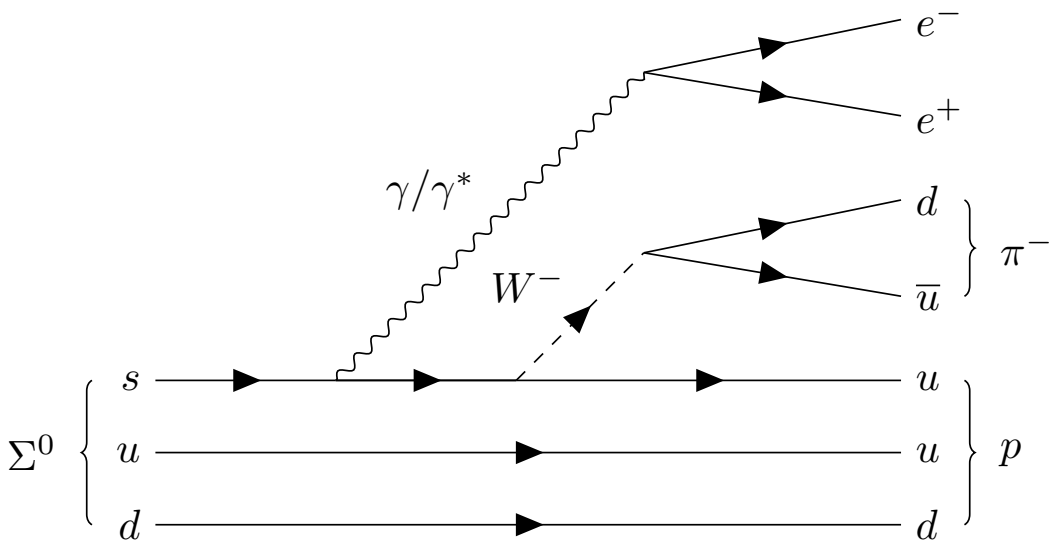

Figure 1.14: Feynman diagram of the Σ^0 decay with sequential decay of the Λ to particles which can be measured by the experimental setup of the HADES detector with optional production of a virtual γ or conversion of the real γ.

Existing Data on the Ratio of Λ/Σ^0

Representing the lightest strangeness containing baryons, particular interest in the Λ and Σ^0 production is obviously justified because those fundamental baryons offer a basis for the understanding of strangeness production mechanisms. Due to their similarity in all quantum numbers and mass, the ratio of Λ/Σ^0 is usually shown because most systematic uncertainties cancel out.

The scarce world data of measured Λ/Σ^0 ratios is illustrated in figure 1.15. The introduction of $\Lambda_{f.o}/\Sigma^0 = (\Lambda - \Sigma^0)/\Sigma^0$ is advantageous, as it provides a description of the ratio at production and eliminates the contribution from the decay of the Σ^0 to the Λ baryons that are produced at freeze-out.

For large center of mass energy, the ratio converges against a constant ratio slightly below $R = 3$, which is argued to be determined by the isospin relation of the Λ as singlet in comparison to the Σ triplet [124]. However, based on the extant body of knowledge, there appears to be an absence of any underlying significance in this value [123][125]. For decreasing excess energies down to a few MeV above Σ^0 production threshold, $\Lambda_{f.o}/\Sigma^0$ is rising dramatically up to a value above 30 in p+p collisions. In fact, this is intuitive, since at threshold the density of states $\rho(E)$ decreases significantly and thus the Λ production is preferred over the Σ^0 production. In addition, the influence of final state interactions in p+p collisions is discussed in great detail [122][125]. Lacking data from heavy ion collisions, obviously this observable is from particular interest, especially since the solid line also predicts in rise for small energies in p+Nb collisions. At $200\,\text{GeV}$ beam energy STAR [126] measured the Λ/Σ^0 ratio of $6.25^{+8.1}_{-4.5}$ in p+Au collisions which is not included due to its inability to provide additional information, which is a

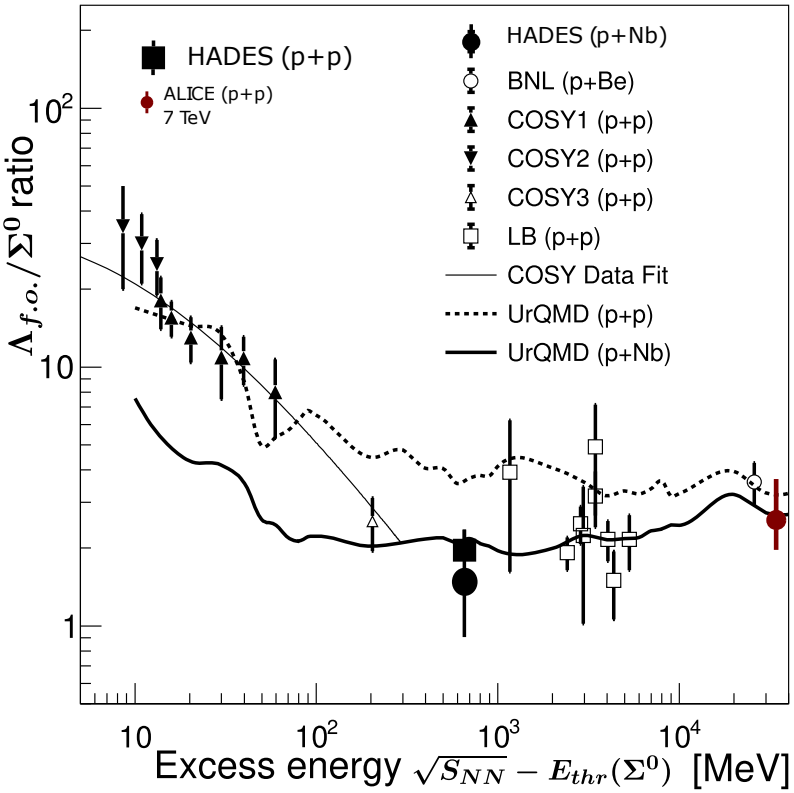

Figure 1.15: Available world data of Λ/Σ^0 ratio measurements. Figure taken from [121] and adapted with additional data points from HADES [122] and ALICE [123]. More details are written in the text.

consequence of its substantial error.

1.7 Theoretical Models

The experimentally extracted observables provide insight to heavy ion collisions and their state of dense matter. The interpretation of those observables requires a fundamental understanding of the processes which took part in the creation and evolution of the fireball. Therefore, several fundamentally different theoretical approaches were developed, which describe heavy ion collisions. The existing statistic models assume a state of matter which is in equilibrium and thus all observables are described by a stochastic probability distribution at the chemical freeze-out at a macroscopic level. On the other hand the time dependent microscopic transport models which are based on attractive and repulsive interactions are utilized to describe the evolution of strongly interacting dense matter [127].

1.7.1 Statistical Hadronization Approach

Statistical hadronization models have successfully been used throughout the years for the description of hadron production at all energy regimes [128][129]. The

key assumption of the statistical hadronization models is that the created hot and dense matter is in thermal equilibrium. Under this condition, a macroscopic thermodynamic description of this state can be performed, requiring only a few macroscopic parameters. Especially for the highest energies, where a quark gluon plasma is formed, the data is described exceptionally well [130].

The thermodynamic quantities describe the system of all hadronic states, including all mesonic and baryonic resonances. Within the framework of the hadron gas model, all these hadronic stats contribute to the partition function Z [129].

$$\ln Z(T,V,\mu) \approx \left[\sum_{i\,\epsilon\,mesons} \ln Z_i(T,V,\mu)\right] + \left[\sum_{i\,\epsilon\,baryons} \ln Z_i(T,V,\mu)\right] \tag{1.13}$$

The excited resonances have a large influence as shown in [131] [132], adding up predicted hadronic states resulted in a much better description of the experimental data due to the resulting feed down contributions. The chemical potential μ consists of the contributions from the electric charge, baryon number and strangeness, μ_Q, μ_B, μ_S. Those potentials ensure conservation laws on average. The grand canonical partition function Z_{GCE} itself is calculated as

$$\ln Z_i = \frac{V g_i}{2\pi^2} \int_0^\infty \pm p^2 dp \ln\left[1 \pm \exp -(E_i - \mu_i)/T\right] \tag{1.14}$$

where V is the volume, g_i the spin degeneracy factor, T the temperature, E_i the particles total energy and μ_i the chemical potential ensuring average conservation of the quantum numbers. Applying the model to the data, the particle yield fit is minimized via

$$\chi^2 = \sum_i \frac{(N_i^{exp} - N_i^{model})^2}{\sigma_i^2} \tag{1.15}$$

χ^2 is calculated by summing up all considered particle species i, while weighting them individually by their experimentally extracted uncertainty σ_i^2. This uncertainty is calculated as the sum of the systematic as well as the statistical errors $\sigma = \sqrt{\sigma_{sys}^2 + \sigma_{stat}^2}$ from experiment.

1.7.2 Transport Approach

Differently to the model ansatz for statistical hadronization, all transport models require far more physical details about the microscopic interactions and their time evolution. In general, the transport approaches do not rely on the assumption of an equilibrium, which is the essential prerequisite for the statistical hadronization models. Different reaction and thus production mechanisms for the wide beam energy range of around 1 GeV up to a few TeV is challenging for transport models when describing the reaction with a superposition of the underlying processes [133]. Especially for the low energy regime of moderate T and μ_B there is no solution to calculate QCD from first principles. Models thus highly rely on experimental observables [134]. In general, transport models require input parameters like hadron masses, decay width, branching ratios but also additional information about the cross sections, which might also depend on density. The density within the nuclei is defined by the Woods-Saxon distribution as

$$\frac{dN}{d^3r} = \frac{\rho_0}{\exp\frac{r-r_0}{d}+1} \tag{1.16}$$

which can be modified in terms of deformation or additional Fermi-motion. All transport models are based on hadron propagation including all possible interactions. Thus the fundamental equation of the transport model approaches is the relativistic Boltzmann equation (see 1.17) which treats binary reactions between all implemented particle species [135].

$$p^\mu \cdot \partial_\mu f_i(x^\nu, p^\nu) = C_i \tag{1.17}$$

This equation is based on the continuity equation of free non-interacting particles ($C_i = 0$). The subscript i denotes the particle type and f_i is the corresponding distribution function. Interactions are added with the collision term C_i which itself consists of terms enhancing the particular particle yield by production mechanisms or decreasing the yield by decays.

For large energies reached at RHIC and LHC, the transport model approaches are combined with hydrodynamic model approaches, leading to hybrid models which are describe data with high accuracy [136]. At lower energies, modeling of the resonances becomes important. The Breit-Wigner cross section is utilized for phenomenological description of the available data.

Predictions of the particle production at low beam energies from various transport models are compared in figure 1.16. On the one hand they are very similar in their prediction of hadrons that do not contain strangeness, but on the other hand they differ quite dramatically when including strangeness. Especially for the Ξ^-, which contains two strange quarks and thus shows increased sensitivity. Extended analysis within the UrQMD framework is performed to study the influence of multi-step reactions with strangeness exchange which seem to be crucial to understand the Ξ^- production [137].

Transport codes are divided into those that use the BUU-type event generation approach, where particles are propagated by solving density functionals, and

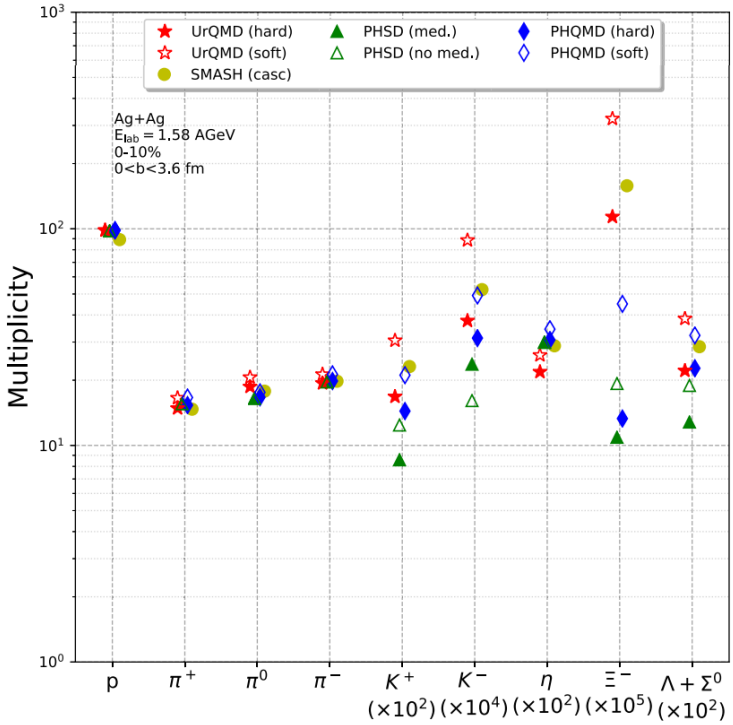

Figure 1.16: Particle production multiplicities predicted by different transport model approaches for Ag+Ag collisions at a kinetic beam energy $E_B = 1.58$ AGeV [138].

those that use the QMD approach. For the latter, the time evolution of nucleons is propagated as wave packets. Besides this categorization, all models can differ in their set of input parameters. Examples for both types of models are given in the following subsections.

1.7.2.1 GiBUU

The Giessen Boltzmann-Uehling-Uhlenbeck (GiBUU) approach is based on the Kadanoff-Baym equation which describes the time evolution of the phase space density [139] [140]. Introducing interactions in form of external forces to the free continuity equation 1.17 leads to the Vlasov equation

$$\Big[\partial_t + (\nabla_p E)\nabla_r - (\nabla_r E)\nabla_p\Big] f(x,p) = 0 \tag{1.18}$$

where mean field potentials are included [139]. An collision term can be introduced which considers production as well as decays of each particular particle species. Adding this additional collision term of the from $C(x,p) = C_{\text{gain}}(x,p) + C_{\text{loss}}(x,p)$ to the free propagation leads to the relativistic Boltzmann equation. Combining it with the external force results in the final Boltzmann-Uehling-Uhlenbeck equation (BUU):

$$\left[\partial_t + (\nabla_p H_i)\nabla_r - (\nabla_r H_i)\nabla_p\right] f_i(\vec{r}, t, \vec{p}) = C[f_i, f_j, \dots] \tag{1.19}$$

The equation is the fundamental basis not only for GiBUU but also for SMASH [141] and PHSD [142]. It determines the phase-space probabilities for interactions in specific time steps. Within these time steps, the propagation is performed assuming a mean field potential. With the inclusion of Fermi-smearing and Pauli-blocking and multi-step collisions including final-state interactions and off-shell potentials, various medium effects are simulated within GiBUU. This is particularly required for an estimation of the production rates close to threshold. Phase space densities are determined by a set of test particles, were the result is exact for $N_{\text{TestParticle}} \to \infty$ and guarantees locality of interactions. Strangeness production within GiBUU is modeled by the channel

$$NN \to BYK \tag{1.20}$$

where N is either a proton or neutron, $B = N$ or Δ; $Y = \Lambda$ or Σ and $K = K^+$ or K^0 [143]. Since strangeness is only produced in a small fraction of the NN collisions, a strangeness specific parametrization based on resonance formation is applied. Those baryonic resonances $R = \Delta^*$ or N^* are produced via $NN \to NR$ and decay via $R \to YK$. The cross sections from [144] are parameterized by

$$\sigma(s) = a(s/s_0 - 1)^b (s_0/s)^c \tag{1.21}$$

with a channel dependent production threshold s_0 and fitted parameters a, b, c.

1.7.2.2 SMASH

Also SMASH (**S**imulating **M**any **A**ccelerated **S**trongly Interacting **H**adrons) is based on the BUU equation, where only two-body interactions are implemented [145].

Resonant cross sections within SMASH are implemented very similar to UrQMD while non resonant cross sections which rely on parameterizations are similar to GiBUU. This is of particular interest, since the latter is the most dominating process for strangeness production. Thus yields are expected when comparing UrQMD and SMASH, which is also visible in figure 1.16. Also the test particle ansatz is the same as in GiBUU. However, compared to GiBUU, SMASH does not include off shell transport. Furthermore, additional resonances are included to improve precision. Strangeness production in SMASH is mostly performed via $N^\star$ resonances, namely $NN \to NN^\star \to NYK$ where the branching ratios are constrained by the PDG and partial wave analysis from the HADES collaboration [146].

1.7.2.3 UrQMD

UrQMD is based on the **Q**uantum **M**olecular **M**odel (QMD) approach [147]. Compared to the BUU type models, UrQMD is using a many-body approach to achieve

the molecular dynamics description. Particles are described as wave packages of finite width in the form

$$\Phi_i(\vec{p_i}, \vec{r_i}, \vec{r}, t) = (\frac{2}{(L\pi}))^{\frac{3}{4}} \exp\left\{ -\frac{2}{L}(\vec{r} - \vec{r_i}(t))^2 \right\} \exp\left\{ (i/\hbar)\vec{p_i}(t) \cdot \vec{r_i} \right\} \tag{1.22}$$

A product of coherent states is calculated as shown in [133]:

$$\Psi(\vec{r_1}, \vec{p_1}, \ldots, \vec{r_A}, \vec{p_A}, \vec{r}, t) = \prod_{i=1}^{A} \Phi(\vec{r_i}; t) \tag{1.23}$$

Here $\vec{r_i}$ and $\vec{p_i}$ are the variables within the variational principle used in the Hartree equation. Those are used to minimize the energy functional of initial state. The resulting equations of motions are calculated by time derivatives [148].

$$\frac{\vec{R}_i}{dt} = \vec{\nabla}_{P_i} \langle H \rangle \quad \text{and} \quad \frac{\vec{P}_i}{dt} = -\vec{\nabla}_{R_i} \langle H \rangle \tag{1.24}$$

Production rates can be calculated by assuming a Hamiltonian of the form $H = \sum_i T_i + 1/2 \cdot \sum_{ij} V_{ij}$. Strange particle production within UrQMD is only performed via resonance excitations of meson and nucleon induced reactions. A large advantage of QMD models compared to BUU models, is that particle correlations as well as fluctuations can be studied, but no medium modifications are implemented. The molecular models struggle with Pauli-blocking and mean field requirements. This issue appears due to the missing symmetrization of the N-body state, which is calculated by the product of all single particle states. Additionally QMD is strictly conserving energy and momentum which is treated differently in the BUU type models. Nuclei formation by clusterization is not included and if required is performed afterwards in the form of an afterburner.

CHAPTER 2

HADES

2.1 GSI Accelerator Setup

The HADES experiment is located at the GSI Helmholtzzentrum für Schwerionenforschung which was founded in 1969 in Darmstadt, formerly named "Gesellschaft für SchwerIonenforschung". It is the largest non-university research centre in the state of Hesse. In order to achieve its research goals, GSI also has a strong focus on design, construction and operation of heavy ion accelerators. The institute's research activities encompass a diverse range of fields, including atomic physics, plasma physics, materials research, biophysics and medical development, as well as information technology in general in addition to the major aspect, nuclear and hadron physics. A number of experimental setups were designed to investigate exotic nuclei, including R3B, FRS-ESR [149], SHIP [150] and TASCA [151]. In contrast, HADES explores the properties of nuclear matter at high net baryon densities and moderate temperatures. This physics program has already been investigated by KaoS [152] and FOPI [153], and will in future be further pursued by CBM. The CBM experiment is currently under construction and will provide additional and complementary information about the properties of matter under extreme conditions [154].

The existing accelerator system is schematically shown in figure 2.1. The UNILAC provides different ions with energies up to 11.4 MeV/u which are injected in the SIS18 with a small horizontal emittance of only 0.42 mm mrad which was measured with Uranium ions in 2022 [156]. SIS18 with a circumference of 216.72 m and a magnetic rigidity of 18 Tm accelerates the injected positively charged ions up to 1-2 AGeV, dependent on the mass and charge of the ions [157]. The beam is extracted either into storage rings or for direct delivery to experimental targets, as in the case of HADES, e.g. HADES uses beams of heavy ions of different size, protons and even pions.

The HADES experiment itself is a fixed target experiment which was developed and optimized since the early 1990s.

Figure 2.2 shows the layout of HADES with all subdetectors as used for the analysis presented in this work. The upgraded RICH and the newly installed electromagnetic calorimeter are of particular interest, as both were newly installed

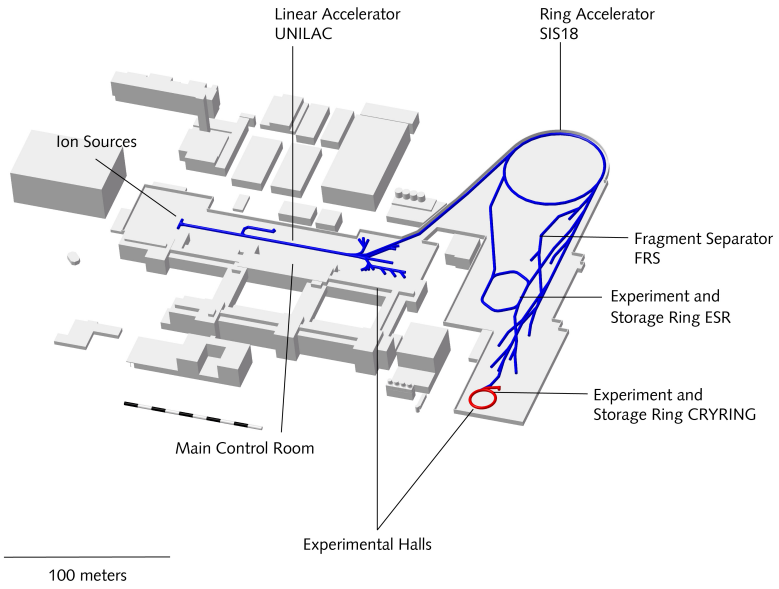

Figure 2.1: Layout of the GSI accelerators [155].

for the March 2019 beamtime. The HADES experiment fulfills the following requirements:

- High acceptance for various particle species, especially leptons
- High reconstruction efficiency for leptons above 100 MeV/c
- Momentum resolution of $\frac{\Delta p}{p} \approx 1\,\%$ for dileptons in the mass range of 200−1000 MeV/c^2 which results in a mass resolution of similar precision
- Capability of measuring high interaction rates, requiring fast electronic readout with sufficient radiation hardness
- Differentiation of rare probes by excellent hadron/lepton separation
- Minimal conversion probability to avoid additional noise in the rare leptonic decay channels

Since its inception HADES has undergone numerous upgrades of detectors as well as readout electronics. Although being primarily build for the measurement of dileptons, HADES also possesses excellent capabilities in the investigation of strangeness production and correlations.

2.2 Experimental HADES Setup

HADES is a sophisticated experimental setup in order to measure a large variety of information necessary to understand heavy-ion and hadron collisions. There-

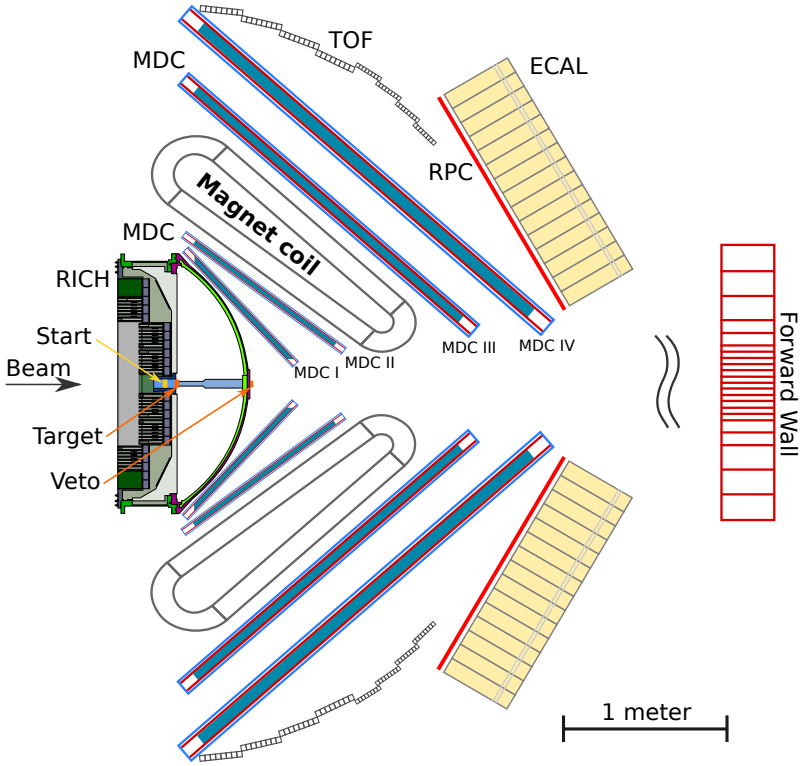

Figure 2.2: The HADES experiment with all sub detectors which were used in the corresponding beamtime in March 2019. Figure taken from [158].

fore, HADES consists of several sub-detector systems each being optimized for specific measurements. All information is combined in order to finally describe the properties of the created matter. All sub-systems depicted schematically in figure 2.2, are described in the following sections.

2.2.1 Start-VETO Detector

The start detector is the first sub detector of the whole HADES experiment. Several challenging requirements are fulfilled by the START detector. A high resolution timing information (T0) with a precision of $\sigma_{T_0} = 50$ ps is provided at interaction rates larger than 10^5 events/s. In addition, the material has to be withstand to high radiation intensity since the beam is going through the start detector. A single-crystal Chemical Vapor Deposition (scCVD) diamond detector fulfills all requirements, offering fast drifting electrons and low interaction probability. As additional advantage, no external cooling is required for diamond detectors [159]. The detector is located 2 cm in front of the interaction target [160]. Despite the detector's inherent radiation hardness, damage can not be fully avoided. Thus, an additional dynamic holding structure allows to change the position with regards to the beam in nine different positions facilitating the replacement of damaged components with new material [161].

The start detector is only 70 μm thick to avoid beam interactions and covers

an area of $4.7 \times 4.7\,\mathrm{mm}^2$. 16 strips of $300\,\mu$m each allow a precise beam profile measurement which is improved in A+A collisions compared to proton or pion induced reactions. The VETO detector is diamond based as well and has dimensions of $8 \times 8\,\mathrm{mm}^2$ and a thickness of $300\,\mu$m. It is placed 70 cm behind the START detector. The combination of START and VETO allows precise anti-coincidence measurements which are used to discard events without nuclear reactions. Additionally, events with reactions of the ion beam fragments are rejected, since here no precise timing is measurable.

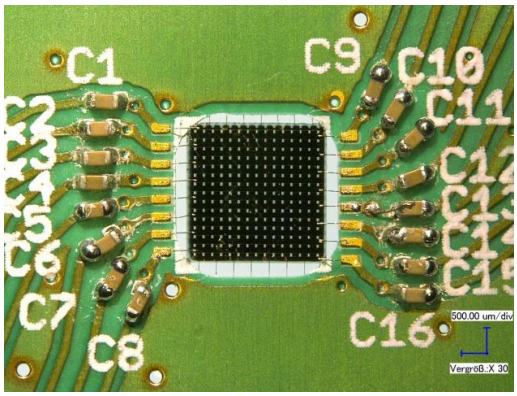

(a) Photograph view of the HADES START detector [161].

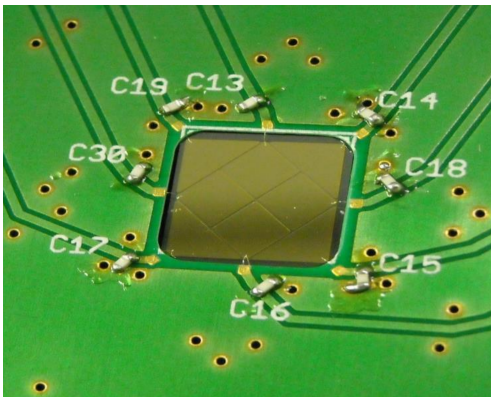

(b) Photograph view of the HADES VETO detector [161].

2.2.2 Target

The silver target which was used in March 2019 consists of 15 segments of $40\,\mu$m thickness each and 3 mm gaps in between the segments. This non-intuitive setup is chosen in order to reduce secondary interactions of the produced particles in the target material. Distances and sizes of the segments chosen such, that produced particles in the detector acceptance do not cross a second target layer. Thus, also less converted are seen in the detector. Integrated over the 15 segments of 0.6 mm thickness each, an interaction probability of $1.5\,\%$ is achieved [162]. This results in a conversion probability in the target region below $1\,\%$. These requirements force a reduced material budget, but the with the used solution high interaction rates around 15-20 MHz are achieved.

In figure 2.4 the mechanical construction of the target is displayed. The silver target segments of 2.2 mm diameter are attached to a capton foil. The foil is placed in different azimuthal orientations which leads to a homogeneous material budget distribution. This is important to avoid additional systematic uncertainties for conversion probabilities.

2.2.3 RICH

The performance of dielectron analysis and all $e^{\pm}$ related analysis highly depends on the RICH detector. The HADES RICH is designed as hadron blind **R**ing **I**maging

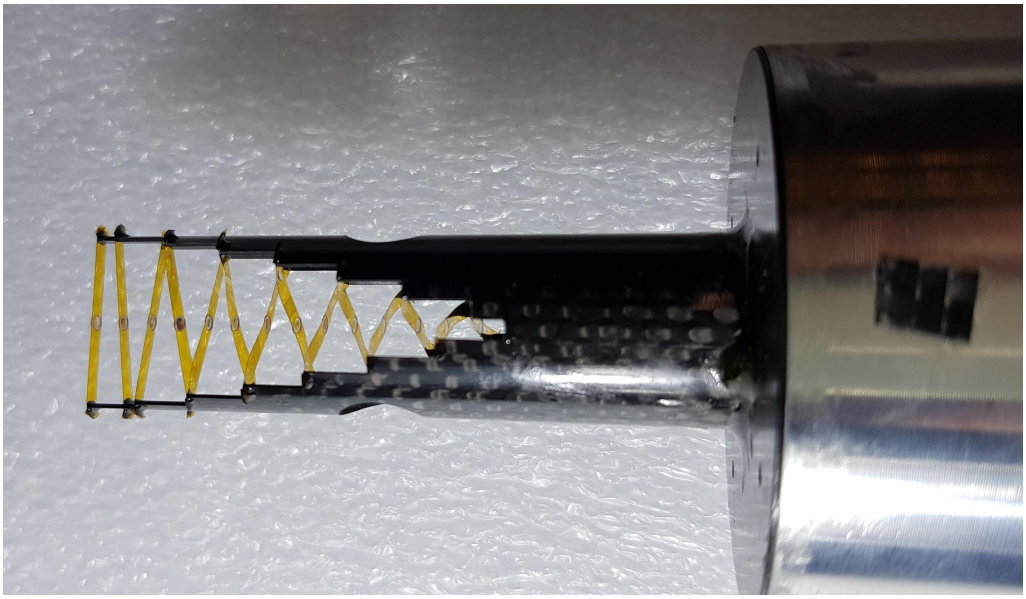

Figure 2.4: Photograph of the Ag target for the beamtime in March 2019.

CHerenkov detector which allows the separation of the rare $e^{\pm}$ from the highly abundant hadrons. Especially the separation between leptons and the lightest hadrons, the charged pions is needed for momenta above p=500 MeV/c. The time-of-flight based PID selection can not distinguish electrons and pions any more, due to timing resolution. Based on the Cherenkov effect, which is a threshold effect, the electron selection in the RICH is much more precise than a conventional velocity measurement. Especially for the discrimination power of the pions as lightest hadrons and $e^{\pm}$ this effect is required. The electron threshold is known to be p≈10 MeV/c. In contrast, the charged pion threshold at p=2.6 GeV/c is significantly enhanced, thereby enabling a high degree of discrimination power for the separation of pions and electrons.

2.2.3.1 Cherenkov Effect

The RICH is based on the Cherenkov effect, which occurs when a particle traverses a dielectric and transparent medium with a velocity $\beta = v/c_0$ larger than the velocity of light c in this specific medium. Due to the refraction index of each individual medium $n = n(\lambda) > 1$, the velocity of light in media $c_n = c_0/n$ is reduced, compared to the one in vacuum c_0. Thus, the required condition for producing Cherenkov light can be expressed as

$$v > c_n = c_0/n \rightarrow \cos\theta_T = \frac{c_n}{v} = \frac{c_0}{\beta c_0 n} = \frac{1}{\beta n} \tag{2.1}$$

where θ_T is the threshold angle of the Cherenkov radiation. Charged particles transversing a medium polarize this medium.

In figure 2.5 the schematic representation of the Cherenkov effect is illustrated. On the left side, a particle with velocity $v < c/n$ is transversing the medium. Due to the electromagnetic charge of the particle, a local polarization takes place. If the particle exceeds a velocity of $v = c/n$, the polarization is not shielding itself symmetrically and thus, a radiation is emitted. The propagation of the coherent wave front is illustrated on the right side.

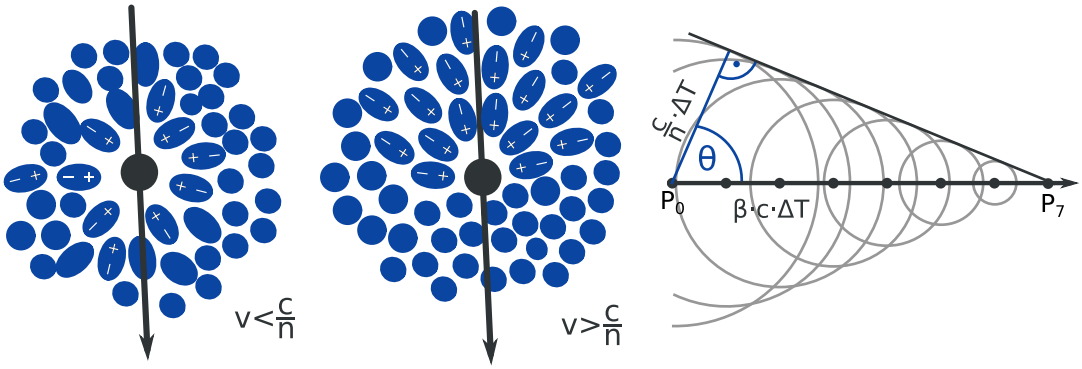

Figure 2.5: Cherenkov radiation production scheme. Figure taken from [158], where it was modified from [163]. Additional information is written in the text.

The Frank-Tamm formula 2.2.3.1 describes the emitted frequency and thus energy spectrum of the Cherenkov radiation photons [164]:

$$\frac{d^2E}{dxd\omega} = \frac{q^2}{4\pi}\mu(\omega)\omega\left(1 - \frac{c^2}{v^2n^2(\omega)}\right) \tag{2.2}$$

The total energy, W, emitted by the charged particle during its trajectory, measured in terms of the path length, L, is calculated as outlined in [163]:

$$W = \frac{e^2L}{c^2}\int\limits_{\beta n>1} \omega d\omega\left(1 - \frac{1}{\beta^2n^2}\right) \tag{2.3}$$

The quality of measuring the charged particle is directly related to the total amount of measurable Cherenkov photons N_γ which is a fraction of the N photons emitted in the energy range corresponding to λ_1 and λ_2.

$$N = 2\pi\alpha L\left(\frac{1}{\lambda_2} - \frac{1}{\lambda_1}\right)\left(1 - \frac{1}{\beta^2n^2}\right) \tag{2.4}$$

where $\alpha = e^2/\hbar c$ is the electromagnetic fine structure constant and n the index of refraction where the dependency on ω is either neglected or averaged.

2.2.3.2 Photon Detection Using Photo-Multipliers

Since this work is especially related to the detection possibility of low energy photons and the RICH as well as the electromagnetic calorimeter are based on photo

multipliers, a short introduction on the principle functionalities is given, see figure 2.6.

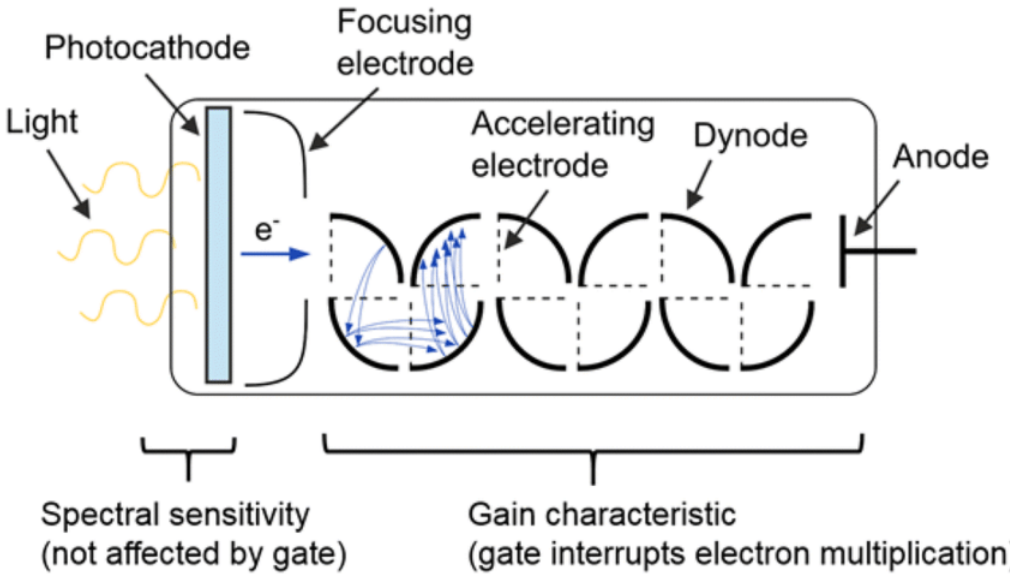

Figure 2.6: Schematic layout of photo-multiplier tubes. Figure taken from [165].

The produced Cherenkov photons have energies of a few electronvolts (eV) corresponding to visible light or light near the ultraviolet spectrum, e.g. $\lambda = \frac{hc}{E} \approx$ 500 nm for 2.5 eV photons. The Cherenkov photons will hit the photo cathode and produce photo electrons as displayed in figure 2.6. With the following dynodes the signal is multiplied, providing a finally measurable signal for the readout electronics at the anode.

RICH

The upgrade of the HADES RICH was successfully finished in 2018. The RICH is now equipped with **M**ulti-**A**node **P**hoto-**M**ultipier **T**ubes (MAPMTs) from Hamamatsu of type H12700 and new readout electronics. The resulting increase in number of measured photoelectrons, coupled with their enhanced spatial resolution, has enabled the development of novel analysis techniques, not being possible before.

The HADES RICH detector is build around the target in front of the magnetic field as shown in figure 2.2 which sets strict limits to the spatial dimensions. On the other hand this position provides only a low amount of material budget and no magnetic field in front of the RICH.

The HADES RICH is a gaseous RICH detector with C_4H_{10} as radiator gas. The refraction index of n=1.0014 results in a threshold value of $\gamma_{\text{threshold}}$=18.9 which translates to momentum thresholds of $p_{thr}(e^{\pm})$=9.64 MeV/c, $p_{thr}(\mu^{\pm})$=1990 MeV/c and $p_{thr}(\pi^{\pm})$=2635 MeV/c. Thus, a high discrimination power between electrons and all heavier particle species is achieved. The produced Cherenkov photons

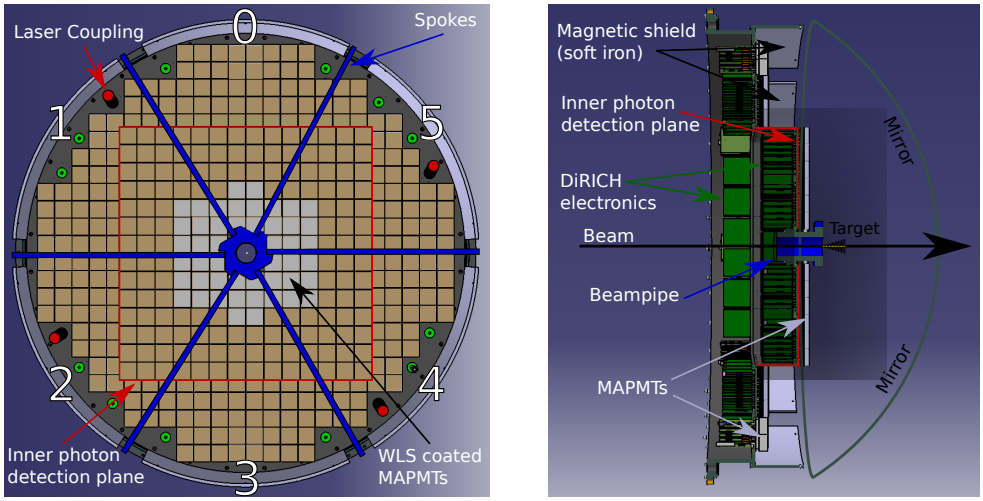

(a) Front view of the HADES RICH (b) Side view of the HADES RICH

Figure 2.7: Schematic view of the upgraded RICH detector. Figure taken from [166].

are reflected and focused by an aluminum coated mirror with a radius of curvature of 870 mm and are detected by 428 MAPMTs each consisting of 64 individual channels. As depicted in figure 2.7 these MAPMTs form two distinct planes with different distances to the mirror [167].

The most inner 14×14 MAPMTs are shifted 120 mm towards the mirror. This setup is chosen to roughly follow the focal plane, resulting in sharp rings with small variations in ring radii as it will be shown later in chapter 4.8. HADES uses Hamamatsu H12700 MAPMTs with quantum efficiencies of 10 % for the lowest and highest measurable photon wave length of 200 nm and 550 nm and reaches quantum efficiencies of 35 % around 350 nm. In the inner most part of the MAPMT plane, 48 MAPMTs obtained a wavelength shift coating (WLS) which allows to absorb high energetic photons and re-emit larger wavelength which then are detectable [168] [166].

2.2.4 Magnet

In the HADES experiment, the magnet for momentum reconstruction is placed between the inner and outer multi-wire drift chambers which will be described in chapter 2.2.5. Besides the high geometrical acceptance and low material budget in the acceptance, the magnet has a high field strength in a very limited area in order to bend the traversing particles strong enough for good momentum determination with out reaching into the RICH or TOF detector. A superconductive magnet with an induced torodial magnetic field fulfills all requirements, also being compact and energy efficient [169]. The six superconducting coils are placed symmetrically around the beam axis as shown in figure 2.8. With a working current of 3566 A, a maximum magnetic field strength of 3.77 T is achieved. The different fields inside a coil or in between two coils are shown in figure 2.9. For the

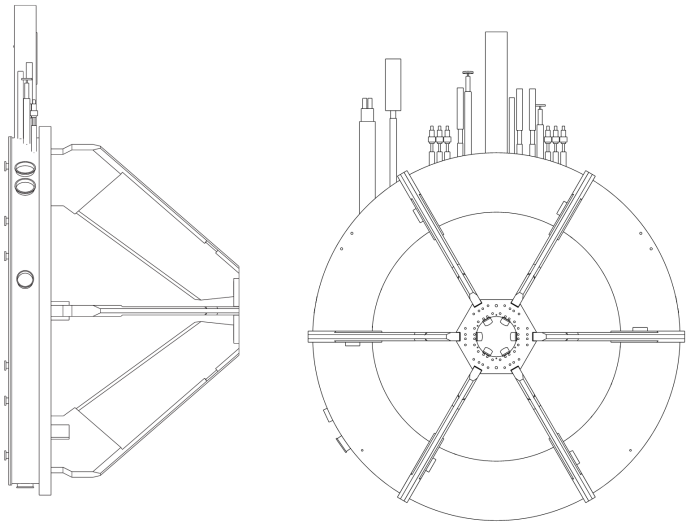

Figure 2.8: Geometry of the superconducting HADES magnet coils which induce a torodial magnetic field in a very limited region. Figure taken from [77].

beamtime in March 2019 which is used in this work, the nominal current was set to 3200 A which is ≈90 % of the maximum setting [1].

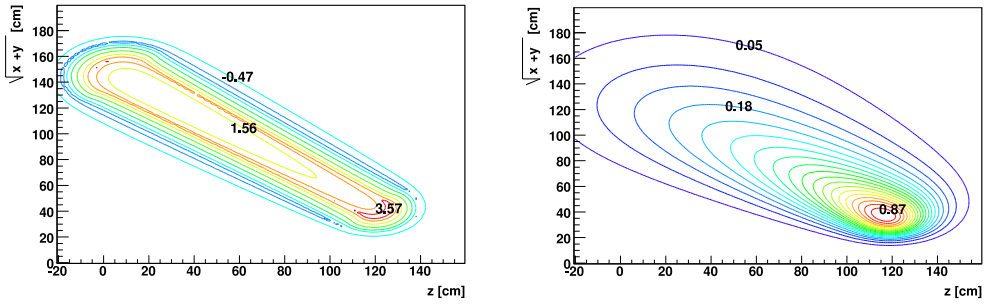

(a) $\phi = 30°$, slice within a coil **(b)** $\phi = 0°$, slice in between two coils

Figure 2.9: Magnetic field strength in dependence on z (along the beam axis) and r (perpendicular on the beam axis) for 2 representative ϕ values. The contour gap sizes are 0.24 T in (a) and 0.046 T for (b) [77].

Those field maps were measured by utilizing Hall probes. The extracted resulting field maps are in good agreement to simulations which were performed with GARField and TOSCA [170][77].

2.2.5 Mini-Drift Chambers

The **M**ini-**D**rift-**C**hambers (MDC) enable the track reconstruction of charged particles. In HADES four planes provide the spatial information of the charged par-

[1] In addition a small data set of ≈10 % of the total statistics of Ag+Ag collisions was taken at 1.23 AGeV beam energy at reduced magnetic current settings of 2500 A and 200 A, respectively.

ticles. The MDCs are divided into the six trapezoidal chambers which cover the full azimuth angle ϕ besides small acceptance holes in between the sectors filled with holding structures. To cover polar angles of $17° < \theta < 85°$ the MDC dimensions scale with the distance to the target and take the magnetic field between MDC planes two and three into account. Table 2.1 summarizes the corresponding dimensions for each individual layer [171]. The size of the cells is chosen such that an almost constant granularity is achieved. In addition to the dimensions, also the gas mixture is listed. The mixture becomes important for the specific energy loss, used for hadron identification in section 4.

Argon is used as counting gas and Carbon-Dioxid is added as quenching gas, which absorbs photons that have been produced from recombination, thus reducing background.

Plane	Sense wires [counts]	Cell size [mm × mm]	Active covered area [m^2]	Gas volume [l]	Counting gas composition
MDC I	1006	5 × 5	0.35	18	Ar (70 %), CO2 (30 %), H2O (1000 ppm)
MDC II	1104	6 × 5	0.53	27	Ar (70 %), CO2 (30 %), H2O (3000 ppm)
MDC III	1098	12 × 8	2.21	194	Ar (70 %), CO2 (30 %)
MDC IV	1168	14 × 10	3.21	321	Ar (70 %), CO2 (30 %)
Total	4376		6.3	560	

Table 2.1: Specifications of the individual MDC layer geometry per sector [172].

The 4376 sense wires per sector result in a total amount of 26256 wires. Each plane consists of six layers which all have different orientation within their x-y plane to increase the resolution and to allow for the removal of ghost tracks. The two wires layers in the center, which have the same orientation of the wires, are shifted by half the distance between two wires to avoid redundant information.

Ionizing charged particles traversing the MDCs will then induce a measurable current. The potential- and cathode- wires are made from aluminum of only 80-100 μm diameter. The signal wires even only have a diameter of 20-30 μm. All this effort is made in order to have very low material budget in the MDCs. The cathode wires are operated with a voltage of 1750-2150 V, depending on the plane. All information is read out by customized boards which are attached to the holding structures in between two sectors which avoids additional material inside the active volume.

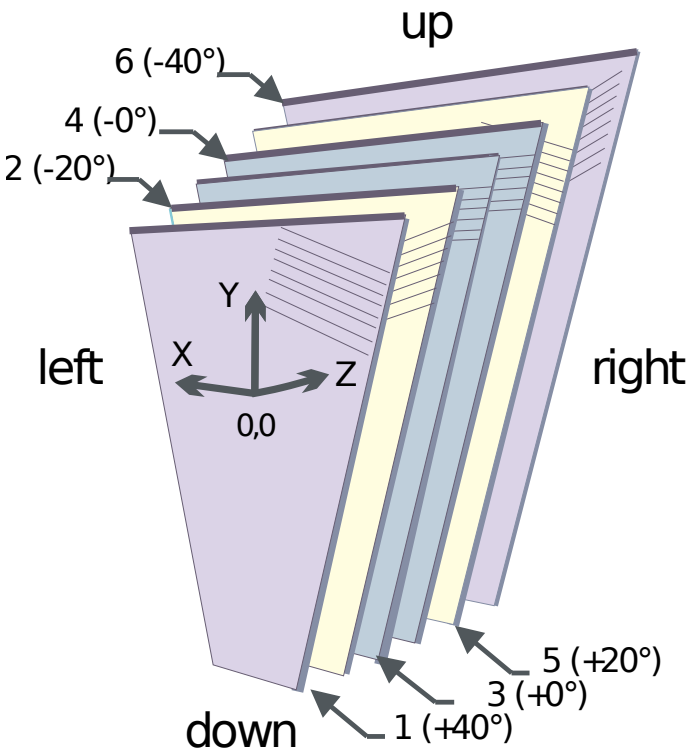

Figure 2.10: Schematic layout of one sector of one plane with its six individual layers which have different spatial orientation in the x-y plane. Figure taken from [173].

2.2.6 META Detector System

The Multiplicity-Electron-Trigger-Array of the HADES experiment is divided into the **R**esistive **P**late **C**hamber (RPC) and the **T**ime **O**f **F**light detector (TOF). Both provide a high resolution time-of-flight measurement, however requirements are different because of occupancy. Both detectors cover the full azimuth angle ϕ and both subdetectors combined cover the same polar angle as the MDC described in section 2.2.5.

2.2.6.1 Resistive Plate Chamber

The **R**esistive **P**late **C**hambers (RPC) cover the region of small polar angles $18^\circ < \theta < 45^\circ$ which corresponds to the region with high track densities within the acceptance. Their trapezoidal shape for each sector is displayed in figure 2.11. In total, the RPCs have an effective area of 8 m^2 for all six sectors combined.

The RPC was installed in 2010 and replaced the previously used TOFINO significantly improving granularity and time precision which now reaches 50 ps. Its double layer structure which is shown in figure 2.11 allows redundant timing measurement for improved timing resolution [174].

With three columns and 31 cells per column a total amount of 186 individual cells per sector is used, which results in 1116 for all sectors. Each cell is a full

detector system in itself, neighbouring cells are shielded with aluminium. Thus the timing measurement should be free from crosstalk.

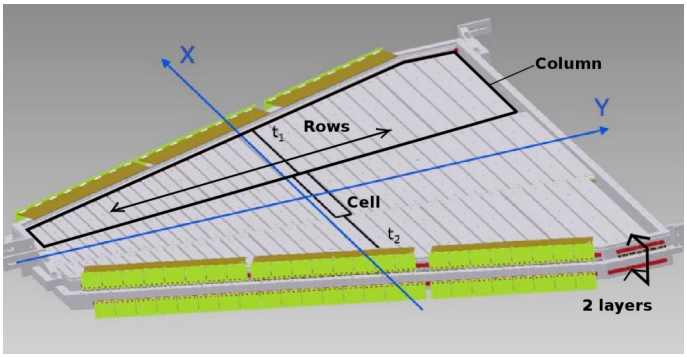

Figure 2.11: Schematic view of one sector of the RPC with its two individual layers. The orientation of the columns and rows is explained in the figure. Figure taken from [175].

The structure of a single RPC cell is displayed in figure 2.12. The cells of the both layers are shifted with respect to each other to obtain enhanced resolution as well as detection efficiency. As mentioned before, each cell is shielded with an aluminum box which isolates the active media inside. The gaps of 0.27 mm between the Soda Lime Silicate glass which is used as resistive material and the anodes and cathodes which are made of aluminum is filled with a gas admixture composed of 90 % Freon and 10 % Sulfur Hexafluoride. This provides a timing resolution of down to σ^t_{RPC} =50 ps, a spatial resolution of σ^r_{RPC} =1.2 cm and still reaches efficiencies around 100 % [175]. The average resolution is σ^t_{RPC} =77 ps for single hits and σ^t_{RPC} =83 ps for cells with an additional particle traversing the neighbouring cell. The RPC measures all kind of ionizing particles which path through the active medium by creating a shower of ionization electrons in the gas admixture. This avalanche which is induced by the electromagnetic field will then be amplified and collected by the readout strips which are connected to both sides of each single cell.

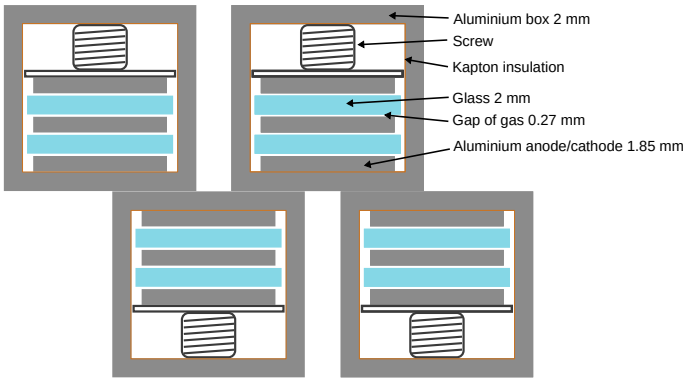

Figure 2.12: Schematic view of the internal components of RPC cells and their orientation to each other with respect to the two layers. Figure taken from [175].

2.2.6.2 Time of Flight detector

For the large polar angles 44° $< \theta <$88° the HADES **T**ime **O**f **F**light detector (TOF) provides precise velocity information with a resolution of σ_{TOF} =190 ps for electrons [77]. As for the previously mentioned MDCs and RPC the detector is divided in six trapezoidal sectors, almost covering the full azimuthal angle ϕ. This time resolution is achieved by 64 scintillator rods per sector resulting in a total amount of 384 rods. Those rods are made of BC408 plastic scintillator material which satisfies the requirements of high reconstruction efficiency with $\approx 10^4\,\gamma$/MeV and a short decay time of 2.1 ns to avoid large dead times of the detector. In addition to those requirements, the granularity is chosen such to fulfill the capability of measuring polar dependent high track multiplicities and avoid double counting of multiple charged particles hitting the same rod. Therefore the innermost 192 rods are chosen to consist of an effective area of 20×20 mm^2 while the rods at higher polar angle θ are of size 30×30 mm^2 with a variation of the rod length between 1-2 m.

The amount of scintillation photons rises in dependence on the deposited energy of the charged particle traversing the TOF. The scintillation light will be read out by individual photo-multiplier tubs (PMT) which are attached at both ends of each rod. The general working principle of PMTs has already been explained in section 2.2.3.

2.2.7 Electromagnetic Calorimeter

Besides the RICH which was upgraded for the FAIR phase-0 campaign, a newly installed **E**lectromagnetic **Cal**orimeter (ECal) was used for the first time for the HADES detector setup in the Ag+Ag beamtime in March 2019. This enrichment allows direct measurements of γ's, while in previous beam times only photon conversion could be used for photon reconstruction [176]. This is particular difficult since the HADES experiment has been optimized towards low conversion probabilities as pointed out in section 2.2.2. With the ECal, a tremendous improvement for the reconstruction of electromagnetic decays has been achieved, including π^0, η as well as $\omega \rightarrow \gamma\pi^0$ and $\Sigma \rightarrow \Lambda\gamma$ decays and several exited baryon states. The energy measurement in the ECal is complementary to the ToF information, thus improving the separation between π and $e^{\pm}$, in particular for p>400 MeV/c.

The electromagnetic calorimeter of the HADES detector is positioned posterior to the RPC, with sufficient distance to permit air flow. In total it covers an area of approximately 8 m^2 [177] [178]. The gap between the RPC and the ECal is rather constant with a value of about 20 mm. The ECal setup follows the partition into six sectors and therefore only suffers from small acceptance holes in ϕ as all other subdetectors. With 163 modules per sector, the fully equipped electromagnetic calorimeter will contain 978 lead glass modules. The trapezoidal arrangement of the modules leads to 15 rows of increasing length of the 15 kg lead glass modules which results in a total weight of 15 tons for the modules only.

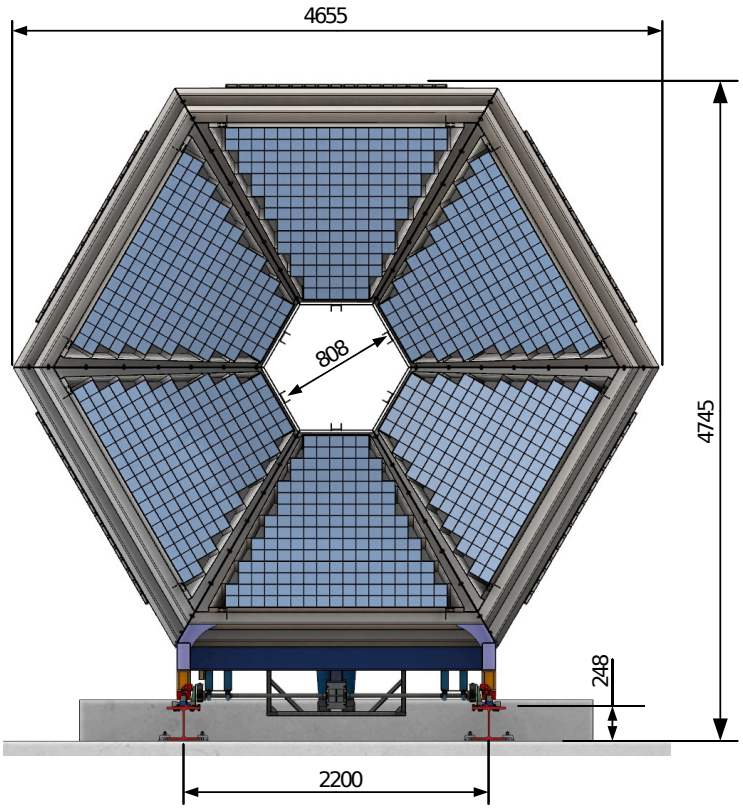

Figure 2.13: Frontal view of the HADES electromagnetic calorimeter with its spatial dimensions which correspond to a coverage in polar angle theta of $12° - 45°$ and the HADES - typical six sectorial azimuth angle coverage which only has minor acceptance gaps between sectors. Figure taken from [177].

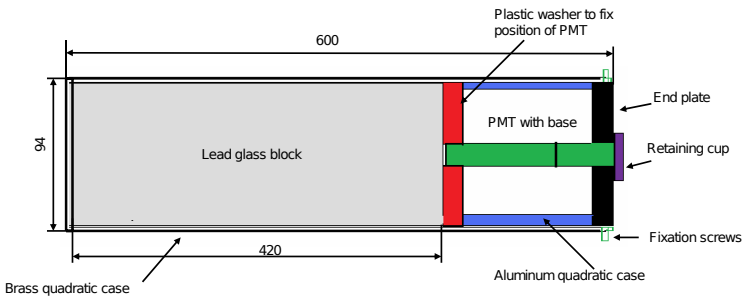

Figure 2.14: Schematic view of one module of the HADES electromagnetic calorimeter. Figure taken from [177].

These modules as main component of the HADES ECal are reused and modified from the OPAL electromagnetic calorimeter. Figure 2.14 displays schematically one module, consisting of a large lead glass block of 420 mm length and $92 \times 92\,\mathrm{mm}^2$ front size. These dimensions allow to measure a large part of the electromagnetic shower which evolves through the lead glass block. The signal is then read out by a PMT in the back. As homogeneous calorimeter the signal evolves though the whole lead glass and is only read out behind the lead glass

compared to a sampling calorimeter where several layers of absorption material and scintillating medium are alternating.

For a wave length of 400 nm the index of reflection of lead glass is 1.708. With a radiation length of X_0 =2.51 cm, the total length of the modules is even 16.7 X_0, which allows for precise energy determination. Photons and electrons are thus developing an electromagnetic shower and are stopped in the material, depositing their full energy. On the other hand, hadrons only loose part of their energy. In order to stop them, even more material is needed, as seen in hadronic calorimeters. For this specific reason, calorimeters are always placed behind all other sub detector systems.

2.2.7.1 Operation Principle of the ECal Measurement

The following section will briefly describe the fundamental principles which are utilized for measuring the electromagnetically interacting particles, in particular photons and electrons with the HADES ECal. Lead glass is chosen as material of the modules for its high atomic number Z since the interaction probability of photons and any electromagnetically charged particle rises with Z. The photon which is of special interest can interact with the material via several effects. While Compton scattering, and the photoelectric effect dominate at small photon energies below 1 MeV, the electron-positron pair production is the most relevant process for high energies. According to this scale, all HADES related photons are high energetic photons. As soon as one of these high energetic photons traverses the lead module, electron-positron pair production will occur. These electrons and positrons will then produce Bremsstrahlung which results in a large number of high energetic photons that can then be converted and proceed sequentially. This sequence of processes will continue and create a so called shower until the energy of the photon is too small to induce pair production anymore. Mathematically, the radiation length X_0 is introduced as average distance within which an electron loses its energy expect $1/e$ [179]. Analog to this definition, the probability of a photon underlying electron-positron pair production can be expressed as $< I(x) >= I_0 \exp -\frac{7}{9}\frac{x}{X_0}$ where the factor 7/9 is derived from the photon pair production cross section. These definitions allow to estimate the evolution of the shower within one module as schematically displayed in figure 2.15. As reminder the HADES electromagnetic calorimeter cells provide a thickness of ≈17 X_0.

2.2.8 Forward Wall

The HADES Forward Wall is placed 7 m behind the target along the beam axis and covers the full azimuthal angle ϕ and small polar angles of 0.33° $< \theta <$7.17°. The positioning is chosen such that the forward wall covers large regions of the emission of participants and light nuclei created in A+A collisions. This information is valuable for the reconstruction of the event plane, necessary for the analysis of flow. In deuteron induced reactions, the forward wall can tag forward going protons, thus allowing to distinguish between quasi free pp or on interactions.

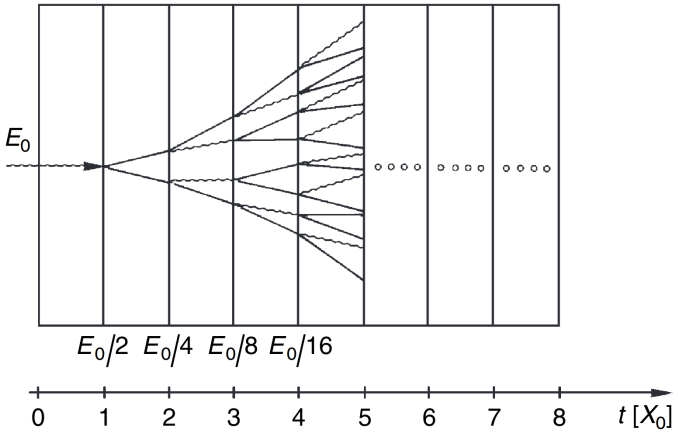

Figure 2.15: Schematic view the evolution of an electromagnetic shower. Figure taken from [180].

For precise measurements, different granularities are used for different polar angle regions, because the polar angle is the main factor for particle multiplicity. The system consists of 288 scintillation cells which are capable of measuring charged particles. The most central 140 cells require the highest granularity and thus have the smallest dimensions of $4\times4\,\mathrm{cm}^2$. In the intermediate theta range, $8\times8\,\mathrm{cm}^2$ cells are utilized while the most outer regions consist of 84 cells with an extended size of $16\times16\,\mathrm{cm}^2$. All detector cells are made of plastic scintillators, based on BC408 polystyrene. They all have a length of 2.54 cm [181]. In this setup, the forward wall covers an area of $180\times\ 180\,\mathrm{cm}^2$ with a small hole of $8\times8\,\mathrm{cm}^2$ centered around the beam axis to avoid direct interaction with the beam ions. Similar to the HADES RICH photomultiplier arrangement, also the Forward Wall does not follow the sectorial partitioning. The resulting timing resolution for the most abundant particles, the protons, is in the order of 500 ps which belongs to an integrated momentum resolution of 11 %. The event plane resolution is about 34 ° for the most central events and down to 46 ° for more peripheral events corresponding to an impact parameter of b =8 fm.

2.2.9 Central Trigger System

The **C**entral **T**rigger **S**ystem (CTS) is responsible for the very first decision, in general whether an event fulfills the requirements of being relevant and thus has to be stored on the file system or not. In the HADES experiment, several trigger levels provide this information. The first level trigger takes the raw detector hit information into account. Obviously, the trigger conditions highly depend on the collision system itself. In the analyzed data set of Ag+Ag at E_{kin} =1.58 AGeV, the first level trigger condition is based the raw detector hits in RPC and TOF. In this beamtime the number of hits has to be larger than $N_{\mathrm{RPC+TOF}}$ >=5 in order to fulfill the requirements of the **P**hysics **T**rigger **2** (PT2) and $N_{\mathrm{RPC+TOF}}$ >=20 for PT3. In general, trigger requirements depend on the collision system and centrality.

Since the aim of this beam time was a large statistics data set of the most central events, only one out of 32 more peripheral events which do fulfill PT2 but not PT3 were stored. No second level trigger was used in this beam time. In principle, this could be used for example for only recording events which contain RICH rings. This would allow exceptionally high performance for specific rare probes, like e.g. vector mesons. As next step of data processing, the Event Builders wait for the termination of all signal transports of the different **F**ront **E**nd **E**lectronics (FEE). Only then, the collected information of all FEE is combined to obtain an event. All events which were selected by the CTS to be interesting physics cases by the CTS and correctly collected by the Event Builder are available for further analysis steps. In the physics analysis additional event selection criteria are required, based on further criteria as explained in chapter 3. These stored so called **H**ADES **L**ist mode **D**ata (HLD) files will be calibrated in further steps which are described in section 2.2.10.1.

All information which is provided to the CTS is also tracked by the **D**ata **A**c**Q**uisition (DAQ) system, which performs continuous quality surveillance during data taking to guarantee optimal data quality. A more detailed description of the CTS and DAQ for the previous Au+Au beam time can be found in reference [182]. Additional updates towards the Ag+Ag beamtime for this thesis are summarized in [183] [184].

2.2.10 Software Framework

2.2.10.1 HYDRA - The Software Analysis Framework

For analyzing the HADES data, the **H**ADES s**Y**stem for **D**ata **R**eduction and **A**nalysis **2** framework (HYDRA2) is required [185]. It is based on the CERN ROOT [186] framework which is widely spread in particle physics and based on C++. HYDRA2 adds HADES detector related information to the framework like the geometry and response of the HADES sub detectors. Each sub detector class consists of variables for the measurable raw detector signal, parameter sets for the calibration and hit finding algorithms. Low level analysis is performed for extracting the optimal calibration parameters which then are used for the combination of different sub detectors to deliver full track reconstruction methods. These methods lead to a tremendous data reduction and results are stored as **D**ata **S**ummary **T**ape (DST) which is of major interest for the basis high level analysis. Analysis is then performed on calibrated and reconstructed data, avoiding redundant running of the HLD files. The DSTs have the same structure for simulated and experimental data. However, the simulated events have additional classes filled with input information like the generation process, production vertex, or particle ID. Various models can be used for generating simulated data, see section 1.7.2 for a brief overview. The present study employed HYDRA2 version 5.6b and data generation five throughout the whole analysis.

2.2.10.2 UrQMD

Ultra **r**elativistic-**Q**uantum-**M**olecular-**D**ynamic (UrQMD) simulations are often used as multi-purpose event generator [135]. The microscopic transport model is designed for pp, pA as well as AA collisions for the whole GSI SIS18 energy regime and beyond and delivers all necessary information about the kinetic phase space distribution of all created particles, except the rare dielectrons. More details are written in section 1.7.2.

2.2.10.3 PLUTO

For rare probes like dielectrons or also few strangeness consisting particles, PLUTO [187] is often used to artificially enhance specific sources within a background from e.g. UrQMD or real events or to simulate certain sources on their own. This ansatz enables the generation of sufficient statistics for all cases. PLUTO is written C++ which allows good integration in the HADES HYDRA simulation chain. Consequently, this method is a common technique to extract knowledge on detector response for rare signals. Therefore, the process of sampling is executed by means of the specification of a particular phase-space distribution. The distribution is generally defined by a specific temperature for the designated channel. Details about input parameters for the simulation of Σ^0 and Λ follow in chapter 7.

2.2.10.4 GEANT

All simulated particle trajectories through the detector geometry including the magnetic field will be calculated by GEANT [188], the **GE**omety **AN**d **T**racking (GEANT) routine. GEANT calculates the interaction of all particle species with the different detector materials including Bremsstrahlung, conversion, secondary particle production and further physics processes. GEANT thus provides realistic energy loss and background enhancement which is related to the material budget and thus highly depends on particle properties as polar angle θ and momentum p. Currently the proposal of changing from GEANT3 to GEANT4 is under investigation for better description of energy loss and fragmentation processes [2].

[2]The updated version GEANT4 is written in C++, compared to GEANT3 which is still FORTRAN based.

CHAPTER 3

Event Selection

This chapter deals with the selection of the collected events which were stored during the beamtime to ensure required data quality.

As first step in the event selection, a removal of events contaminating a pure Ag+Ag interaction sample is performed. Therefore all events are discarded which are produced elsewhere than in the target region. In addition, also pile-up events, i.e. several events in coincidence are discarded by the following criteria. The influence of the successively applied selection criteria is displayed in figure 3.1 where a subset of all events is analyzed. While the relative amount of accepted events is denoted in black, the red distribution shows the relative amount of rejected events in relation to the amount of events which survived all previously applied selection steps.

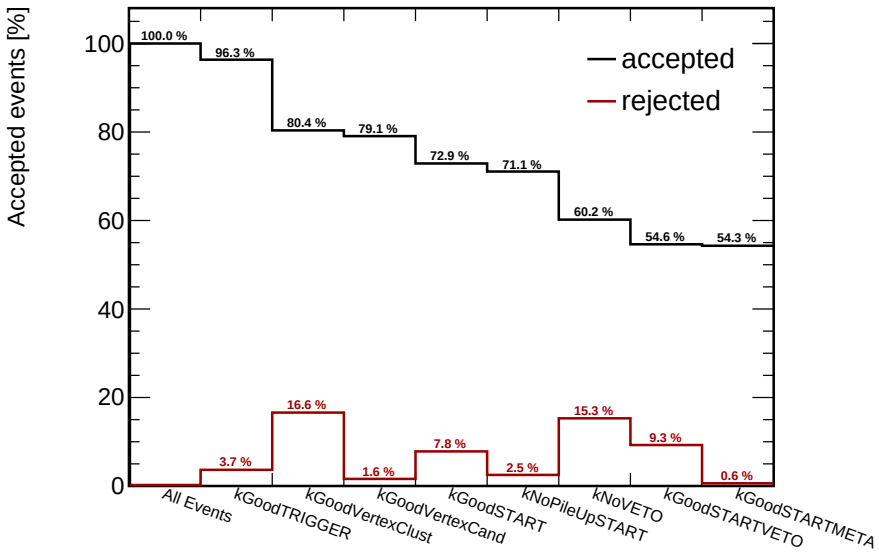

Figure 3.1: Differential event selection efficiency and corresponding relative amount of rejected events for the applied selection criteria for a representative set of $813 \cdot 10^6$ events.

- kGoodTrigger: As first requirement, a minimum of 20 hits in the RPC+TOF detectors rejects unphysical events as well as more peripheral events. In HADES this selection is denoted as **P**hysics **T**rigger **3** (PT3) event. Figure 3.3 shows, that this PT3 trigger selects the $51\,\%$ most central events without bias, while having a steeply changing acceptance for less central events.

- kGoodVertexCluster: The vertex position estimation based on the inner MDCs is performed and retrieves the probability distribution of the target layer where the event took place. Only converged fitting results with a reconstructed z-vertex > -70 mm are accepted in this step.

- kGoodVertexCand: Analogue to the kGoodVertexCluster, this method allows only events with a reconstructed event vertex with a z-vertex position in the target region (> -70 mm) with respect to the more precise method which utilizes fully reconstructed tracks, not only the inner MDCs.

- kGoodStart: In addition, in a window $5 - 9$ ns after the start detector time, hits in the META detector are required. For good Ag+Ag collisions this is certainly fulfilled, since there are always fast particles, and the PT3 trigger already required hits in RPC+TOF.

- kNoPileUpSTART: The term pile-up is used for events which consist of several interactions which took place at the same time and could not be distinguished because being so close in time. Different event vertices in space and time can lead to poor timing resolution and thus a wrongly reconstructed event vertex. This is particular from interest for off-vertex topology selection. Also, track multiplicities may be enhanced and thus the centrality class would be assigned wrongly. Those events are discarded by removing events with an additional hit in the START detector within 15 ns around the START hit corresponding to the event.

- kGoodVETO: Similar to the previously described selection, all events with a registered VETO hit within 15 ns around the START time are neglected, since a reaction with the target is unlikely in this case. In combination with PT3, this can only happen if several collisions took place at the same time.

- kGoodSTARTVETO: Only events where each START hit has a corresponding VETO hit after $15 - 350$ ns is evaluated to be of the desired quality. This coincidence trigger ensures the correct assignment of the proper timings which are assigned to all particle candidates in the following analysis.

- kGoodSTARTMETA: This cut is similar to the previous selection criteria in this list, but instead of the VETO detector, META hits are used. A time window of $80 - 350$ ns after the START hit is scanned for an additional START hit and in addition to this second start hit, RPC+TOF signals in a time window of $7 - 12$ ns afterwards are searched for. If at least four correlated META hits are found, the START is neglected due to existing pile up.

3.1 Centrality

For the characterization of any heavy ion collision, the centrality of the collision is of fundamental interest since the majority of physical observables is directly connected to the centrality. In heavy ion collisions, the collision does not always take place head-to-head, but often in a peripheral way, were the minimal distance between the center of the two colliding nuclei corresponds to the impact parameter. In figure 3.2 this parameter is denoted as b and in combination

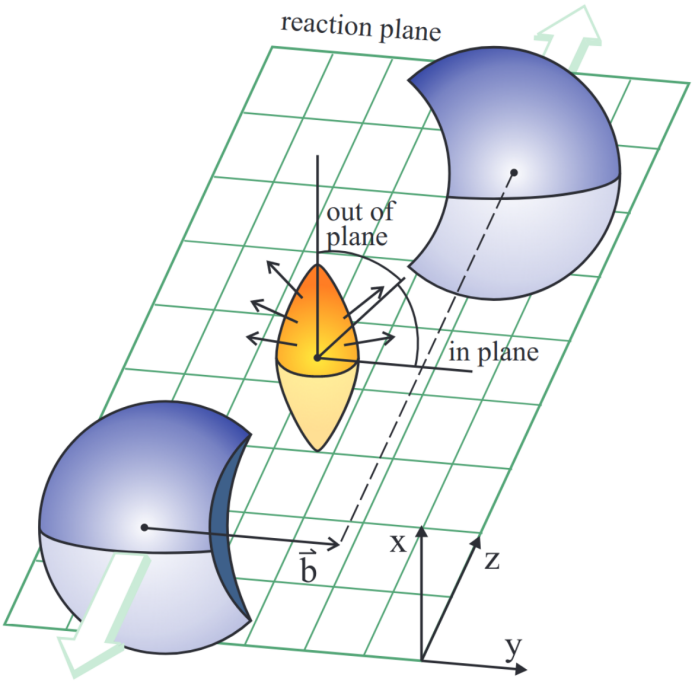

Figure 3.2: Geometric view of a heavy ion collision where the nuclei traverse in z direction [189].

with the overlap zone of the projectiles, it defines the interaction plane. Central events correspond to a large amount of participants which is directly correlated to the size of the overlap region, which is depicted in orange. The non interacting nucleons in blue are called spectators and will not traverse the HADES acceptance. A large number of participants result in many produced particles, thus the amount of reconstructed tracks is utilized to quantify the centrality which is convertible to an impact parameter. The Glauber Monte Carlo model [190] allows the estimation of the centrality via the amount of detected signals in the RPC and TOF which together cover the full HADES acceptance of full azimuth angle φ and polar angle region of $18° < \theta < 85°$. This approach was already successfully used for the HADES Au+Au beam time at $E_{kin} = 1.23$ GeV with a detailed description of the procedure in [191]. The same strategy is applied to the Ag+Ag data at

$E_{kin} = 1.58$ GeV where the resulting comparison between the model calculations and the measured data is depicted in figure 3.3.

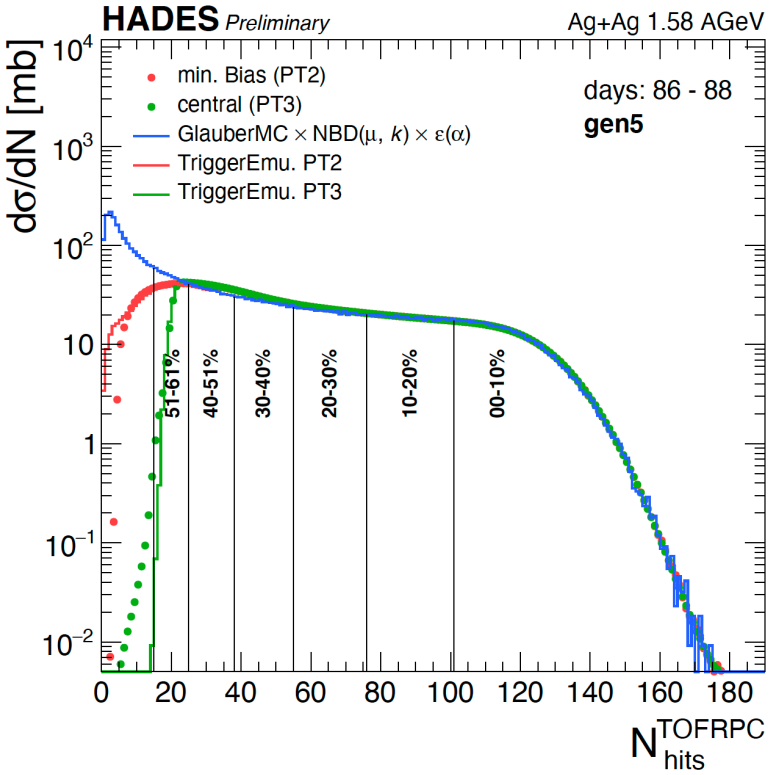

Figure 3.3: Centrality estimation for the recorded Ag+Ag events and comparison to the Glauber Monte Carlo model calculations. The figure is taken from [192].

The correlation between the amount of RPC and TOF hits to the differential cross section in figure 3.3 shows a perfect agreement up to the $30\,\%$ most central events. Starting there towards lower centrality, the deviations increase with decreasing amount of RPC and TOF hits. For this reason, only events in the most central $0 - 40\,\%$ are analyzed in this work. The borders of the centrality classes of 10% width each are stated in table 3.1.

Class	$b_{min} - b_{max}$	$\langle b \rangle$	$\langle N_{part} \rangle$	ΔN_{part}
00-10	0.0-3.8	2.53	160.9	$\pm$6.9
10-20	3.8-5.4	4.64	114.5	$\pm$6.2
20-30	5.4-6.6	6.02	81.1	$\pm$5.1
30-40	6.6-7.6	7.11	56.5	$\pm$5.4

Table 3.1: Centrality class estimation from the Glauber Monte Carlo model approach.

3.2 Event Vertex Estimation

In addition to the centrality selection, an event vertex selection is performed, to ensure the quality of the recorded data. Especially for analysis which depend on the vertex position [1] this selection criteria provides a more uniform event characteristic. The event vertex reconstruction method which was used in this work is described in chapter 4.3. The event vertex distributions which are displayed in figure 3.4 show several aspects for the z component as well as within the x-y plane. The z-vertex distribution clearly shows the target structure of the 15 thin Ag layers.

A decrease of interaction probability is visible for the more downstream oriented layers. All z-vertices in the range of $-70\,\text{mm} < z < 0\,\text{mm}$ are accepted because rejected vertices outside this range are unlikely to originate from a good Ag+Ag collision. For the same argumentation, events are rejected with a radial distance in the x-y plane above $3\,\text{mm}$ compared to the most probable reconstructed position. In the experimental data, the intensity maximum is extracted by fitting a Gaussian which retrieves a position of $-0.56\,\text{mm}$ in x and $-0.31\,\text{mm}$ in y.

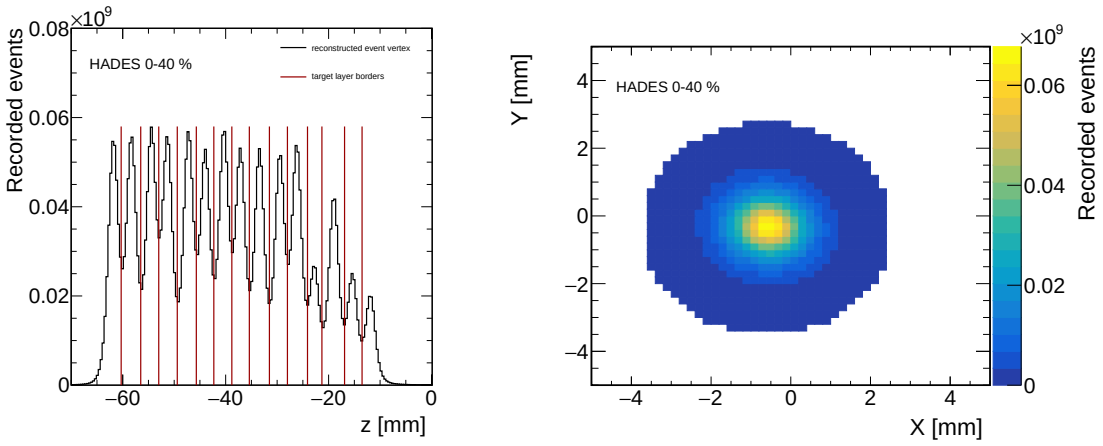

(a) z-vertex (b) x-y-vertex

Figure 3.4: Event vertex distributions in all three spatial dimensions after selection criteria. The left figure shows the reconstructed z-vertex position in black with the corresponding target layer borders displayed as red lines. The right plot shows the corresponding x-y event vertex distribution. More details are written in the text.

The exact values for the z-vertex target borders can be found in appendix A.3. Combining those event vertex selection criteria, another 2.0 % of the events are discarded. As this is the last basic event characteristic selection, the remaining amount of $4.72{\cdot}10^9$ events are analyzed. This represents a fraction of 34.6 % of all recorded Ag+Ag events at 1.58 AGeV.

[1] Especially the analysis of hadrons which contain strangeness rely on the decay vertex analysis which is displaced with respect to the primary event vertex.

CHAPTER 4

Particle Selection

In heavy ion collisions at around $\sqrt{s_{NN}} = 2.55$ GeV, sufficient energy is available to create various different particle species. Dependent on the lifetime of the produced particles, only those particles which reach the tracking chambers can be reconstructed directly. In addition to their lifetime, non zero electromagnetic charge is necessary for tracking as described in section 2.2.5. Particles decaying before or inside the detector can be reconstructed using the information of the decay products.

4.1 Track Finding Algorithm

As first step of the data analysis, the raw detector hits are combined to gain information about the trajectory of the particle which crossed the detector system. As mentioned in chapter 2.2.5, in HADES the MDCs provide those information by converting the drift times into distances and thus provide spatial hits.

With the spatially limited magnetic field in between MDC II and MDC III, a straight line fit is performed for the combination of the first two MDCs, called "inner MDCs", as well as for the combination of MDC III and MDC IV which are correspondingly called the "outer MDCs".

Figure 4.1 depicts the principle idea of the clustering algorithm in the MDCs. All fired wires are projected into a projection plane, where the projection takes place with respect to the target position. The reconstructed clusters are then used to build track segments. This procedure is utilized for the inner MDCs while the outer MDCs projections are performed with respect to the intersection point of the inner tracklet with the virtually kick plane. Combining a reconstructed segment from the inner MDCs and one from the outer MDCs results in a track candidate. The deflection in the kick plane allows the momentum determination. The outer track segment is always matched to a hit cluster in the RPC and TOF detectors which providing the timing information. In addition, all tracks are matched to the closest ring in the RICH detector which will give a first estimate towards electron identification.

All corresponding fired drift cells which participate for any track candidate are then overlayed in the two-dimensional projection plane as shown in figure

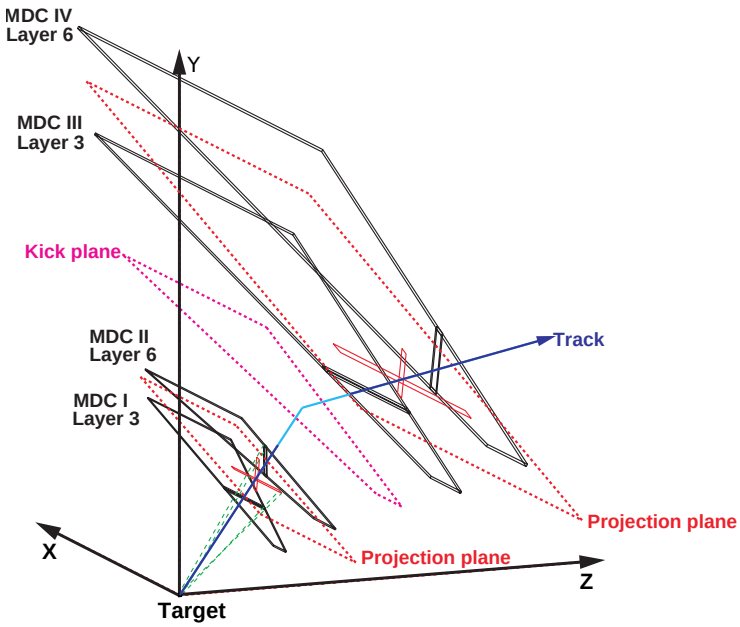

Figure 4.1: Schematic view for the track reconstruction algorithm. The virtual projection planes for the inner and outer MDCs as well as the virtual kick plane are shown to guide the eye [77].

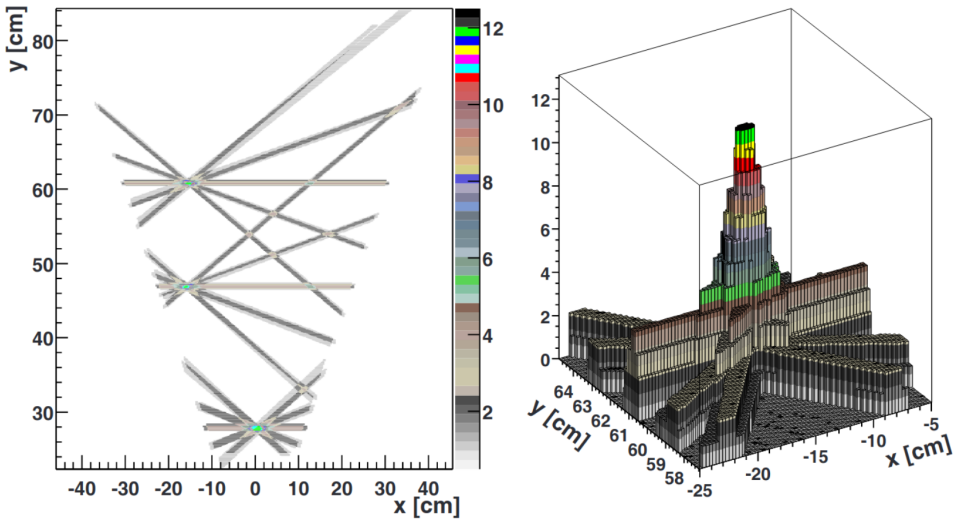

Figure 4.2: Left: Projection plane of the drift cells, Right: visualization of the intensity structure of the overlayed drift cell signals [77].

4.2. Wrongly fired wires or accidental wire crossings may still lead to so called "ghost tracks". Those fakes are in many cases distinguishable when compared to true clusters. In general those fake clusters have diminished average cluster amplitudes, cluster sizes as well as a reduced amount of unique wires which only contribute to this cluster and thus allow discarding these spurious clusters.

4.2 Momentum Reconstruction

The deflection of charged particles in the magnetic field is utilized as fundamental tool for the momentum measurement of charged particles. In HADES, three different momentum reconstruction approaches are used. They are described in the following in the order of increasing precision. The both latter described methods both rely on information derived from previously calculated values and estimations. This reliance justifies the three-step process.

4.2.1 Kick Plane Method

The kick plane method convinces with a very fast estimation but lacks precision. In this method, the whole deflection which occurs within the extended spatial magnetic field is replaced by a single kick, applied at a virtual assumed kick plane which is almost centered in the area of the magnetic field, as depicted in figure 4.1. The position of the kick plane was determined with GEANT3 and allows momentum determination by the calculated deflection angle which is transcripted to a momentum in a precalculated look up table [77]. The momentum kick p_k is derived by

$$\mid \vec{p}_{in} - \vec{p}_{out} \mid = \mid p_k \mid = 2p \sin \frac{\Delta\theta_k}{2} \tag{4.1}$$

where the deflection angle is denoted as θ_k. Of course the total deflection also depends on the orientation of the velocity of the particle with respect to the magnetic field

$$\vec{p}_K = \int q(\vec{v} \times \vec{B}) dt \tag{4.2}$$

Formula 4.2 is an integration over the Lorentz force in the whole area of the magnetic field. Thus the particle trajectory change is stated as deflection angle and can be described as

$$\Delta\theta_k = \int_{l_{in}}^{l_{out}} B \sin\alpha dl = K(l_{out} - l_{in}) \tag{4.3}$$

Where the angle between track and magnetic field is denoted as α and K is a constant which depends on the polar and azimuth angle of the track. The HADES geometry orientation is chose such that $\sin\alpha \approx 1$. A Taylor expansion in $\sin\frac{\Delta\theta_k}{2}$ yields in the final expression

$$p = \frac{1}{2}\frac{p_{k0}}{\sin\Delta\theta_k/2} + p_{k1} + 2p_{k2}\sin\Delta\theta_k/2 \tag{4.4}$$

4.2.2 Spline Method

In HADES, as second method of momentum extraction, a cubic spline approach is used for modeling the charged particle trajectory. The detector hits from the MDCs are taken into account as well as the first and second spatial derivatives of their fit function which represents the track candidate [77]. For each of the four MDCs, one mid chamber intersection point is defined as shown in figure 4.3.

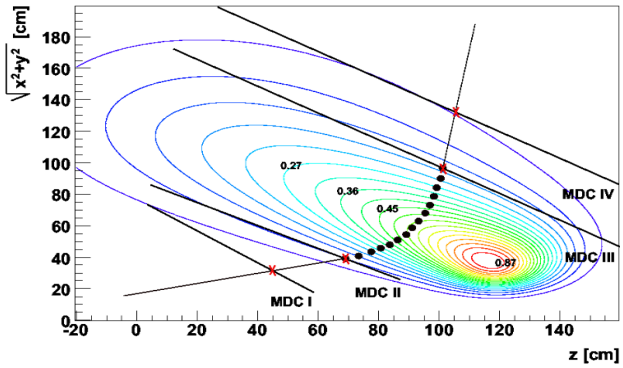

Figure 4.3: Cubic spline approximation with the four mid chamber interaction points marked in red and only 15 out of 50 points displayed in the magnetic field region, where the evaluation of the magnetic field takes place [77].

Starting with these four points, the trajectory inside the magnetic field area is interpolated with a cubic spline model. Therefore, the area in between the second MDC plane and the third one, 50 equidistant points are extracted from the trajectory. Instead of the continuous deflection, the deflection is described as sum of the deflections at the 50 chosen points. On each of theses points, the magnetic field map is evaluated and allows for an individual momentum estimation. Combining the information of all 50 points lead to a much more precise momentum estimation than the previously explained Kick Plane method. The uncertainties extracted from GEANT simulations result in a momentum and polar angle dependent momentum resolution of σ_p/p =(1.0-4.5) %.

4.2.3 Runge-Kutta Method

The most precise and thus standard method for momentum determination is the Runge-Kutta method, which solves the physical equation of motion within a magnetic field. The resulting second order differential equations are solved in a recursive way by a fourth order Runge-Kutta approach. The previously explained spline interpolation points are reused for extrapolation towards the following points as well as preliminary momentum and polarity estimation. This knowledge is combined with the vertex and the track orientation from the inner and outer track segments. The momentum is optimized iteratively to describe the MDC hits. The quality of the resulting momentum estimation can be quanti-

fied by the normalized χ^2_{RK} which is later referred to in the track quality selection.

All three momentum reconstruction methods fully neglect possible energy loss of particles traversing the detector material as well as multiple scattering. These effects are estimated to be small since the material budget within the area of track extrapolation stays below $0.5\,\%$ radiation length. Since the uncertainty estimation is only calculated assuming uncorrelated track parameter errors, a comparison to the Kalman filter approach is currently under investigation for possible optimization [193]. The overall momentum resolution is aimed to be improved by better accounting for uncertainties while extrapolating the tracks.

4.3 Event Vertex Reconstruction

The resolution of the collision position in time and space is crucial for high precision measurements of the physical observables. In HADES, three different methods of event vertex reconstruction exist. The first method uses only MDC clusters, while the second method uses inner track segments from combining the inner MDC clusters. The third method is most precises and used in this work. This method takes all information of the fully reconstructed track candidates into account and extrapolates the Runge-Kutta track towards the target region. All candidates are weighted by their according χ^2 track quality parameter, ensuring a small impact of wrongly reconstructed track candidates.

4.4 Track Quality Condition

The first quality check of the tracks, which were reconstructed by the track finding algorithm as described in 4.1, is coded in the so called "kIsUsed" flag. This condition requires hits in the subdetectors which are needed to determine **P**article **ID**entification (PID) of the track. Those subdetectors are namely the MDC chambers for tracking and momentum reconstruction, and the META detector for the velocity estimation as minimum for a differentiation between different species of charged particles. In addition, χ^2_i of the track segment in front of the magnetic field and χ^2_t as total track fitting quality are used as selection criteria. The spectrum after these soft precuts which are used in the kIsUsed requirement is displayed in figure 4.4 on the right. The large impact of background rejection compared to no cuts (left side of figure 4.4) allows to see the band of K^+-mesons by eye.

4.5 Reconstructed Mass

In section 1.6 the properties of the Σ^0 are summarized. Neglecting the possible Dalitz decay, its only decay is the $\Sigma^0 \rightarrow \Lambda + \gamma$ channel. In any case a Λ baryon is

produced. Hence the only reconstructable decay channel of the Λ must contain charged particles which is given by $\Lambda \rightarrow p + \pi^-$. This section will focus on the particle reconstruction of the produced daughter particles from Λ baryons.

Using the measured momentum and velocity of a track, formula 4.5 describes the correlation of the observables to the rest mass.

$$m = p \cdot \frac{1}{\beta\gamma} = p \cdot \frac{\sqrt{1-\beta^2}}{\beta} = p \cdot \sqrt{\frac{1}{\beta^2} - 1} \tag{4.5}$$

The detector resolution of the Time-of-Flight detectors TOF and RPC may lead to velocities $\beta > 1$ in particular for leptons and thus imaginary masses. This is tolerated for leptons but not for hadrons in this thesis due to the chosen selection criteria on the reconstructed mass.

The implemented selection of particles by their reconstructed mass is used in the same way for RPC and TOF since it is only used as a wide preselection step and will not effect the off vertex topology analysis (see equations 4.6 and 4.7). In addition this integration over both subdetectors avoids as many systematic differences as possible. This rather wide cut also reduces possible uncertainties if simulations and experimental data differ significantly. The two figures 4.4 display the measured particle velocity on the y axis in dependence on the momentum and particle charge. The calculated theoretical mass curves of the PDG masses of protons and π^- are displayed in addition as these are of interest for this analysis. In section 5.1 the rare probes of strangeness are highlighted. Using all that knowledge, only soft cuts were applied here before the off vertex topology cuts.

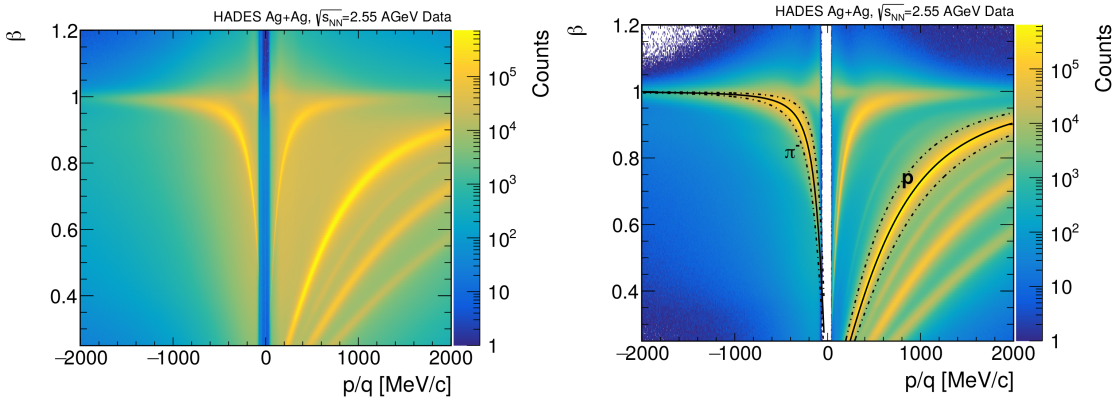

(a) No track quality cuts are applied

(b) After track quality selection which are explained in chapter 4.4

Figure 4.4: The removal of reconstructed tracks of unsatisfying quality leads to an improved separation power between charged particle tracks in terms of their reconstructed mass.

Figure 4.6 displays the positively charged particles with measurable momentum $p > 50\,\text{MeV/c}$ which are already shown in figure 4.4 (b). The PDG masses of

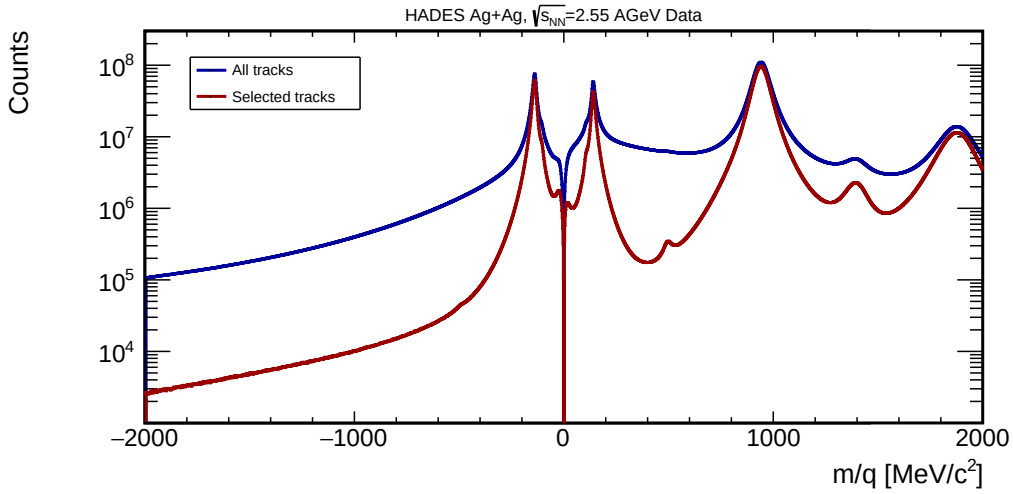

Figure 4.5: Influence of the track quality selection on the reconstructed mass of the track candidates.

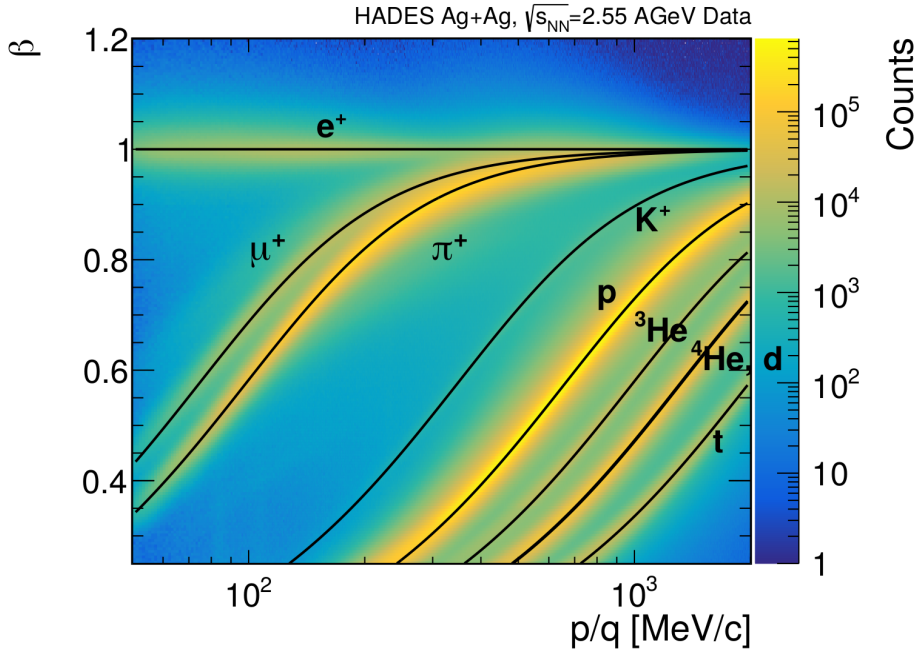

Figure 4.6: Reconstructed positively charged particles and their theoretical curves in solid lines.

the reconstructable hadrons and fragments are represented by the solid lines. By using the logarithmic x-axis, the separation between μ^+ and π^+ is clearly visible, especially for low momentum regions below $200\,\mathrm{MeV/c}$. The final cut values for protons and π^- from the Λ decay in terms of the reconstructed mass are

$$0.8 \cdot m^p_{PDG} < m^p_{rec} < 0.8 \cdot m^p_{PDG} \tag{4.6}$$

for protons and

$$0.7 \cdot m^{\pi^-}_{PDG} < m^{\pi^-}_{rec} < 1.3 \cdot m^{\pi^-}_{PDG} \tag{4.7}$$

for the pions respectively. These cut windows are represented in figure 4.4(b) as dashed lines. For the π^- the reconstructed mass will be used later on in a more strict way for the multivariate cut analysis to distinguish between pions and myons, which differ only by $30\,\mathrm{MeV/c^2}$.

4.6 Energy Loss

Besides particle identification with the reconstructed mass, the energy loss of the particle is utilized to improve the purity of particle identification.

$$\frac{dE}{dx} = Kz^2\frac{Z}{A}\frac{1}{\beta^2}\left[\frac{1}{2}\ln\frac{2m_e c^2\beta^2\gamma^2 W_{max}}{I^2} - \beta^2 - \frac{\delta(\beta\gamma)}{2}\right] \tag{4.8}$$

The **B**ethe-**B**loch (BB) equation 4.8 describes the mean energy loss [194], which is induced by electromagnetic interactions of the traversing particles through matter. The formula is applicable for all particles besides electrons in the energy range $0.1 < \beta\gamma < 1000$.

In HADES, two subdetectors, namely TOF and MDC provide information about the energy loss of the particles which were measured. Since the TOF is only providing information for polar angles $\theta > 45°$, the specific energy loss of the MDC was used as they cover the full HADES acceptance.

Figure 4.7 shows the measured energy loss of the preselected protons and π^- and the theoretical BB-curve in black. While no contamination is seen for the π^- on the left side, the proton sample still contains of a contribution of π^+ for small momenta. Those obviously wrongly identified pions can be well described by the theoretical BB- π curve. Thus π^+ are rejected by a very lose selection cut of

$$(\frac{dE}{dx})_{measured} < 0.3 \cdot (\frac{dE}{dx})_{theo} \tag{4.9}$$

which is depicted in red in the right plot. While the energy loss is widely used with great success for distinguishing light nuclei from protons, in this analysis the impact is very limited.

The phase space distributions of the hadrons after the lose reconstructed mass selection and the removal of wrongly identified protons via the specific

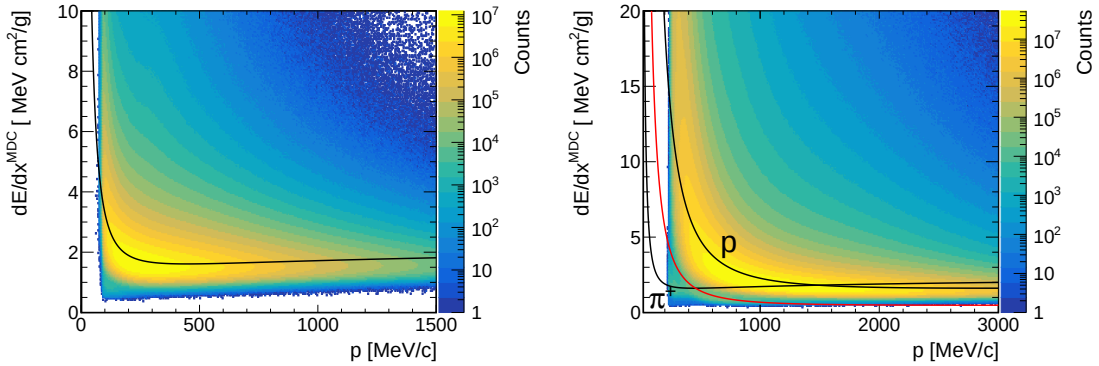

(a) Remaining π^- candidates **(b)** Remaining p candidates

Figure 4.7: The measured energy loss in the MDCs for π^- on the left and protons on the right respectively after the reconstructed mass preselection.

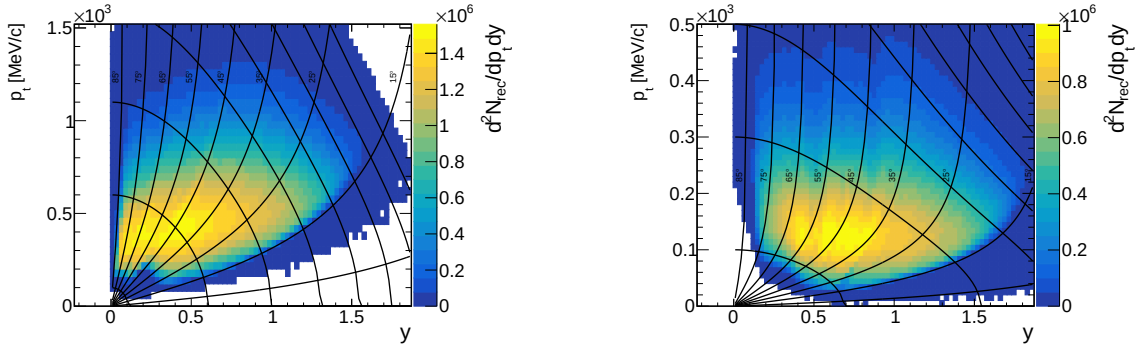

(a) p_t-y distribution of all proton candidates in the $0-40\,\%$ most central events

(b) p_t-y distribution of all π^- candidates in the $0-40\,\%$ most central events

Figure 4.8: On the left hand side, the phase space distribution of all proton candidates is shown, while the π^- candidates are shown on the right. Additional details are written in the text. Distributions are shown after the soft preselection using the reconstructed mass and energy loss.

energy loss in the MDC are displayed in figure 4.8. The grid visualizes the acceptance constrains of the HADES detector by equidistant distances in polar angle θ of $10°$, and in the total particle momentum. The momentum steps are $200\,$MeV/c for the π^- and $500\,$MeV/c for the proton, both starting with the first line at $p = 100\,$MeV/c. The acceptance borders in polar angle θ highly depend on the magnetic field and the target position and thus can differ to results from different beam times. The total phase space coverage of hadrons is located in a very favorable region, as for the kinetic beam energy of $E_{kin} = 1.58\,$AGeV midrapidity lies at 0.82 which is nicely centered in the HADES acceptance.

Figure 4.9 summarizes the average multiplicity for the preselected p and π^-. The large average numbers would result in an overwhelming contribution of mostly uncorrelated combinatorial p π^- pairs of $N_r(p\pi^-) = 54.4\,$/evt. Thus strict

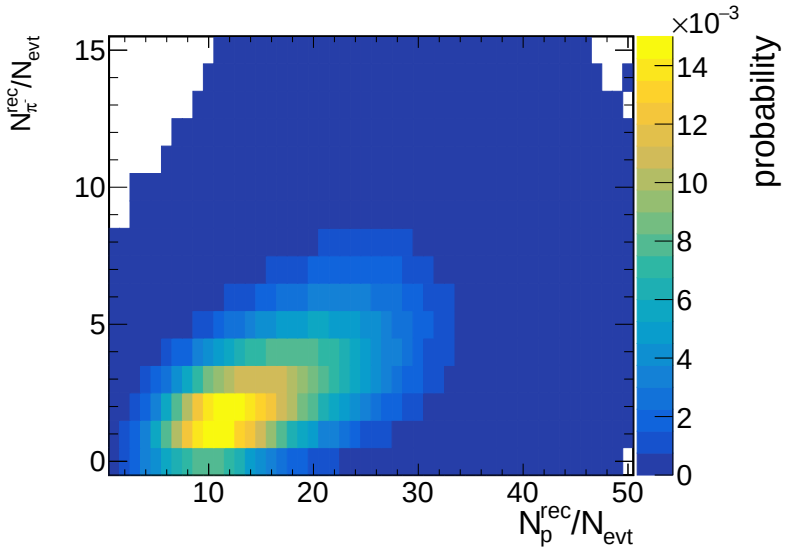

Figure 4.9: Amount of reconstructed protons and π^- in the $0-40\,\%$ most central events after reconstructed mass selection.

pair cuts will be introduced later in chapter 5 to reduce the background.

4.7 Photon Identification

Since the decay of the Σ^0 to 100% occurs via electromagnetic interaction either the real photon, or the virtual photon, showing up as e^+e^- pair, needs to be identified. Potentially, the real photon converts into an e^+e^- pair as well. Differentiating between Λ and Σ^0 production rates thus necessitates the identification of photons or e^+e^- pairs.

The newly installed electromagnetic calorimeter allows the direct reconstruction of the real photon without relying on the conversion method which had been used for previous beam times in several analysis [176][121][195]. The small mass differences from Σ^0 to Λ result in a low energy photon of $\Delta M \approx 77\,\mathrm{MeV/c^2}$ in the center of mass rest frame. As the electromagnetic calorimeter was newly installed, special care was taken in this analysis to (re)calibrate the ECal, check stability of signals for all cells and carefully investigate the acceptance asymmetry as only parts of the sectors were in operation.

4.7.1 Photon Selection

Obviously photons are massless and therefore travel with the speed of light through the HADES detector. The velocity thus allows to distinguish between heavy and thereby slow hadrons and the photons. Since the calibration of the ECal was not finished while analyzing the data, several, additional aspects had to be taken into account for the photon selection:

- The used DSTs contain information about the energy of the ECal cluster, which are not fully calibrated.
- The timing information is not properly calibrated, leading to different expected time of flight values for photons.
- The simulations do not describe the experimental data in major aspects like energy resolution and timing resolution. As both resolutions in fact clearly depend on the deposited energy, a dependency in terms of the particle energy would be needed in the simulation.

The third item is the reason to use the simulations as rarely as possible for the extraction of the selection criteria. Nevertheless the kinematic distribution and the overall detector response will be used, since these distributions are expected to be well described by simulations.

As first step, for photon identification, the data set is cleaned up in order to suppress possibilities for systematic errors.

4.7.1.1 Cluster Position

As pointed out in chapter 2.2.7, the acceptance of the electromagnetic calorimeter during the Ag+Ag beamtime was constrained to two almost fully equipped sectors out of six. The nominal acceptance covers polar angles in the range of $12°$ up to $45°$. Several cells showed diminished quality during the calibration process and thus are removed from the data set for experimental and simulated data. All cells which were removed for the analysis are listed in appendix B.2.

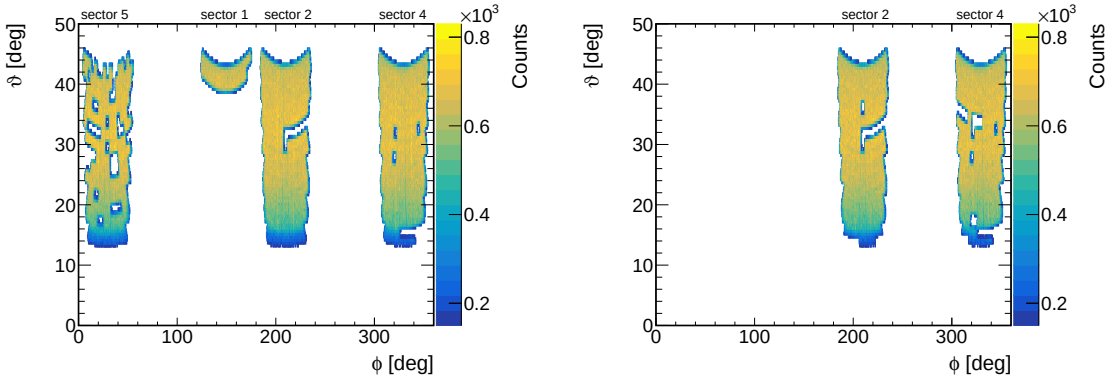

Figure 4.10: Coverage of the cells of the electromagnetic calorimeter. On the left side, all cells are shown which were available during the beamtime in March 2019 while of the right side only cells which are used in the analysis after removing cells with decreased quality are shown.

The acceptance coverage of the electromagnetic calorimeter is displayed in figure 4.10 in terms of polar angle ϑ and azimuth angle ϕ. The values were extracted from simulated photons which were produced in the target region which is in perfect agreement to experimental photon candidates in experimental data. While sector five contains many widely spread acceptance holes and sector one consists only of the cells in the two rows of largest theta values, sectors two and four were almost fully equipped. Thus only sectors two and four are taken into account for the further analysis. However, also in these two sectors, a few cells were showing low quality after calibration and thus were rejected. By comparing figure 4.10a to 4.10b the removal of cells at small polar angles for sector two and a row at intermediate polar angles around $\vartheta = 35°$ for sector four can be seen.

Figure 4.11 shows a schematic topology map highlighting regions in which photon conversions takes place. For small polar angles, additional material

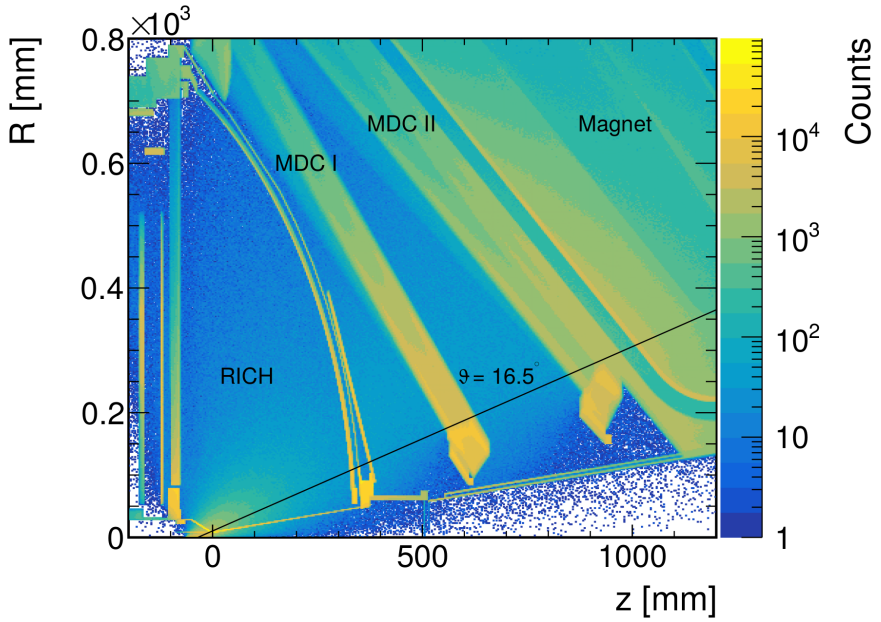

Figure 4.11: Schematic view of the HADES conversion topology with respect to the distance towards the beam axis denoted as R and the spatial position along the beam axis denoted as z. Further details are written in the text.

budget is located within the acceptance of the electromagnetic calorimeter. Clearly visible in figure 4.11 is the inner holding structure of the first chambers of the MDCs. To avoid enhanced conversion probability which yields to enhanced background, all ECal cells with $\vartheta < 16.5°$ are neglected for the γ analysis. The distribution of the polar angle ϑ of all clusters is shown in figure 4.12 for experimental and simulated data. The black data points represent the experimental data where obviously no separation between photons and background can be displayed. The red data points represent all photons which were produced in UrQMD simulations, while the blue data points show all clusters which were produced by UrQMD particles which were no photons. This includes all charged

and uncharged particles, as well as noise which is uncorrelated to particles. The green data points show the PLUTO generated γ from Σ^0 decay where the decay was embedded in UrQMD. For the purple data points the Σ^0 from PLUTO was embedded in experimental data. All distributions are normalized to their corresponding integral. The accepted area is marked as green shaded area. As described, small polar angles are rejected to avoid enhanced background from conversion (see figure 4.11).

The large bin-by-by changes of the cluster yield versus ϑ are a result of the spatial resolution of the cells: Clusters of only one cell, which is most common, are just assigned to the ϑ value of the cell center. The black data points consist of γ and background and thus are expected to be located between the blue and red data points. Since in real data there is more background than in simulation, especially at small polar angles, the black data points overshoot the blue data points. Here the photon yield is drastically reduced compared to the background.

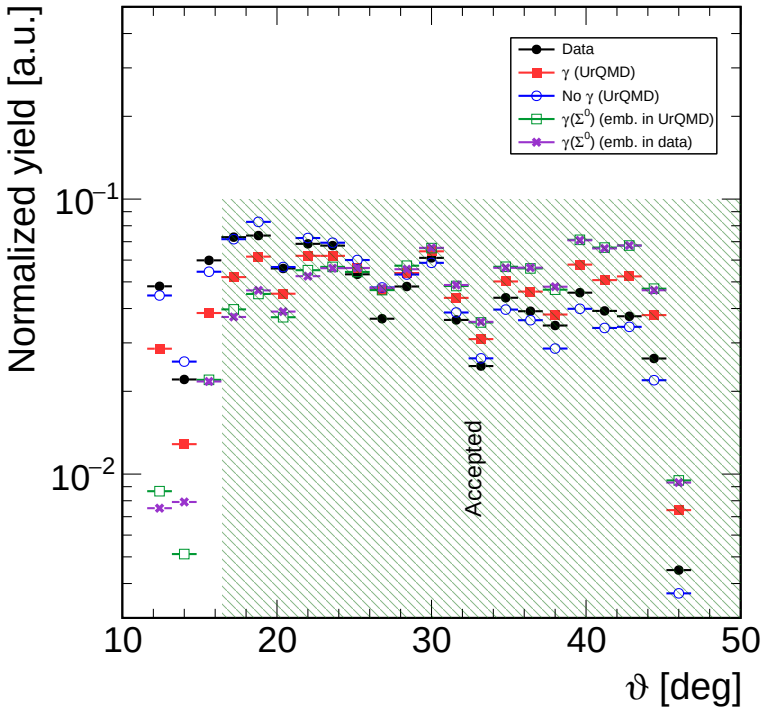

Figure 4.12: Polar angle distribution of all measured or simulated clusters. The accepted ϑ range is indicated by the green shaded area. More details are written in the text.

4.7.1.2 Cluster Candidate Matching

After selecting the acceptance with properly working cells, the remaining background needs to be further suppressed. As first step, clusters which were produced by charged particles should be removed from the sample. Therefore each reconstructed particle track which fulfills the track quality parameters described in section 4.4 is checked for a correlation to a cluster. During the track finding algorithm, a track-cluster matching probability $\chi_{track-cluster}$ is calculated, which allows to quantify the probability of this track to be the origin of a certain cluster. The normalized probability distribution of this track-cluster matching is displayed in figure 4.13. The color code is the same as for figure 4.12 and will stay the same for the following figures in this chapter. The blue curve of UrQMD background contains mostly charged tracks, and thus rises for small values of $\chi_{track-cluster}$. Similar behaviour is observed in the experimental data in black, while the true γ from simulation do not peak at small values. The distributions in purple and green which both represent the γ from Σ^0 decays differ significantly, which proves that a realistic description of the background track density is required. This naturally is the case if embedding Σ^0 baryons in data, but obviously the situation is different in UrQMD simulations.

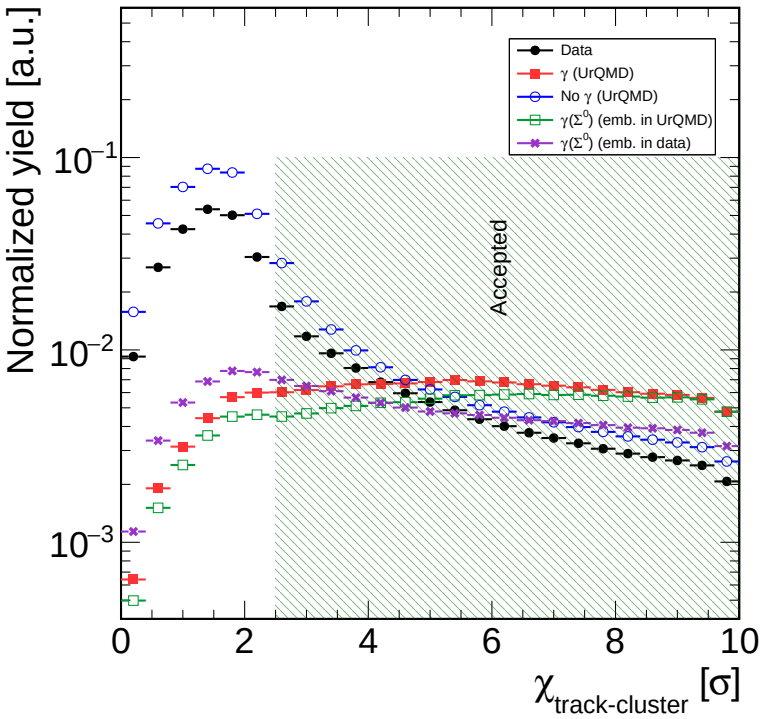

Figure 4.13: Matching quality of the cluster to reconstructed charged particle tracks. More details are written in the text.

The visualization of this difference in figure 4.13 this explains, why embedding in real data was performed and will be used for further efficiency corrections. In

addition to the cluster-track matching, also all cluster with nearby RPC hits are rejected, even if no charged particle track was found next to the RPC hit. This method is justified, because the RPC covers the full acceptance of the electromagnetic calorimeter and being located directly in front of the ECal.

4.7.1.3 Cluster Time

In addition to the removal of the charged particles, the timing information of the corresponding cell of the electromagnetic calorimeter can be utilized for a time of flight measurement. The leading edge of the cluster is combined with the start detector to obtain the time difference Δt while the distance of the cell to the event vertex is calculated for the path length. The resulting integrated velocity distributions are shown in figure 4.14 where photons should occur at $\beta = 1$. Obviously, in experimental there is a lot of additional background, which contributes to all regions in the velocity distribution.

As the timing resolution and background in simulations is not described realistically, comparing simulations of Σ^0 embedded in UrQMD or data, only a wide cut of $\beta > 0.8$ for photon candidates is applied here. More precises solutions are described in section 4.7.2.

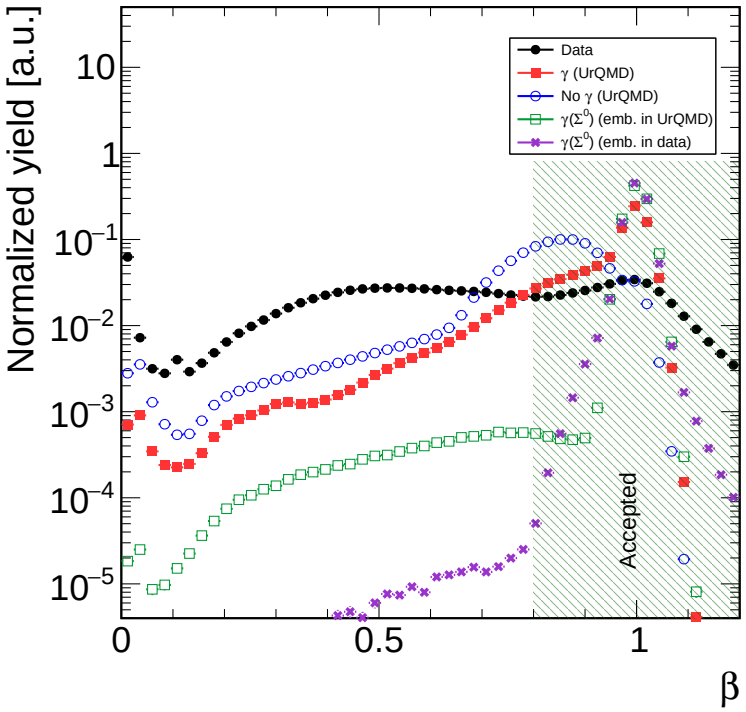

Figure 4.14: Reconstructed velocity from the measurement of time-of-flight and path length, assuming uncharged particles, traversing straight from the event-vertex to the cell of the electromagnetic calorimeter. More details are written in the text.

4.7.1.4 Cluster Energy

In addition to the previously mentioned cuts, also the cluster energy is taken into account for background suppression. In figure 4.15 the cluster energy distribution for the clusters remaining after the previous cuts is displayed. For choosing a cut value we rely on the simulations, which describe the kinematics properly. Obviously, the ECal cells are not capable of reconstructing energies below 40 MeV as seen in experimental data, while the simulations are not describing this efficiency drop. Therefore, a minimum value of at least $E = 40$ MeV must be chosen. By comparing the energy of γ from Σ^0 decays to all energies, a cluster energy in the range of $E = 60 - 250$ MeV is required. This selection window removes only a marginal amount of signal photons while still keeping a broad window, to not restrict the invariant mass range of $\Lambda\gamma$ pairs.

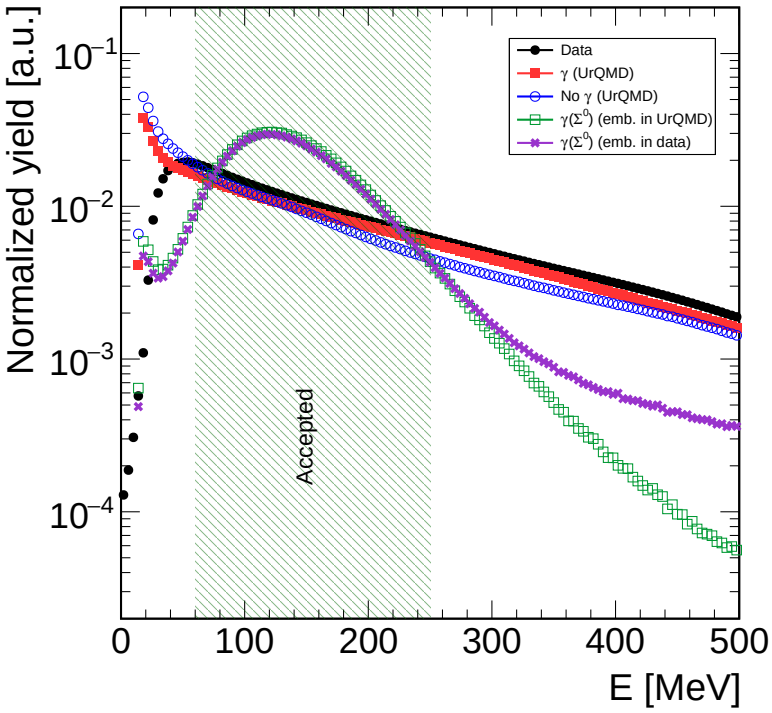

Figure 4.15: Reconstructed cluster energy of all clusters remaining after the previous cuts, for the different sources. More details are written in the text.

4.7.1.5 Cluster Size

In section 2.2.7 the geometry and position of the electromagnetic calorimeter in relation to the rest of the HADES experiment is described. The granularity of $92\,\text{mm}\times92\,\text{mm}$ per ECal cell leads to many clusters of size one which correspond to a single, isolated cell delivering all information. In case of a cluster of size > 1 the energy splits into the different cells. The resulting energy spread needs to be

described properly in terms of energy loss and energy resolution. In the actual status of the ECal, those uncertainties would hamper the analysis results, so all cases with cluster size > 1 are removed from the sample.

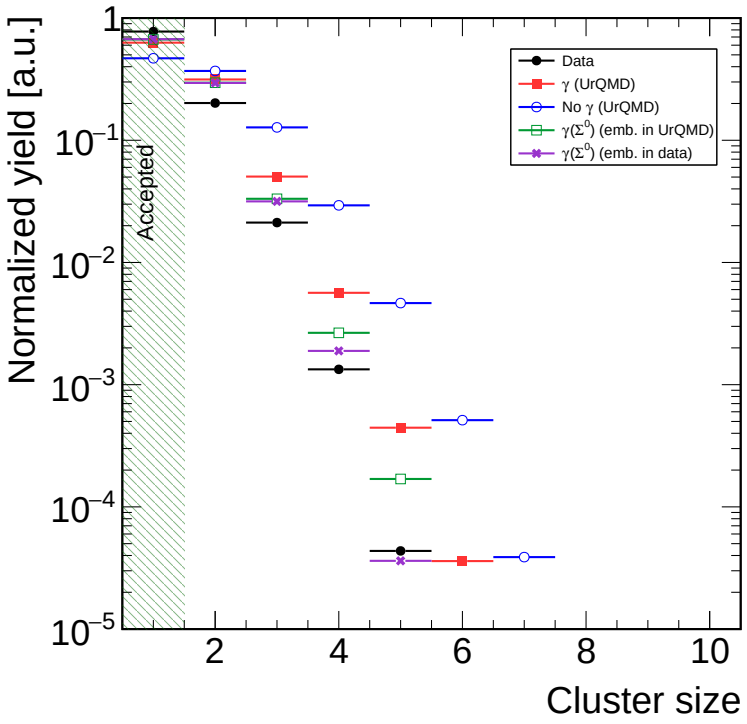

Figure 4.16: Cluster size of all clusters remaining after the previous cut for the different sources.

Figure 4.16 shows the probabilities of clusters to be formed by a certain number of cells for simulated and experimental data after all previously applied selection criteria.

In simulations, photons mostly have a signal only in one cell, while any other particle shows a wider cluster size distribution. This effect is strongly correlated to the incoming angle which is perpendicular for photons. Any other electromagnetically charged particle is bent in the magnetic field and thus comes at different angles and thus produces signals in several cells. In experimental data, several additional background sources exist, which produce mostly clusters of size one. This usually is noise unrelated to physics.

A summary of the applied selection criteria is displayed in figure 4.17, which is for each source normalized individually to all available good cells which were producing a signal. Differences between embedding of signal photons from Σ^0 decays in UrQMD events to real data are clearly visible. Mostly, they consist of the differences due to the matching to RPC clusters. As this is more realistic, in all following steps always the embedding into real data is referred to.

This cut selection efficiency is combined later with the acceptance and the quantum efficiency of the PMT to obtain the overall reconstruction efficiency.

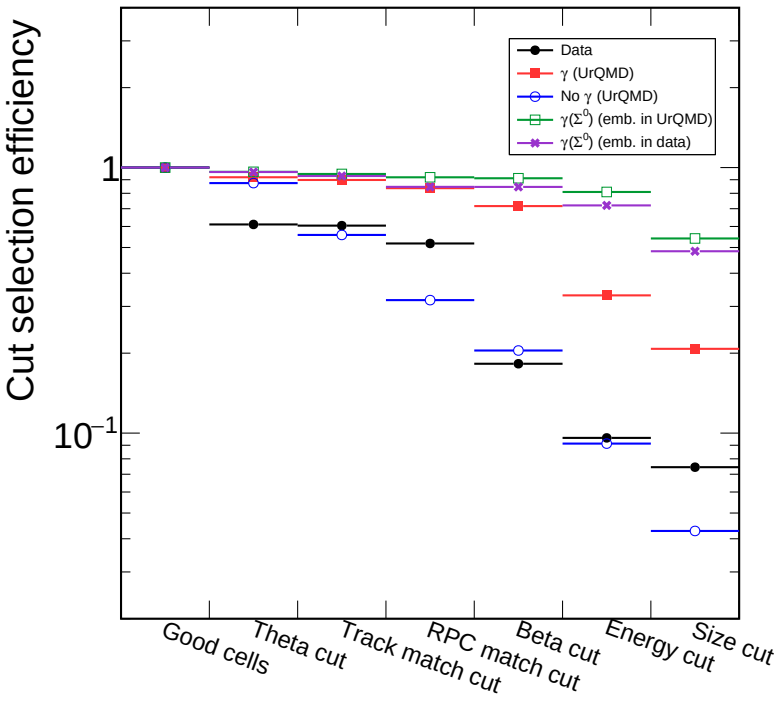

Figure 4.17: Cut selection efficiency for the various cuts described in the text in this chapter.

The distributions after successive application of all selection criteria are attached in appendix B.1.

4.7.2 Time Recalibration

In comparison to the already existing subdetectors, the calibration of the ECal changed a lot during this analysis due to the fact that the ECal was used for the first time and had to be understood and calibrated.

Nevertheless the extracted signals were not stable versus the different sectors, cells and time windows within the beamtime. The following two sections will deal with these irregularities and monitor them. This lead to the conceptional idea of a timing recalibration which is rather simple: since all photons have the same velocity $\beta = 1$, independent on their energy, the velocity spectrum must peak at one, integrated over all other observables. Whenever this is not true, the remaining shift arises by a rather poor purity of the photon sample and thus a non neglectable amount of noise which delivers random time information. A sharp cut on the timing information is essential for the removal of slow hadronic background such as uncharged neutrons, which are indistinguishable in terms of the remaining selection parameters.

For this timing analysis, clusters of the electromagnetic calorimeter of each size are taken into account. However, clusters should not be matched to an RPC

cluster and not be matched to a charged track within 3σ matching quality. In addition, only clusters of energy $E > 500\,\text{MeV}$ are taken into account, since clusters of smaller energy are contaminated by more background. In addition, the energy resolution is much worse so that in many cases no clear timing peak was visible. Those selected clusters were analyzed for each cell of both sectors used. The timing, i.e. β- distribution is analyzed in terms of time stability during the beamtime. An example of sector 4, cell number 224 is shown in figure 4.18a. Within this plot, three time slots are marked, and their projections on the measured velocity are displayed in figure 4.18b to visualize the instability during the beamtime.

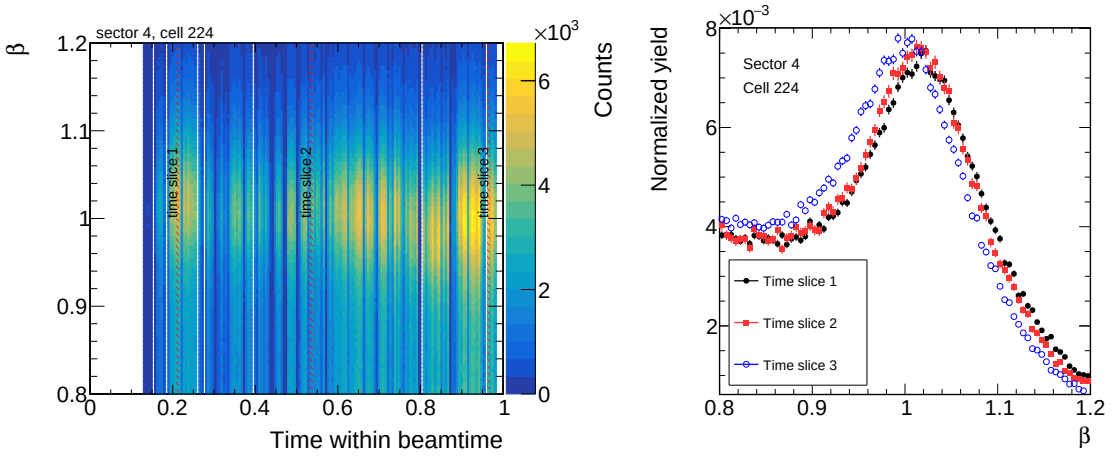

(a) (b)

Figure 4.18: On the left side the β distribution of an example cell is shown for beam time slices of 3 hours each. Besides the intensity fluctuations which are correlated to the amount of recorded events, the differences in the most probable value of β are crucial for background rejection. Three projections of different time windows within the beamtime are shown as an example on the right side for the same cell of the same sector.

In figure 4.19 effects of the position of different cells in the ECal are visible. While the cells at larger polar angle ϑ which refer to larger cell numbers do not contain large amount of background, the cells at smaller ϑ suffer from enhanced background.

Each time slice is fitted with a Gaussian, and the β-values for the mean $\pm 1\sigma$ are stored. All cells without converging fits are rejected. In addition all distributions where the left border was below $\beta = 0.9$ were rejected.

A summary of two individual example cells is depicted in figure 4.20 where the β-values for mean $\pm 1\sigma$ of the fits are shown. While the upper border of the symmetrically assumed Gaussian is displayed in bright green, the lower limit is shown in darker green. Any cells without a converging fit are removed from the sample and marked with a red cross. Several structures are visible: There is a the significant drop in β after one third of the beamtime due to changes in the software procedure. The values fluctuate and show a slow increase of the

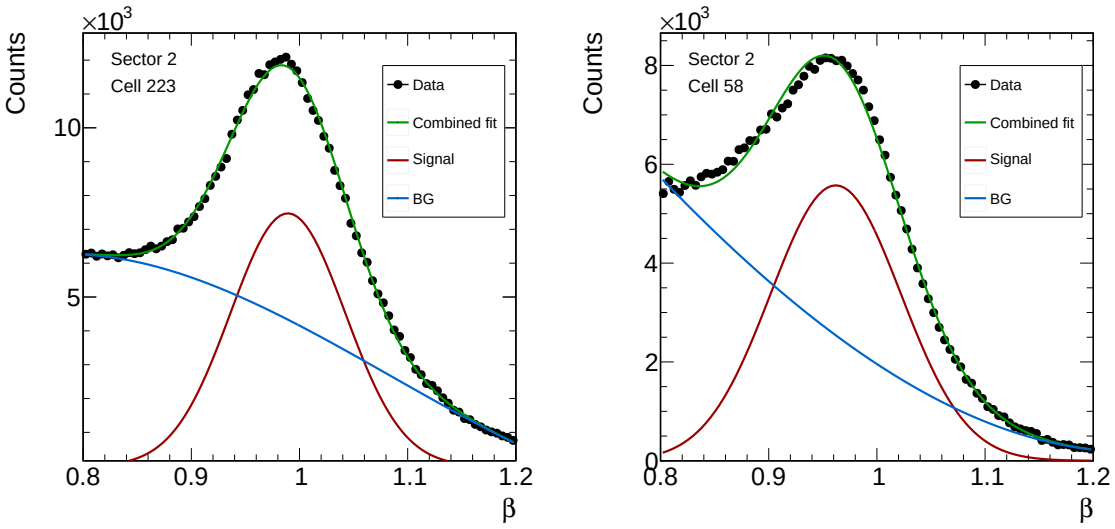

(a) (b)

Figure 4.19: Two examples of fitting results of the β distribution for different cells for a specific time window of three hours. The black dots describe the experimental data which are fitted by the green function which consists of a Gaussian and a third degree polynomial. The Gaussian distribution in red is considered to originate from the γs while the background is depicted in blue and contains all remaining contaminations.

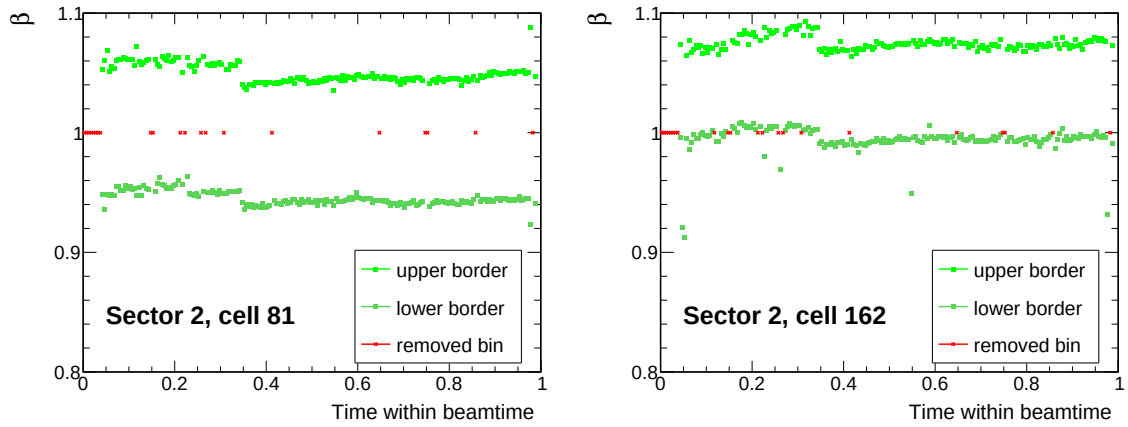

(a) (b)

Figure 4.20: Time dependency of the β distributions of two specific cells, where the cell in figure 4.20a is taken from an intermediate ϑ region, while the right side 4.20b describes the behaviour of a cell of the outer most row of cells, which have a systematic shift towards high β values.

mean β with time. All these effects are taken into account when applying the β-selection criterion based on time dependent individual fits of the β distributions. This method also allows the usage of the most outer row of the ECal, where β-values are considerably larger than on average and expected as it is visible in figure 4.20b.

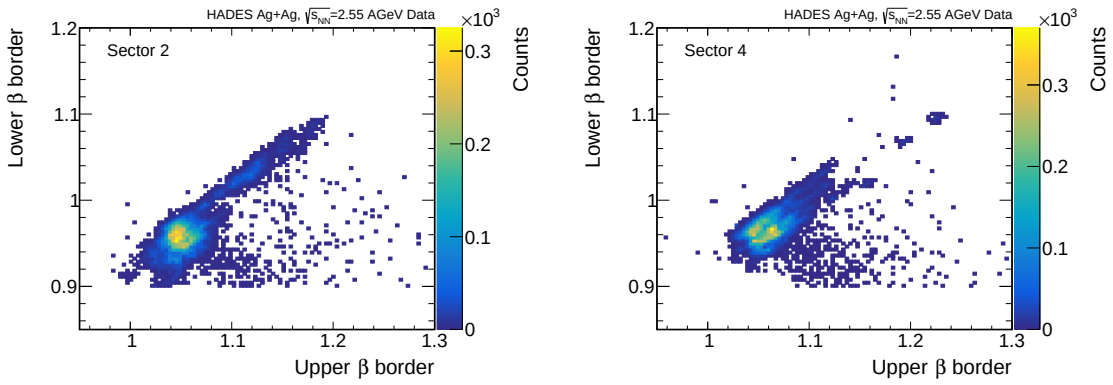

(a) (b)

Figure 4.21: Selection criteria, integrated over all cells and the whole beam time shown for sector 2 (left) and sector 4 (right). Additional details are written in the text.

The overall performance of the timing of the electromagnetic calorimeter is displayed in figure 4.21 for sectors 2 and 4 individually. There, the value of the lower border (mean-1σ) is plotted in dependency on the upper border (mean$+1\sigma$). The closer both values are, the more narrow the Gaussian fit was, which is directly correlated to a more precise time resolution. For both sectors, the main structure is visible around $\beta_l \approx 0.95$ and $\beta_u \approx 1.05$ which refers to a Gaussian at $\beta \approx 1$ and a width of $\sigma \approx 0.05$.

4.7.3 Energy Recalibration

In addition to the calibration of the timing information the energy needs an additional calibration as well. In comparison to the calibration of the time, in this case there is no standard candle like the $\beta = 1$ condition. As result, the energy can be adjusted only via the invariant mass reconstruction of a particle decaying into a photon. The energy recalibration which is used in this thesis was first shown in [196]. It relays on π^0 decays into two photons. For each decay, the two photons have to be detected in the ECal and thus will produce two clusters. The invariant mass is now plotted for each cell independent on the cell of the second photon. Within this method, the resulting π^0 peak is shifted to its nominal mass by changing all photon energy by the energies difference extracted from the invariant mass formula, equation 4.5. After 15 iterations of this method, this cell dependent correction factor is applied.

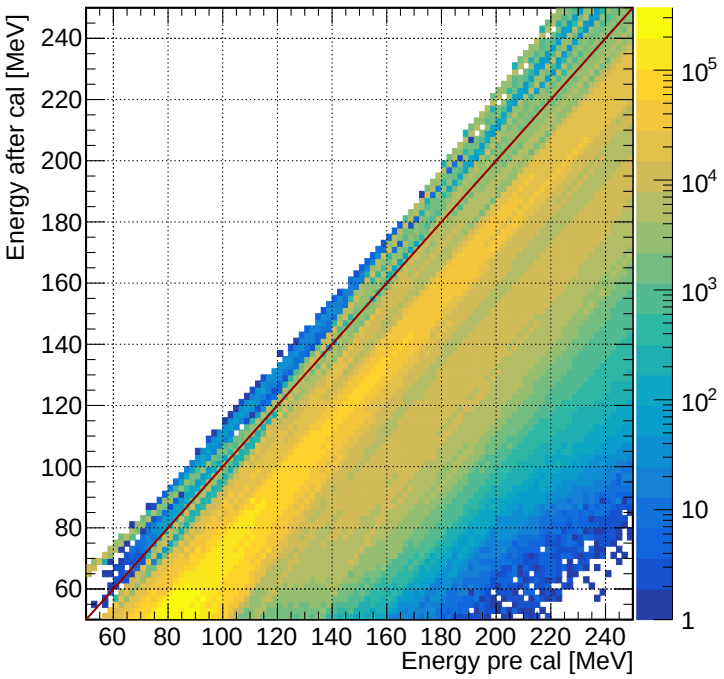

Figure 4.22: Energy recalibration of ECal clusters, performed by using π^0 mass peak information.

Figure 4.22 shows the impact of the ECal energy recalibration integrated over all cells. The value of the cluster energy after recalibration is plotted versus its value before the correction. The diagonal is drawn in red to visualize the large effect. The correction reduces the value of the reconstructed energy on the order of 30-40 MeV for small energies and by approx. 20 MeV for intermediate energies of around 200 MeV. The implemented method works for clusters of each size, since it corrects each single cell individually before adding up the corrected energy values.

The corrected energy is calculated by the following equation:

$$E_{\text{new}} = c_{\text{ECorr}} \cdot (\text{ADC}_0 + e^{\text{ADC}_1 + \text{ADC}_2 \cdot \text{TOT}}) \tag{4.10}$$

The recalculated energy E_{new} depends now on a cell dependent constant correction factor c_{ECorr}, the measured TOT, three fit parameters ADC_0, ADC_1 and ADC_2 which are extracted cell wise by fitting the energy in dependency on the TOT as described in [197].

4.8 Lepton Identification

This section deals with the reconstruction of the leptons from the channel $\Sigma^0 \rightarrow \Lambda e^{\pm}$ which can be used as crosscheck to the reconstruction of the $\Lambda\gamma$ channel, described in section 6.1. In principle two different mechanisms can produce a final state with a dilepton pair. A Dalitz decay of the Σ^0 baryon would produce an e^+e^- pair, however it was never observed so far, only an upper limit for the branching ratio of $5 \cdot 10^{-3}\,\%$ is listed in the PDG. This upper limit is extracted by QED calculations [198]. Second, a conversion of the Σ^0 decay photon produces leptons. They can be reconstructed if the conversion takes place in front of the MDCs inside the RICH around the target area, such that charged tracks will be measured. HADES is optimized for lepton analysis and thereby suppresses conversions by low material budget. In the Ag+Ag beamtime in March 2019 the integrated conversion probability was $\approx 1\%$ in the region of the RICH [166]. Combining both possibilities the resulting ratio of leptons/photons for the Σ^0 decay should still be on the order of a few percent at maximum. In this analysis as first step, all leptons are identified, rejecting hadronic background as strong as possible. Later, specific cuts on the specific signature of leptons from a Σ^0 decay are applied.

4.8.1 Track Quality

During track reconstruction, the track candidates receive several flags, summarizing the quality. Track candidates are formed out of all possible combinations of tracklets in the inner segments (MDC I and MDC II) and those segments in the outer (MDC III and MDC IV), the latter are already combined with a META hit. Theses combinations result in various scenarios of mismatchings. Since there is no magnetic field in the inner MDCs, any e^+e^- pair from conversion with small opening angles may not be distinguished due to limited resolution. After the magnetic field, those leptons separate spatially which dramatically enhances their reconstruction probability.

Besides this case, it can also occur that several META hits are matched to one track. In this case the META match quality is providing the necessary information, which track was more likely to be the origin of the META hit and thus should be matched. The META matching χ^2_{META} in equation 4.11 is calculated by extrapolation of the reconstructed track towards the META detector.

$$\chi^2_{META} = \sqrt{\left(\frac{dx}{\sigma_x}\right)^2 + \left(\frac{dy}{\sigma_y}\right)^2} \tag{4.11}$$

The distances from the track extrapolation are denoted as dx and dy while the known detector uncertainties are written as σ_x and σ_y. A match of a META hit to several tracks might also happen, the trivial assignment is also performed by the META matching quality. Sorting by χ^2 removes most of the mismatches since each detector hit is used only once. Allowing the inner MDC hits to be shared for

multiple tracks is a solution and summarized in appendix A.4. In summary, the same preselection like for hadrons in form of the kIsUsed flag 4.4 is requested, selecting $\chi^2 < 1000$ which is a rather wide window.

4.8.2 Reconstructed Mass

For distinguishing the rare electrons and positrons from the remaining particle species, the advantages of the RICH are necessary. Before it is used for the selection, a sample of possible candidates is needed. In addition to the track quality requirement explained in chapter 4.1, the calculated reconstructed mass is taken into account. Especially at small momenta, the separation power of the reconstructed mass is tremendous, while for increasing momenta, the reconstructed masses of e and π become indistinguishable and the RICH information is required. Thus a cut on the reconstructed mass $m_e^{rec} < 0.7 m_\pi^{PDG}$ is applied. By the choice of this specific criterium, any interference between selected π^- and electron candidates is excluded by definition due to the π^- selection stated in equation 4.7.

4.8.3 Ring Track Matching Quality

In addition to track quality and the reconstructed mass, the quality of the RICH ring-track matching is utilized for suppression of tracks with wrongly assigned lepton ID.

Similarly as for the META hits, random combinations of rings to tracks, result in large impurities in the lepton sample. A ring-track matching quality is defined in similarly to the META matching quality as:

$$RMQ = \sqrt{(\vartheta_{Track} - \vartheta_{Ring})^2 + ([\phi_{Track} - \phi_{Ring}] \sin \vartheta)^2} \tag{4.12}$$

Thus the **R**ICH-**M**atching-**Q**uality (RMQ) in equation 4.12 describes the goodness of the matching in terms of polar angle ϑ and azimuth angle ϕ. Within this matching criterium, multiple scattering of lepton tracks is taken into account by a correction which is extracted and explained in more detail in [166].

The fraction of mismatched ring-track combinations can be estimated by the so called RICH rotation technique: The RICH detector is rotated by $180°$ in the software around the beam axis and ring-track matching is performed, resulting in only random matches by definition. This procedure allows to estimate the amount of random matches. The $180°$ rotation in azimuthal angle ϕ fulfills all RICH related $90°$ symmetries as well as the HADES $60°$ sector symmetry.

Figure 4.23 shows the behaviour of the RMQ value for all particles which survive the tracking quality selection. The plot is created for one day of statistics only, representing the whole beam time. Since all matches are accepted, a large amount of mismatching appears even in the original, unrotated data denoted in black. The RICH rotation does not need normalization and thus the subtraction of the rotated spectrum provides the background free RMQ distribution for true

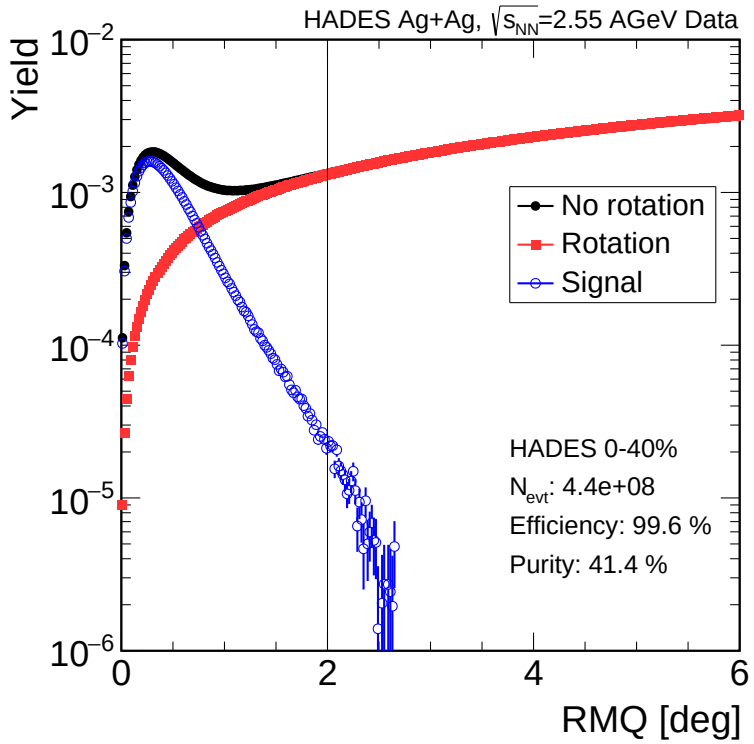

Figure 4.23: RMQ calculation in experimental data from the RICH rotation technique in logarithmic representation for all possible lepton track candidates.

matches denoted in blue. For the following analysis, only electron and positron tracks with $RMQ < 2^{\circ}$ are taken into account, which corresponds to a momentum integrated efficiency of 99.6%. Already in this step, a purity of $41.4\,\%$ is achieved without any additional PID method. The RMQ cut was analyzed in addition in dependence on polar angle θ and momentum of the electron track candidate. However, this did not improve the selection and thus is not used.

4.9 Ring Quality

Besides the matching quality of the reconstructed ring to the track candidate, the ring itself is selected based on several observables. The ring radius is geometrically given by the distance between the RICH mirror and the MAPMTs which reconstruct the reflected Cherenkov photons. The separation of the RICH MAPMT plane in inner and outer part was performed to achieve approx. constant ring observables over the full acceptance. As shown in [195] simulations describe the experimental RICH data with its minor polar angle dependency rather well in terms of ring radius and number of reconstructed Cherenkov photons per ring.

Figure 4.24 shows the reconstructed ring radius in dependence on the number of calibrated Cherenkov photon hits (so called “Cals”) from simulated electrons which passed the previously described track quality selection. Only rings within

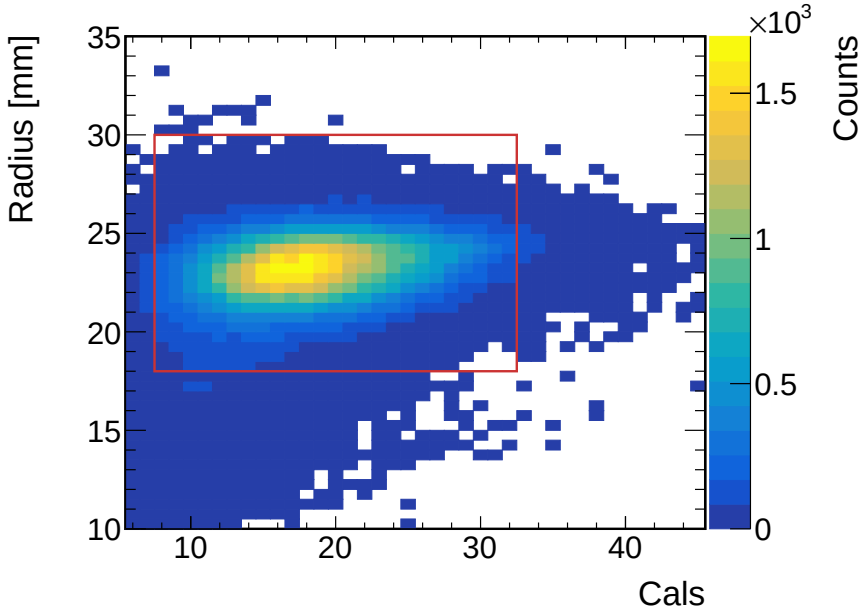

Figure 4.24: Reconstructed RICH ring radius in dependence on the number of measured photons along this ring for simulated $e^+$and e^- from Σ^0 photon conversions.

the red box were taken into account in the further analysis which results in 5.0% rejection due to ring quality [1].

In figure 4.25 the impact of the track selection quality is visible. Using all tracks which is depicted in black tends to use rings with a smaller amount of Cals and a smaller ring radius. The distribution in red shows only those tracks which fulfill the additional RICH matching and reconstructed mass conditions. A clear reduction of the rings of bad quality is seen. Afterwards the ring quality selection rejects the remaining rings with $N_{Cals} < 8$ or $N_{Cals} >= 31$ as well as ring radii of $r < 18.0$ mm or $r > 30.0$ mm.

With these cuts, a high lepton purity on the order of $\approx 99\,\%$ is achieved for the momentum range of interest of p< 250 MeV/c as shown in figure 4.26. Due to the momentum dependent tracking resolution, the RMQ distribution gets wider for these small momenta, which results in a slightly reduced RMQ cut efficiency of 98.2 $\%$. Additional attempts of improving the Σ^0-lepton separation from background leptons using machine learning algorithms was attempted without success, since all single lepton observables are indistinguishable when comparing background leptons with Σ^0 leptons [199].

[1] In experimental data rings with a very enhanced amount of Cherenkov photons, so called Blobs exist because of crosstalk of the MAPMTs. They are mostly rejected by a maximum amount of Cherenkov photons per ring.

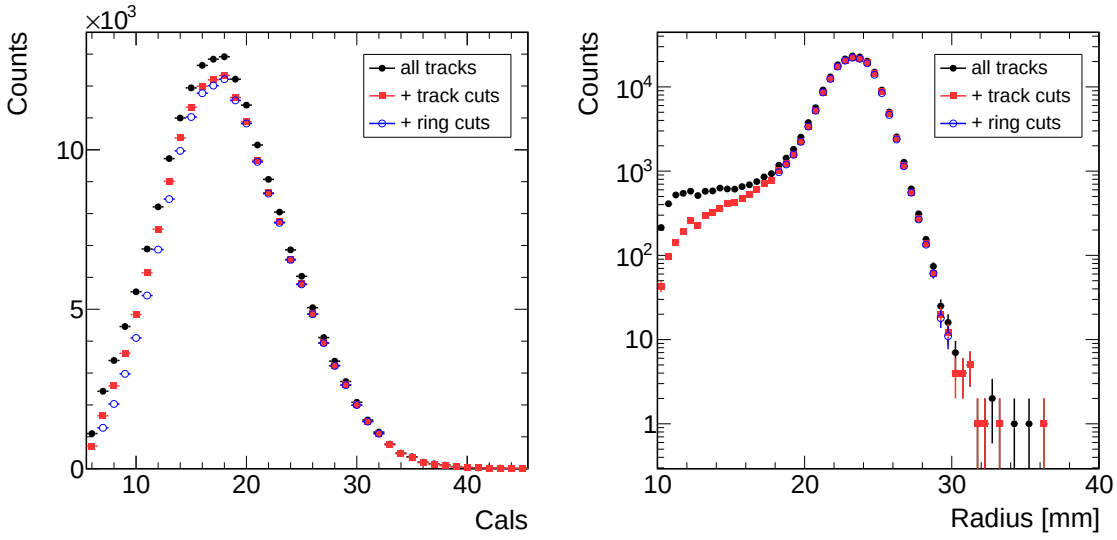

(a) (b)

Figure 4.25: Distribution of RICH observables in simulation after the three mentioned selection steps.

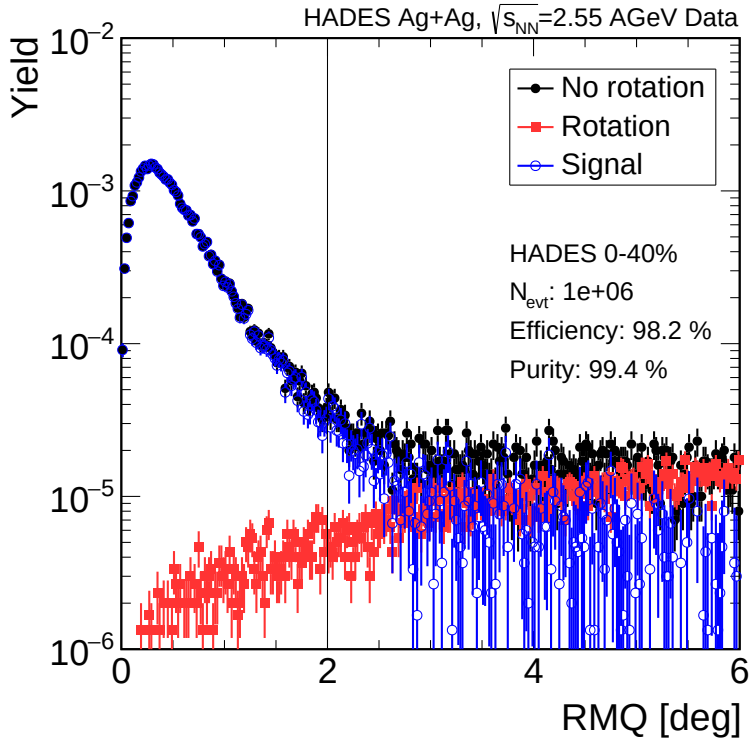

Figure 4.26: RMQ calculation in experimental data from the RICH rotation technique in logarithmic representation after application of all selection criteria.

Amount of Cherenkov Photons

The ring quality is mostly described by the ring radius and the amount of MAPMT pixels with detected Cherenkov photons. In the following figures starting with figure 4.27, different scenarios are displayed where RICH rings were reconstructed. Their reconstructed center is always marked as a black cross while the ring itself is shown in blue. Pixels which contributed to forming the ring are shown in a light blue while the rest of the pixels are depicted in dark blue. The borders of the MAPMT are visible as grid in the background. Since the HADES RICH is placed right behind the target, no magnetic field is influencing the charged leptons and thus gamma conversions yield in dilepton pairs with small opening angles in RICH and the inner MDCs. As pointed out in section 2.2.3, all electrons and positrons above $p \approx 10\,\text{MeV/c}$ produce Cherenkov photons.

Two examples of isolated $e^{\pm}$ rings are shown in figure 4.27. Different physics cases produce such single leptons: dielectron production with large opening angles which might originate from vector meson or other decays or a single lepton from a pair with an unreconstructed partner lepton below Cherenkov photon production threshold of $p < 10\,\text{MeV/c}$, or single electrons from other sources.

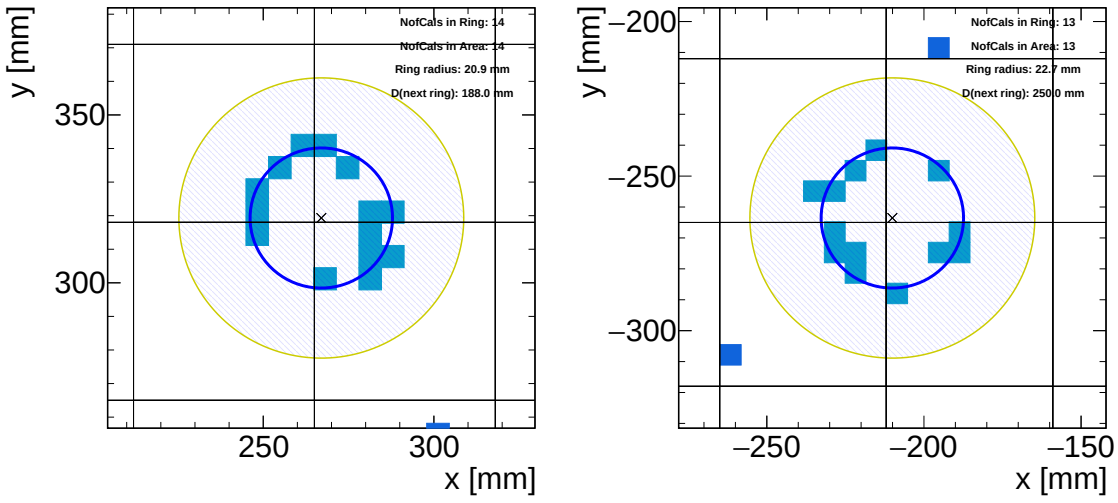

(a) Isolated RICH ring (b) Isolated RICH ring

Figure 4.27: Correctly reconstructed isolated RICH rings from experimental data.

If a dielectron from conversion with small opening angle reaches the RICH and both electrons produce Cherenkov photons, two rings are seen in close vicinity. Those rings might often even overlap. This typical conversion structure is displayed in figure 4.28. In these cases, the rings were separated enough from each other that the ring finder was capable of reconstructing both of them [2].

[2]The second ring is not drawn for improved clarity, but the distance parameter in the upper corner shows the distance to the closest reconstructed ring.

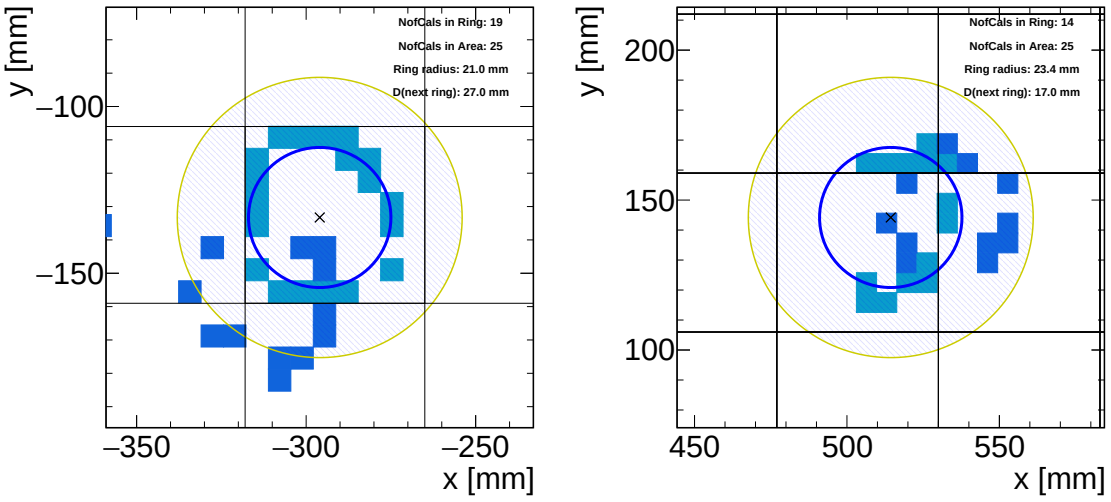

(a) Detected RICH double ring structure (b) Detected RICH double ring structure

Figure 4.28: Correctly reconstructed double rings with an identified (undrawn) second ring close by, from experimental data.

Two examples of the interesting case of an unidentified double ring are displayed in figure 4.29. The ring finder algorithm only found one ring while the amount of detected Cherenkov photon hits is about twice as normal which can be used as signature for a double ring.

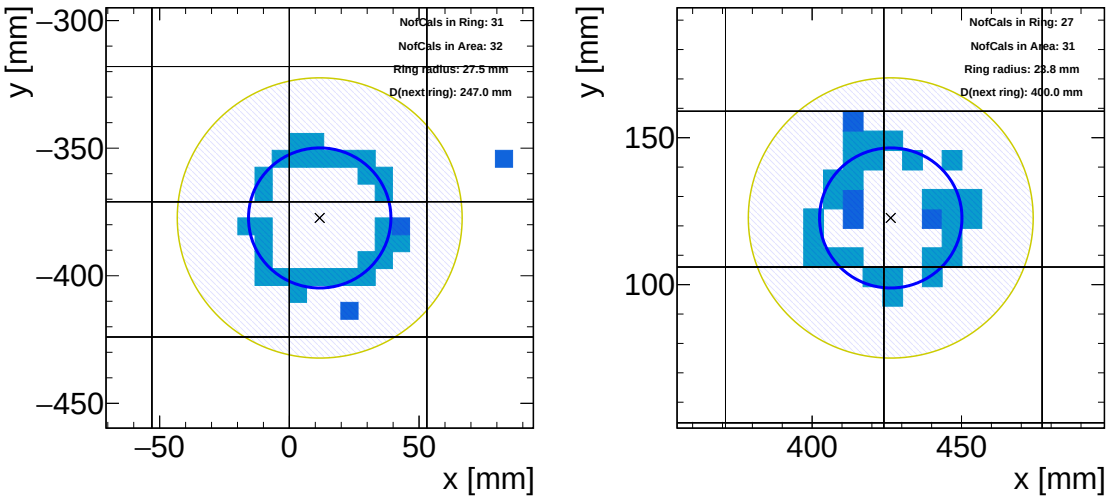

(a) Unidentified RICH double ring structure (b) Unidentified RICH double ring structure

Figure 4.29: Correctly reconstructed isolated RICH ring, with approximately the double number of hits, thus including an overlay of a second unidentified ring. Displays taken from experimental data.

Besides those clear signals, the MAPMT setup sometimes provided signal where almost all pixels of an MAPMT retrieve a signal. Those structure are called “blobs”. The ring finder often fits rings in these blobs, but since they originate from backwards emitted particles which directly traverse the MAPMT plane, no track can be reconstructed in the MDCs. For this reason, blobs are not contributing to the analysis and their random matching to a particle track is minimized by a tight ring-track matching.

CHAPTER 5

Λ Reconstruction

5.1 Off-Vertex Topology

As mentioned in section 1.5, strangeness is produced as rare probe in heavy ion collisions in the energy regime of the SIS18. Predictions and previously realized experiments at SIS18 expect strangeness to be produced approximately in every tenth event. Hadrons which only consist of the lightest u and d quarks occur 4 magnitudes more often.

Selecting p and π^- candidates as explained in chapter 4 would result in approximately 55 pairs per event for the most central $40\,\%$ of the events. This combinatorics would overwhelm any Λ signal, thereby precluding the extraction of the Λ with reasonable significance.

Exploiting the large lifetime of weakly decaying strangeness containing hadrons enables the feasibility of the Λ analysis. The large lifetime of the Λ can be expressed as $c\tau \approx 7.89$ cm which is a good length estimate of the distance, the Λ travels through the detector before decaying. The Λ daughter particles originating from a secondary vertex, which thus is a few centimeters displaced with respect to the event vertex. For HADES, this distance is measurable and relies on a precise tracking as well as event vertex reconstruction, as delineated in section 3.2. The event vertex reconstruction is highly precise due to the substantial number of charged tracks observed in Ag+Ag collisions. The resolution of the reconstruction is $\sigma_z \approx 1.2$ mm in the beam direction and $\sigma_{x/y} \approx 2$ mm in the perpendicular direction.

In figure 5.1 the decay topology of a Σ^0 baryon is shown schematically with the black lines representing the traveled path of the produced particles and the green lines depict calculated values which are used for the Off-Vertex selection criteria. The parameter “VerDistP” is the minimal distance of the extrapolated proton track to the event vertex. Small values of this distance strongly hint for a particle production right at the event vertex and thus can be rejected.

The same procedure is performed for the π^- with the parameter “VerDistPiMLam”, where also small distances are rejected. For the combination of $p\pi^-$ which form the Λ candidate, the point of closest approach of the Λ extrapolation to the vertex, “VerDistLam” should point to the event vertex. Only in this case, the Λ

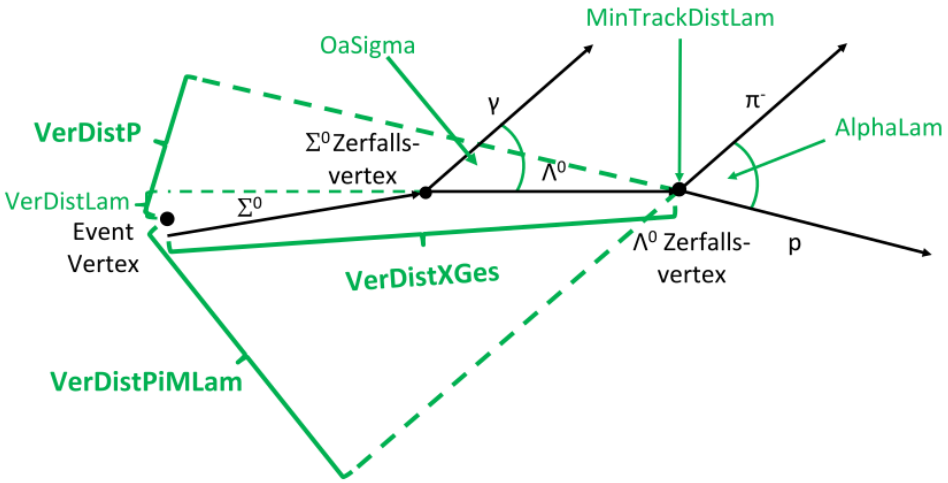

Figure 5.1: Schematic view of the Σ^0 and following Λ decay topology with respect to the event vertex. The distances are not to scale, the Σ^0 decays right at the event vertex while in the scheme the decay length of the Σ^0 is exaggerated for better visualization. Figure taken from [200] and adapted for this analysis.

could have been produced at the event vertex. Since the Σ^0 lifetime is tiny, there is no difference in the topology whether a Λ was produced directly or it was produced via the decay of the Σ^0. This is different for the double weak decay of Ξ^-.

Since two straight lines only rarely have an intersection point in three dimensions, the minimal distance of the $p\pi^-$ pair is calculated and used to quantify the possibility of having the same origin. The minimal distance of the individual tracks of the $p\pi^-$ pair is called "MinTrackDistLam" and should obviously be small for Λ decays. The point of closest approach of the $p\pi^-$ which is identified as secondary vertex should then have a large distance to the event vertex, called "VerDistXGes".

For random combinations of hadrons which are directly produced at the event vertex via the strong interaction such a crossing occurs only rarely. Since these parameters are of pure kinematic nature, they are all correlated to the opening angle "AlphaLam" between the $p\pi^-$. Additionally, all candidates are rejected where the secondary vertex has a reconstructed z value which is smaller than the z value of the event vertex. This is nonphysical since the Λ must have been produced near the target area and traveling in direction of the detector to decay into a measurable $p\pi^-$ pair [1]. All cuts values are given in the following section.

5.2 Multivariate Analysis

Despite the wealth of information provided by the topology of the Λ decay, the separation of the signal from the combinatorial background remains a significant challenge, largely due to the multitude of intricate correlations between the

[1] The beamline corresponds to the z-axis.

observables. The application of graphically chosen cuts in one or two dimensions will yield significantly inferior results in nonlinear problems compared to multivariate analysis. In light of these facts, numerous established libraries offer a multitude of methods for optimization. With regard to the reconstruction of the Λ particle, the **T**oolkit for **M**ult**V**ariant **A**nalysis (TMVA) is deemed the most suitable option [201]. Since it is a standard ROOT library, compatibly with the HADES software is assured. As underlying architecture for the multivariate analysis, a Multi-Layer-Perceptron with two hidden layers, comprising 11 neurons in the first hidden layer and 9 neurons in the second hidden layer, is selected.

Multi-Layer-Perceptron

Already in 1962, Frank Rosenblatt published the fundamental idea of mimicking the brain of living organisms for classification purposes [202]. All **M**ulti-**L**ayer-**P**erceptrons (MLP) contain an input layer, an output layer and a various amount of hidden layers in between. Any layer consists of neurons which can only be connected with neurons of the previous and later layer. For a fully connected MLP each neuron is connected to each neuron in the previous and following layer. The calculated value of each neuron is defined by the neuron response function. The neuron response function of each neuron depends on the neurons from the previous layer, the weights of the connection and an additional bias [201]. For the activation function α, following forms are available:

- Sigmoid: $\alpha = \frac{1}{1+e^{-x}}$, which is the standard configuration of the TMVA MLP
- Tanh: $\alpha = \frac{e^{x}-e^{-x}}{e^{x}+e^{-x}}$, comparable alternative with similar shape as sigmoid
- Linear: $\alpha = x$, trivial activation function which was not tested in this thesis

The default setting with sigmoid activation function is used for the MLP. The synapse function κ can be expressed in one of the following formula:

- $\kappa = w_0 + \sum_{i=1}^{N} y_i \cdot w_i$, sum
- $\kappa = w_0 + \sum_{i=1}^{N} (y_i \cdot w_i)^2$, squared sum
- $\kappa = w_0 + \sum_{i=1}^{N} |y_i \cdot w_i|$, absolute sum

Where N refers to the amount of neurons in the previous layer, with the neuron values y_i and the corresponding weights w_i.

To guarantee optimal performance, the sample of signal and background events has to fulfill certain conditions. This preselection is shown in figure 5.2 and is applied on top of the selection criteria already discussed in chapter 4. It removes many obvious background cases and assures high discrimination power afterwards, since the distributions of the observables which are given to the neural net to distinguish are rather similar.

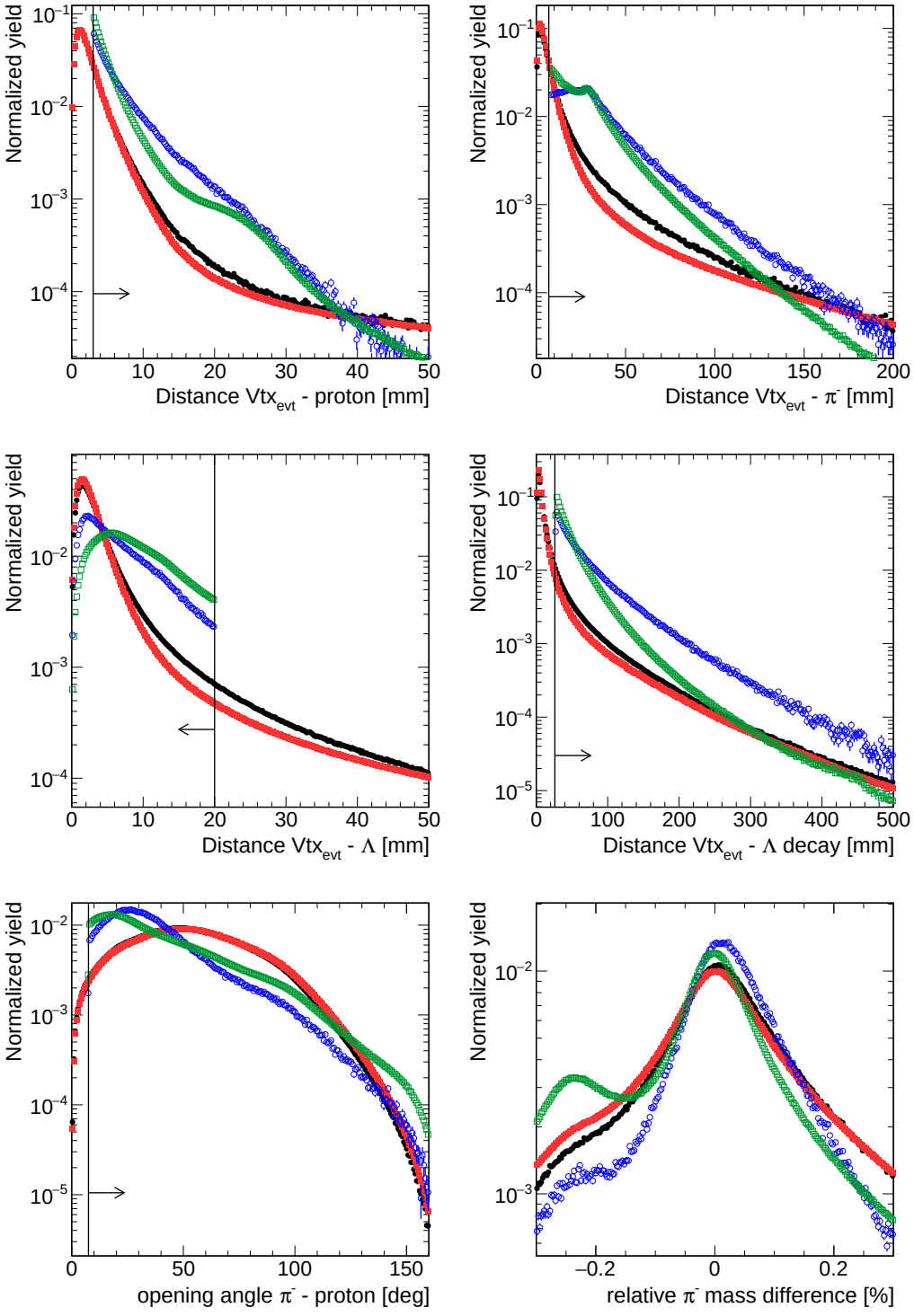

Figure 5.2: Distribution of the input variables for the neural network in one dimensional representation.

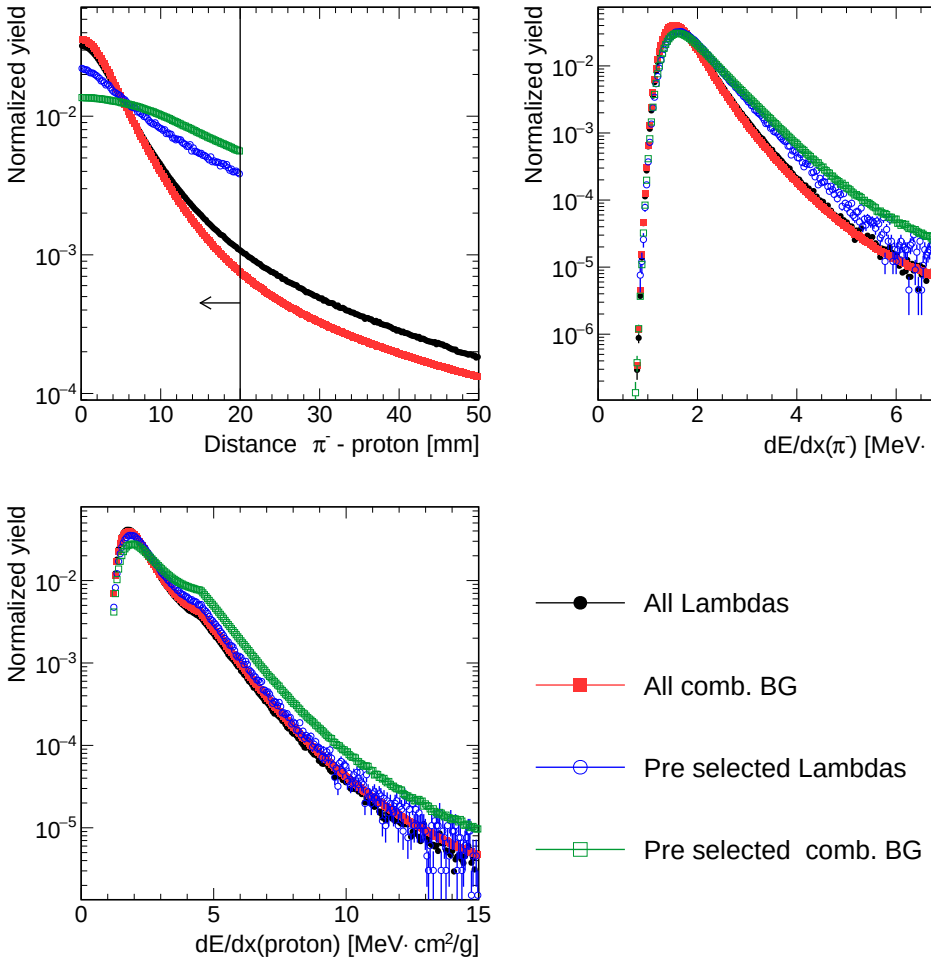

Figure 5.2: Distribution of the input variables for the neural network in one dimensional representation. More details are written in the text.

The input variables are summarized in figure 5.2 where true Λ signals were compared to combinatorial background pairs of $p\pi^-$. This combinatorial background also consist of pairs where one of both particles origins from the signal source, to mimic all possible background sources. Background sources like this are important because they tend to show a similar topology as the signal.

The preselection criteria were applied to avoid training and evaluation of the neural net with combinatorial background pairs, which do not have sufficient similarities to the expected behavior of the Λ candidates. The vertical black lines visualize the preselection cut values. The arrow indicates the part of the distribution which survives the preselection criterium.

Significant differences in the distributions are visible before and after preselection for all variables. The impact is large, especially for the variables which refer to vertex measurements and thus depend on the decay topology.

Training of the MLP was performed with $\approx 100 \cdot 10^6$ UrQMD events. Since

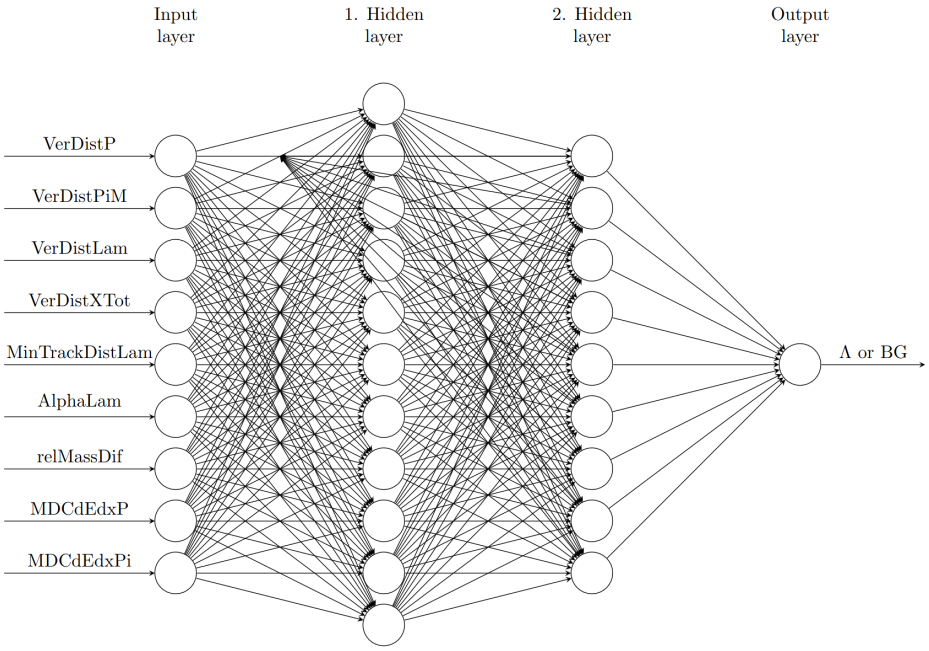

Figure 5.3: Architecture of the Multi-Layer-Perceptron with nine input variables, 2 hidden layers and the output classification node. The output node is the summarized evaluation of the MLP which ranges from zero for background to one for a signal.

this MLP is a supervised neural network, the possibility of embedding Λ into real data events is not possible, because Λ being present in data are unlabeled. They would then wrongly contribute to background and thus reduce the power of the Multi-Layer-Perceptron separation capability.

With variables which only depend on $p\pi^-$ correlations, not using single particle observables, embedding into real data events is possible. In this case background events can also be extracted from event mixing. Figure 5.3 visualizes the architecture of the Multi-Layer-Perceptron. Starting from 9 input variables, two hidden layers with 11 and 9 neurons are used for the classification given to the output layer. The network is fully connected. Table 5.1 summarizes the parameters which were used for the training process. Tests with smaller sample sizes verified the stability of the resulting quality compared to various settings.

The quality of the MLP performance is extracted from the experimental data. Since the neural network was trained with simulations only, the experimental data is unknown and thus independent considering the possibility of over-fitting on simulation.

The influence of the individual preselection steps is shown in figure 5.4 in a logarithmic representation. While there is no Λ signal visible after the first four selection steps, the signal rises and get enhanced after reducing the combinatorial background by two orders of magnitude.

The evaluation of the MLP in dependency of the invariant mass of the $p\pi^-$ pair is displayed in figure 5.5. The logarithmic representation visualizes the behaviour of the combinatorial background pairs as well as the signature of the Λ

TMVA MLP option	Setting
Number of cycles	500
Hidden layers (neurons per layer)	2 (11,9)
Activation function	Sigmoid
Estimator type	Cross entropy
Variable transformation	Normalization
Overfitting test rate	Each 10^{th} epoch

Table 5.1: Parameter settings for the training of the Multi-Layer-Perceptron, more details are written in the text.

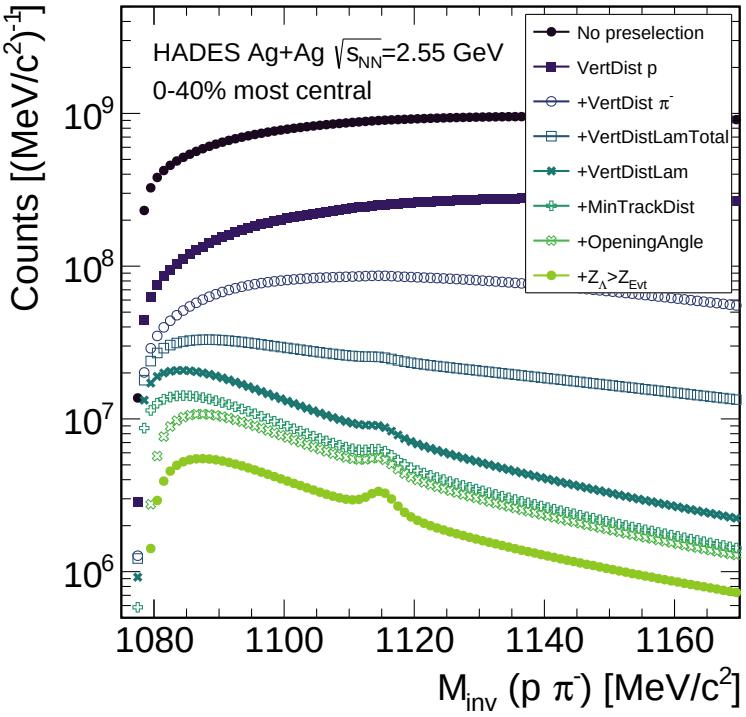

Figure 5.4: Invariant mass distribution of $p\pi^-$ pairs representing the Λ candidates which survive the different preselection steps which are sequentially applied. It is explicitly desired to select only in a loose manner, to keep room for improvement by the following classification of the artificial neural network.

around its mass of $M_{inv}(p\pi^-) \approx 1115\,\mathrm{MeV/c^2}$. Here, MLP evaluation values lie above 0.9 which allows a large background suppression. Since the MLP does not only contain parameters of the correlation between proton and π^- but additionally uses the distance of the proton or π^- track to the event vertex independently on the second daughter particle, the case appears where one of both particles ori-

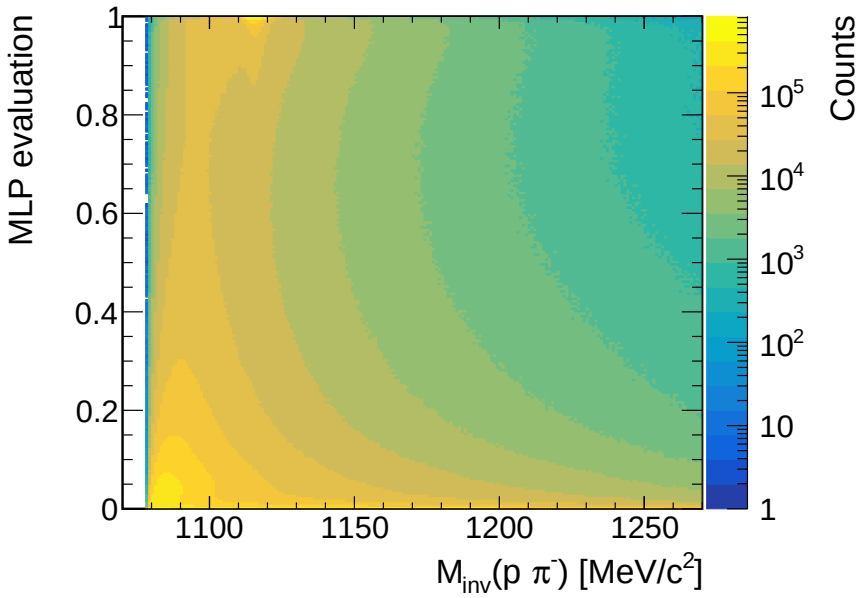

Figure 5.5: MLP evaluation distribution in dependence on the mass of the $p\pi^-$ pair. Only those Λ candidates are taken into account which passed all preselection criteria.

gins from a Λ while the partner does not. These combinatorial background pairs have mostly small MLP evaluation output but can be also reach large MLP evaluation values, especially for small invariant masses of $M_{inv}(p\pi^-) < 1100\,\text{MeV/c}^2$.

The behavior of the MLP evaluation of various invariant mass regions of the $p\pi^-$ pairs as well as from event mixing in the 2σ region of the nominal Λ mass is displayed in figure 5.6. While the true Λ candidates are displayed in black for a mass window of 1σ around the nominal PDG mass or 2σ (red), the blue curve shows the behavior of $\pi^- p$ pairs from the so called sideband regions. Those sidebands are defined as $p\pi^-$ pairs in an invariant mass region which does not contain Λ signals. However, the region is situated in close proximity to the nominal mass region, thereby ensuring analogous kinematics as the signal. In this particular instance, those sidebands are defined as $1100\,\text{MeV}/c^2 < M(p\pi^-) < 1105\,\text{MeV}/c^2$ for the left and $1125\,\text{MeV}/c^2 < M(p\pi^-) < 1130\,\text{MeV}/c^2$ for the right sideband respectively. In addition, the neural network response from uncorrelated pairs from event mixing is shown in green. Obviously the separation power is largest at MLP values close to 1. The Λ candidate sample still contains quite some background, which leads to a rise of the red and black curve to low MLP evaluation values. Additionally, the different behavior of sidebands and event mixing is evident, most probably this is due to different kinematics and mass windows. Still both tend to have low MLP values. The quality and separation power of the MLP is tested with experimental data and summarized in figure 5.7.

To derive those plots, a scan of the MLP impact was performed in same event data and mixed event data.

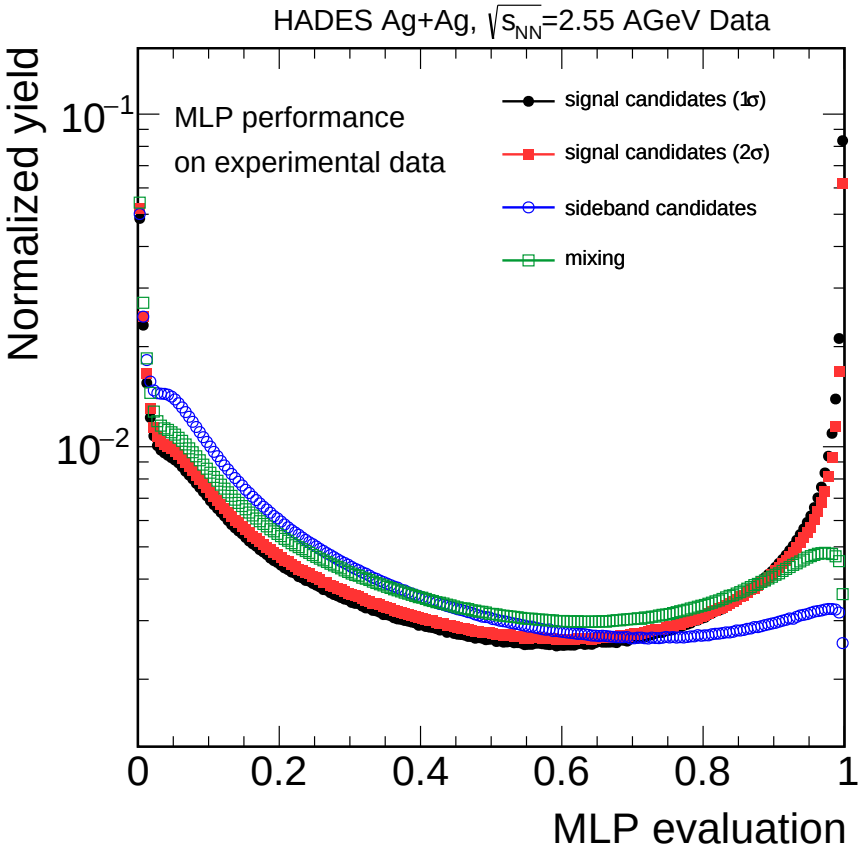

Figure 5.6: MLP evaluation distribution for pairs in the signal region, for event mixing and so called side bands. More details are given in the text.

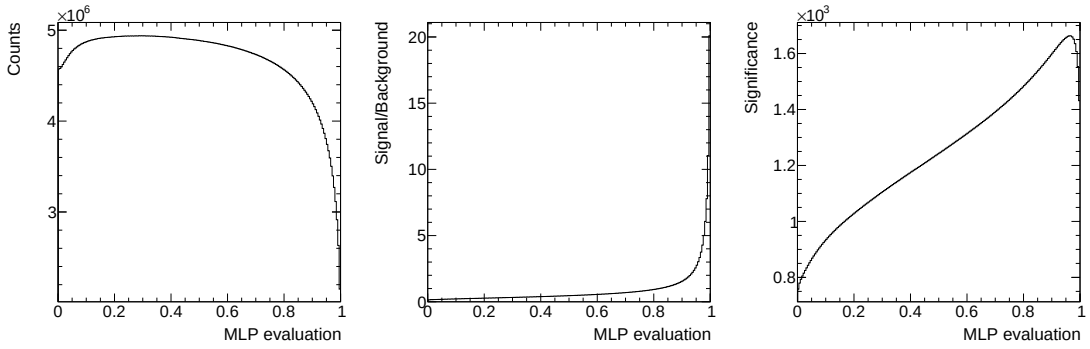

Figure 5.7: Estimation of the MLP performance in real data in terms of raw Λ counts after background subtraction (left), the corresponding ratio of signal Λ to the combinatorial background (center) and the significance (right). In all cases, the background is estimated via the event mixing technique in a 2σ window around the nominal Λ mass. More information is written in the text.

The raw counts (S) in the Λ peak are extracted in a 2σ window around the

nominal Λ mass are extracted by subtracting the background from event mixing. The background counts (BG) are calculated in the same window to calculate the Signal/Background ratio and the significance as Significance:=$S/\sqrt{S+BG}$. While the amount of reconstructed Λ baryons is rather constant for intermediate MLP values, this number strongly drops at values larger than 0.9. Because the combinatorial background decreases even more, a steep rise of the signal to background ratio is seen. The significance is combining the amount of statistics with the signal to background ratio and thus is used for the choice of the MLP evaluation cut value.

The behaviour of the raw counts at low MLP values is an artefact caused by the very loose preselection criteria. They generate large combinatorics and thus imperfect background description.

5.3 Background Estimation and Signal Extraction

For the cut optimization of the classification output of the neural network, the separation of the data in signal and background is required. Therefore a description of the combinatorial and thus uncorrelated background is required.

Those uncorrelated combinations, specially their mass dependence, are mainly a result of particle multiplicity $M(p_t, \theta, \phi)$ per event and the feasibility of the detector to reconstruct in this phase space region $\epsilon(p_t, \theta, \phi)$. Various common approaches of combinatorial background description exist, namely:

- Event mixing technique [203]: The mixed-event technique uses p and π^- tracks (per definition uncorrelated and independent) from different events which can be characterized in a similar way. This is important to avoid any event bias. Understanding the impact of multiplicity M and efficiency ϵ, events which behave similar with respect to those observables are classified as similar and are considered for event mixing. In HADES, the event classification contains:

  1. The particle track multiplicity, since detector efficiencies highly rely on the track density. Thus a central event does not produce the same polar angle distribution of charged tracks as a peripheral event.
  2. The z-vertex position: Since the target has a length of several centimeters (dependent on the target setup), the produced particles have different acceptance ranges. This leads to a different kinematic distribution and thus a bias in the modeled background if those events are mixed with each other.
  3. The event reaction plane: The asymmetric distribution in azimuth angle ϕ which occurs due to the medium densities around the interaction point also influence the measured multiplicity. In most types of analysis the ϕ dependencies can be neglected, since the integral over ϕ still delivers the same polar angle distribution.

4. The time within the beamtime: During the process of data taking single motherboards of the detector were running instable during specific periods of time. When a piece of hardware was not working properly, it was replaced within the next beam break in which the cave could be accessed. Mixing is done only within a small time interval of $\approx 1h$ performed to avoid any pollution of inhomogeneity.

The advantage of the event mixing technique is an almost infinitive amount of statistics by combining many events, and also takes all asymmetric detector effects into account.

- Rotation technique: Similar to the mixed event, this technique uses pair which are uncorrelated by definition. However this technique generates those pairs within the same event. The advantage is, that by definition event characteristics, mainly the multiplicity in dependence on polar angle can not cause a bias. The background is calculated by rotating the ϕ angle of one of the particles from the $p\pi^-$ pair by a value which fulfills the symmetry of the detector. In HADES this method is used with a shift of $\Delta\phi = 60°$ which corresponds to the azimuth symmetry of the 6 sectors described in chapter 2. For an analysis which consist of e^- or e^+, the rectangular inner RICH plane (see section 2.2.3) constrains the symmetry such that a rotation of $\Delta\phi = 180°$ is optimal in terms of taking all detector acceptances into account. This rotation method is not working in cases of an asymmetric detector. Since the setup of the Electromagnetic calorimeter of March 2019 contains only 2 out of 6 sectors, this method is not used in the later $\gamma\Lambda$ analysis.

- Sideband interpolation: In this simple approach, the invariant mass spectrum around the Λ peak is divided in 3 regions: The signal region and invariant mass regions left and right to the signal, which are at least 3σ separated from the signal peak position. This constrain avoids signal contributions in the sidebands, which would lead to a systematic overestimation of the background in this sideband region. The signal peak must be dominant and clear to avoid introducing biased systematic uncertainty. An analytical function is then chosen to describe the combinatorial background which then can be interpolated into the signal region. Especially for signals with high purity, this estimation in sufficient since the total counts of the signal do not rely on a precise background description.

Comparing these methods, the largest advantage of the event mixing technique is its consistency in the multi differential analysis which will be summarized in chapter 5.4. Different kinematic constrains in different phase space regions highly influence the combinatorial background shape. Thus, several background descriptions would be needed when fitting it using e.g. the sideband method.

The $p\pi^-$ spectrum of pairs from same events and the normalized spectrum of $p\pi^-$ from mixed events are displayed in figure 5.8. The normalization of the mixed event spectrum was performed by scaling to the sidebands.

$$\mathrm{fS}_{Mix} = \frac{\int_{1080}^{1100} dN/dM + \int_{1130}^{1160} dN/dM}{\int_{1080}^{1100} dN_{\mathrm{mix}}/dM + \int_{1130}^{1160} dN_{\mathrm{mix}}/dM} \tag{5.1}$$

Here it is important to avoid signal contribution within the sidebands, which would result in an overestimation of the background. Since the background description is very precise in the full invariant mass region, an invariant mass region of $> 6\sigma$ distance is chosen for the borders of the sidebands, which will provide a stable result even in case of imperfect peak position. The resulting scaling factor fS_{Mix} is rather arbitrary since the yield in the mixed event spectrum can be regulated by the mixing depth. This parameter controls the amount of stored particles within each event class and thus the number of tracks each particle is mixed with.

A minimum of 50 tracks is required in this analysis, from which event mixing takes place. In addition, only a randomized sub sample of 1% of the possible Λ daughter particles were used for the mixing procedure, to reduce the runtime of the code. This additional method is only valid for particles with a large amount of statistics and thus neglectable statistical uncertainties.

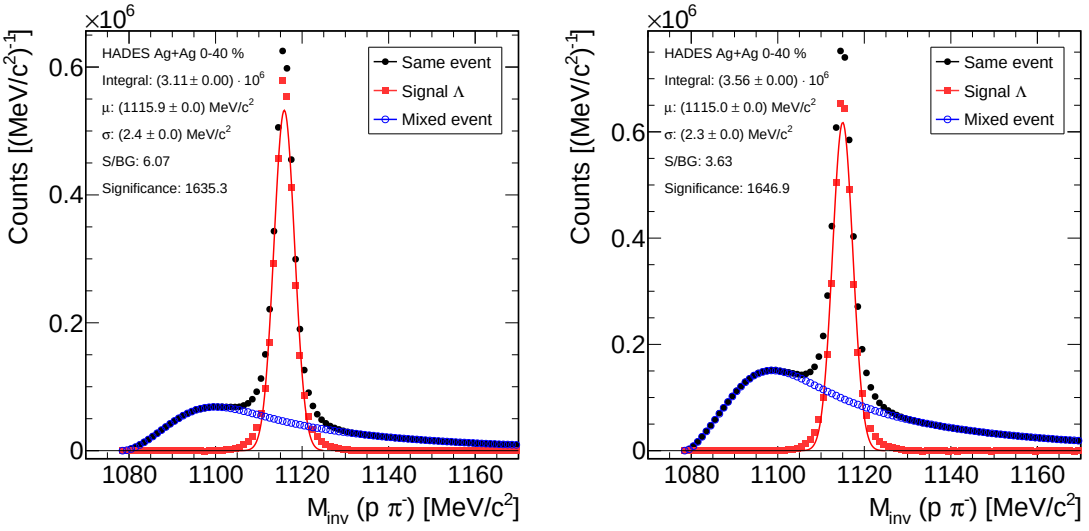

Figure 5.8: Same event $p\pi^-$ pairs depicted in red, normalized combinatorial background estimation from event mixing technique in blue. The left plot shows the Λ selection with $NN_{out} = 0.98$ which is later on used for the Σ^0 reconstruction, the right plot shows the Λ selection with $NN_{out} = 0.95$ which is used for the multi differential analysis. More details are written in the text.

Since the Λ reconstruction highly depends on the vertex correlation of both daughter particles, those cuts have to be applied also for event mixing. Single

particle selection criteria which are uncorrelated from the decay partner are performed already when selecting the candidates for event mixing.

Invariant mass spectra of Λ candidates are shown in figure 5.8 for different neural net classification evaluation selections $NN_{out} > 0.98$ on the left and $NN_{out} > 0.95$ for the right plot. Shown are same event spectra in black, event mixing spectra (blue) which nicely describe the background, and the signal spectrum (red), obtained by subtracting the scaled event mix (formula 5.1) from the same event spectrum. The integrated yield is extracted from counting the entries of the signal Λ within the mass region of $1110 < \mathrm{m}_{p\pi^-}\ [\mathrm{MeV/c^2}]^{-1} < 1120$.

This is also the range, from which the Λ are taken into account for the further Σ^0 analysis. This value is corresponding to a range of $\approx 2.17\sigma$, where the width σ is estimated by a single Gaussian fit, also denoted in red in figure 5.8. The minimum of the y-axis ranges down to -2.0% of the maximum, the black horizontal line is drawn at 0 counts in order to mark the optimal background description. The centrality dependent spectra integrated over the full phase space for both cut sets are attached in appendix A.5.

5.4 Multi-Differential Analysis

The selection criteria in the previous chapters were chosen such, that a multi-differential analysis over a large phase space region can be performed. The phase space is represented by the two variables rapidity y and transverse momentum p_t.

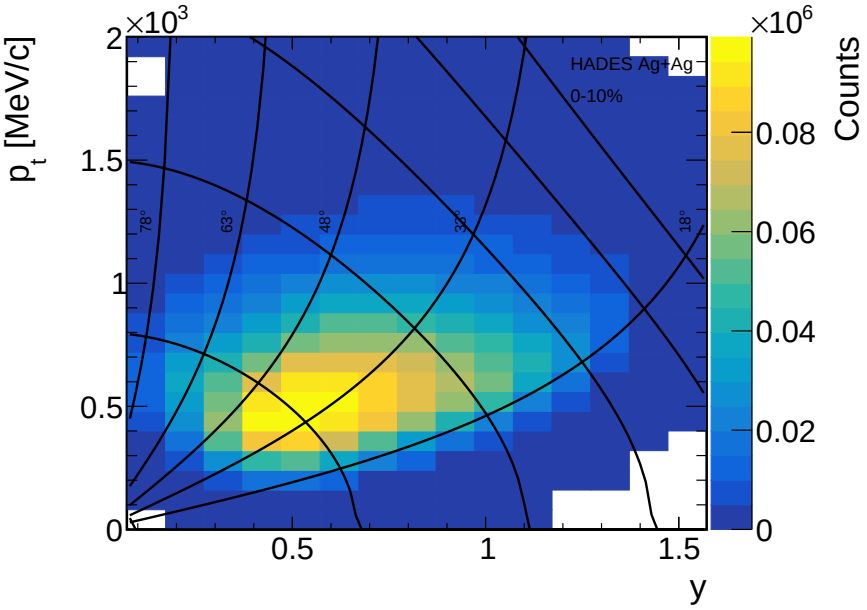

Figure 5.9: All possible Λ candidates including combinatorial background as function of transverse momentum p_t and rapidity y.

Particle production is centered at mid-rapidity and for isotropic emission equally distributed in p_x and p_y, thus p_t is a good representation. Total momentum and polar angle are important observables for the efficiency of track reconstructions. Thus efficiency changes along this plane as indicated in figure 5.9 with the solid lines. The polar angle θ lines are shown in $15°$ steps in the range of $18° - 78°$ while the momentum lines are perpendicular to θ and are illustrated for $n = 0-5$ values of $p = 100$ MeV/c+ n$\cdot 700$ MeV/c. Additional information about rapidity and transverse momentum are attached in A.2.

Figure 5.9 shows the reconstructed proton π^- pairs, regardless of their origin. Thus it provides a map of Λ candidate density. Invariant mass distributions of $p\pi^-$ pairs have been calculated for all $y - p_t$ bins. After subtracting the combinatorial background, which was determined by the event mixing technique for each individual bin the raw Λ counts remain.

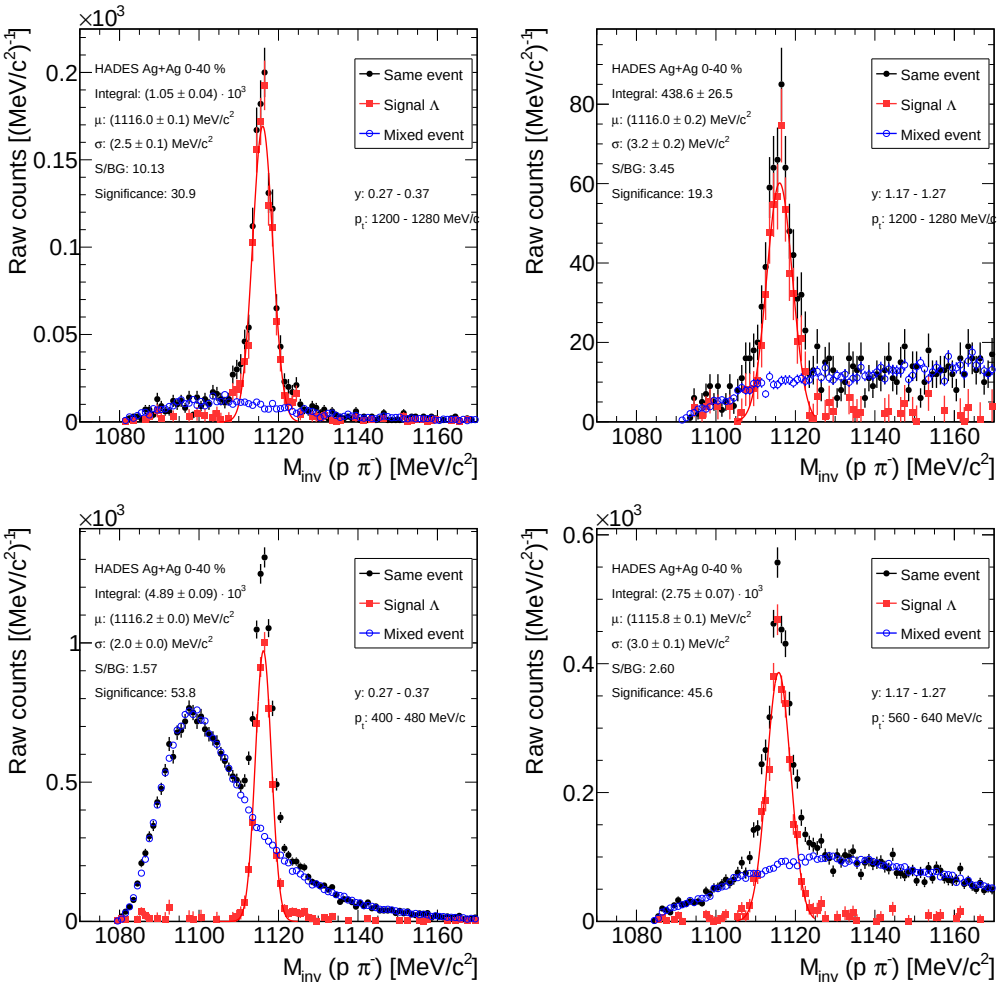

Figure 5.10: Example bins at the borders of the HADES acceptance. The different shapes of the kinematic distributions of the background are precisely described by event mixing for the whole phase space.

Besides the very different shape of the background distribution which is simply an attribute of the possible kinematic combinatorics after the applied selection steps, a clear systematic tendency appears in terms of the amount of background. While the backward rapidity bins with small transverse momenta contain the largest amount of background, the high transverse momentum region results in the cleanest spectra.

Extracted raw Λ counts are displayed in figure 5.11 for the most central events (0-40 %).

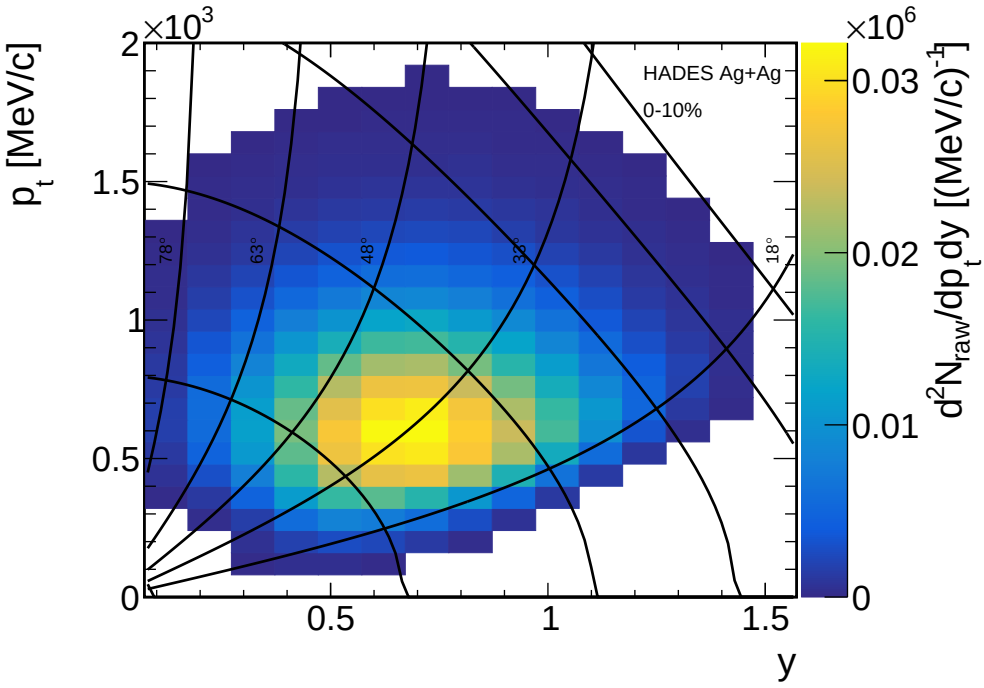

Figure 5.11: Remaining Λ candidates after subtracting the combinatorial background which is estimated for each bin individually from event mixing, as function of transverse momentum p_t and rapidity y.

Its clearly visible, that the distribution is not symmetric around mid-rapidity, since the acceptances and reconstruction efficiencies behave asymmetrically.

5.5 Efficiency and Acceptance Correction

The number of raw reconstructed Λ counts extracted e.g. from figure 5.8 highly depends on the selection criteria. Therefore a correction in terms of efficiency and acceptance is applied to the data. This allows cut independent data and also the comparison to other analysis. The corrections in efficiency and acceptance are extracted from simulated data. The thermal generator tool PLUTO [187] was used to produce Λ baryons with a reasonable expected kinematic distribution. As input parameter for the $p_t - y$ distribution, a temperature of $T = 105$ MeV is used

with vanishing blast, polar anisotropies and flow. The same parameters are chosen for the latter Σ^0 production. In both cases, the thermally produced baryon is embedded in a simulated UrQMD event and alternatively in an experimentally measured event. Embedding the simulated Λ into a real event is evaluated to be more precise since occupancy effects in the detectors have systematic deviations in simulations from data. Especially investigating different centrality classes, the different track densities in simulation and data will produce wrong reconstruction efficiencies. In chapter 7 this effect is also discussed for γ reconstruction in the electromagnetic calorimeter. The acceptance correction takes the limited phase space region into account, which the experiment is sensitive to. Correcting for this acceptance, a model dependent uncertainty from the extrapolation in uncharted regions is induced. For signals with large statistics and large phase-space coverage, the extrapolation can be minimized and the correction is thus more independent from simulations.

A multi-differential analysis in terms of $p_t - y$ which is described in the following chapter thus avoids this model dependent extrapolation uncertainty to a large extend and will be used for highest accuracy Λ measurements.

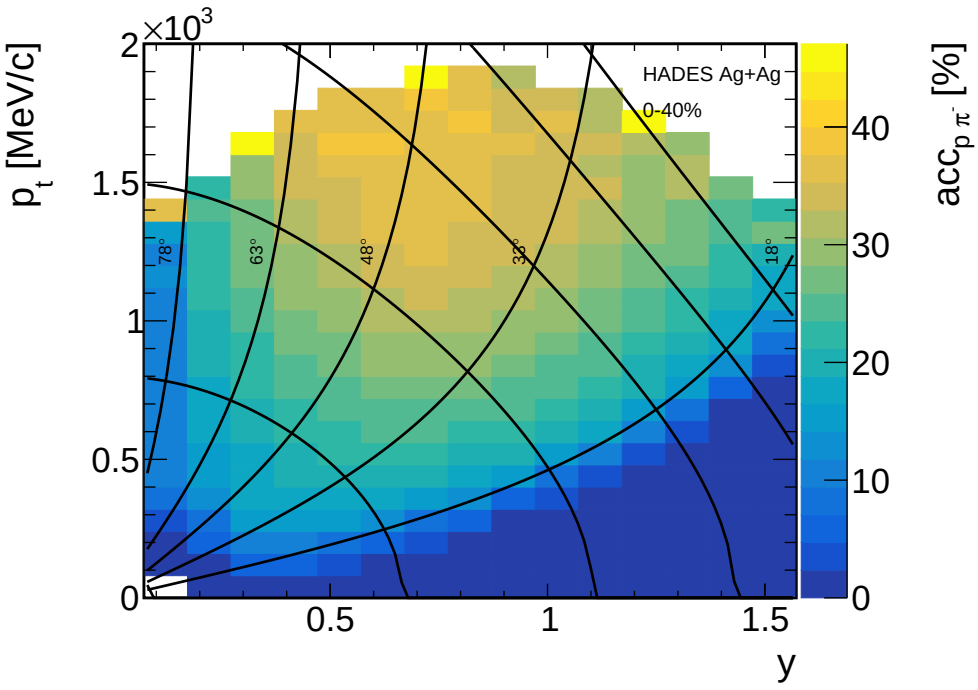

Figure 5.12: Λ acceptance as a function of transverse momentum p_t and rapidity y. The $\theta - p$ grid is the same as explained earlier.

The acceptance of charged tracks is defined by the relative amount of produced particles which traverse the active medium of the detector and were measurable by the four MDCs as well as the RPC or TOF. These information would be sufficient for PID by the reconstructed mass measurement. A unstable particle

is defined to be in acceptance if all daughter particles from the decay are in acceptance. The resulting acceptance distribution for the Λ is displayed in figure 5.12.

The detector borders for polar angles $18° - 78°$ are also visible in the Λ acceptance reflecting the single particle acceptance. Since the proton obtains a large amount of the four vector of the Λ, the borders are rather sharp. The maximum at intermediate θ is explained by the large opening angle of the π^- to the proton and thus also to the Λ pointing vector. The overall acceptance structure is obtained by folding the acceptance matrices of the single daughters. Their acceptances are visualized in A.6. This definition of acceptance is only dependent on the detector geometry and thus independent on track multiplicities and centrality. Since all Λ decay channels were simulated, already at this stage the branching ratio in the investigated channel of $\Lambda \to p\pi^-$ is included in the stated acceptance.

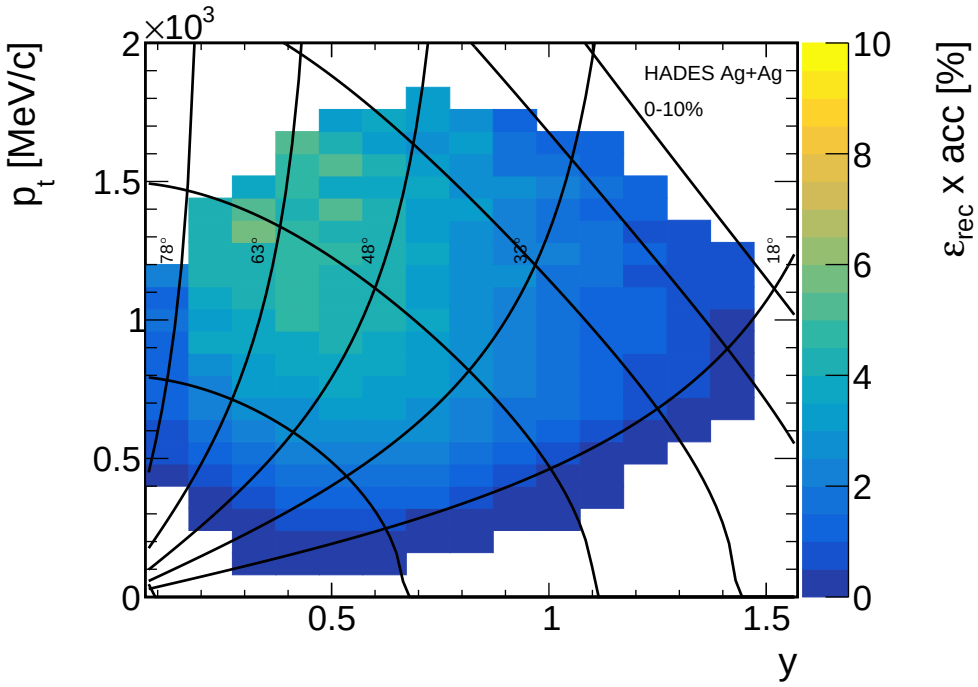

Figure 5.13: Λ reconstruction efficiency and acceptance as a function of transverse momentum p_t and rapidity y. The representation in $\theta - p$ is again overlayed as grid. More details are written in the text.

The reconstruction efficiency of the weakly decaying Λ particle in this analysis is mainly determined by the pair topology cuts, thus the efficiency correction is applied on the $p\pi^-$ pair basis. This efficiency correction is performed within the acceptance borders. To be specific, correction in terms of efficiency and acceptance are applied as

$$\frac{d^2N_{Corr}}{dp_t dy} = \frac{d^2N_{Raw}}{dp_t dy} \times (acc(p_t, y)\varepsilon_{rec}(p_t, y))^{-1} \tag{5.2}$$

where the efficiency times acceptance matrix is combined in a total efficiency.

$$\varepsilon(p_t, y) = acc(p_t, y) \cdot \varepsilon_{rec}(p_t, y) = \frac{d^2 N_{Rec}(p_t^{rec}, y^{rec})}{dp_t dy} / \frac{d^2 N_{Gen}(p_t^{MC}, y^{MC})}{dp_t dy} \tag{5.3}$$

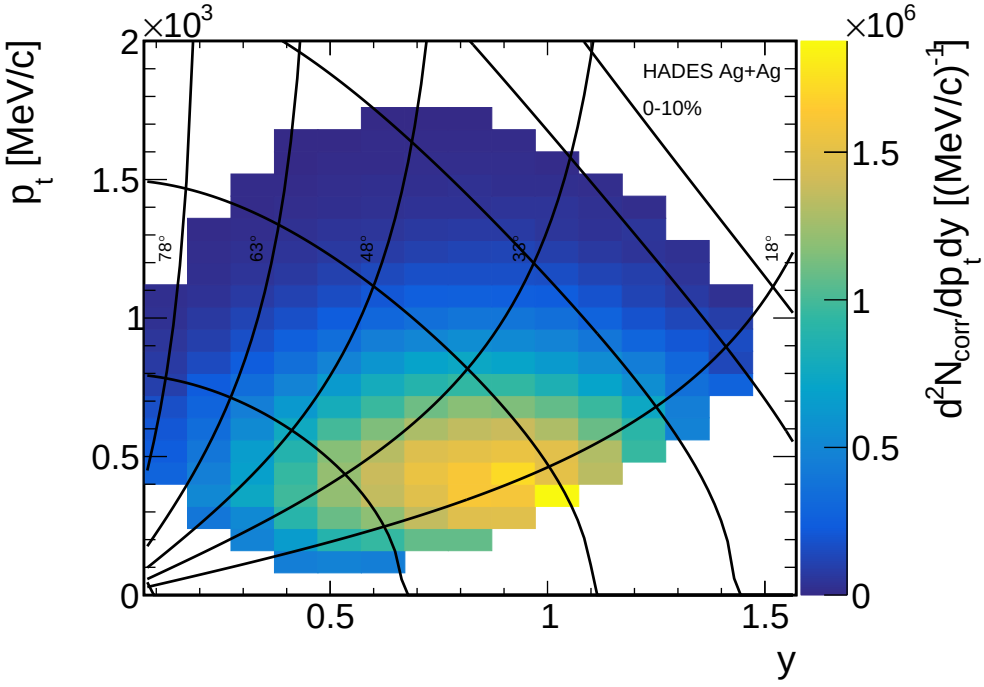

Figure 5.14: Efficiency and acceptance corrected Λ candidates after subtraction of the combinatorial background as function of transverse momentum p_t and rapidity y.

The raw Λ yield in each phase space bin is now individually scaled with the corresponding efficiency and acceptance correction factor which results in the spectrum shown in figure 5.14. This distribution is rather symmetric around mid-rapidity although experimental constrains of the detector acceptance borders are asymmetric.

Quite some part of the forward acceptance, in particular at low transverse momenta is not covered. This non measured region is smaller in backward rapidity.

While for the generated input distribution, the Monte Carlo information of the kinematics are used, for the reconstructed Λ, the reconstructed kinematic observables are taken into account when calculating the efficiency. Figure 5.15 visualizes the resolution of the reconstructed rapidity and transverse momentum observables of the simulated Λ baryons. The dashed vertical lines always represent the desired optimal resolution without any detector reconstruction inaccuracy. Clearly this ideal case can never be reached, but there is no systematic deviation from this ideal case in terms of the phase space description used in this

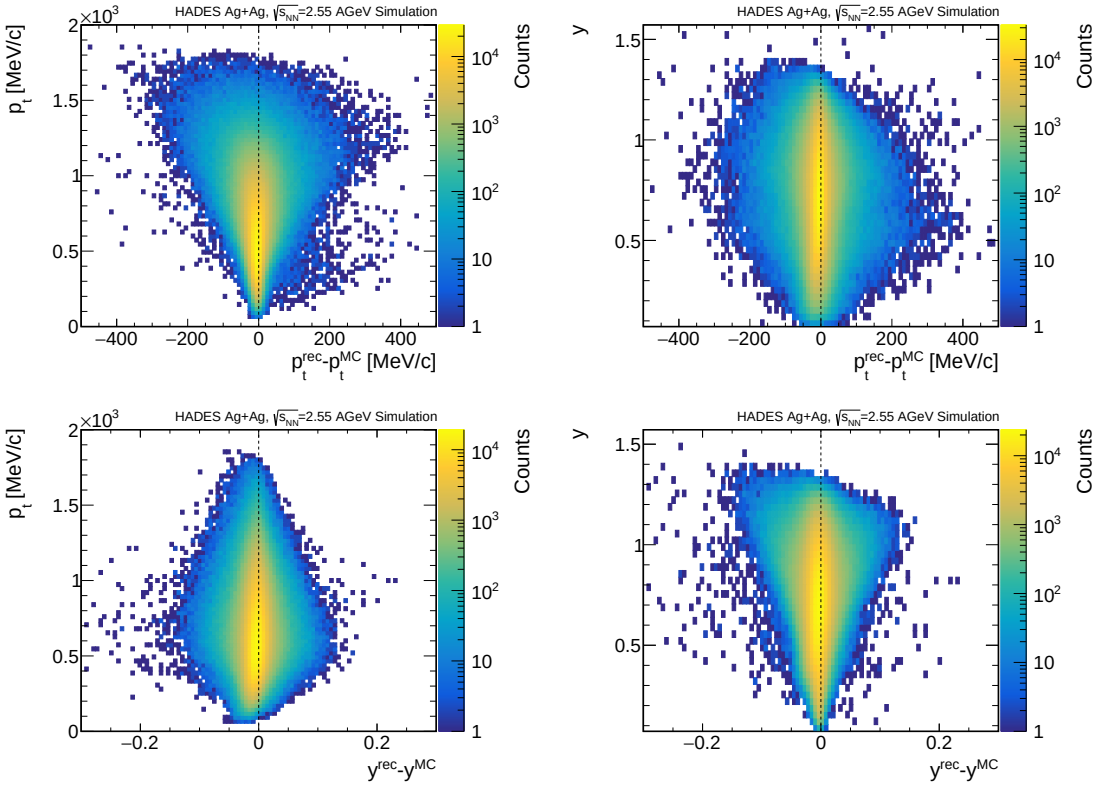

Figure 5.15: Resolution of the phase space parametrization of the thermally generated Λ baryons in the simulations.

analysis. The uncertainties of the corrected yield in each bin are of statistical and systematic nature. Systematic uncertainties are estimated by a variation of selection criteria. In the standard analysis, only bins with a raw yield $N_{raw}(\Lambda) > 500$ were taken into account in order to get reliable results. This value corresponds to a bin wise statistical uncertainty of $< 5\%$.

As explained in section 1.3, heavy ion collisions create dense and hot strongly interacting matter. The time evolution of this matter is often described as thermal fireball. Assuming particle production by a thermal source leads to a Boltzmann distribution, describing the kinematics:

$$\frac{d^2N}{dp_t dy} = Cp_t\sqrt{p_t^2+m^2}\exp\left(-\frac{\sqrt{p_t^2+m^2}}{T_{eff}}\right) \tag{5.4}$$

The transverse momentum dependence in each rapidity bin is now fitted with this Boltzmann distribution 5.4 which allows to extrapolate into uncovered phase space regions. Those fits provide the extrapolation factor which is used to scale the p_t integrated rapidity values for missing acceptance. Example bins for mid-rapidity are shown in figure 5.16 for different centrality classes while p_t distributions for forward and backward rapidity are compared in figure 5.17.

The extrapolation factors F_{ex} describe the fraction of total reconstructable Λ to the overall produced Λ in each rapidity bin. F_{ex} reaches from values of $\approx 50\,\%$ for the least accessible backward rapidity and $400\,\%$ for the most forward rapidity region. This shows the limited accessible phase space for the Λ reconstruction in forward rapidity for the HADES experiment. Around mid-rapidity, extrapolation factors of less than $10\,\%$ are achieved for all centrality classes, which is most important in order to describe the dominant part of the Λ production properly.

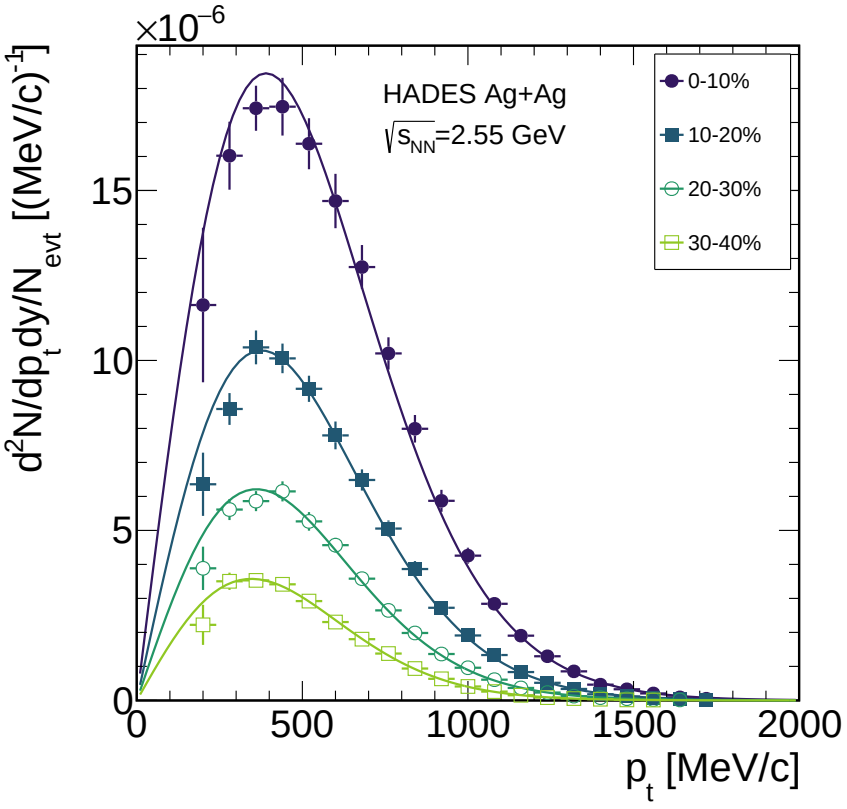

Figure 5.16: Transverse momentum distributions and fit results of the Boltzmann distributions for mid-rapidity ($y_0 \pm 0.05$) data for the four different centrality classes. More details are written in the text.

Each p_t distribution is integrated and extrapolated to determine Λ production in rapidity bins. The extracted rapidity distribution is expected to be symmetric around mid-rapidity. Using this constraint, the rapidity distribution can be extrapolated and integrated to extract a total Λ yield per event. This result is shown in figure 5.19. Extrapolation factors for the p_t distributions for all different centrality classes are displayed in figure 5.18.

If the fit is not fixed to be symmetric around y_0, the fit evaluates a y_0 of ≈ 0.857 which would correspond to a beam energy of $E_{kin} \approx 1.75$ AGeV. The whole analysis is performed in $10\,\%$ centrality bins. Integration of the rapidity distribution provides us the multiplicities as listed in table 5.2.

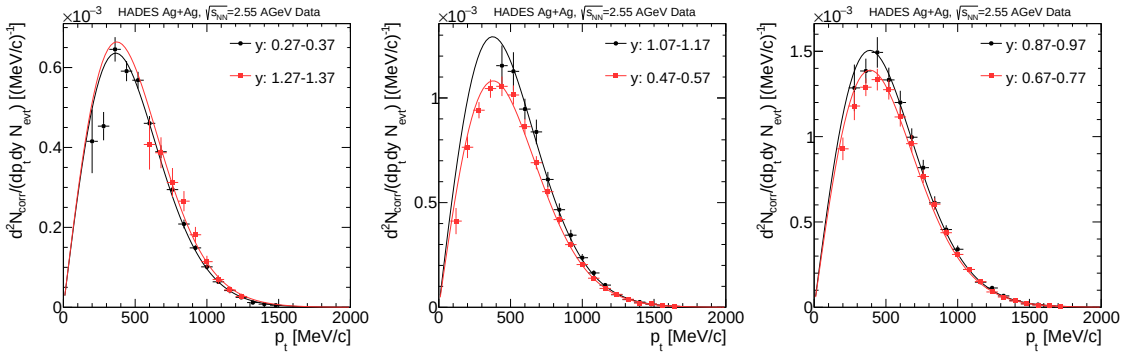

Figure 5.17: Comparison of transverse momentum spectra of the forward/backward rapidity bins, being symmetric around mid-rapidity for the most central 0-10% Ag+Ag collisions. The left plot is comparing the most forward to backward rapidity bins, the middle describes an intermediate $|y - y_0|$ bin while the right picture is closest to mid-rapidity.

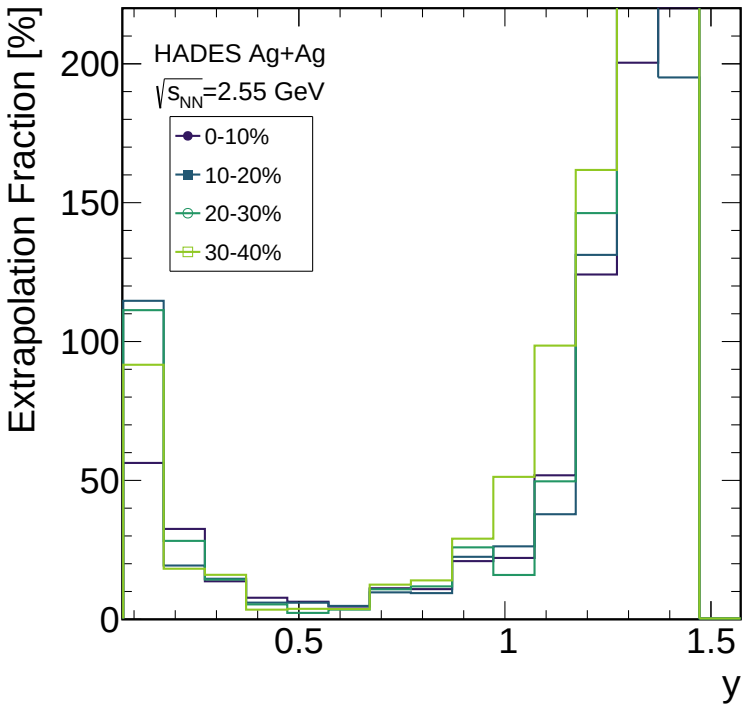

Figure 5.18: Extrapolation factor F_{ex} of the p_t distribution in dependence on rapidity. F_{ex} is extracted, comparing the efficiency and acceptance corrected yield in the specific rapidity bin, compared to the p_t integrated value, thus, also including the uncovered transverse momenta regions.

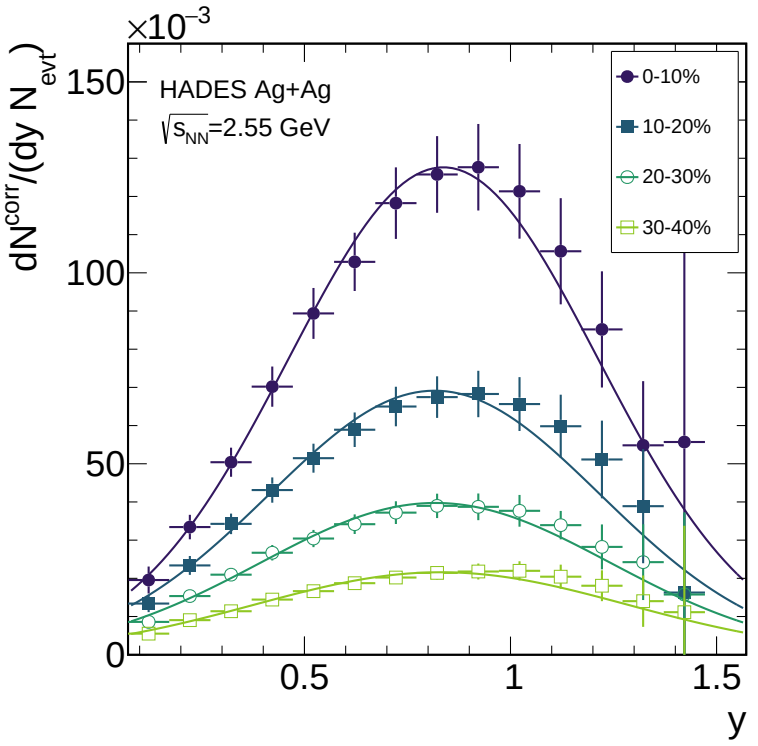

Figure 5.19: Rapidity distribution of Λ production in four centrality bins. Rapidity values are obtained from p_t integrated and extrapolated transverse momentum measurements. The resulting spectrum is fitted by a Gaussian distribution centered at mid-rapidity ($y_0 = 0.82$) which allows the extrapolation to full phase space.

Formula 5.5 describes the expected behavior of the temperature extracted from the Boltzmann fit with respect to rapidity, y_0 represents the mid-rapidity value of 0.822 for a collision energy of $E_{kin} = 1.58$ AGeV. Fit values are shown in figure 5.20 and nicely follow this expectation.

$$f(y) = \frac{T_{eff}}{cosh(y - y_0)} \tag{5.5}$$

A summary of all efficiency and acceptance corrected rapidity and transverse momentum bins is displayed in figure 5.21 for the $0 - 10\%$ most central events. The mid-rapidity bin is represented as dark green full circles which covers a transverse momentum range of $160\,\text{MeV/c} < p_t < 1760\,\text{MeV/c}$. Figure 5.21 also shows the clear phase space restrictions for the most backward and in particular also for the most forward regions. In general, p_t coverage is better at backward rapidities. The most forward rapidity bin allows only for the measurement of $p_t \approx 500 - 1200\,\text{MeV/c}$. Exact ranges of course always depend on selection criteria.

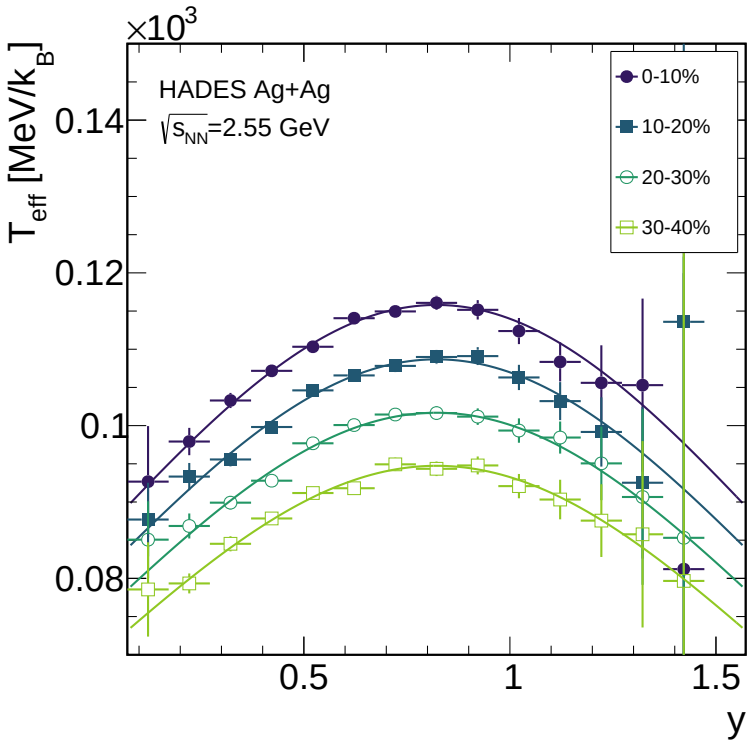

Figure 5.20: Rapidity dependence of the slope parameter of the Boltzmann fits of the p_t distributions. The effective temperature is fitted with equation 5.5 where the fit parameter at mid-rapidity refers to the effective temperature of the medium. Only statistical uncertainties are shown.

Centrality class	Multiplicity [1/evt]	Temperature [MeV/k_B]
$0-40\%$	$0.057 \pm 0.01 \pm 0.04$	$110 \pm 1 \pm 8$
$0-10\%$	$0.119 \pm 0.01 \pm 0.08$	$116 \pm 1 \pm 5$
$10-20\%$	$0.071 \pm 0.01 \pm 0.05$	$109 \pm 1 \pm 5$
$20-30\%$	$0.043 \pm 0.01 \pm 0.04$	$101 \pm 1 \pm 5$
$30-40\%$	$0.025 \pm 0.01 \pm 0.03$	$95 \pm 1 \pm 5$

Table 5.2: Lambda multiplicity for different centrality classes. In Addition to the absolute yield, the effective temperature is given. The large uncertainty in the integrated $0-40\%$ most central events results from the overlay of the different temperature fits.

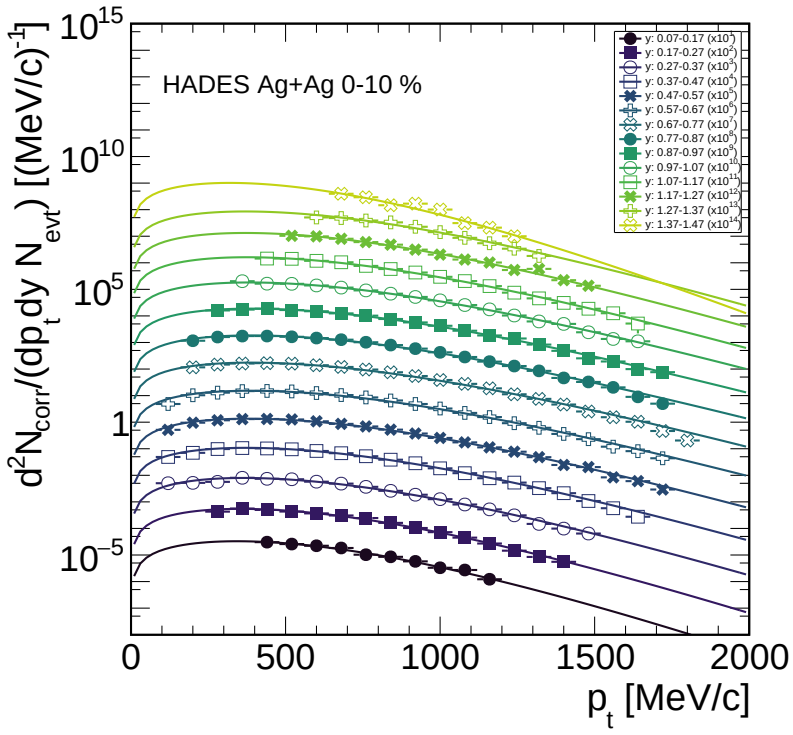

Figure 5.21: Transverse momentum spectra of all different rapidity bins for the most central $0-10\%$ Ag+Ag collisions. All bins are scaled with a factor 10^i starting with the most backward rapidity bin denoted in dark color, up to the most forward rapidity bin denoted in bright color.

A summary of the Λ baryon analysis is stated in table 5.2 where the first uncertainty always represents the statistical uncertainty while the second uncertainty represents the systematical uncertainty. This dominates the overall uncertainty of the measurements. The systematic uncertainty are estimated by comparing different sets of selection criteria. For the total multiplicity a significant contribution of the uncertainty comes from a comparison of the Gaussian fit to the fit without fixing its mean to mid-rapidity.

CHAPTER 6

Σ^0 Reconstruction

This chapter deals with the extraction of the Σ^0 signal by combining the reconstructed Λ candidates with a photon (section 6.1), using the information from the electromagnetic calorimeter. Alternatively, if the photon may have converted, the RICH is utilized to reconstruct this photon via its conversion leptons (section 6.2).

6.1 $\Lambda\gamma$ Analysis

This section deals with the formation of $\Lambda\gamma$ pairs and the reconstruction of the Σ^0. As pointed out in chapter 1.6, the branching fraction of the Σ^0 into $\Lambda\gamma$ is $\approx 100\%$, where only a small fraction ($< 3\%$) of Dalitz decays Λe^+e^+ are predicted by QED [198]. In addition, the feeddown of higher mass resonances is negligible since only the $\Sigma(1385)$ and the Ξ^0 have known branching fractions into the $\Lambda\gamma$ channel. Their branching ratios are 1.2% for the $\Sigma(1385)$ [204] and $1.2 \cdot 10^{-3}$ for the Ξ^0 [205]. Due to their large masses and thus also larger production thresholds compared to the Σ^0, no contamination of any additional resonances are assumed for the HADES energies.

For the formation of a $\Lambda\gamma$ pair, only $p\pi^-$ pairs in the invariant mass range of $1110 - 1120\,\mathrm{MeV}/c^2$ are taken into account, and afterwards setting their mass to the nominal Λ mass. Only those pairs are also taken into account for the event mixing.

However, although the Λ shows a good signal-to-background ratio of > 6 in this mass range, many uncorrelated $\Lambda\gamma$ pairs and thus a huge background are expected for different reasons: Only few of the Λ baryons originate from a Σ^0 decay. In addition, there is a large number of reconstructed γ candidates, still after all the selection steps presented in chapter 4.7. For events with a reconstructed Λ, the reconstructed photon multiplicity per event is $N_\gamma^{rec} = 0.39/evt$. This resulting amount of uncorrelated $\Lambda\gamma$ pairs is further increased as low energy photons are taken into account due to small mass difference of Λ and Σ^0.

In chapter 5, different background estimation techniques were introduced. For the Σ^0 only the event mixing approach can be used. The sideband fitting procedure does not suite the analysis, since the broad peak in the invariant mass

spectrum is located near the maximum of the combinatorial pairs due to their phase space distribution. The rotation technique does not suite the analysis, because the acceptance of the γ from the electromagnetic calorimeter is highly restricted and not symmetric at all.

In order to correctly describe the background with the event mixing, possible remaining correlations have to be included in the mixing. Due to the combination of a secondary decay with two charged tracks and the photon, there might be some hidden correlations. The Λ itself decays after a few centimeters, while the proton and π^-, which are seen in the detector may interfere with the reconstructed γ. The γ reconstruction is influenced by nearby charged tracks, because clusters are removed, that have some track close by. As this is a kind of opening angle cut, this effect has to be mimicked in the event mixing.

The intersection point of the protons and π^- in the electromagnetic calorimeter are estimated using the combined information of their inner and outer track segments. While the azimuth angle ϕ is constant for both segments, the polar angle ϑ differs for inner and outer segments, due to the magnetic field in between. The distance of the proton and the π^- from one event to the ECal cell of the γ candidate of another event are approximated as

$$OA = \sqrt{(\Delta\theta)^2 + (\Delta\phi)^2} \tag{6.1}$$

where $\Delta\phi$ is defined as $\phi_{track} - \phi_{cluster}$ and $\Delta\theta$ is defined as $\theta_{track} - \theta_{cluster}$ respectively where $\theta_{track} = 0.5 \cdot (\theta^{inner}_{track} + \theta^{outer}_{track})$.

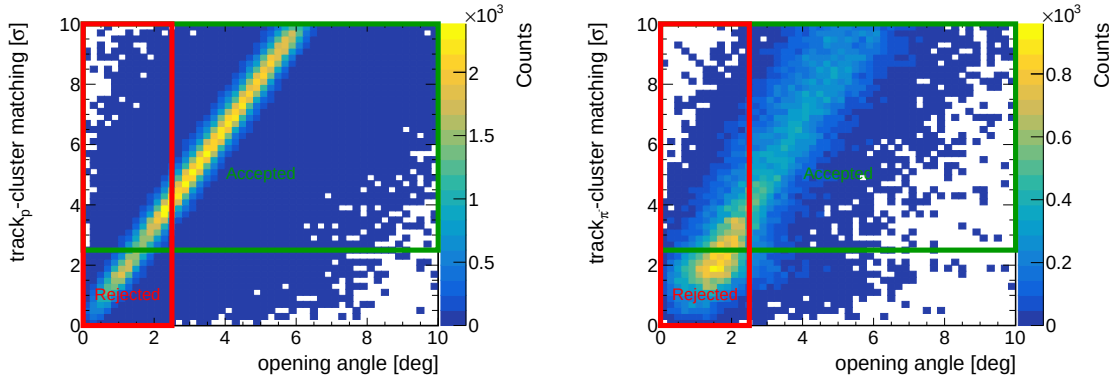

(a) p-track cluster matching

(b) π^--track cluster matching

Figure 6.1: Representation of the track-cluster matching for protons (a) and π^- (b) in dependence on the opening angle parameter from equation 6.1 in mixed events.

In figure 6.1 the relation of the track-cluster matching σ (for details see chapter 4.7) and this approximation OA is displayed for all identified protons and π^- from an event, i.e. after the reconstructed mass cuts from event mixing.

The green box represents the area, where an ECal cluster is accepted in terms of the matching during the γ selection. The red box shows the track-cluster matching which is removed from the final sample of $\Lambda\gamma$ pairs in the event mixing as well as the same event spectra.

The influence of this selection is depicted in figure 6.2 for the proton-γ distance in the electromagnetic calorimeter plane versus the invariant mass of the $\Lambda\gamma$ pair. The plot shows the ratio of results from same events and mixed events, thus allowing to proof whether these correlations are the same.

Besides large fluctuations at the phase space borders due to low statistics, a clear region of reduced values is visible for very small values of the proton-γ opening angle.

As indicated by the red box, these pairs are removed by this selection in figure 6.1.

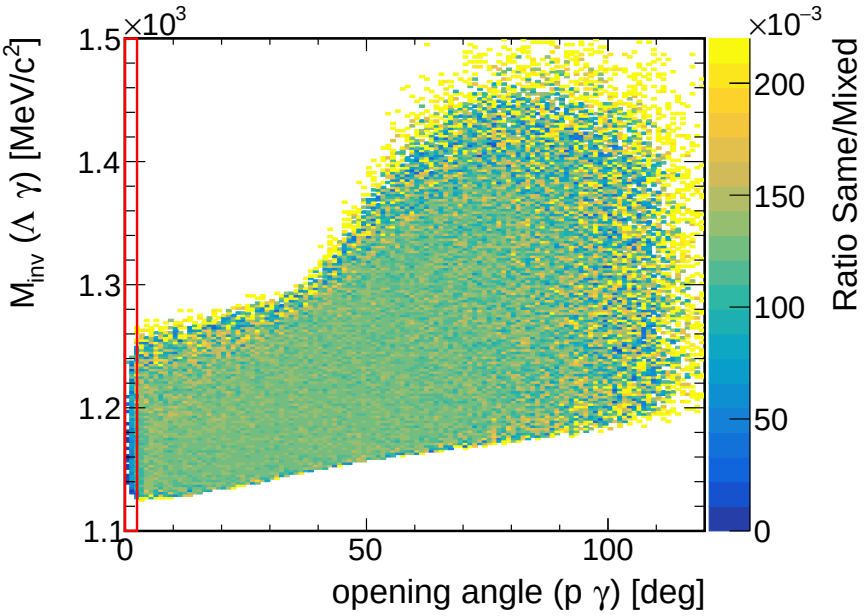

Figure 6.2: Ratio of the amount of reconstructed $\Lambda\gamma$ pairs from data in dependence on invariant mass and opening angle of the proton and γ (see equation 6.1) from the Λ decay.

This cut removes 0.30% of all Σ^0 candidates from the same event spectrum but 0.51% of the pairs from the mixed event. The raw spectra from same and mixed events are attached in appendix B.5.

After the removal of those correlations that are different in same events and mixed events, the invariant mass spectrum of the remaining $1.21 \cdot 10^6$ $\Lambda\gamma$ pairs is displayed in figure 6.3 in black as well as the $9.50 \cdot 10^6$ $\Lambda\gamma$ pairs from the event mixing technique in blue. Scaling of the mixed event spectrum was performed in the same way as for the Λ, where side bands were normalized to the same event spectrum. For the left side band, all pairs with $M_{inv} < 1145\,\mathrm{MeV/c^2}$ were taken into account, while for the right side band, pairs in the range of $1235\,\mathrm{MeV/c^2} < M_{inv} < 1290\,\mathrm{MeV/c^2}$ are considered.

The side bands are chosen to keep a 3σ distance to the reconstructed Σ^0, in order to avoid contamination of the signal $\Lambda\gamma$ pairs in the side band regions. Af-

ter the subtraction of the normalized event mix background, the red distribution displays the remaining signal.

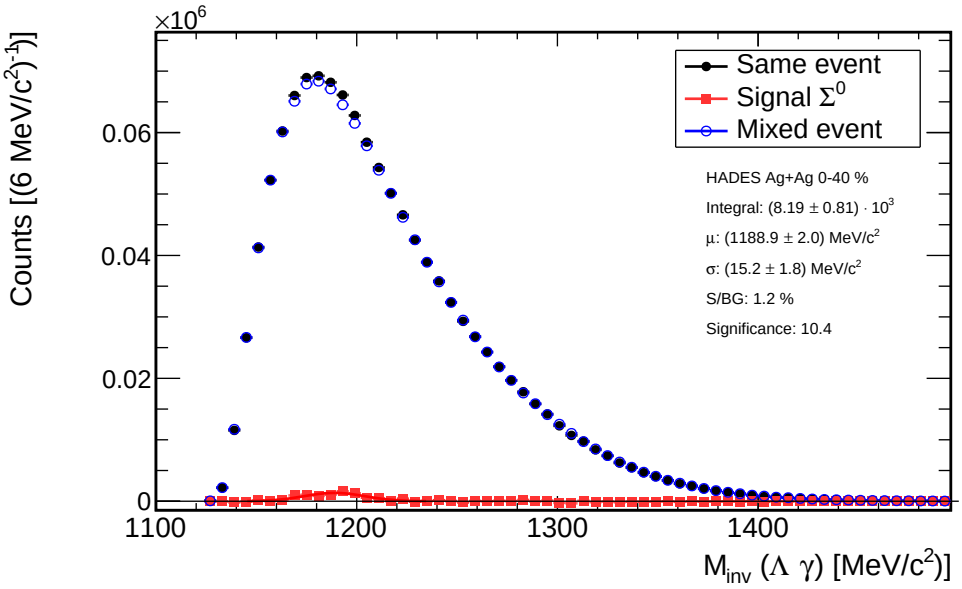

Figure 6.3: Invariant mass of all reconstructed $\Lambda\gamma$ pairs from same events (black), the event mixing technique (blue) and the remaining distribution (red) after subtracting the event mixed spectrum from the same event spectrum.

Obviously the event mixing technique describes the combinatorial background with very high precision, which is visible for the full invariant mass region, since the blue and black data points overlay perfectly and subtracted values of counts align around zero, with statistical fluctuations only as shown in figure 6.3.

Around the Σ^0 pole mass region of $m_{\mathrm{PDG}}(\Sigma^0) = 1192.6\,\mathrm{MeV/c^2}$ differences between the blue and black distributions arise, which is also visible in the red signal distribution. The remaining signal is then parametrized with a Gaussian. The Gaussian fit of the signal spectrum is shown in figure 6.4.

The reconstructed mean value of the Σ^0 mass is shifted by $3.7\,\mathrm{MeV/c^2}$ towards lower masses with respect to the PDG value. This artifact is due to the difficult calibration of γs in the electromagnetic calorimeter, especially for low energies $< 100\,\mathrm{MeV}$. They are particularly important in this analysis. Most probably, the correction of energy loss of low momentum photons is still not sufficiently precise. This assumption is supported by the fact, that the Σ^0 mass rises when excluding low momentum photons as depicted in appendix A.8.

The final energy calibration was optimized to describe the π^0 mass [197] for all π^0 momenta. However, also for other hadrons including γs in the reconstruction, as e.g. the η meson, differences in reconstructed masses are observed in experimental data compared to the expected PDG values. In addition to the γ energy calibration, the combinatorial background is most abundant in the signal region,

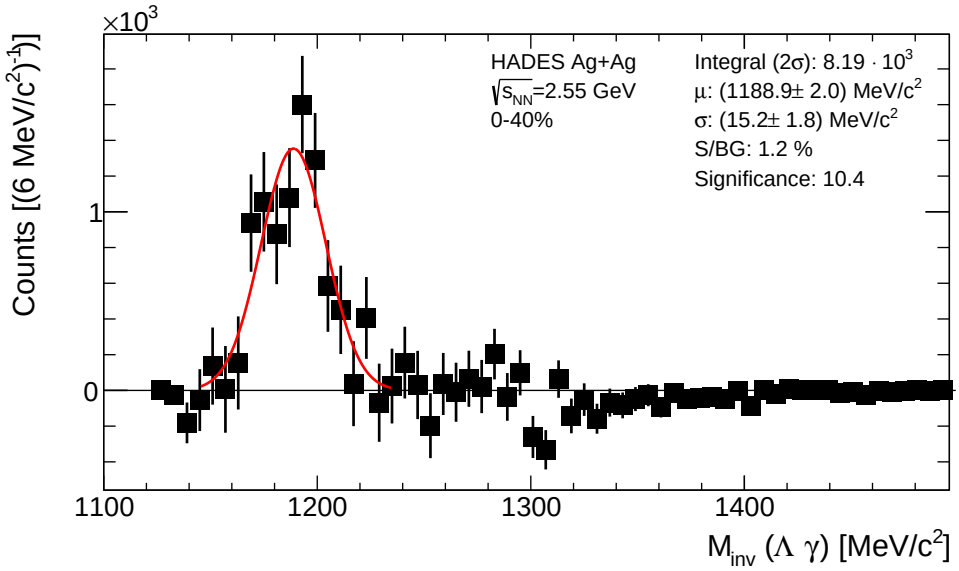

Figure 6.4: Invariant mass of all $\Lambda\gamma$ pairs from same events remaining after subtracting the event mixed spectrum from the same event spectrum. Additional information is written in the text.

which also induces a systematic dependency. Systematic studies concerning the integrated yield are performed in chapter 6.3.

The width of the Gaussian fit to the Σ^0 signal is dominated by the energy resolution of the γ, while the influence of the Λ mass resolution is neglectable. The width of $\sigma = 15.2 \pm 2.0\,\text{MeV/c}^2$ is slightly larger than the width extracted from simulated Σ^0 which are embedded in real data, resulting in $\sigma_{sim} = 12.3 \pm 0.4\,\text{MeV/c}^2$. This reduction is also expected due to the imperfect description of the energy resolution of the γ in simulations.

The accessible phase space of the Σ^0 candidates, i.e. the $\Lambda\gamma$ pairs is shown in figure 6.5. To be as comparable as possible to the true Σ^0 distribution, only Σ^0 candidates within 1σ around the nominal PDG mass are taken into account in the experimentally measured data. Still, this distribution contains a lot of background as well. Multi-differential extraction of the Σ^0 is not possible in data due to the small statistics in the measured signal. In simulations shown in figure 6.5b, only true Σ^0 are selected for this distribution. This distribution is very comparable to the experimental phase space distribution although the experimental data is dominated by combinatorial background being a factor 100 larger than the Σ^0 signal.

Furthermore, the coverage around the mid-rapidity region of $y = 0.82$ is a large advantage of this measurement. While most of the statistics is around mid-rapidity with transverse momenta around $p_t = 400 - 800\,\text{MeV/c}$, the coverage reaches up to $p_t = 1500\,\text{MeV/c}$ with a rapidity range of $0.15 - 1.5$.

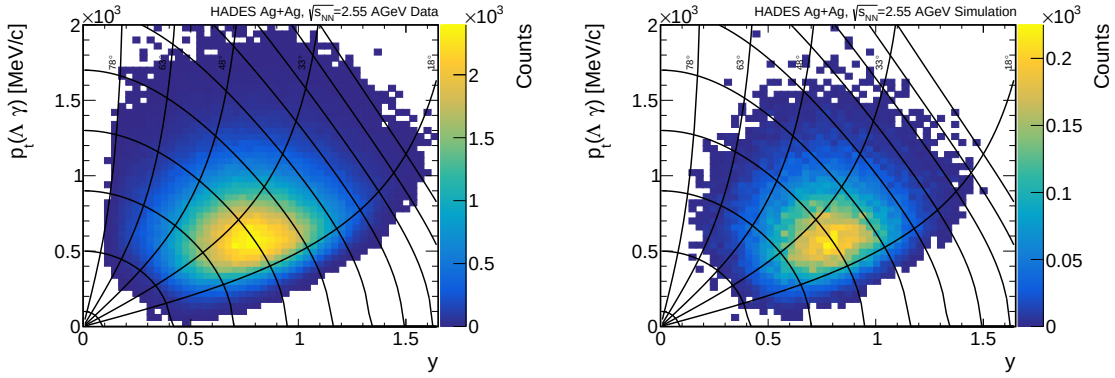

(a) Σ^0 candidates from experimental data (b) True Σ^0 signal from simulation

Figure 6.5: Phase space coverage of the reconstructed Σ^0 candidates. For experimental data (left) a mass cut of $\pm 1\sigma$ around the nominal PDG mass is used for all $\Lambda\gamma$ pairs is shown in this figure. In the experimental data (left), the background is still included while the figure on the right shows the true signal distribution extracted from simulation.

6.2 $\Lambda e^{\pm}$ Analysis

The most crucial part of the Σ^0 analysis in the $\Lambda e^{\pm}$ channel is the low energy of the γ or virtual photon in case of a Dalitz decay, which splits into the energies carried by both daughter leptons. In chapter 4.8, the detector acceptance borders of electrons and positrons were introduced. They differ in particular for low momenta, thus restricting the reconstruction sensitivity of the e^+e^- pair from γ conversion or γ^* decay, respectively. In figure 6.6 the kinematics are visualized by utilizing the simulation of photons which originate from Σ^0 decays.

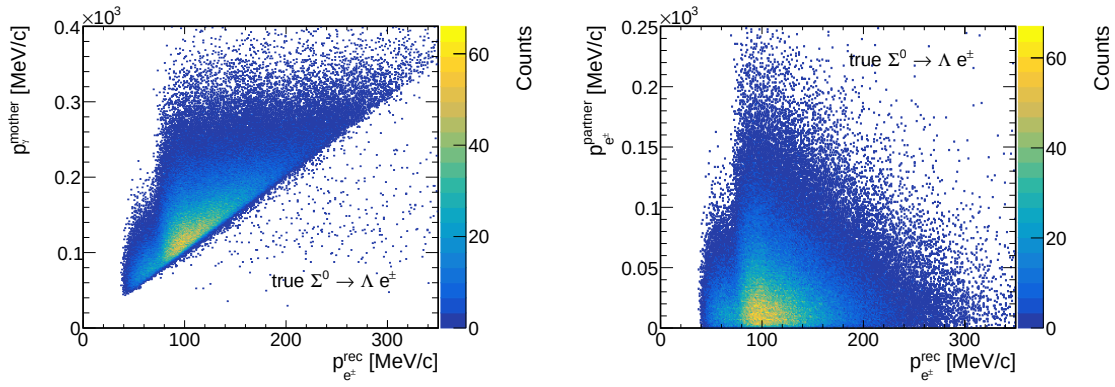

(a) (b)

Figure 6.6: Momentum distribution of the γ (mother) and conversion partner ($e_{partner}$) from simulations versus the momentum of reconstructed single leptons from Σ^0 decays in simulation. More details are written in the text.

In both plots, 6.6a and 6.6b the momentum of a reconstructed single lepton from a Σ^0 decay is plotted on the x-axis independent on its electromagnetic charge or any information on the Λ baryon. On the y-axis of the left plot, the true momentum of the mother (γ) is displayed. On the right side, the momentum of the partner lepton momentum is shown independent on being reconstructed or not. In both cases the momentum thresholds for the different charges are visible for the reconstructed leptons as acceptance edges around 40 MeV/c for positrons and 80 MeV/c for electrons. Most reconstructed leptons obtain a momentum around 100 MeV/c, with only marginally larger γ momentum. This results in a missing partner lepton momentum of less than 20 MeV/c in most cases. Obviously, the energy of the γ is distributed very asymmetrically to the two leptons, since only in this case, at least one lepton can be reconstructed.

This leads to the following two conclusions: Selecting the lepton only via the amount of reconstructed Cherenkov photons in the RICH will reduce the statistics significantly due to the Cherenkov threshold of $p_e \approx 10$ MeV/c. Secondly, the partner lepton can be neglected anyway, since its influence is comparably small. The Σ^0 reconstruction using RICH information for the γ reconstruction is thus reduced to a Λe^+ and Λe^- pair analysis [1]. Both cases will be analyzed.

Figure 6.7 shows the sum of all Λe^+ and Λe^- pairs for same events, event mixing and the remaining spectrum after background subtraction. No clear signal can be seen around the expected mass of $m_\Sigma \approx 1190$ MeV/c^2 due to statistical fluctuations and a dominant undershoot for small invariant masses around $M_{inv}(\Lambda e^\pm) = 1150$ MeV/c^2. Still already in this spectrum, a slight hint of a possible Σ^0 signal is seen. The lepton charge separated spectra of Λe^+ and Λe^- are visible in appendix A.10. In the following section, some studies are presented in order to improve the significance of the Σ^0 signal using additional selection criteria on the lepton and the Λ lepton pair kinematics. Theses studies are based on simulations of Σ^0 baryons embedded in real data as described in section 5.5, for realistic background depiction. Properties, like especially kinematics of the lepton or Λe pair can be compared between "signal", i.e. the simulated Σ^0, and data in- and excluding the signal, i.e. Λe pairs from same events or event mixing.

Figure 6.8 shows the lepton momentum distribution from simulated Σ^0 embedded in experimental data for the simulated signal Σ^0 in black, the remaining same event Λe in red and the mixed event Λe pairs in blue. The lepton momentum distributions from mixed events is slightly larger than the one from same events, in particular for low momenta. This is a result of the fact, that the event mix includes the non negligible number of leptons from the embedded Σ^0 signal. This fact, however has no influence on the result but is just a minor flaw.

While the left side (figure 6.8a) contains the leptons from all possible Λe combinations, the right side only takes those with $M_{inv}(\Lambda e) < 1200$ MeV/c^2 into account, which changes the shape of the normalized distributions. As known al-

[1] The attempt of reconstructing both partner leptons does not result in any reconstructed $\Lambda e^+ e^-$ formation around the nominal PDG Σ^0 mass due to the phase space restrictions and thus can not be used at all.

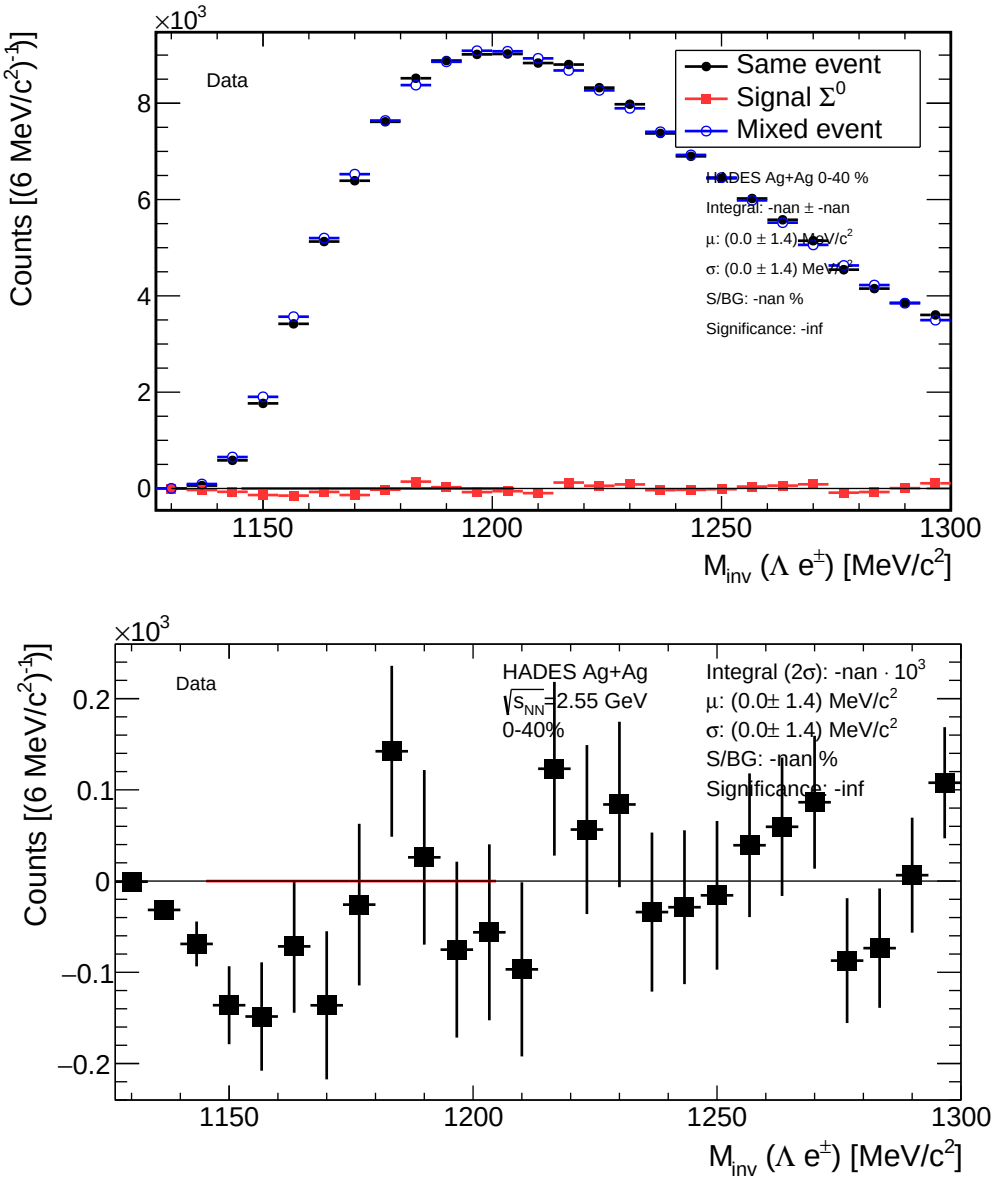

Figure 6.7: In the upper plot shows the invariant mass of all $\Lambda e^{\pm}$ pairs as described in the text from the same events in black, the mixed events in blue and the remaining signal spectrum after subtracting the background. Mixed events were scaled to the same events using the sideband method. In the lower plot, the signal is shown more precisely.

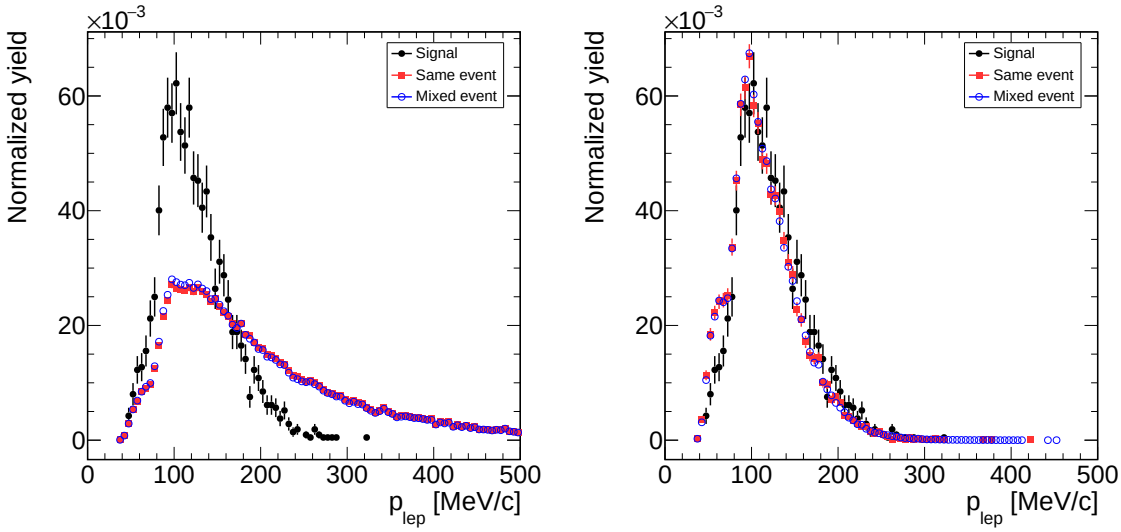

(a) Reconstructed lepton momentum for all Λe pairs, independent of their invariant mass.

(b) Reconstructed lepton momentum for Λe pairs, which have invariant masses lower than $1200\,\mathrm{MeV/c^2}$

Figure 6.8: Dependency of lepton momentum of the Λe pairs from different sources, extracted from data and Σ^0 simulations embedded in data. Additional information is written in the text.

ready from figure 6.6, lepton momenta for the Σ^0 are rather low. However, a restrictive upper cut on the $e\Lambda$ pair mass as suggested by figure 6.8 would significantly influence the lepton momentum distribution and background subtraction.

Thus a lower cut is used, rejecting lepton momenta below $100\,\mathrm{MeV/c}$. With this cut the low momentum leptons which mostly contribute to the background as seen in figure 6.8b are cut off.

In addition to a selection on the lepton momentum, pair correlation cut is induced in form the opening angle α between the Λ and the lepton. Figure 6.9 shows the opening angle distribution α for Λe pairs from signal and background, also for all invariant masses (a) and those with $M_{inv}(\Lambda e) < 1200\,\mathrm{MeV/c^2}$. Obviously, Λe pairs from Σ^0 baryons have lower opening angles. Thus a cut $\alpha < 40°$ will be applied.

Furthermore, an influence of the lepton charge is investigated. For the signal yield, 64.6% of the Λe pairs arise from negatively charged electrons, while for background pairs, only 54.0% are formed by a Λe^-. When constraining the invariant mass of the background pairs to the signal region, still only 58.0% contain an e^-, which is still significantly below the signal yield. Obviously there is a charge inbalance in signal compared to background, after the $p_{e^-} > 100\,\mathrm{MeV/c}$ selection, simulations show twice the efficiency for electrons compared to positrons and thus, deduced from this observation, only Λe^- spectra are shown. The spectra of Λe^+ and the combined $\Lambda e^+ + \Lambda e^-$ are displayed in appendix A.11.

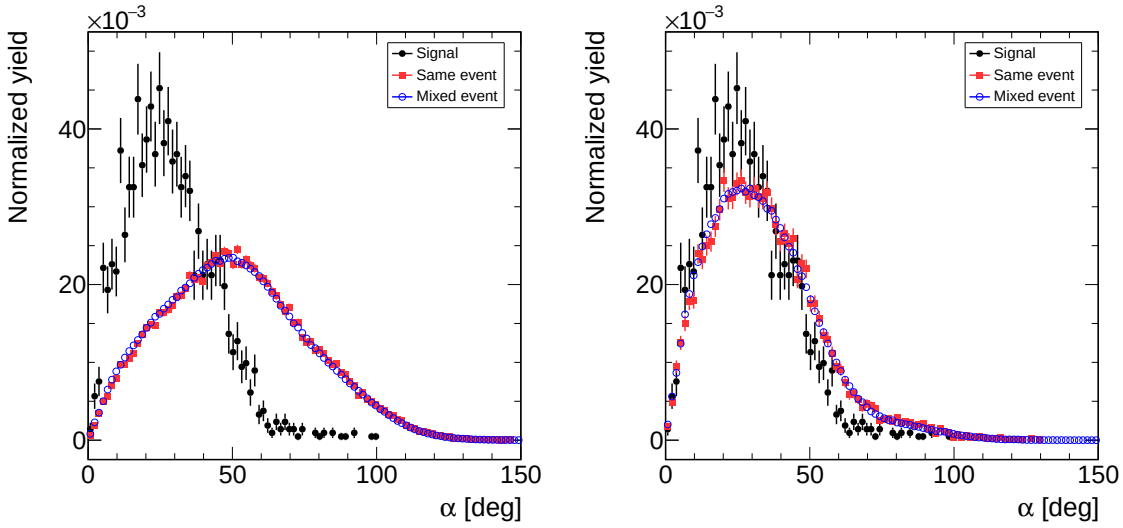

(a) Reconstructed opening angle for all Λe pairs, independent on their invariant mass.

(b) Reconstructed opening angle for Λe pairs, which have invariant masses lower than $1200\,\mathrm{MeV/c^2}$

Figure 6.9: Dependency of the Λe opening angle of Λe pairs from different sources, extracted from simulated Σ^0 embedded in experimental data and simulations embedded in data. Additional information is written in the text.

Selection on Amount of Reconstructed Cherenkov Photons

As discussed, the $\Lambda\gamma$ analysis is reduced to an analysis of Λe^- pairs. However, although the missing lepton partner will not be reconstructed due to its little momentum, it might have left a trace of Cherenkov photons in the RICH, Due to the small opening angle of the e^+e^- pairs from photon conversion, but partially also from Dalitz decays, a second ring should be visible in close vicinity. The identification of the lepton is explained in detail in chapter 4.9. However, this ansatz is challenging here due to the Cherenkov threshold of $10\,\mathrm{MeV/c}$ for leptons.

Figure 6.10 displays the amount of reconstructed Cherenkov photons around the RICH ring of the identified lepton without applying the lepton momentum cut of $100\,\mathrm{MeV/c}$, nor the opening angle cut to the Λ. A double Gaussian peak structure is visible, indicating single and double rings. As pointed out in chapter 2.2.3 the HADES RICH upgrade allowed for separation of conversion and non conversion e^+e^- by distinguishing these two Gaussian distributions.

The distributions show slight enhancement of leptons from Σ^0 compared to background at small values of N_{ACals}, thus no cuts will be applied here, except the loose removal of rings with $N_{\mathrm{ACals}} > 40$ for the reasons described in section 4.9.

To summarize, only electrons with a total momentum of $p_{e^-} > 100\,\mathrm{MeV/c}$ are taken into account which also have an opening angle $\alpha < 40.0°$ to the Λ candidate pointing vector. The selection on the amount of reconstructed Cherenkov photons in the RICH is only used very soft by removing all rings with more than 40 reconstructed Cherenkov photons in vicinity of the ring, to remove blobs which

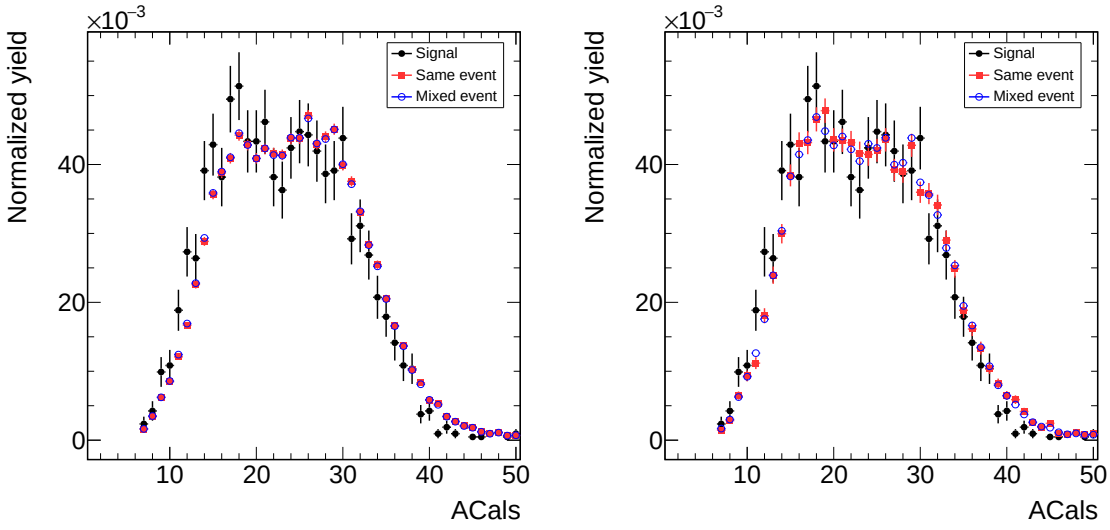

(a) Amount of reconstructed Cherenkov photons for all Λe pairs, independent on their invariant mass

(b) Amount of reconstructed Cherenkov photons for Λe pairs, which have invariant masses lower than $1200\,\mathrm{MeV/c^2}$

Figure 6.10: Number of reconstructed Cherenkov photons in the RICH around the ring of the reconstructed lepton in the Λe pair for different sources, extracted from simulated Σ^0 embedded in experimental data. Additional information is written in the text.

were mentioned in chapter 4.9. Even with separation power available in the amount of reconstructed Cherenkov photons around the ring in the RICH, the loose cut is chosen, due to the already small statistics to optimize the significance.

In figure 6.11 the resulting invariant mass spectra for same events, mixed events and the remaining signal spectrum after background subtraction are shown. Again, the side band method is utilized, normalizing to the invariant mass ranges of $1200\,\mathrm{MeV/c^2} < M_{inv}(\Lambda e) < 1250\,\mathrm{MeV/c^2}$. An enhancement in the Σ^0 mass region is clearly visible. Figure 6.13 shows the signal spectrum only.

The signal can be fitted with a Gaussian to extract the measured Σ^0, alternatively the yield can be extracted summing the entries in the 2σ region around the center. About 420 Σ^0 are measured, however with large statistical uncertainties. The agreement of counting the entries of the histogram and integrating the Gaussian of $3\,\%$ is surprisingly good, even though we would not expect a symmetric Gaussian. The statistical uncertainty of the signal is $28.8\,\%$ and therefore the resulting significance is only 2.8. Thus, the conversion results are finally only taken into account for a validation of the Σ^0 production yield extracted after full efficiency and acceptance correction in the $\Lambda\gamma$ analysis. The shape of the signal distribution in experimental data is similar to the results which are obtained in simulation (see figure 6.13). No strong asymmetry of the peak is observed, which could be induced as bias from only analyzing Λe pairs instead of the full decay mode Λe^+e^-.

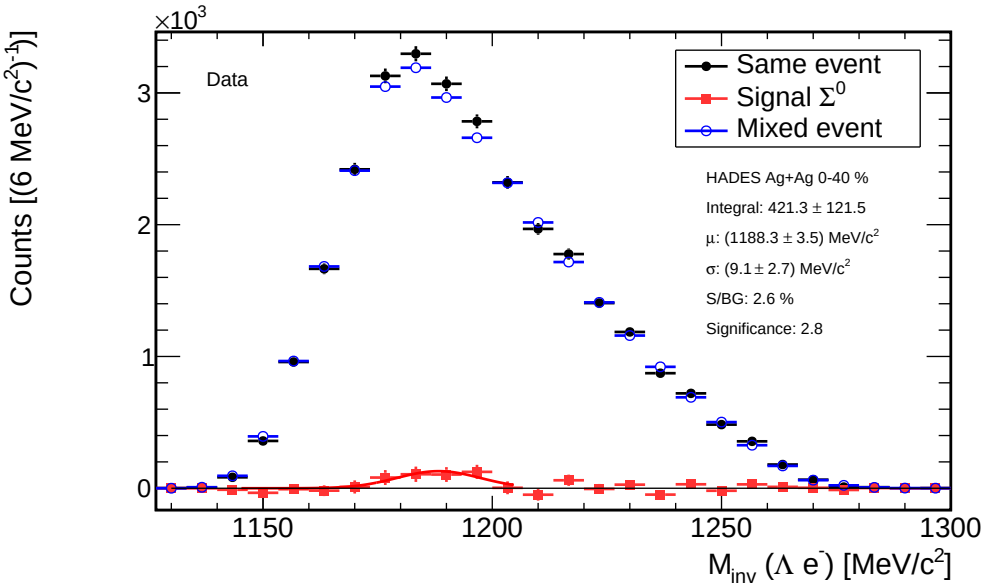

Figure 6.11: Invariant mass of all Λe^- pairs after cuts as described in the text from the same events in black, the mixed events in blue and the remaining signal spectrum after subtracting the background in red. Mixed events were scaled to the same events using the sideband method.

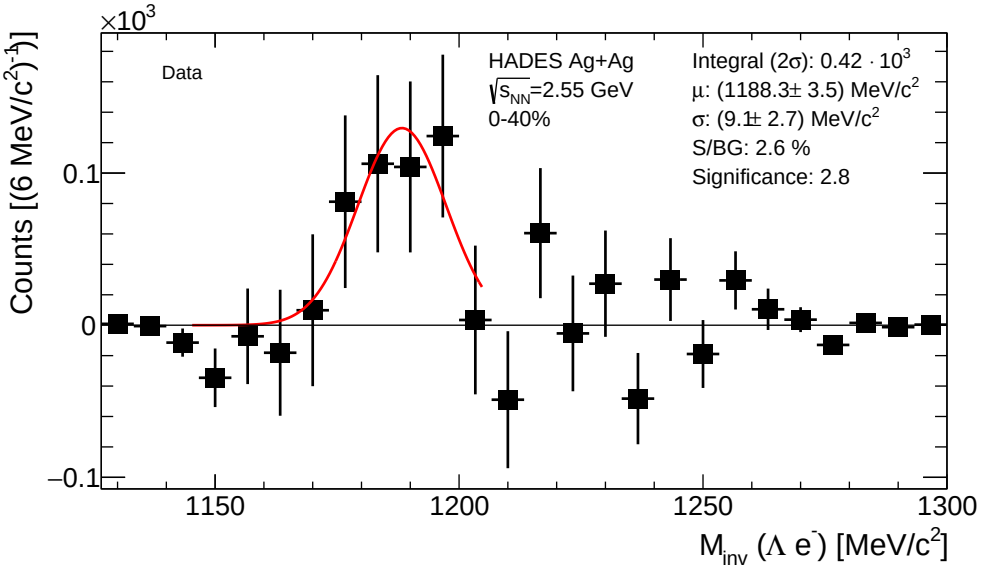

Figure 6.12: Invariant mass of all Λe^- pairs after background subtraction. A Gaussian distribution is fitted to the signal.

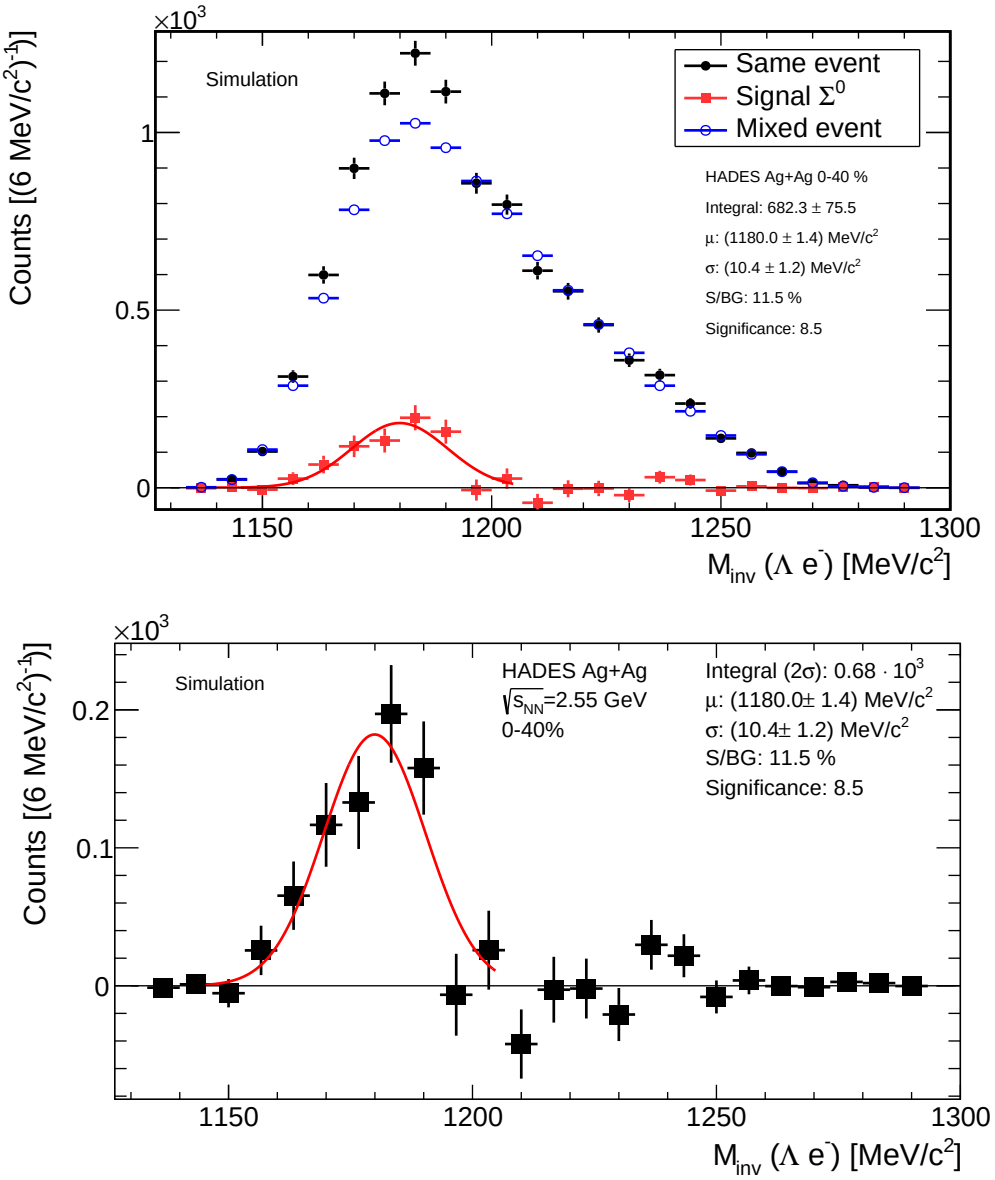

Figure 6.13: Simulated invariant mass of all Λe^- pairs after all cuts for Σ^0 baryons embedded in real data. Top: raw same event spectrum in black, down scaled mixed event spectrum in blue and the resulting signal after combinatorial background subtraction in red.

In addition to the already low statistics, the signal extraction method in simulation is highly systematically dependent from the choice of the side band region, while only minor dependency exists in experimental data. In simulation, this behavior results in a reduced amount of reconstructed signal counts, compared to the true yield which is extracted with Monte-Carlo information by almost $30\,\%$, rather independent on the applied cuts. In the simulation with embedded Σ^0, the signal yield is rising by 62% with a simultaneous reduction of the background by a factor of ≈ 3 when comparing the blue curves in figures 6.13 and 6.12. The extracted signal structure is fitted with a Gaussian which delivers very similar distribution width $\sigma_{exp} = 9.1 \pm 2.7\,\text{MeV/c}^2$ in experimental data and a corresponding width of $\sigma_{sim} = 10.4 \pm 1.2\,\text{MeV/c}^2$ in simulation which is consistent within the errors. The mean of the Gaussian distributions of $\mu_{exp} = 1188.3 \pm 3.5\,\text{MeV/c}^2$ and $\mu_{sim} = 1180.0 \pm 1.4\,\text{MeV/c}^2$ differ slightly larger than the expected fit uncertainties, which is explained by the large statistical uncertainties of the fit in experimental data in addition to the fact of an asymmetric signal yield shape and a resulting discrepancy in order of half of the bin width. Overall the statistical uncertainty of $28.6\,\%$ is in the same order as the systematic uncertainty of $50\,\%$, which is extracted by comparing the influence of the charge selection in simulations and data as well as the induced signal yield extraction error compared to the MC true yield A.9.

6.2.1 Test of Λe Analysis in p+p Data

In February 2022 HADES measured p+p collisions at kinetic beam energy of $E_{kin} = 4.5\,\text{AGeV}$. As the Λe analysis for Σ^0 reconstruction was newly developed for this work, these p+p data were briefly analyzed as proof of concept for this method. The p+p data offer the advantage of higher energy thus larger production cross section and lower background. A sub sample of $15.4 \cdot 10^9$ events was analyzed. The hadron and single lepton selection is exactly the same as for the Ag+Ag data. The same loose preselection for the Λ and described in section 5. The cut of the machine learning evaluation is neglected here, since its not required for a good signal to background. No opening angle cut nor a minimal lepton momentum is required for the Λe pair selection. With less background and higher energies, it is worthwhile checking the hits around the selected Cherenkov ring again. The influence of this cut is thus easier to study here.

Figure 6.14 shows the amount of reconstructed Cherenkov photons versus the Λe invariant mass for the measured p+p collisions from 2022. The horizontal line represents the minimum between the two Gaussians, which is usually used as separation for single leptons from conversion leptons (see section 4.9). The vertical line represents the PDG mass of the Σ^0 baryon. Two bands of detected Cherenkov photons are seen, one for single, one for double rings at 16 and 28 hits, respectively. The maximum close below the PDG mass of the Σ^0 indicates a peak as also seen in figure 6.15. These data allow to select Λe but also presumable $\Lambda e^+ e^-$ pairs by cutting on single or double rings.

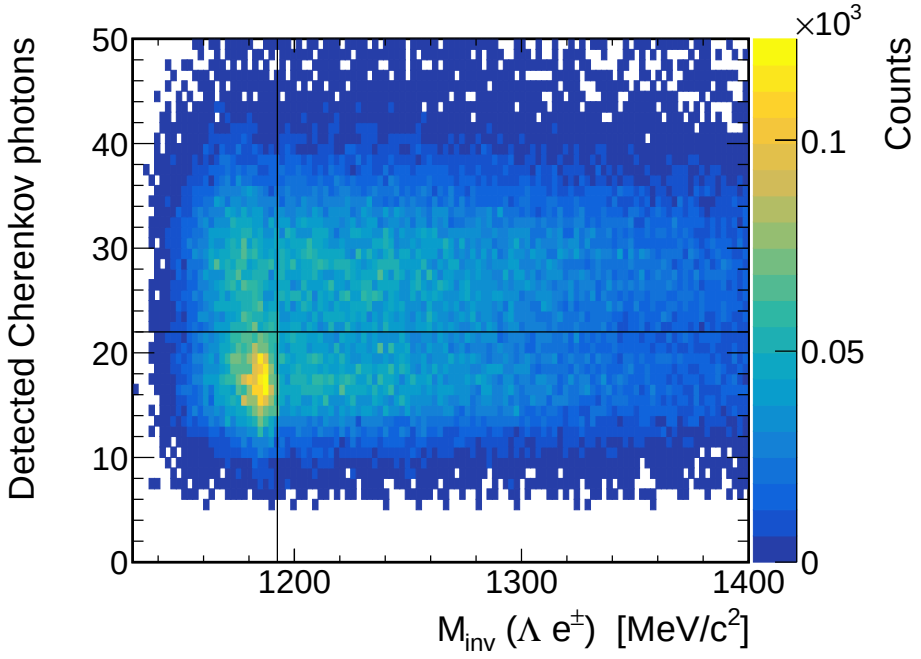

Figure 6.14: Representation of the amount of reconstructed Cherenkov photons around the lepton ring against the invariant mass of the Λ lepton pair for the p+p data from 2022.

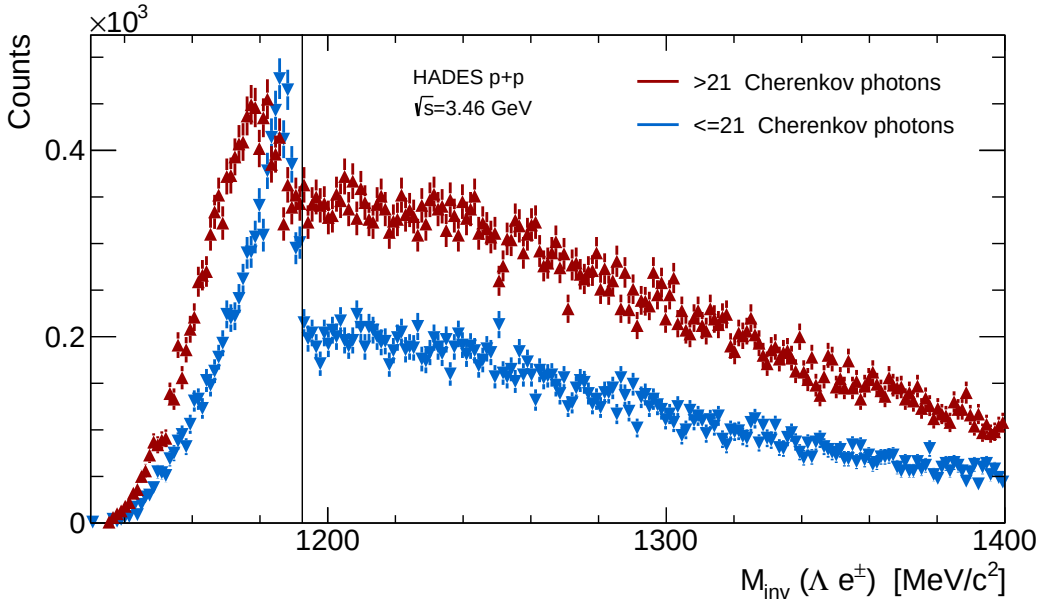

Figure 6.15: Comparison of the invariant mass spectra for low and high amount of Cherenkov photons in the RICH. Additional information is written in the text.

While the blue distribution has a narrow peak close to the PDG mass, the red distribution is shifted towards smaller masses and also broadened. The reason of the narrow peak for selected singe rings is the following: Only e^+ and e^- with $p_e > p_{Che}^{Thr} \approx 10\,\text{MeV/c}$ produce Cherenkov photons under the assumption that the partner lepton has a momentum below this threshold only a single ring is seen. Neglecting the low energy leptons does influence the overall invariant mass calculation only mildly. The opposite case arises for the red distribution, where the partner lepton due to the double ring structure is assumed to have a non negligible $p_e > 10\,\text{MeV/c}$ and thus would change the invariant mass of the Λe^+e^- more significantly. This glimpse into the p+p data clearly shows the great opportunity for more detailed Σ^0 studies even in view of a possible Dalitz decay. This topic is currently investigated in more detail [206].

Applying a strict N_{ACals} cut of $N_{\text{ACals}} > 18$ to the Ag+Ag data is reducing the significance, but show the expected change in the signal shape in data and simulation as depicted in appendix A.12.

6.3 Systematic Uncertainty Estimation

An uncertainty estimation of the Σ^0 yield is performed regarding statistical and systematic uncertainties. Uncertainties in the raw signal count, which are from statistical nature, arise from the limited amount of same events and mixed Σ^0 candidates.

Possible systematic uncertainties can be introduced at various analysis steps:

- Systematic uncertainties in the raw signal count extraction are estimated by using various event classifications during the event mixing, varying the bin width, comparing the Gaussian fit yield to the counted signal sum, dividing the sample in different sub-samples and the most crucial aspect, the size and position of the side bands (see sections 6.3.1 and 6.3.2).
- Comparing different cut sets for estimation of quality of the efficiency correction (see section 6.3.3).
- The additional data driven γ efficiency correction is handled separately by correcting with leptons with different observables in the electromagnetic calorimeter, namely the incoming angle, its energy resolution and path length through the cell (see chapter 7.2).
- Due to the limited statistic of reconstructed Σ^0, no differential analysis is possible, and thus the extrapolation for a full phase space yield relies on the multi differential Λ measurement, performed in chapter 5.4. The same phase space distribution is assumed for the Σ^0.

Overall the mentioned uncertainties are uncorrelated. Thus, the quadratic sum of the different uncertainty sources is calculated (equation 6.2) for the estimation of the total uncertainty.

$$\Delta\Sigma^0 = \sqrt{\Delta^2_{stat} + \Delta^2_{sys}} \tag{6.2}$$

The systematic uncertainty is calculated as in formula 6.3.

$$\Delta_{sys}\Sigma^0 = \sqrt{\Delta^2_{raw} + \Delta^2_{\Lambda} + \Delta^2_{extra.} + \Delta^2_{\gamma,sim} + \Delta^2_{\gamma,data}} \tag{6.3}$$

The uncertainty of the raw signal is $\Delta_{raw} = 5\,\%$. No influence of the bin width and event classification for the event mixing was found, however width and position of the side bands influence the raw signal due to the small signal to background ratio (see section 6.3.2). The uncertainty of the Λ multiplicity was calculated in chapter 5.4 to be $7\,\%$. Importantly, the phase space distribution in p_t and y was measured and parameterized. The same distribution is assumed for the Σ^0.

The efficiency correction in chapter 7 is performed as $(\varepsilon \times a)_{\Sigma^0} = (\varepsilon \times a)_{\Lambda} \cdot (\varepsilon \times a)_{\gamma}$. A difference of the acceptance for the photon of the Σ^0 decay in all events compared to events with a Λ baryon being in acceptance, results in a systematic deviation of $\Delta_{extra.} = 4.8\,\% \approx 5\,\%$.

The by far largest uncertainty results from the photon efficiency calculation. The correction from simulation $\Delta_{\gamma,sim}$ is calculated by a variation of the energy cut value for the photons. On the other hand, all detector instabilities in over the beamtime and timing calibration are calculated from a data driven efficiency correction correction and calculated to be $\Delta_{\gamma,data} = 20\,\%$.

This is by far the largest uncertainty (see section 6.3.3) and estimated by small variations of the data driven β-cut corrected Σ^0 yield as well as variations of the β-cut efficiency estimation method. Those estimations lead to an overall relative systematic uncertainty of $\Delta_{sys}\Sigma^0 = 22.0\,\%$, combined with the statistical uncertainty, the total uncertainty amounts to $\Delta_{tot}\Sigma^0 = 24\,\%$.

6.3.1 Subsample Analysis

The following plots display the signal after dividing the data sample in two subsamples. In the first case, the sample is divided into forward and backward rapidity, which is always stated with respect to the mid-rapidity at $y_0 = 0.822$.

The separation in terms of rapidity results in the plots in figure 6.16 and figure 6.17. The combined Σ^0 yield of the sub-samples of $N_{raw} = 4.58 \cdot 10^3 + 3.66 \cdot 10^3 = 8.24 \cdot 10^3$ is less than 1% larger than the yield extracted from the combined sample in figure 6.4.

The same statement holds true for the separation in two random sub-samples. Those resulting spectra are shown in figure 6.18 and figure 6.19. In addition to the total yield, also the parametrization of the Gaussian fit to the signal is compared in table 6.1.

All parameters extracted from the sub-samples are consistent within uncertainties to the spectrum using all events. Several random subsets were analyzed without qualitative differences, while the plotted subsets are representative for all studies.

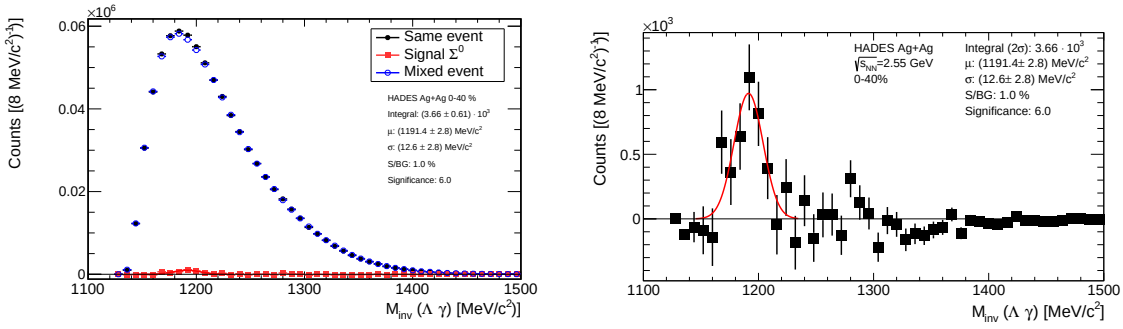

Figure 6.16: Signal extraction when only backward rapidity is taken into account.

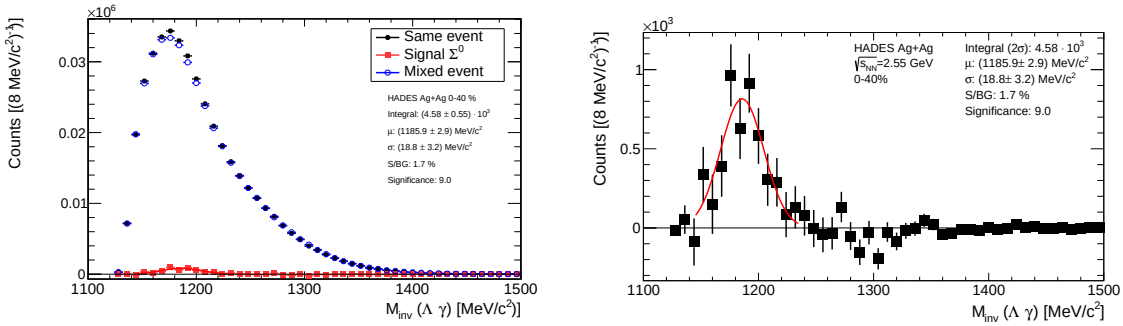

Figure 6.17: Signal extraction when only forward rapidity is taken into account.

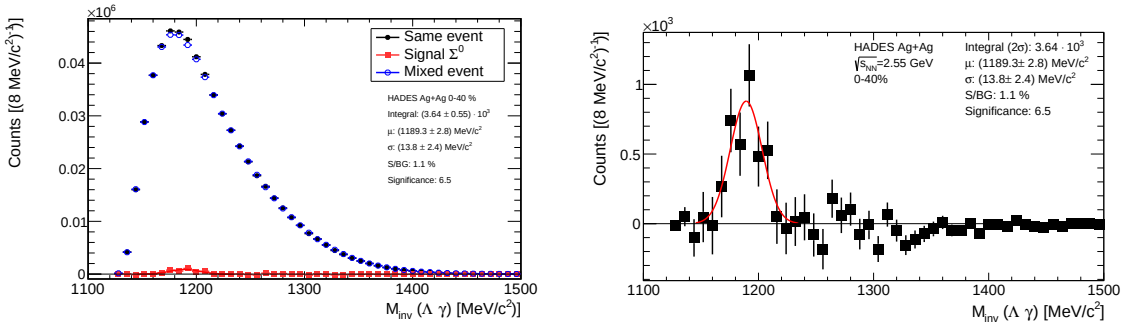

Figure 6.18: Signal extraction of random subset one.

Data sample	Yield $[10^3]$	μ [MeV/c^2]	σ [MeV/c^2]
All events	8.15	1188.9±2.0	15.2±1.8
Backward rapidity	3.66	1191.4±2.8	12.6±2.8
Forward rapidity	4.58	1185.9±2.9	18.8±3.2
Subset 1	3.64	1189.3±2.8	13.8±2.4
Subset 2	4.50	1188.3±3.1	17.3±3.2

Table 6.1: Comparison of the Gaussian fit to the Σ^0 signal for different subsamples.

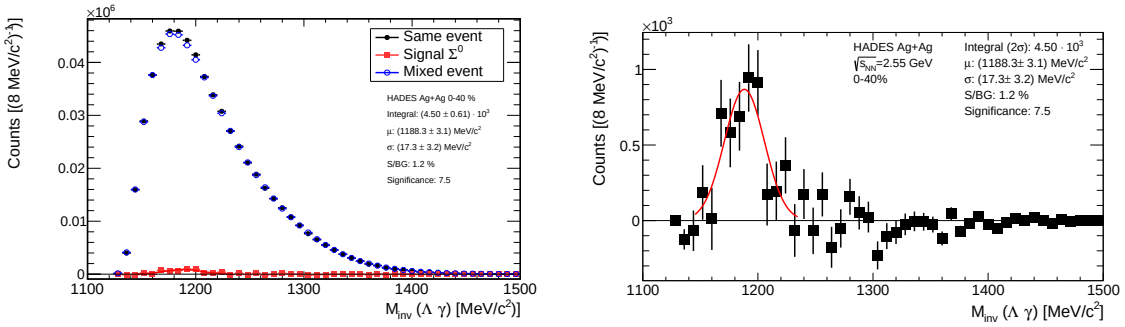

Figure 6.19: Signal extraction of random subset two.

6.3.2 Normalization Ranges

The most crucial aspect of the extraction of the raw signal yield is the choice of the sideband width during the normalization procedure of the mixed event $\Lambda\gamma$ spectrum.

Due to the small invariant mass range measurable below the Σ^0 mass, the left side band can not be varied and stays the same. The parameters of the left sideband are $SB_L^1 = 1130\,\text{MeV/c}^2$ and $SB_L^2 = 1145\,\text{MeV/c}^2$. The right sideband is varied where a summary plot showing relative changes is displayed in figure 6.20.

The error bars represent the statistical uncertainty, obviously deviations are within the statistical uncertainty. The side band width is rising with each variation, including higher invariant masses for the normalization. Variation six is the same as the nominal sideband configuration with values of $SB_R^1 = 1235\,\text{MeV/c}^2$ and $SB_R^2 = 1290\,\text{MeV/c}^2$. The $10\,\%$ rise starting at variation eight is correlated with the statistically fluctuating bin around $M_{inv}(\Lambda\gamma) = 1300\,\text{MeV/c}^2$. The same behaviour is shown in more detail in figure A.18. The systematic uncertainty of the raw counts is thus estimated to not exceed more than 300 counts (i.e. $3.7\,\%$), compared to the standard value, displayed as horizontal line in figure 6.20. The resulting relative uncertainty of $\Delta N_{SB}/N = 0.037 \approx 4\,\%$ is therefore used for the total uncertainty estimation from background subtraction.

6.3.3 Variation of γ Selection Cuts

This section deals with the consistency of the γ selection and its influence on the total Σ^0 yield extraction after efficiency correction. As will be explained in chapter 7.2, the uncertainty of the efficiency correction for the photon selection criteria depends strongly on the timing calibration of the ECal cells, the corresponding uncertainty is $\sigma_\beta^{exp} = 20\%$.

In addition, variations of the energy and the calculated velocity cut are performed in this section to estimate additional uncertainties, arising from these values. Results of the Σ^0 yield relative to the nominal conditions when varying the minimum energy of the clusters are depicted in figure 6.21. All values were calculated by keeping all other cuts the same, and only scanning the selection

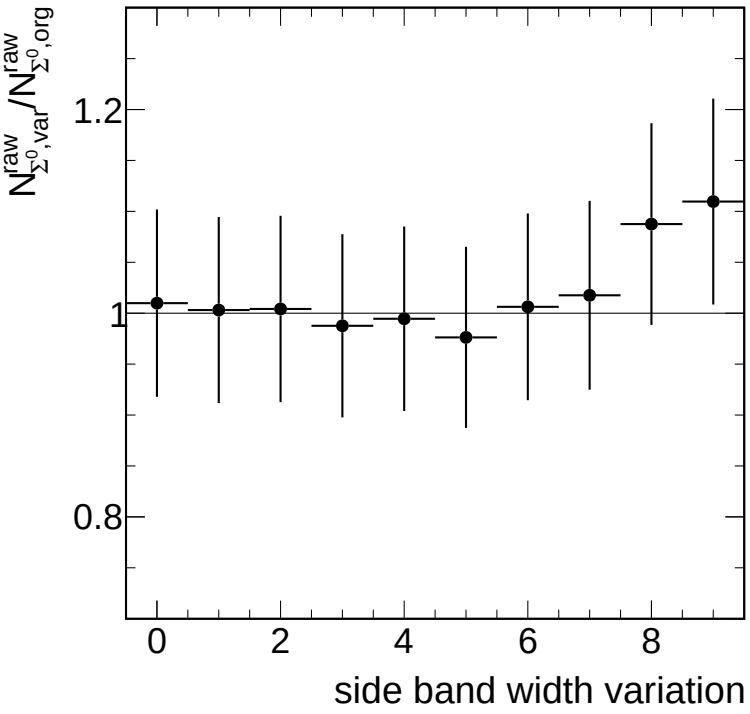

Figure 6.20: Σ^0 raw yield relative to the one using standard values for a variation of the ranges of the right sideband. This is dominating the influence on the total yield. More details are written in the text.

criterion of the minimal energy in experimental data and the simulations which were used to extract the efficiency correction. Around $E_\gamma = 120\,\text{MeV}$, only half of the statistics in the signal is left, which leads to strongly increasing statistical uncertainty. When increasing the minimal energy cut, the signal extraction gets more challenging due to the small statistics and large background. Thus, the systematically decreasing values for $E_\gamma > 100\,\text{MeV}$ lack on overall precision, which leads to an overall estimation of the uncertainty by energy variation of $\sigma^{sim}_{E_\gamma} = 10\%$.

The influence of the β cut on the γ candidate clusters is extracted in the same way: The cut is changed in data and simulations accordingly, to correct proper efficiencies, also from the data driven correction.

The systematic change of the total yield with respect to the standard cut set of $|\beta_{meas} - \beta_{expected}| < 1\sigma$ is displayed in figure 6.22. Only β-cut values up to 1.2σ were taken into account, due to the strongly rising contribution of background, i.e. neutrons and other undetected hadrons.

In fact, the total yield does not change systematically when varying the β-cut. This underlines the stability of the β efficiency correction. In particular the data driven correction is verified by these results. Estimated yield around the nominal standard selection of 1σ are only very slightly reduced compared to the standard selection set.

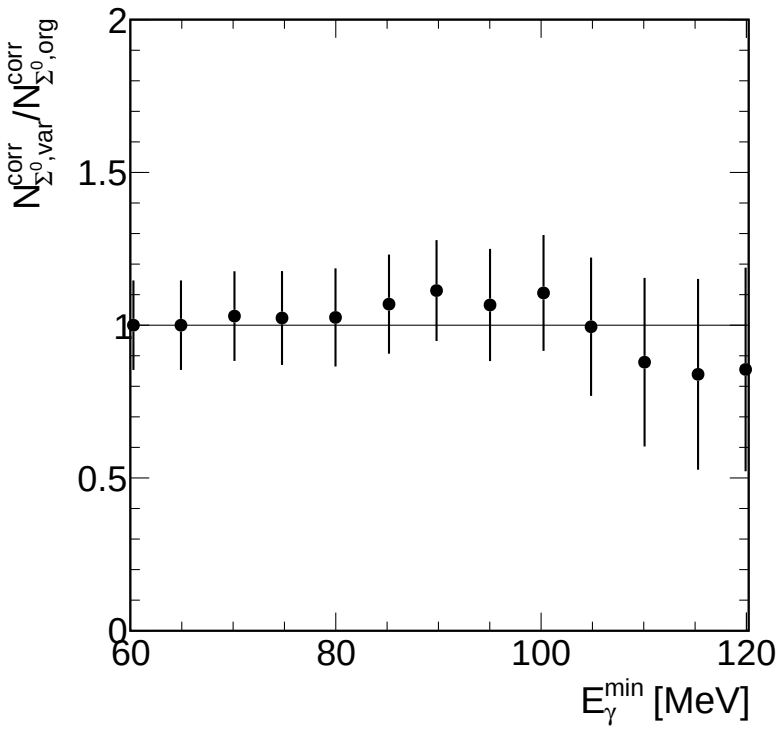

Figure 6.21: Variation of the minimal energy of the cluster in the electromagnetic calorimeter and the relative Σ^0 resulting yield after efficiency correction. More details are written in the text.

In particular for strict β-cuts the statistical uncertainties grow significantly and the ratio of $N^{corr}_{var}/N^{corr}_{org}$ is fluctuating with increasing uncertainty. This evaluation of the β cut consistency is performed for ensuring the overall uncertainty of the β cut to not exceed the systematic uncertainties which arise by the different lepton sample choice for the efficiency estimation, which lead to an uncertainty of $20\,\%$ and dominated the total uncertainty of this analysis as described in detail in chapter 7.2.

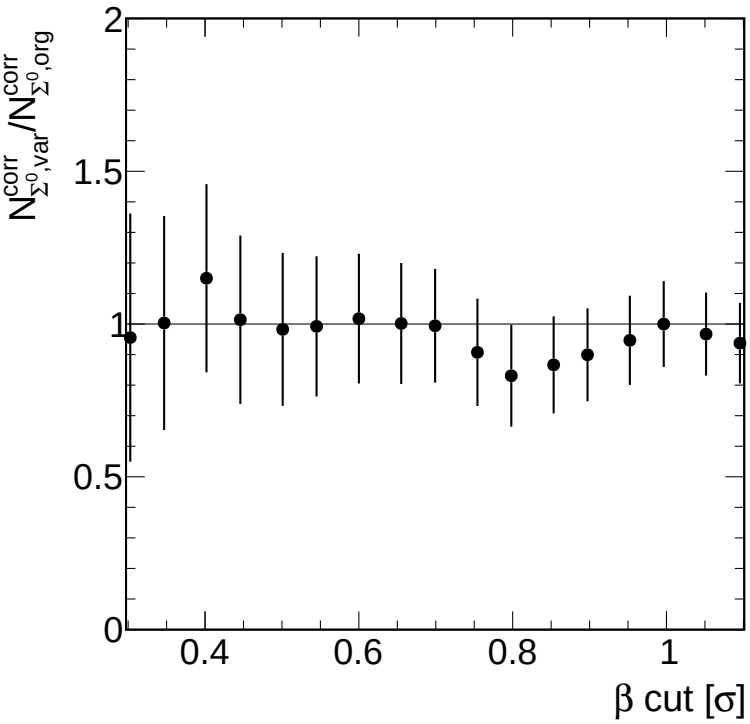

Figure 6.22: Variation of the timing of the cluster in the electromagnetic calorimeter and the resulting relative Σ^0 yield after efficiency correction. More details are written in the text.

CHAPTER 7

Efficiency Correction

7.1 Σ^0 Efficiency Determination

For the correct multiplicity estimation, the acceptance and efficiency of the Σ^0 reconstruction are estimated by Monte-Carlo simulation in the same way as for the Λ baryon in chapter 5. In comparison to the Λ baryon, the statistics of the reconstructed Σ^0 baryon candidates is far below the Λ candidate statistics. Thus, the Σ^0 multiplicity can only be determined integrated over the whole phase space region. The overall efficiency is defined as $\varepsilon^{\Sigma^0}(p_t, y) = \varepsilon^{\Sigma^0}_{rec}(p_t, y) \times acc^{\Sigma^0}(p_t, y) = N^{\Sigma^0}_{rec}(p_t, y)/N^{\Sigma^0}_{input}(p_t, y)$. The acceptance is defined as the product of the acceptance of the Λ and the γ: $acc^{\Sigma^0}(p_t, y) = acc^{\Lambda}(p_t, y) \times acc^{\gamma}(\phi, \theta)$. The reconstruction efficiency $\varepsilon^{\Sigma^0}_{rec}(p_t, y)$ is defined as $\varepsilon^{\Sigma^0}_{rec}(p_t, y) = N^{\Sigma^0}_{rec}(p_t, y)/N^{\Sigma^0}_{acc}(p_t, y)$.

The following distributions show the response of the detector from embedding thermal Σ^0 into real data, as it was already used for the Λ baryon efficiency correction with a temperature of $T = 105$ MeV and vanishing blast, polar anisotropies and flow. All selection criteria are included, besides the β- cut on the γ selection due to the large deviations between experimental and simulated response of low energy γ in the electromagnetic calorimeter. Therefore the following chapter is explaining the determination of additional correction factor ε_β which is extracted from leptons in a data driven approach.

7.2 ECal γ Efficiency Determination

The selection cuts for photons cluster size, polar angle ϑ, energy and cluster-track matching quality are corrected for using the same cuts in simulation. The β- cut however, as it can be seen in section 4.7 is not well reproduced in the simulations. Thus, a data driven correction is applied. In simulations, the timing resolution of the ECal is independent on the deposited energy and does not suffer from any instabilities within the beamtime and calibrations like the time walk correction. Therefore extracted efficiency values are not reproducing reality. Thus, all following efficiency values are purely extracted from experimental data which also has the advantage to include losses due to missing hardware for certain periods of

time. Two different methods will be described to calculate the efficiency and estimate the uncertainties. Both methods rely on additional information provided by leptons which behave very similar to photons in the electromagnetic calorimeter.

Approach via Lepton Efficiency

Electrons are perfect probes for testing the response of the electromagnetic calorimeter, since the signals of electrons, positrons and photons are indistinguishable in the ECal. For this reason, leptons were used for the calibration of the detector and thus can be utilized to determine the efficiency. Therefore a sample of electrons was selected by the default lepton selection criteria (see section 4.8), which take the response of the MDCs, the META detector and most importantly the hadron blind RICH into account. Since the RPC is located directly in front of the ECal, only leptons which obtain their timing from the RPC were used, neglecting leptons with time of flight, measured by the ToF. From this sample, only those leptons which have a matched ECal cluster within a $2\,\sigma$ deviation from the Runge-Kutta extrapolation are used further. For this data driven efficiency correction, it is important to take the whole data set into account to avoid time dependent fluctuations of the efficiency and really obtain the integrated value for the data which was analyzed.

In addition, those ECal clusters have to fulfill all selection criteria which are applied for the photons, besides obviously neglecting the track-matching and the velocity selection.

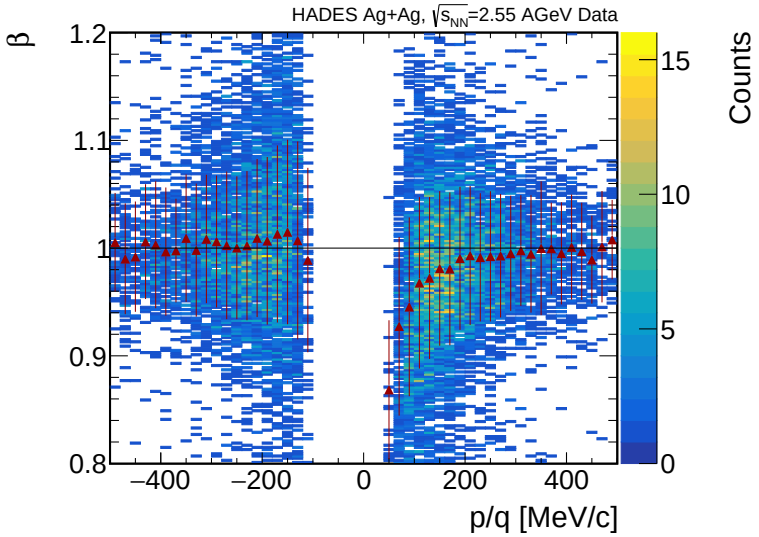

Figure 7.1: Reconstructed β of leptons in the electromagnetic calorimeter with respect to their momentum, separately shown for electrons and positrons. The lepton selection criteria are written in the text.

In figure 7.1 only leptons are plotted for which an additional Λ candidate was reconstructed in the event, to be as independent from any angular emission as

possible. The distribution was compared to a distribution where no additional Λ was requested. No significant deviation from each other is seen.

Obviously, the distributions differ quite substantially for electrons compared to positrons. Besides the different acceptance borders, which allow for positron reconstruction down to $p \approx 70\,\text{MeV/c}$ but for electrons down to $p \approx 110\,\text{MeV/c}$ only, the β distribution is looking rather flat. However, an increase of β with momentum is visible for positrons.

This behavior is based on the time walk calibration, which was used for the experimental data and which is still imperfect for the analyzed data set from March 2019. Possible improvements which will be used for further collected data are described in appendix B.6.

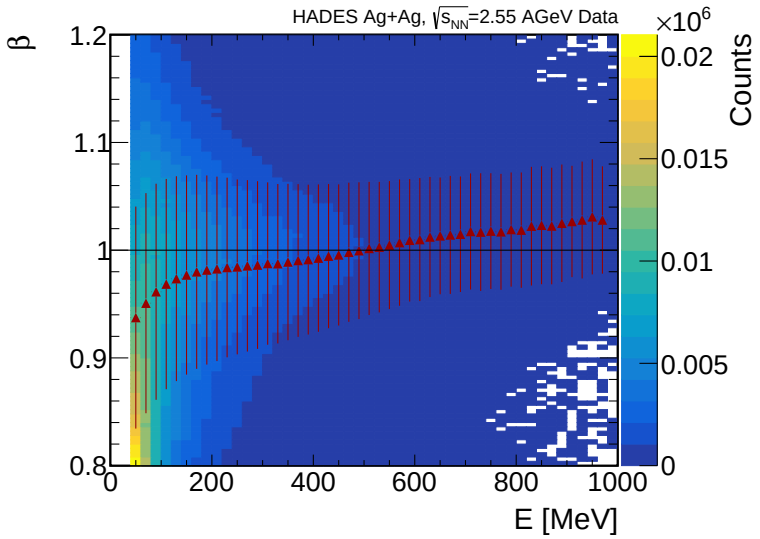

Figure 7.2: Reconstructed β of photon candidates in the electromagnetic calorimeter with respect to their energy. Selection criteria as described in the text.

The increase of β with increasing deposited energy in the electromagnetic calorimeter is also visible for γ candidates as displayed in figure 7.2. Here the standard photon selection from chapter 4.7 applied, besides neglecting the energy cut. The distribution is looking similar to the distribution of positrons, but due to the enhanced background in the γ sample compared to the lepton sample, the widths represented as the error bars are slightly larger for the γ sample.

The distribution of positrons and photons which are extracted from experimental data are overlayed in figure 7.3.

The deviations from $\beta = 1$ for photons which are caused by the imperfect time walk correction are large for small energies below 100 MeV. For large energies β values for photons are rising linearly. Both distributions are in reasonably good agreement for the energy regime of the γ which origin from Σ^0 decays. Their reconstructed mean energy is indicated as green line. Due to the larger background contribution in the γ sample, the distribution widths are larger for photons compared to the lepton sample. As the lepton sample is more pure, those β values,

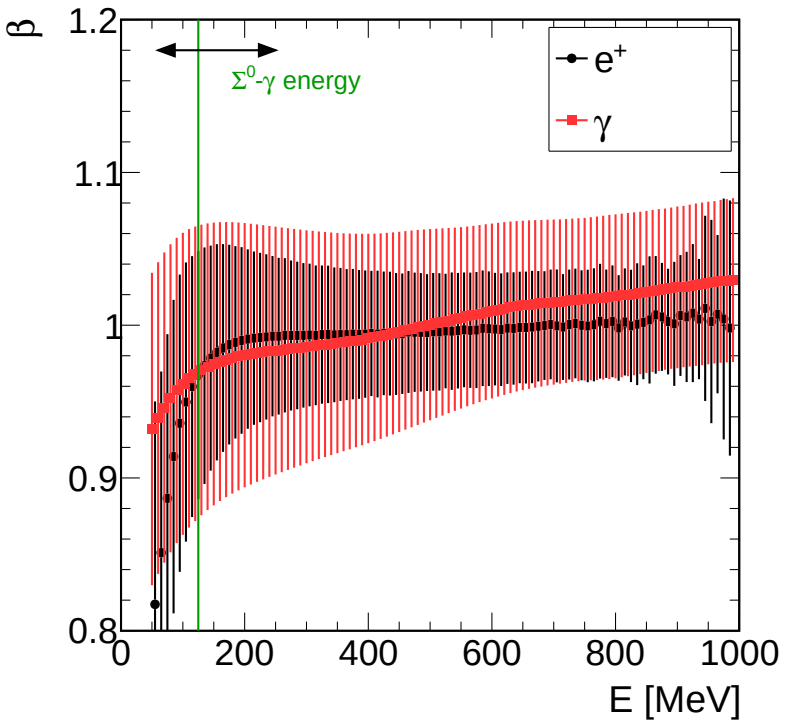

Figure 7.3: Comparison of the positron and photon energy dependency of β in the ECal. The γ distribution in red is shifted by half a bin to smaller values for visualization purposes of the width. The black arrow indicates the total region of accepted photon candidates for the final Σ^0 reconstruction.

mean and width are used for efficiency corrections. In both cases, the resolution is decreasing with decreasing energy.

The efficiency is estimated by applying this β cut on the sample of selected positrons and calculating the loss according to the width of the β distribution. The resulting energy dependent efficiency is shown in figure 7.4, the β cut on data from the electromagnetic calorimeter is applied on a lepton sample. Herby the leptons have to fulfill all criteria as mentioned in chapter 4.8. While the black distribution shows lepton efficiencies for those fulfilling the previously mentioned standard lepton selection criteria, the red distribution includes a more strict lepton selection, requesting matching qualities to be on the highest level: $\chi^2_{RICH} < 1.5\,^\circ$, $\chi^2_{RPC} < 1.5\,\sigma$ and $\chi^2_{ECal} < 1.5\,\sigma$, which provides very clean lepton sample while minimizing any contributions of mismatches. For both cases, only leptons which obtain their time of flight information from the RPC are taken into account. The distributions are fitted with a polynomial of fourth order. The mean energy of the γ from Σ^0 decays which pass all selection criteria, is at $E_\gamma = 125$ MeV and is represented as green vertical line. While at low energies the distributions for the two scenarios are very similar, more strict cut on the lepton sample results in a larger efficiency for high momenta. This hints to a background contamination for the lepton sample at larger energies starting around

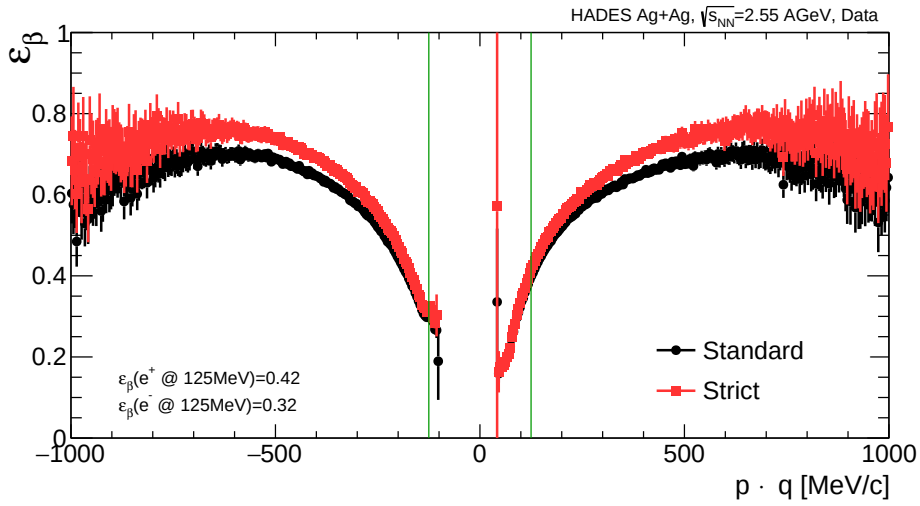

Figure 7.4: Efficiency estimation of the β selection of the photon candidates in experimental data, extracted from leptons. More details are written in the text.

$500\,\mathrm{MeV/c}$ [1].

The β calculation itself is also subject to errors. In particular, the path is not straight from the vertex, unlike the photons. Different methods of the path length calculations for e^+ and e^- (see below) change β and thus change the efficiency of the β-cut by $2\,\%$. A further uncertainty stems from the path calculation within an ECal cell. In particular for the inner cells, leptons enter not perpendicular to the outer surface but under an angle due to the bending from the magnetic field. This thus might influence the response of the ECal cell. Detailed analysis regarding the track length discrepancy were presented earlier [207].

The largest uncertainty, however is determined by the imperfection of the background description of the β cut window using photons as described in chapter 4.7 and thus possible shifts within the timing spectrum as well the differences in total path length of leptons and photons. Those uncertainties can not be distinguished further and lead a relative combined uncertainty of 20% of the photon β efficiency.

The removal of the path length differences of e^+ and e^- and thus also from the photons are performed via comparison of the width of the beta distribution σ which is extracted for different energies in figure 7.5.

Using the fact that leptons and photons behave the same in the ECal, we can use well defined leptons to quantitatively describe the energy dependence of the timing resolution. For a high purity, only leptons with a RICH matching of $RM < 1^\circ$ are taken into account. In addition, only leptons are taken into account where the extrapolated path length of the lepton within the ECal glass module is larger than $L > 100\,\mathrm{mm}$ to avoid distortions from bended leptons contributing

[1] Traversing hadrons deliver an energy deposit of around $500\,\mathrm{MeV/c}$, independent on their energy.

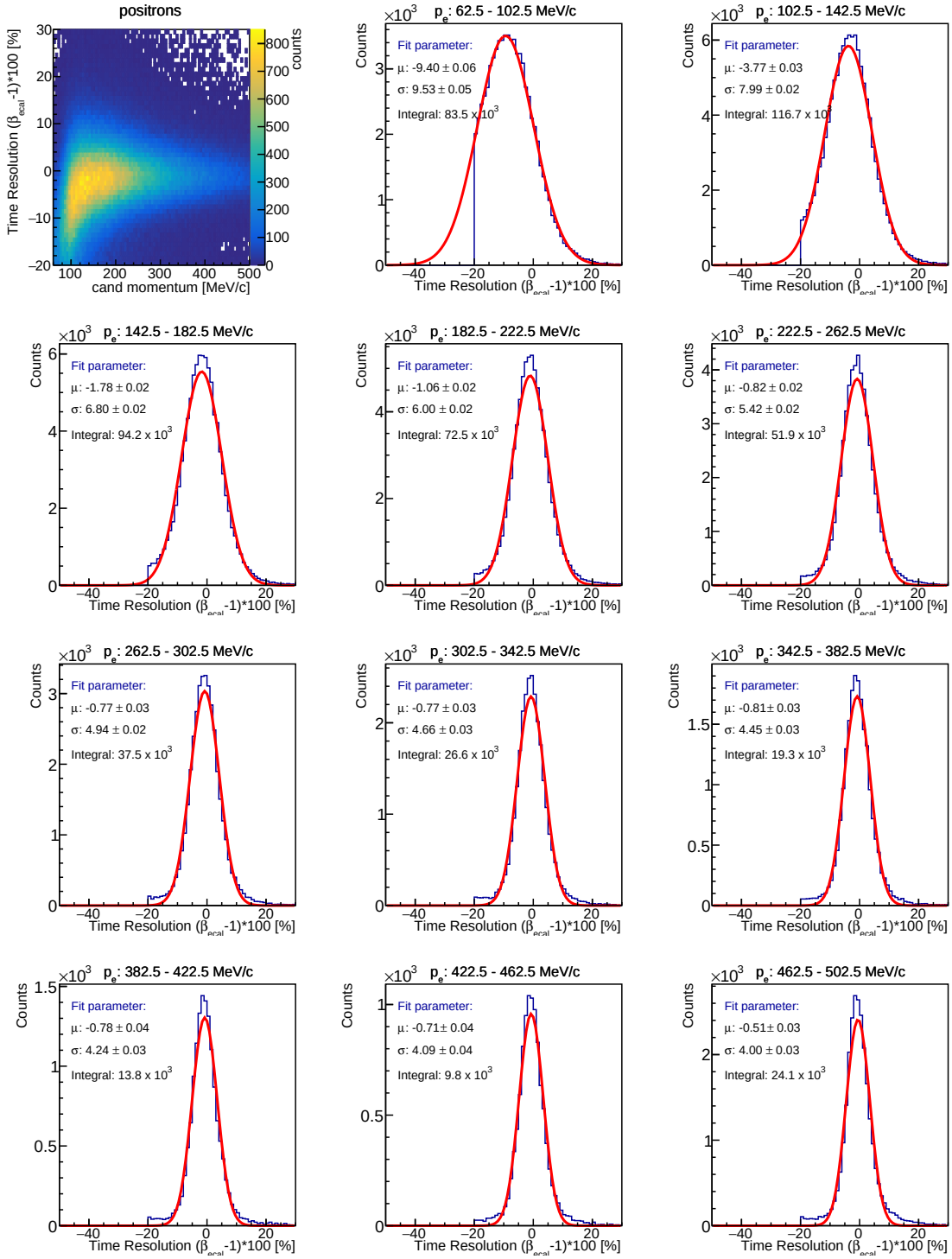

Figure 7.5: Timing resolution of the ECal in percent expressed as $(\beta - 1)$. Plots are shown for e^+ in dependence on their momentum.

to several cells. As visible in figure 7.5, this selection combined with the limited ECal acceptance of only two sectors, features only limited statistics, but the background suppression is outstanding. The purity of the positron sample exceeds $99\,\%$ and is the main advantage for this method. Additionally, this method is independent on the ECal energy calibration since the momentum of the leptons is obtained by tracking provided by the MDCs. The agreement between ECal and tracking is requested to be $|p_e^{MDC} - E_e^{ECal}|/p_e^{MDC}$ <20%. Figure 7.5 shows the dependence of the time resolution of the positrons on their momentum. The picture in the top row on the left displays the correlation in 2 dimensions, while the following figures are projections on the timing resolution axis in steps of Δp=40 MeV/c. The resulting energy dependent width of the timing resolution is shown in figure 7.6.

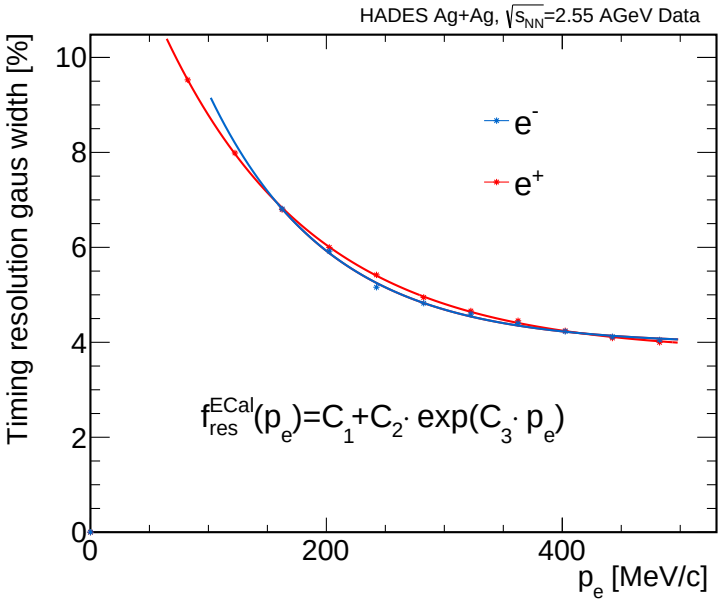

Figure 7.6: The timing resolution of the electromagnetic calorimeter for e^+ and e^- in dependence on their momentum, which was measured by tracking in the MDCs. The positron acceptance reaches to lower momenta.

In addition to the e^+, also e^- are fitted with the same procedure and deliver a similar behaviour of the timing resolution. The major difference is the missing acceptance for low energy electrons, which results in missing data below $p = 165$ MeV/c.

The advantage of this method is the independence on any systematic shift in the β calculation caused by imprecise calibration or track length calculations for the distance of curved tracks in between the RPC and the ECal. For this reason, the width of e^+ and e^- show the same trend and allow a comparison of the width for the energy above 500 MeV for e^-, e^+ and photons. Since the methods allows charge independent time resolution evaluation, it is used to extract the resolution at E $= 125$ MeV which is the mean photon energy for the reconstructed Σ^0 yields:

$$R = \frac{f_{res}^{e^+}(125\,MeV/c)}{f_{res}^{e^+}(500\,MeV/c)} \Big/ \frac{f_{res}^{e^-}(125\,MeV/c)}{f_{res}^{e^-}(500\,MeV/c)} = 0.997 \tag{7.1}$$

As this ratio is remarkably close to 1, this hints to a good understanding of electrons and positrons, in particular of impact of the different track length of them between RPC and ECal.

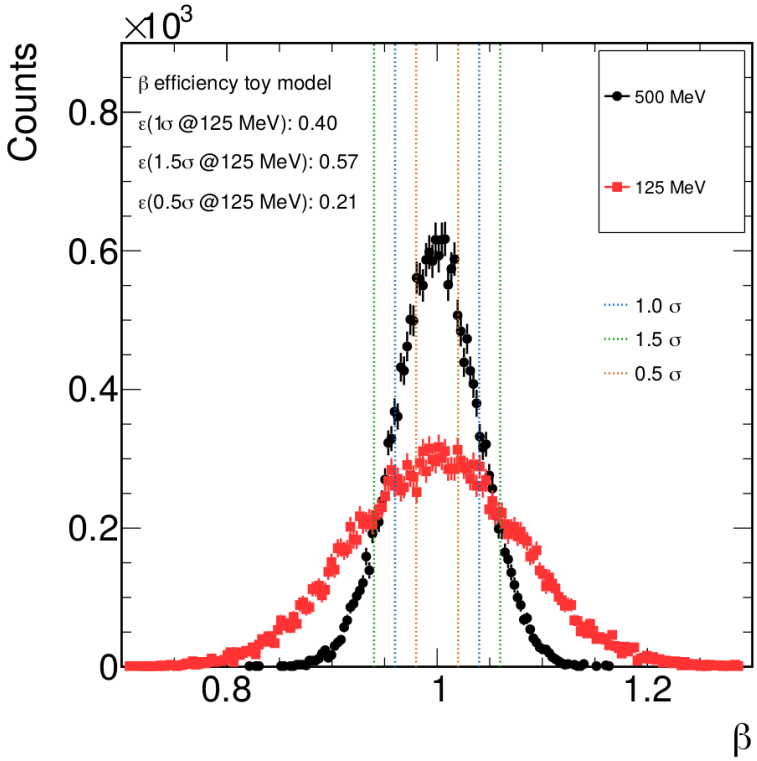

Figure 7.7: Theoretical prediction of the efficiency of 125 MeV photons by calculation from the energy dependent β resolution which was extracted from the leptons.

In figure 7.7 the black points are a generated data sample showing the β distribution of leptons of p=500 MeV using the timing resolution extracted before. The red spectrum represents the β distribution at p=125 MeV. The vertical dashed lines represent the 0.5 σ, 1.0 σ and 1.5 σ regions of the black distribution. Applying those fixed criteria to the spectrum also at $p = 125$ MeV delivers a β cut efficiency of $\varepsilon_\beta = 0.40$ for a 1 σ cut which is the very close to the efficiency calculated from figure 7.4.

7.3 Results

The superior aim of this analysis is the extraction of the Σ^0 baryon multiplicity at the most central Ag+Ag collisions at a center of mass energy of $\sqrt{s_{NN}} = 2.55$ GeV,

corresponding to a kinetic beam energy of 1.58 AGeV. Due to the similarity of Σ^0 and Λ, many systematic uncertainties of the Σ^0 multiplicity estimation can be neglected when the ratio $R_{\Lambda/\Sigma^0} = \Lambda/\Sigma^0$ is inspected. Several transport models expect the phase space distribution of Λ and Σ^0 to be very similar. Thus, all model dependent phase space distribution uncertainties of the Λ and Σ^0 cancel out which leads to the following equation for the efficiency and acceptance corrected ratio of Λ/Σ^0:

$$\frac{N_\Lambda}{N_{\Sigma^0}} = \frac{N_{\Lambda_{rec}}}{N_{\Sigma^0_{rec}}} \frac{\varepsilon_{\Sigma^0}}{\varepsilon_\Lambda} \tag{7.2}$$

The efficiency always consists of the reconstruction efficiency and the overall acceptance $\varepsilon = \varepsilon_{rec} \times acc$. The Σ^0 efficiency itself can be expressed as the efficiency of the Λ baryon and the γ efficiency ε_γ which itself consists of the acceptance, the reconstruction efficiency from the simulation and the additional efficiency of the β cut which is extracted from experimental data. Obviously the main efficiency correction stems from the photon, since all other efficiencies cancle out.

$$\varepsilon_\gamma = acc_\gamma \times \varepsilon_\gamma^{rec} \times \varepsilon_\gamma^{\beta} \tag{7.3}$$

By this definition, the overall Σ^0 efficiency can be expressed as

$$\varepsilon_{\Sigma^0} = \varepsilon_\Lambda \times \varepsilon_\gamma = acc_\Lambda \times \varepsilon_\Lambda^{rec} \times acc_\gamma \times \varepsilon_\gamma^{rec} \times \varepsilon_\gamma^{\beta} \tag{7.4}$$

with the following relation

$$\varepsilon_\gamma = \frac{\varepsilon_{\Sigma^0}}{\varepsilon_\Lambda} \tag{7.5}$$

Including all this in equation 7.2, the finally used formula reads

$$\frac{N_\Lambda}{N_{\Sigma^0}} = \frac{N_{\Lambda_{rec}}}{N_{\Sigma^0_{rec}}} \varepsilon_\gamma \tag{7.6}$$

This assumption holds true with only small uncertainties of $4.7\,\%$ when comparing the acceptance of photons with the acceptance of photons when the Λ is required to be within the detector acceptance as well. In this work $\varepsilon_\gamma^{\Lambda_{acc}}$ was used. The nominator N_Λ refers to the amount of Λ baryons which are used for Σ^0 reconstruction. This excludes all Λ candidates with a reconstructed mass below $M_{inv}(p\pi^-) < 1110\,\text{MeV/c}^2$ as well as all candidates with $M_{inv}(p\pi^-) > 1120\,\text{MeV/c}^2$ which corresponds to roughly 2σ of the Λ invariant mass distribution being purely dominated by detector resolution. For the amount of reconstructed N_{Σ^0}, the estimated signal in the $\Lambda\gamma$ spectrum within a 2σ region around the mean is taken into account. This leads to an additional correction of 4.8% to correct from 2σ to a total integrated value.

As final calculation of the Λ to Σ^0 ratio we end up with

$$\frac{N_\Lambda}{N_{\Sigma^0}} = \frac{3.12 \cdot 10^6}{8.19 \cdot 10^3 \cdot 1.048} \cdot 0.028 \cdot 0.40 = 4.2 \pm 0.9 \tag{7.7}$$

This number of course includes all Λ from Σ^0. Being interested in a ratio which distinguishes between Λ generated as such "at freeze out" and those from Σ^0 decays, the following is done:

After extracting the Σ^0 multiplicity and the integrated ratio of N_Λ/N_{Σ^0}, the Λ to Σ^0 ratio at freeze-out is calculated by subtracting all reconstructed Λ candidates which originate from the Σ^0. This is providing the largest Λ contribution from feed-down compared to other sources at HADES energies around the Λ threshold. By this consideration the freeze-out ratio $R_{f.o.}(\Lambda/\Sigma^0)$ is calculated by

$$R_{f.o.}(\Lambda/\Sigma^0) = \frac{\Lambda - \Sigma^0}{\Sigma^0} = R(\Lambda/\Sigma^0) - 1 = 3.2 \pm 0.7 \tag{7.8}$$

This ratio is compared to theoretical model predictions from transport models and statistical model approaches in chapter 8. In combination of the Λ/Σ^0 ratio and the precise multi differential Λ multiplicity extraction in chapter 5.4, the Σ^0 multiplicity can be extracted for the most central 0-40$\%$ Ag+Ag collisions as

$$M(\Sigma^0) = M(\Lambda)/R(\Lambda/\Sigma^0) = (0.014 \pm 0.002_{stat.} \pm 0.004_{sys.})/\text{Event} \tag{7.9}$$

This method provides a multiplicity estimation, which is robust to model dependent phase space distributions. As pointed out in section 6.3, the differences induced by this phase space distribution is smaller $5\,\%$. This is even more important since the generated PLUTO phase space distribution, e.g., differs substantially from the transport models as shown in figure 7.8.

Those differences in rapidity clearly show the necessity of the multi differential phase space analysis of the Λ which is taken into account for all Σ^0 multiplicity estimations [2]. In addition, the extracted result is in good agreement with the measurement in the Λe^- channel, which due to the large statistical and systematic uncertainties delivers only a rough estimate of $M(\Sigma^0) = (0.010 \pm 0.003_{stat} \pm 0.006_{sys})/\text{Event}$.

This analysis presents the first Σ^0 production rate in heavy ion collisions at low energies, in particular even below the corresponding nucleon-nucleon production threshold. The measurement thus provides insight in additional medium modifications and multi step processes in heavy ions collisions which differs from the available measurements from Σ^0 production in p+p collisions.

[2]The PLUTO Σ^0 distribution was generated without additional blast, which results in a more narrow rapidity distribution

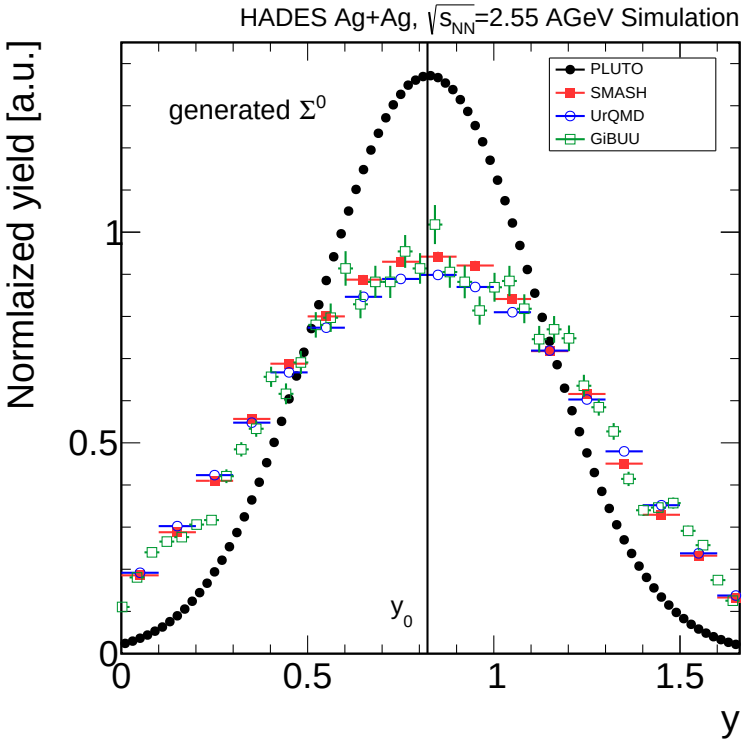

Figure 7.8: Rapidity distribution of the generated Σ^0 from different simulation models. The PLUTO distribution which is used for the embedding into real data differs to the overall consistent transport models.

CHAPTER 8

Comparison to Theory

8.1 Statistical Hadronization Model

As pointed out in chapter 1.7.1, the statistical hadronization approach is successfully used in a wide range of center of mass energies ($\sqrt{s_{NN}}$) in heavy ion collisions. The simple consideration of all hadrons being produced in a thermally equilibrated hadron gas thereby differs significantly from microscopically calculated transport approaches. The thermal model calculations in this thesis were performed with Thermal-FIST [132], which includes a more accurate description of resonances, compared to THERMUS [208]. For strangeness production at low energies, e.g. the SIS18 regime, the ensemble is chosen to be a strangeness canonical one. This ansatz requires strangeness to be strictly conserved within a small sub-volume of the collision, called the strangeness canonical volume of radius R_C. This canonical ensemble thus describes the particle multiplicities with exactly conserved quantum numbers in a locally determined region [209]. This additional requirement suppresses strangeness production compared to the expected value from the full reaction volume V and leads to a better description of the experimentally measured data.

Another option of the description of additionally reduced strangeness production at small $\sqrt{s_{NN}}$ is the usage of a strangeness suppression factor [210]. This is neglected in this thesis.

For the following calculations, Thermal-FIST was used which includes the particle lists from the PDG data base 2020. This increases precision compared to the previously available data sheets. The most naive assumption of an ideal hadron resonance model without extended hadron volumina was applied. Breit-Wigner resonance widths are fixed to be energy dependent. Constant branching ratios without an additional energy dependence were used for the fitting procedure. The overall ratio of electromagnetic charge to baryon charge is predetermined by the Ag+Ag system and thus fixed to a value of $Q/B = 0.44$. The energy dependent Breit-Wigner is used in this work. It is not capable of describing the $\Delta(1232)$ width and the influence of neglecting the Δ resonance width is analyzed in great detail in reference [211]. The uncertainty in the $\Delta(1232)$ resonance width which is rising up by uncertainties by any kind of πN interaction is neglected by

forcing its width to be zero. The influence on the uncertainty of the fit parameters of this width is within the fit uncertainties as shown in [212].

Particle	Multiplicity	Uncertainty	Reference
N_{part}	161	13	[213]
p	77.8	8.0	[214]
π^0	11.85	1.1	[195]
π^+	9.6	0.7	[215]
π^-	13.9	1.3	[215]
Λ	0.12	0.0041	this work
η	0.253	0.08062	[195]
K^+	0.086	0.014	[216]
K^-	0.00137	0.0001533	[216]
K_s^0	0.045	0.0015	[214]
Φ	0.000382	9.3e-05	[216]
Ξ	6e-5	2.5e-5	[214]
Σ^0	0.028	0.006	this work

Table 8.1: Measured hadron multiplicities from the 0-10% most central HADES Ag+Ag collisions with an up-scaled amount of protons to account for the unfitted light nuclei. More details are written in the text.

For the fitting procedure of the 0-10 % most central HADES Ag+Ag data at 1.58 AGeV beam energy, multiplicities stated as in table 8.1 are used. The mixed-canonical ensemble is used, which as pointed out earlier, introduces the strangeness-chemical potential to the grand canonical.

Values for the Λ and Σ^0 hyperons are taken from this work. The Λ yield was measured in the $0-10\,\%$ most central events while for the Σ^0 yield, a centrality independent ratio of Λ/Σ^0 was assumed to scale the Σ^0 yield which was extracted in the $0-40\,\%$ most central events. The amount of overall participants is provided in [213]. The proton yield is taken from [214], as well as the amount of K_s^0 and Ξ^-. Values for the rare hyper-nuclei Hypertrition and Hyperhydrogen-4 are not used for the following fitting procedure at all, although being available [214]. Charged pions and light nuclei are taken from [217] with minor optimizations [215]. The yield for the charged kaons are taken from [216] while the estimation of π^0 and η mesons are taken from the 4-electron analysis in [195].

In general, handling of the light nuclei is treated in two separate ways: Either the light nuclei are reconstructed and fitted, or the amount of measured protons

has to be scaled up for the missing fraction of protons, which is bound in light nuclei. Especially the lightest bound nuclei, the deuteron, is contributing the most with containing roughly $\approx 20\%$ of all protons. In table 8.1, the up-scaled value for the protons is shown, accounting for the fraction of protons in light nuclei. The unscaled values is stated in the appendix in table A.14.

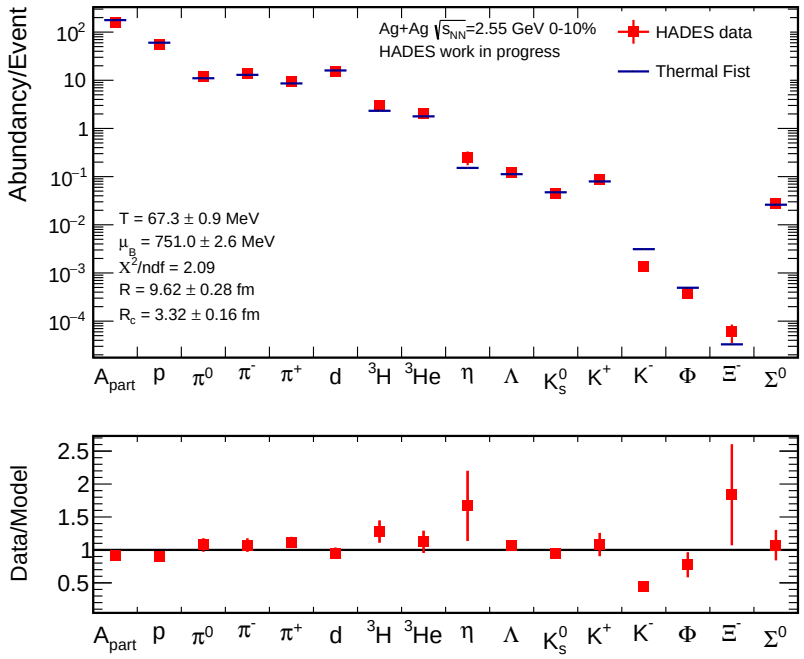

Figure 8.1: Fit with Thermal-FIST of the combined HADES data for the 0-10% most central events of Ag+Ag collisions in the upper plot and the resulting ratio of experimental data to the model predictions below. The K^- is excluded from the fitting procedure. The light nuclei are included in the fitting procedure. More details are written in the text.

The values for the fitting procedure without light nuclei are summarized in table 8.1 while the light nuclei multiplicity with unscaled amount of protons is listed in table A.14 for completeness. In figure 8.1 the light nuclei are included in the fit, while in figure 8.2 the they are excluded. The statistical model fits were done without using the K^- meson, since the K^- has been proven to be not produced in thermal equilibrium, but a large fraction of K^- of about 15-25 $\%$ is produced by feed-down from ϕ meson decays in heavy ion collisions at SIS energies [218][216]. The influence of the K^- to those fits would be important for the description of the overall strangeness production. Its inclusion to the fits is shown in appendix A.15.

Including the Σ^0 to the fit does not influence the resulting parameters, differing only in the order of 0.1%. With one additional free parameter the resulting χ^2/ndf is 2.33.

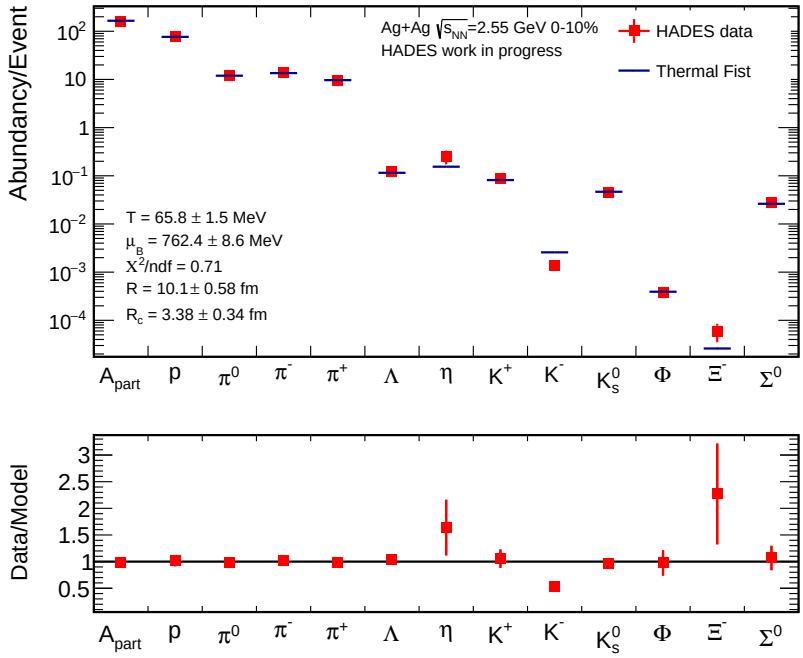

Figure 8.2: Fit with Thermal-Fist of the combined HADES data for the 0-10% most central events of Ag+Ag collisions in the upper plot and the resulting ratio of experimental data to the model predictions below. The K^- is excluded from the fitting procedure. The light nuclei are not included in the fitting procedure. More details are written in the text.

Instead of the strangeness-suppression radius R_C, the strangeness-suppression fugacity factor γ_s is tested as well. The factor γ_s describes the production probability of $\gamma_s = (2s\bar{s})/(u\bar{u} + d\bar{d})$ which thus is in the range of $0 \leq \gamma_s \leq 1$ [219]. In a collision with perfect strangeness equilibrium, $\gamma_s = 1$ is expected while the suppression factor decreases for small $\sqrt{s_{NN}}$ as for the SIS18 energy regime [220]. For consistency, all previously extracted parameters T, μ_B, R are fixed in Thermal-FIST and only γ_s is fitted, resulting in a $\gamma_s = 0.13$. Even with a good $\chi^2/ndf = 2.35$, this value has to be handled carefully, since the ϕ production is underestimated by 3.2σ while at the same time the K^- yield is overestimated by 4.2σ.

When all parameters are freely fitted, the result is $\gamma_s = 0.13$ with a nonphysical volume of 995 fm^3 and $\chi^2/ndf = 2.33$. Thus the description in terms of γ_s is still imperfect with uncertainties on the order of $\Delta\gamma_s = 0.1$. This is still significantly lower than the expectation of $\gamma_s \approx 0.5$ from the parametrization in [221].

8.2 Transport Model Calculations

In addition to fits with the statistical model, additional transport model predictions were calculated. Besides the total particle production yield, these models allow for differentiation in phase space. This allows to compare results also for kinematic parameters and not only integrated values.

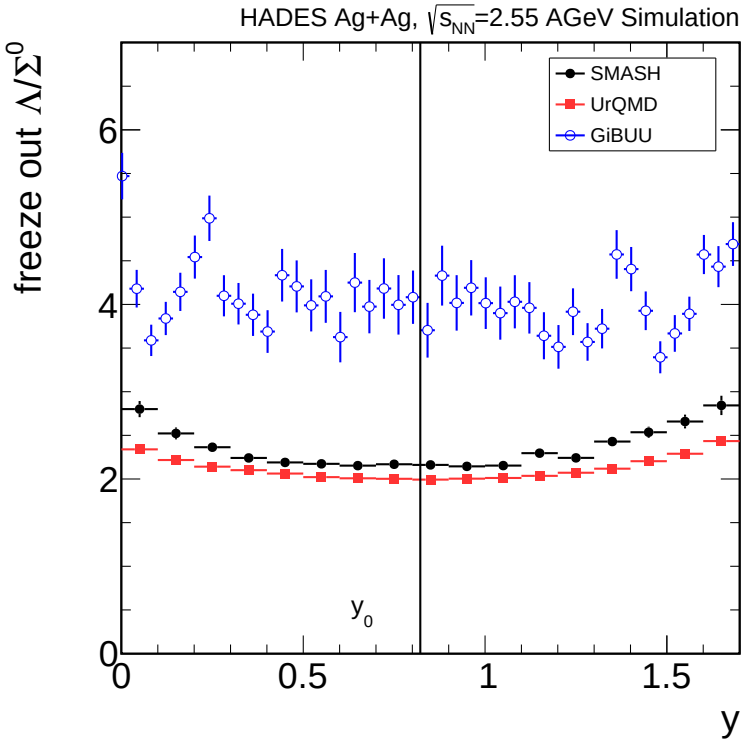

Figure 8.3: Transport model predictions for the Λ to Σ^0 ratio in dependence on rapidity for 0-40% most central Ag+Ag collisions at $\sqrt{s_{NN}} = 2.55$ GeV. The rapidity integrated value from data lies at 3.2 ± 0.7.

The ratio of Λ/Σ^0 at freeze-out is plotted in figure 8.3 as function of rapidity. In this plot, the results from SMASH (v3.0) [222], UrQMD (v3.4) [135] and GiBUU (r2021_01) [140] are overlayed. Compared to the model predictions from SMASH and UrQMD which are in good agreement to each other, there is a clear difference to the GiBUU which shows values larger by a factor of approx. 2. All three models tend to a rather constant behavior of Λ/Σ^0 in terms of rapidity. Especially around mid-rapidity which is visualized as vertical black line, all distributions are flat. For distances of $|\Delta y| = y - y_0 > 0.5$ from mid-rapidity, a slight increase is visible for UrQMD and SMASH which is not influencing the integrated result due to the small contributions from those regions. Overall, the stability of Λ/Σ^0 versus rapidity is promising to not introduce errors in the extrapolation. This is impor-

tant, since the integrated Σ^0 yield is extracted from Λ analysis assuming similar phase space distributions.

CHAPTER 9

Discussion

9.1 Strangeness Balance

Strangeness balance calculations utilize strangeness conservation within the strong interaction, in order to predict particle multiplicities, even for unmeasured particle species [1]. Heavy ion collisions start with a system without net strangeness and thus also the final state has to have an equal amount of s and $\overline{s}$ quarks. The baryonic matter asymmetry at SIS18 energies and thus the missing energy for anti-baryon production leads to the fact, that nearly no baryons with $\overline{s}$-quarks are produced. This means that all $\overline{s}$-quarks form mesons. Assuming that due to the large net-baryon density most of the s-quarks end up in baryons, K^- production is neglected for this estimation. Summing up the most common net-strangeness (s-quark) containing baryons thus provides a rough estimate of the total strangeness production:

$$N(s) = N(\Lambda) + N(\Sigma^+) + N(\Sigma^0) + N(\Sigma^-) \tag{9.1}$$

As $\overline{s}$-quarks are assumed to show up in mesons only, the number of produced $\overline{s}$-quarks is expressed as

$$N(\overline{s}) = N(K^0) + N(K^+) \tag{9.2}$$

Assuming identical production rates of $N(K^0_L) = N(K^0_S)$, in equation 9.2, K^0 can be expressed as $2K^0_S$, which is experimentally measured.

With production rates of the listed particles on the order 10^{-2} per event in most central Ag+Ag collisions at $\sqrt{s_{NN}} = 2.55$ GeV, Λ, Σ as well as the positively and neutrally charged kaons are still at least two orders of magnitude more common than any other strangeness containing hadron, namely Ξ, Ω or K^-. Hence the latter are neglected. Since the reconstructed Λ-baryons naturally contain all Σ^0 baryons, all Σ states can be expressed by the measured Λ multiplicity.

Σ^0, Σ^+ and Σ^- baryons are weighted accordingly with the isospin asymmetry of the enhanced amount of down-quarks compared to up quarks due to the N/Z ratio in Ag.

[1] This method has already been applied to previous HADES data [101].

Centrality	Production rate [10^{-2}]				Σ^0/Λ
	Λ	Σ^+	Σ^0	Σ^-	
0-10%	10.09	2.20	2.39	2.60	0.24
10-20%	6.00	1.36	1.48	1.61	0.25
20-30%	3.47	0.90	0.98	1.06	0.28

Table 9.1: Summary of the strangeness balance consideration which was calculated in [214] based on the measured Λ rates, including the isospin asymmetry existing in Ag+Ag collision. The given Λ rate excludes Λ from Σ^0 decays.

In table 9.1, the value for the reconstructed amount of $\Lambda + \Sigma^0$ is consistent within the stated errors to the multiplicity which is extracted in this thesis in chapter 5.4. The values in table 9.1 are calculated from the measured $\Lambda + \Sigma^0$ multiplicity as well as the K_s^0 multiplicity only.

The averaged ratio of $\Lambda/\Sigma^0 = 4.0 \pm 0.1$ for the most central $0 - 30\%$ of the collisions shows a small centrality dependency. This effect has already been seen in the strangeness balance consideration of the K states [214]. The predicted Λ/Σ^0 ratio is slightly larger than the ratio measured in this thesis (3.2±0.7), even with consideration or the large errors in the measured data. A possible explanation for the difference of the measured ratio to the ratio estimated under isospin considerations are additional nucleon-hyperon interaction within the created hot and dense matter. Isospin exchange reactions can take place in the form of

$$Y_1 N \rightarrow Y_2 N \tag{9.3}$$

where Y_1 is either a Σ^0 or a Λ and Y_2 the opposite particle while the participating nucleus N in initial and final state is either a proton or a neutron. This reactions could re-distribute Λ to Σ^0 assuming that created Σ^0 decay before another interaction could take place. In addition, this simplified strangeness balance does not account for the different masses of the baryons, which especially for Λ and Σ^0 close to threshold may play a crucial role.

9.2 Comparison to Existing World Data and to Theoretical Models

As mentioned in chapter 1.6, the simultaneous measurement of Λ and γ is challenging in order to reconstruct the Σ^0. Thus, there are not many data points for Σ^0 multiplicities available. Especially heavy ions reactions which lead to large combinatorial background are challenging. Thus, almost no data is available for A+A collisions while there is more data from p+p, see figure 9.1.

Right now, only data from p+p collisions have been measured at COSY in the energy regime below $\sqrt{s_{NN}} = 3.2\,\text{GeV}$ [124][223][224]. Those data points repre-

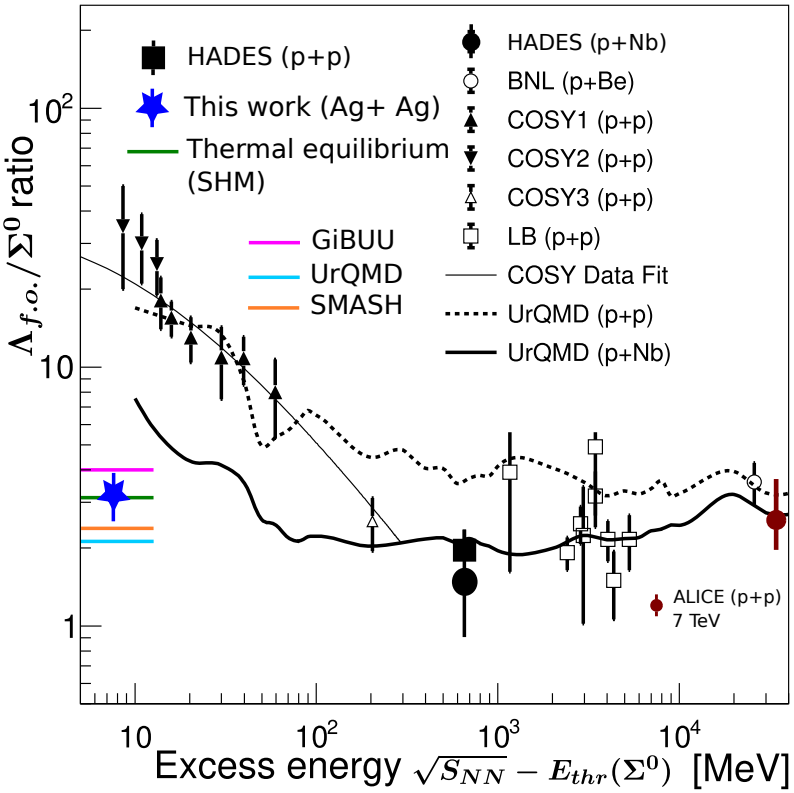

Figure 9.1: Final freeze-out ratio of Λ/Σ^0 baryons in comparison to available world data and theoretical predictions for Ag+Ag collisions at 1.58 AGeV beam energy from thermo-statistical model calculations as well as from several transport models. Figure taken from [121] and the new, additional data points from this thesis as well as data from the HADES [122] and the ALICE experiments [123] are added. The data point from this work is shifted by 80 MeV to larger values for visualization purposes. However, this places this measurement into perspective to the available data. Further information is written in the text.

sent the ratio of the exclusive cross sections of $pp \rightarrow pYK^+$, where Y represents either a Σ^0 or Λ hyperon. Obviously, for the reconstructed data from this work, the inclusive measurement $NN \rightarrow YX$ is accessible and included in the plot. X can contain any possible combination of particles. However, at Λ threshold not much more than the mentioned exclusive channel should be open.

HADES already contributed to the world data with a measurement from pp collisions at a kinetic energy of 3.5 GeV and p+Nb collisions at the same energy [121] [122]. Also here, the data point from pp collisions represents the exclusive ratio of cross sections $\sigma(pp \rightarrow p\Lambda K^+/pp \rightarrow p\Sigma^0 K^+)$. The p+Nb data point describes an inclusive measurement.

Additional data from p+p collisions in the intermediate energy regime of excess energies of $\epsilon_{\Sigma^0} = 1 - 5$ GeV are collected in Landolt-Börnstein [225]. Data from Alice [123] is from an inclusive measurement as well, but on much higher energy. Their measurement underlines, that beyond threshold effects, reaching

out to approximately 100 MeV, the Λ/Σ^0 ratio is rather energy independent.

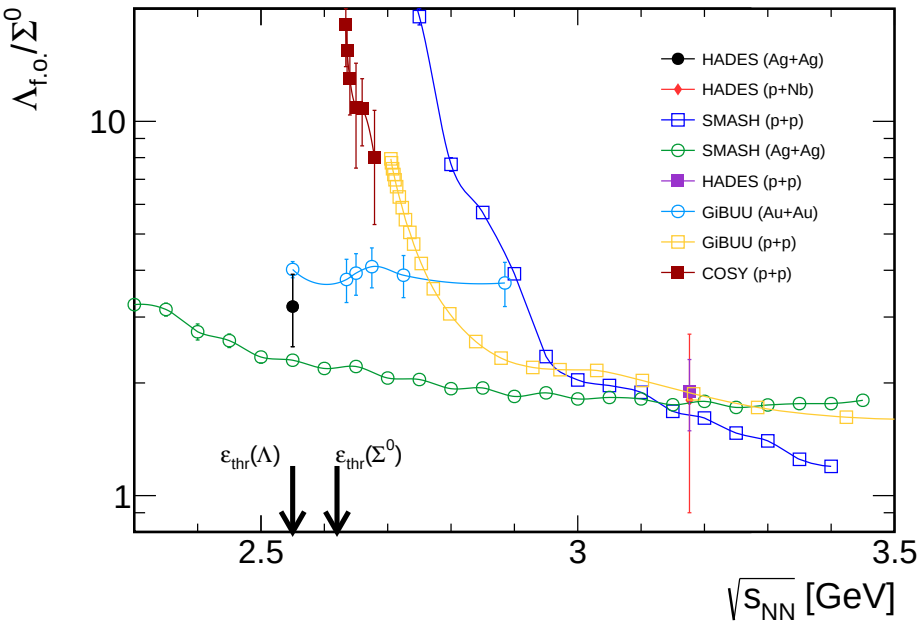

Figure 9.2: Zoom in of the Λ/Σ^0 ratio at freeze-out into the region of small excess energies. The HADES data point now is correctly placed. Additional information is written in the text.

A detailed view of the same data points is seen in figure 9.2, where the x-axis is shown as linear scale and reaches down below the Σ^0 threshold energy of $\varepsilon_{thr}(\Sigma^0) = 2.62$ GeV. The NN threshold values for Σ^0 as well as Λ production are indicated. The Λ threshold is tantamount to the general strangeness production threshold. All experimentally measured data in this figure are displayed with closed symbols, while the additionally added transport model calculations are represented as open symbols. For better visualization, all points from p+p data or simulation are depicted as squares while values from heavy ion collisions are represented as circles. The additional p+Nb data point is presented as diamond.

Measured Λ/Σ^0 ratios in p+p collisions show a strong rise towards the production threshold of Σ^0 which clearly is correlated to the latter and energy conservation. An important result from this work is the observation that obviously the NN-threshold is not relevant for the measured Ag+Ag collisions. Similar observations are known from strangeness production below threshold, as e.g. measured by HADES in Au+Au collisions at 1.23 AGeV beam energy [226] as well as p+Nb at 3.5 GeV beam energy [227]. Interestingly the Λ/Σ^0 ratio seems to be close to the same value as observed for large energies. These features seem to be captured well by the transport calculations, at least qualitatively. In detail, as shown in the previous plot, the data point extracted in this thesis is located directly in between

the transport model estimations of GiBUU [2] and SMASH. For the energy scan of SMASH, only statistical errors are plotted. Strikingly the GiBUU transport simulations of proton-proton collisions in yellow are in good agreement to the experimentally measured p-p data from COSY in dark red, while SMASH overshoots them quite significantly. This is the inverted behavior to the results of simulations of heavy ion collisions. The Λ/Σ^0 ratio which is extracted within this work as first experimental data point of heavy ion collisions in figure 9.2 confirms the qualitative behavior of the transport models, which predicted a rather constant ratio of Λ/Σ^0 in heavy ion collision compared to the steep rise in elementary p+p collisions at high energies.

In addition to the thermal fits as discussed in chapter 8, a more simple consideration assuming or testing thermal production can be made, based on Λ and Σ^0 multiplicities alone. Since all quantum numbers of the Λ and Σ^0 baryons are the same, the temperature of the created hot and dense matter can be estimated by only taking the Λ/Σ^0 ratio at freeze-out into account.

Assuming thermal production, the ratio of the partition function of Λ and Σ^0 which is proportional to the ratio of multiplicities at freeze-out can be approximated as

$$R_{f.o.} = c \cdot \exp\left(\Delta m / T\right) \tag{9.4}$$

Thus, the temperature is calculated as

$$T = \frac{\Delta m}{\ln(R_{f.o.})} = \frac{77\,\mathrm{MeV/c^2}}{\ln(3.2)} \approx 66\,\mathrm{MeV} \tag{9.5}$$

Even within the large uncertainties of the Λ/Σ^0 ratio measurement, this temperature estimation allows a comparison to the statistical model approach in both possible ensembles, the strangeness-canonical and the grand-canonical ensemble without strangeness containing particles [216].

In figure 9.3, results are shown in the μ_b vs. T plane of the phase diagram for various thermal fits of HADES data. In addition, results from other A+A experiments at low energies are added.

The black circle fits used the parametrization of [128], the empty triangles stem from reference [228] while the HADES data of p+Nb and Ar+KCl [229] are fitted with THERMUS [208]. The Ag+Ag data were fitted with Thermal-FIST [132] as extensively described in chapter 8.

The uncertainties of the HADES data are averaged by different fitting approaches in- and excluding excited nuclei. The HADES Λ/Σ^0 data point relies on the uncertainties of the Σ^0 only since the comparable small Λ uncertainties cancel out in the ratio. The HADES Λ/Σ^0 data point is located at a temperature which is $\approx$ 10 MeV below the result from the full statistical model fit. This is consistent within the errors stated for each method individually.

[2] The first GiBUU data point at $\sqrt{s_{NN}} = 2.55$ GeV represents an Ag+Ag simulation, not Au+Au but the qualitative behavior is expected to be the same.

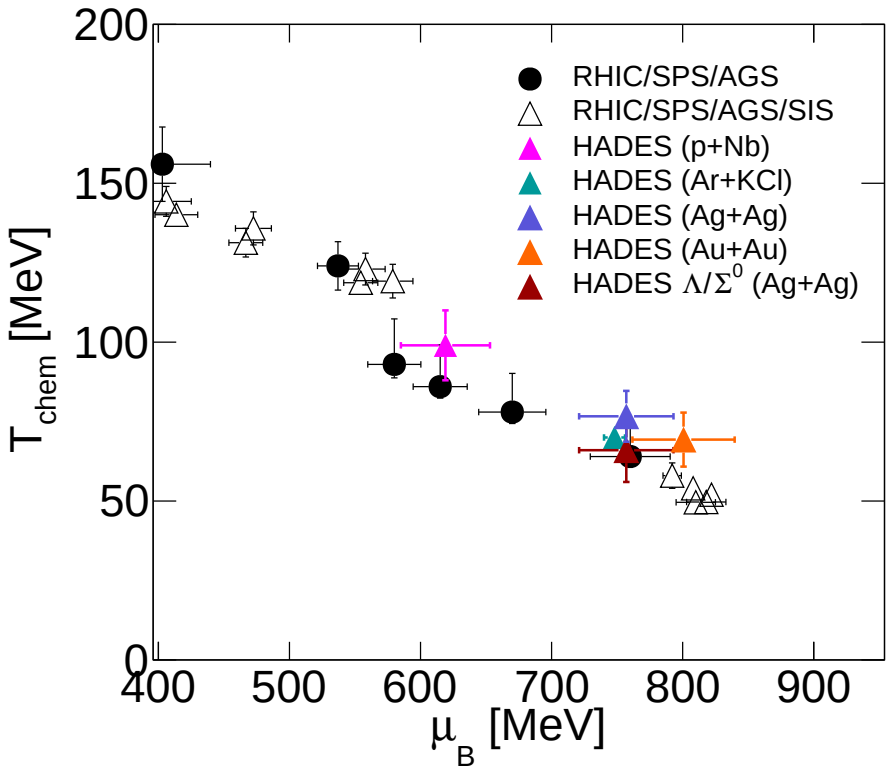

Figure 9.3: Illustration of the location of the freeze-out of heavy ion collisions, as determined by HADES in the $T - \mu_B$ plane of the QCD phase diagram. Modified figure taken from [230] where it was modified from [229]. Further information is written in the text.

In summary, the overall emerging picture is, that particle production including strangeness at HADES energies can successfully be described in a thermal picture. Results on (T,μ_B) values extracted without and with including strangeness are consistent to each other and consistent with a temperature estimate based on the Λ/Σ^0 ratio alone. These results are in line with the finding that the extracted Λ/Σ^0 ratio is within errors the same as in measured high energy p+p collisions and the thermal ansatz at high energies. Obviously, the (sub-) threshold production of Σ^0 baryons in Ag+Ag collisions is not influenced by the NN production threshold.

9.3 Outlook

The new electromagnetic calorimeter as well as the upgrade of the RICH detector in HADES were utilized in this work to study the Σ^0 baryon production. While the upgrade of the RICH was finished for data taking of Ag+Ag collisions analyzed in this work, the electromagnetic calorimeter still only had two out of 6 sectors equipped. By now, all sectors are equipped with lead glass modules and their readout, which will dramatically improve the acceptance for γ reconstruction without relying on conversion. Besides the acceptance, also the energy resolution of the new modules increased for even better performance of γ reconstruction. On top of this improvement, the calibration of the electromagnetic calorimeter timing will be improved as suggested in appendix B.6 for all newly collected data. Even without being able to reconstruct a significant signal in the Λ+lepton channel for this work, the feasibility of reconstructing Σ^0 baryons in this channel was proven. The teaser in chapter 6.2 shows the powerful RICH ability of separating leptons from conversion from leptons of any other source, leading to the opportunity to search for the Dalitz-decay of the Σ^0. This would give insight into the form factor, which has never been measured so far. In addition to Σ^0 baryons, various hyperons will be measured in the p+p data from February 2022 which will give additional insight in hyperon production [231] where the fully equipped ECal is a crucial improvement compared to the existing p+p data from 2007.

The reconstructed freeze-out ratio of Λ/Σ^0 is well fitting to thermal model approaches, while the transport models do show differences. Still, with these new data and first measurement in A+A at low energies, they can constrain their parametrization on hyperon production in (sub-)threshold heavy ion collisions. With the optimized ECal acceptance new measurements will include reduced systematic errors which will also lead to a more precise temperature estimation from the Λ/Σ^0 ratio. As soon as the FAIR facility is operational, the knowledge about the hyperon production will grow when combining the complementary acceptances of HADES and CBM, to understand nuclear matter at high densities which is still an open question in astrophysical descriptions of neutron stars.

APPENDIX A

Additional Figures

A.1 Center-of-Mass Energy

In heavy ion collisions, the available energy within the collision is often described in two different quantities, namely the kinetic beam energy or the center of mass energy. Since all results are compared in terms of the more general center of mass energy $\sqrt{s_{NN}}$, the fundamental derivation is shortly summarized. The sum of available 4-momenta of the participating nuclei leads to

$$s = \left[\begin{pmatrix} E_1^{lab} \\ \vec{p}_1 \end{pmatrix} + \begin{pmatrix} E_2^{lab} \\ \vec{p}_2 \end{pmatrix} \right]^2 \tag{A.1}$$

The total energy in the lab system is always calculated as $E = E_{kin} + m$. For a fixed target experiment, the 4-vector properties of the target nuclei can be simplified to

$$s = \left[\begin{pmatrix} E_1^{lab} \\ \vec{p}_1 \end{pmatrix} + \begin{pmatrix} m_2 \\ \vec{0} \end{pmatrix} \right]^2 \tag{A.2}$$

$$= (E_1^{lab})^2 + 2E_1^{lab}m_2 + m_2^2 - p_1^2 \tag{A.3}$$

$$= 2E_1^{lab}m_2 + m_2^2 + m_1^2 \tag{A.4}$$

In the last calculation step, the relation $E = \sqrt{m^2 + p^2}$ is used. The general result for $\sqrt{s}$ is thus written as

$$\sqrt{s} = \sqrt{m_1^2 + m_2^2 + 2E_1^{lab}m_2} \tag{A.5}$$

For a collider system, the center of mass energy is given as

$$s = (E_1 + E_2)^2 - (\vec{p_1} + \vec{p}_2)^2 \tag{A.6}$$

$$= m_1^2 + m_2^2 + 2E_1E_2 - 2\vec{p}_1\vec{p}_2 \tag{A.7}$$

For a symmetric collision systems with $\vec{p}_1 = -\vec{p}_2$ and $m_1 = m_2$, the final result reads $\sqrt{s} = 2E$.

In the SIS18 energy regime of $E_{kin} \approx 1 - 2$ AGeV, the collision of nuclei are described as superposition of nucleon-nucleon reactions, where the nucleon masses are used and $\sqrt{s}$ is always referred to $\sqrt{s_{NN}}$.

A.2 Rapidity/Transverse Momentum

The transverse momentum in HADES is always calculated with respect to beam axis, if not stated differently. Thus, the following equation describes the calculation of the transverse momentum:

$$p_t = p \cdot \sin\theta \tag{A.8}$$

Where p is the total particle momentum and θ the polar angle to the beam axis. Many physical observables are related to the transverse momentum, which is not dependent on the boost of the initial system. In heavy ion collisions, most of the combinatorial background obtains a low transverse momentum since the spectators of the collision still travel along vanishing $p_t = 0$ MeV/c. On the other hand, rapidity quantifies the relative amount of the energy in longitudinal momentum compared to the total energy of the particle. The rapidity is defined as:

$$y = ln\frac{E + p_z}{E - p_z} \tag{A.9}$$

As result, the phase space for a particular particle of known mass m can be transformed analytically from p_t, y to θ, p which is shown as additional grid in most phase space distributions in this thesis for visualization purpose. In comparison to the phase space description in p/θ, the p_t/y representation has the huge advantage of a symmetric particle production rate around midrapidity, which is used for a quality estimation. Nevertheless the transformation of the representation from any distribution $D(p_t, y)$ to $D(p, \vartheta)$ is bijective and thus from same quality.

A.3 Target Layer Positions

Target layer	$z_{min}[mm]$	$z_{max}[mm]$	$\Delta z[mm]$
1	-70.0	-60.3	9.7
2	-60.3	-56.5	3.8
3	-56.5	-53.0	3.5
4	-53.0	-49.4	3.4
5	-49.4	-45.7	3.3
6	-45.7	-42.3	3.4
7	-42.3	-38.8	3.5
8	-38.8	-35.4	3.4
9	-35.4	-31.5	3.9
10	-31.5	-28.0	3.5
11	-28.0	-24.1	3.9
12	-24.1	-21.3	2.8
13	-21.3	-16.9	4.4
14	-16.9	-13.5	3.4
15	-13.5	0.0	13.5

Table A.1: Summary of the values of the target layer position determination which is part of the event classification for the event mixing technique.

A.4 Influence of Inner MDC Sharing

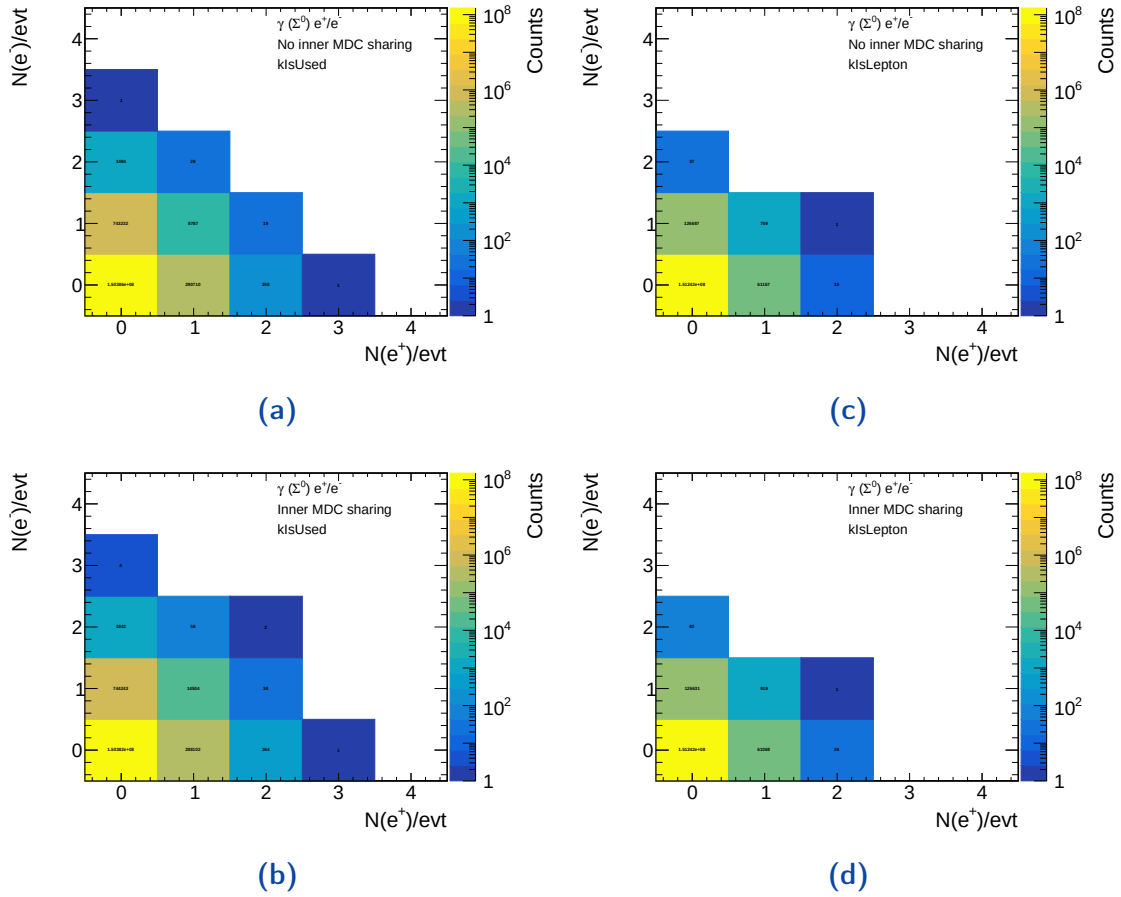

Figure A.1: The amount of reconstructed e^-/e^+ tracks from the $\Sigma^0 \to \gamma \to e^+e^-$ decay.

The upper row displays the standard track finding algorithm, while the figures in the bottom row the track sorting was rerun, allowing several reconstructed track candidates to share hits from the inner MDCs. The plots in the left column require only reasonable track quality. In the right column, also a RICH ring is requested. All plots are extracted from Σ^0 embedded in real data, and thus combine efficiency, acceptance and branching ratio as well as conversion probability in the detector. Since the RICH was optimized to avoid conversion, many conversions take place beyond the RICH, and thus do not produce rings. For those rare cases, where the tracking could reconstruct both e^+e^- track, only in $8.6\,\%$ of the cases the tracks are matched to a ring for the setup with inner MDC sharing and 6.3% without this sharing. The single particle reconstruction efficiency for the cases where only one lepton is reconstructed does not change at all. Even after these loose pre selections, the efficiency to reconstruct both leptons with ring is

$\epsilon_{\gamma_{conv}} = 6 \cdot 10^{-6}$ with allowing MDC share and $\epsilon_{\gamma_{conv}} = 5 \cdot 10^{-6}$ in the case without sharing.

A.5 Uncorrected Λ Spectra

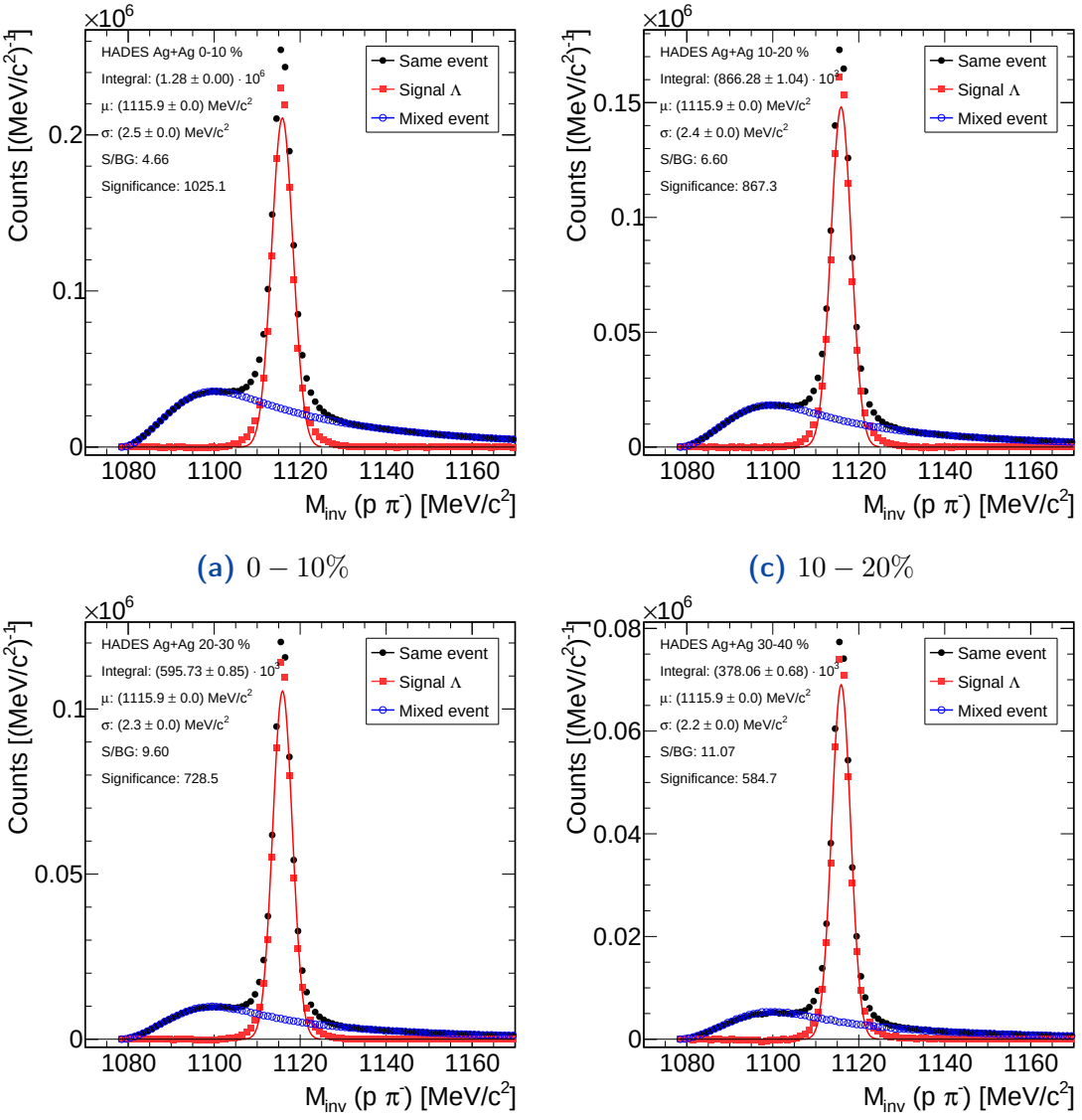

(a) $0 - 10\%$ **(c)** $10 - 20\%$

(b) $20 - 30\%$ **(d)** $30 - 40\%$

Figure A.2: Raw Λ counts differentiated in 10% centrality bins for the more strict selection on the neural net evaluation of $\mathrm{NN}_{eval} > 0.98$.

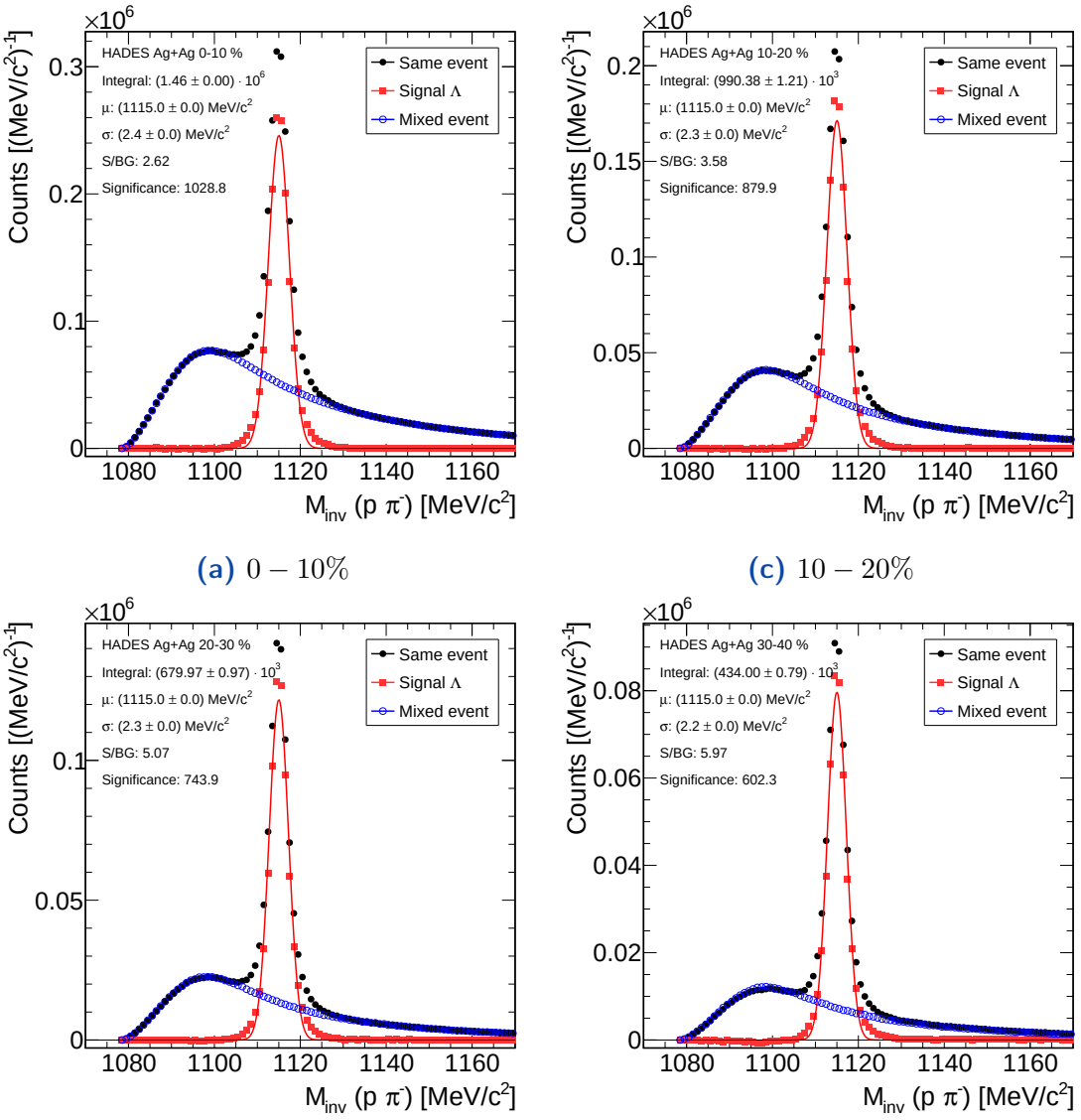

(a) $0-10\%$ **(c)** $10-20\%$

(b) $20-30\%$ **(d)** $30-40\%$

Figure A.3: Raw Λ counts differentiated in 10% centrality bins for the selection on the neural net evaluation of $\mathrm{NN}_{eval} > 0.95$ which is used as base line for the final extraction of the Λ multiplicity.

A.6 Partial Acceptance of the Λ

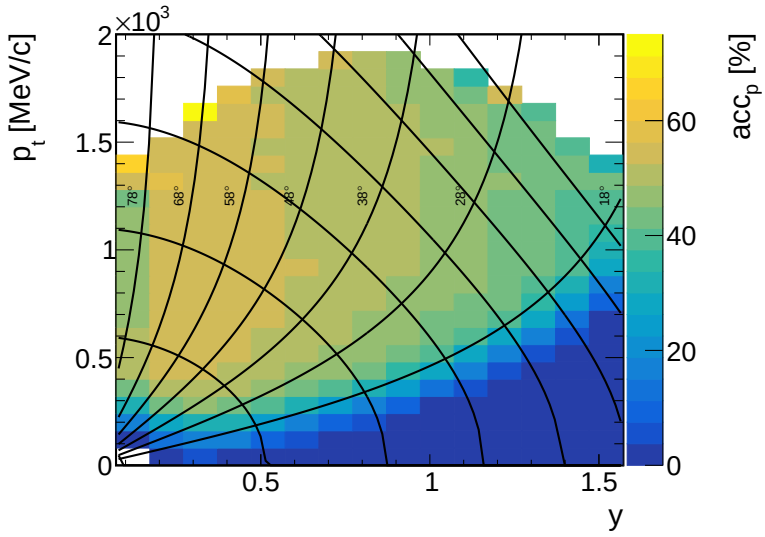

Figure A.4: Λ transverse momentum p_t and rapidity y distribution, in the case where at least the proton from the Λ decay is in the HADES acceptance.

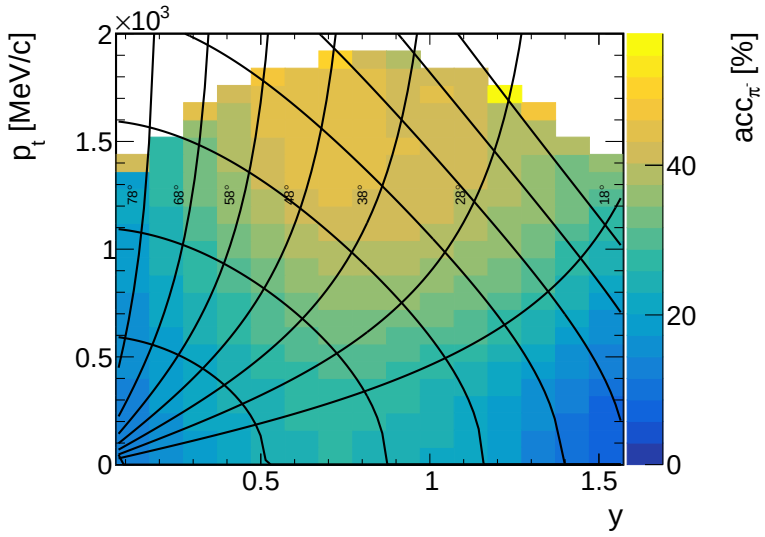

Figure A.5: Λ transverse momentum p_t and rapidity y distribution, in the case where at least the π^- from the Λ decay is in the HADES acceptance.

A.7 Transverse Momenta of the Λ

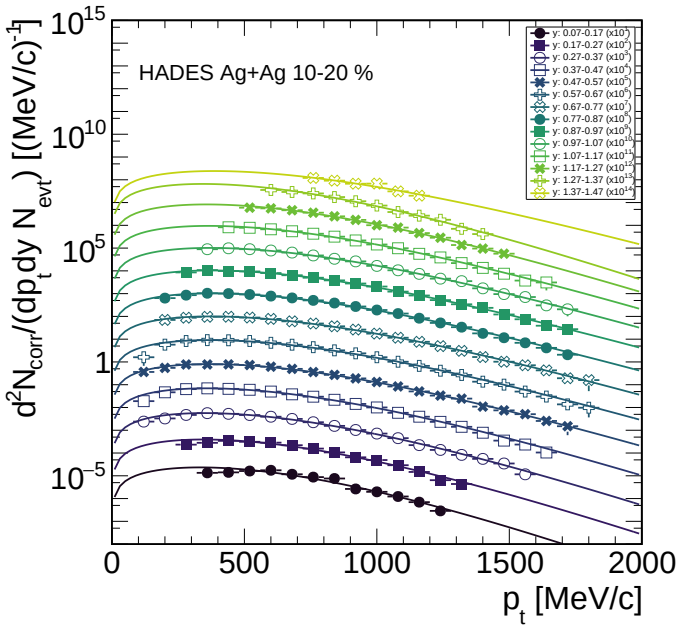

Figure A.6: Λ transverse momentum p_t distribution, for the $10-20\%$ most central events for the different rapidity bins.

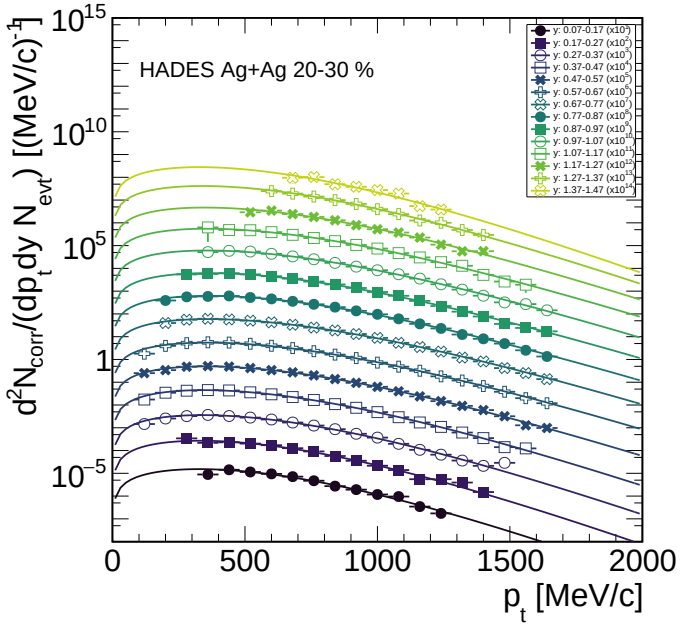

Figure A.7: Λ transverse momentum p_t distribution, for the $20-30\%$ most central events for the different rapidity bins.

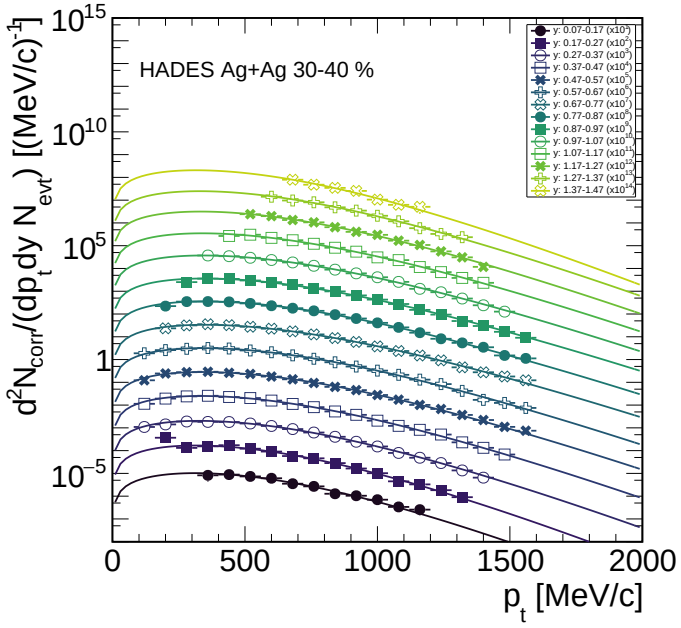

Figure A.8: Λ transverse momentum p_t distribution, for the $30-40\%$ most central events for the different rapidity bins.

A.8 Photon Energy Variation - Background Shift

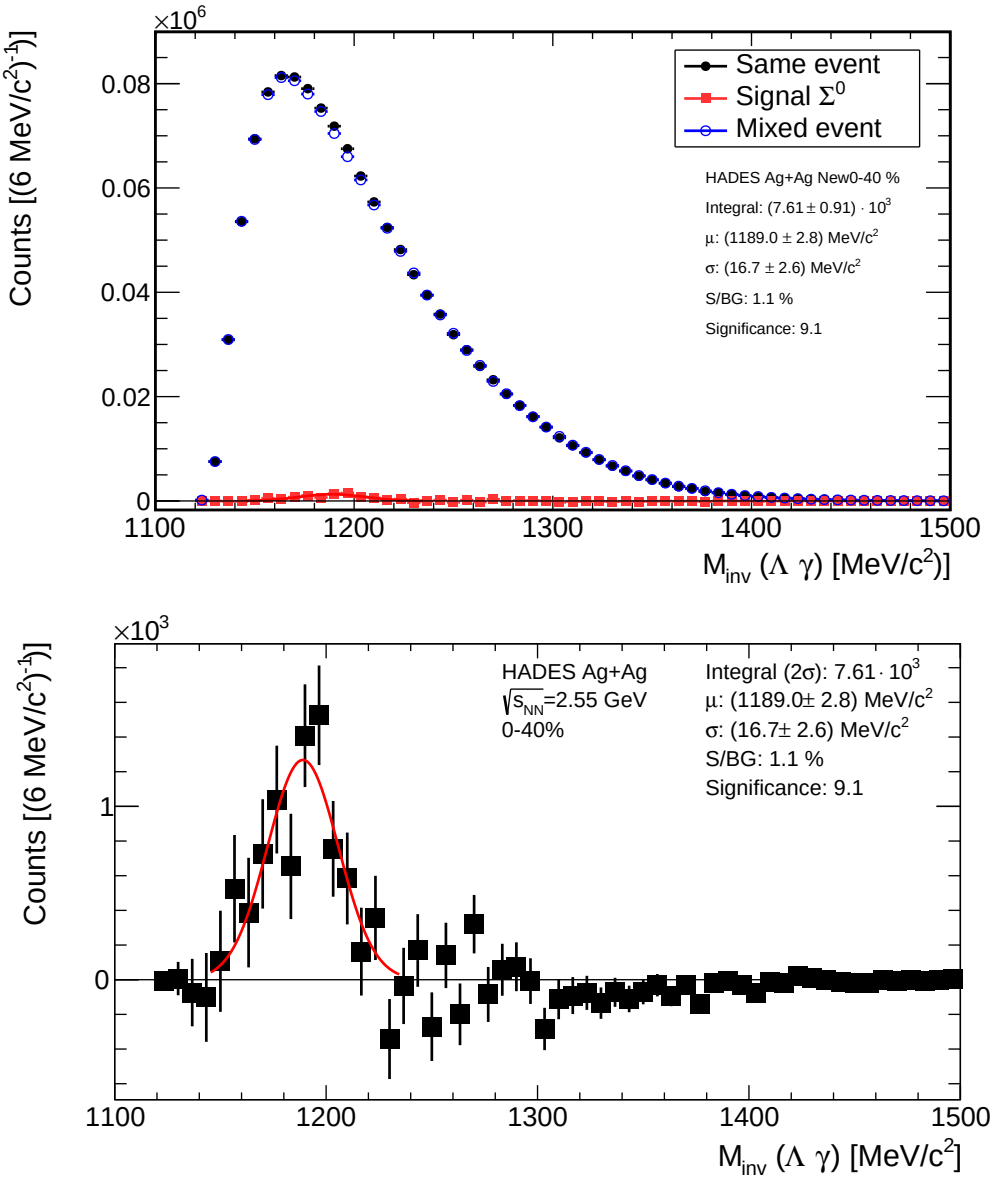

Figure A.9: The upper plot shows the invariant mass of all $\Lambda\gamma$ pairs as described in chapter 6.1 for experimental data from the same events in black, the mixed events in blue and the remaining signal spectrum after subtracting the background. Mixed events were scaled to the same events using the sideband method. In the lower plot, the remaining signal spectrum is shown more precisely. In this case, a lower cut on the γ energy of $E_\gamma > 40\,\text{MeV}$ is applied. This shifts the maximum of the background distribution to the left side of the extracted signal.

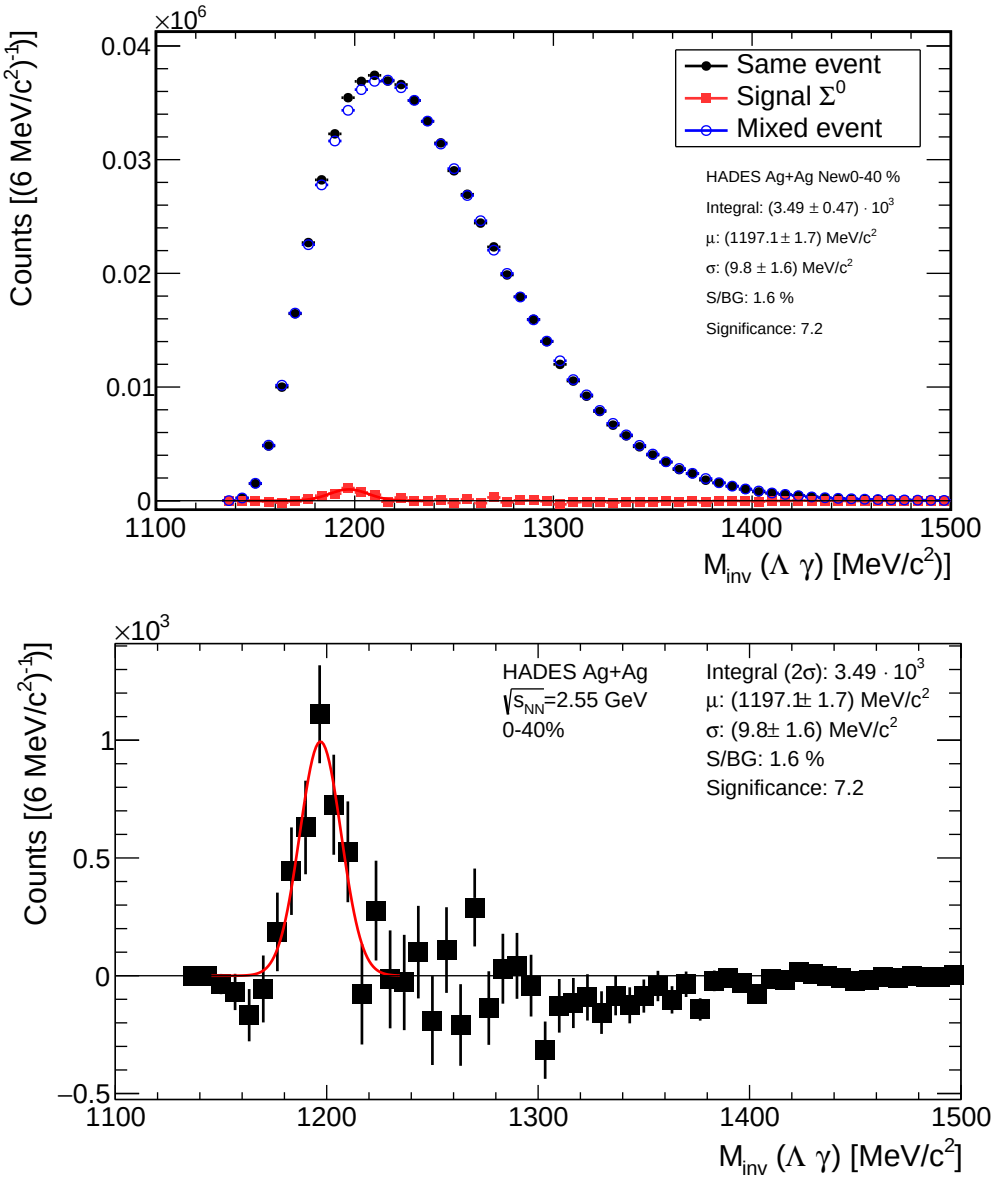

Figure A.10: The upper plot shows the invariant mass of all $\Lambda\gamma$ pairs as described in chapter 6.1 for experimental data from the same events in black, the mixed events in blue and the remaining signal spectrum after subtracting the background. Mixed events were scaled to the same events using the sideband method. In the lower plot, the remaining signal spectrum is shown more precisely. In this case, a lower cut on the γ energy of $E_\gamma > 120\,\text{MeV}$ is applied. This shifts the maximum of the background distribution to the right side of the extracted signal.

A.9 Conversion Method - Monte-Carlo-Simulation Yield Comparison

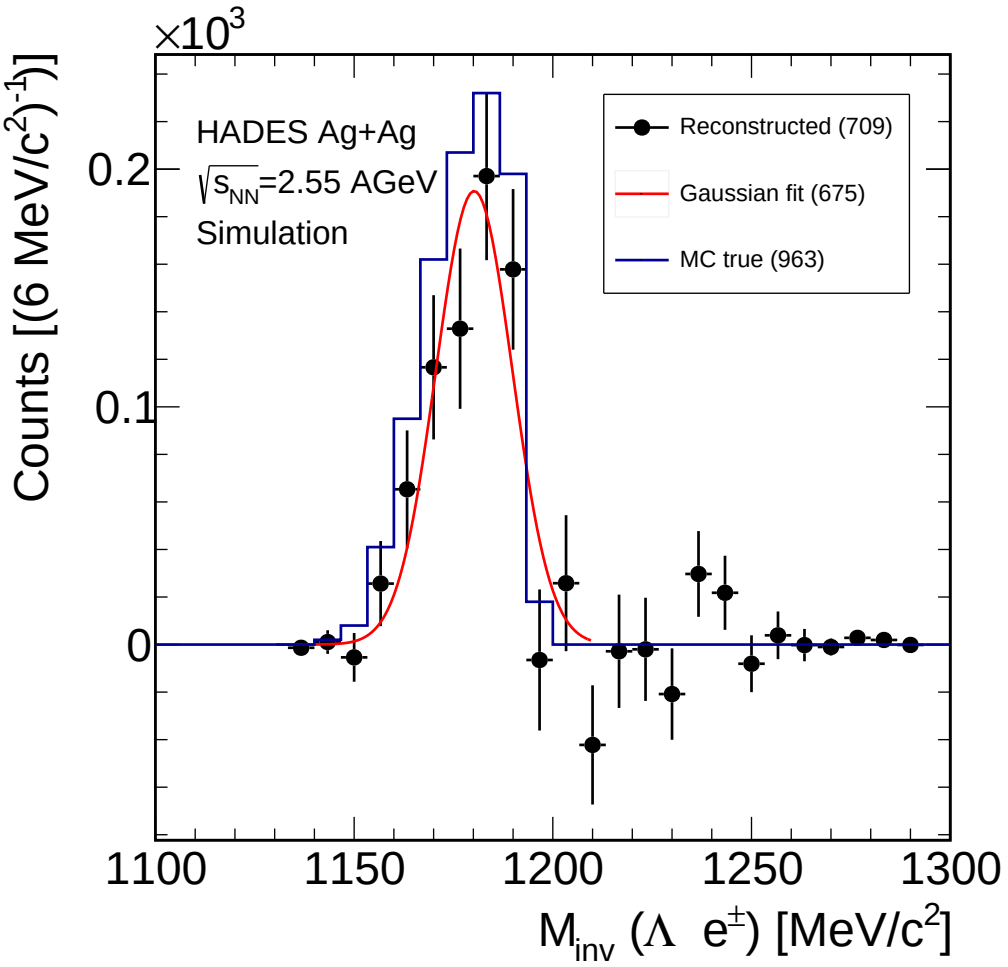

Figure A.11: Comparison of the reconstructed Λe^- yield in simulation as black points and the corresponding Gaussian fit in red. The blue line is the true MC result, which is enhanced significantly.

A.10 Conversion Method - Lepton Charge Dependent Spectra

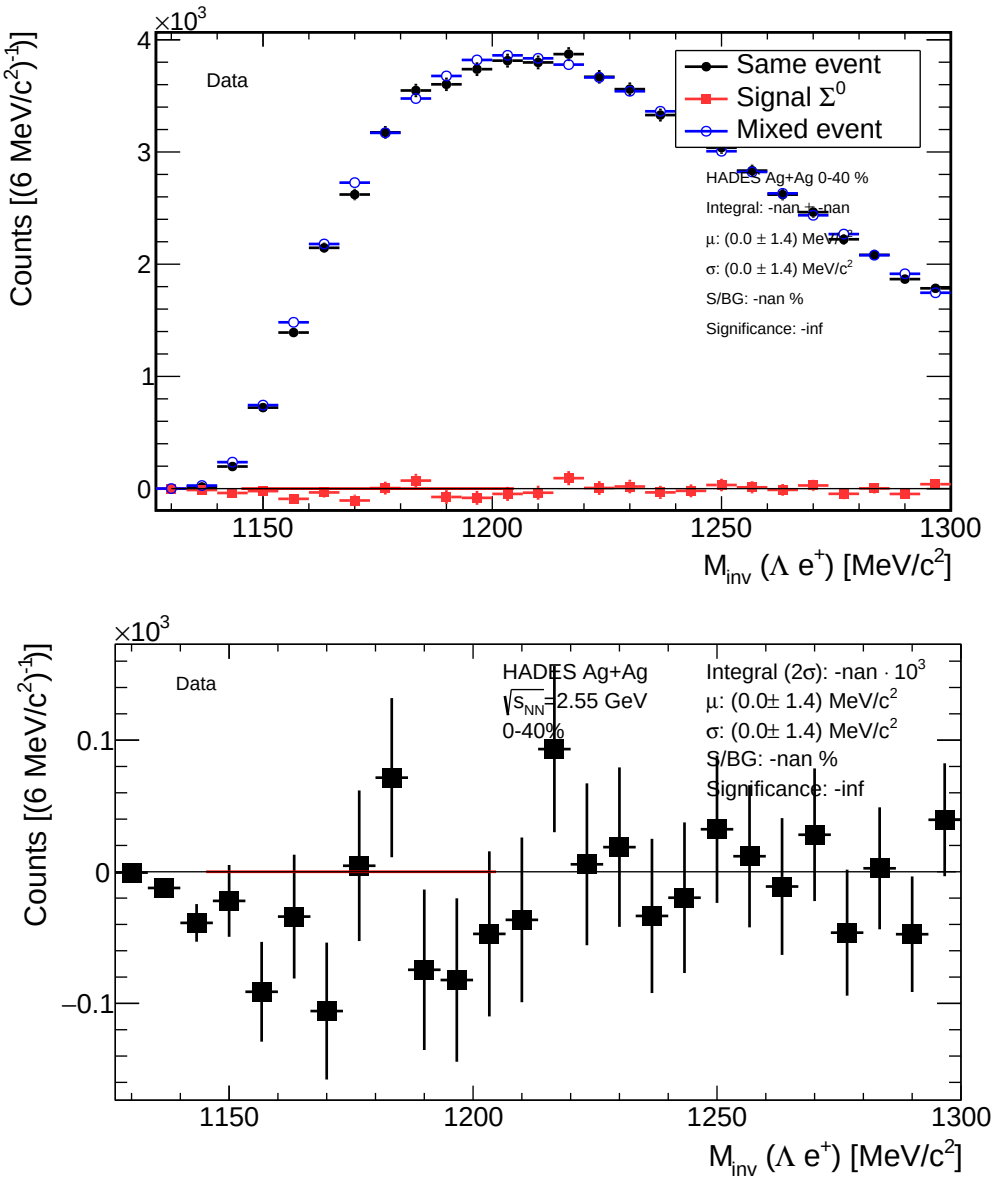

Figure A.12: The upper plot shows the invariant mass of all Λe^+ pairs as described in chapter 6.2 for experimental data from the same events in black, the mixed events in blue and the remaining signal spectrum after subtracting the background. Mixed events were scaled to the same events using the sideband method. In the lower plot, the signal is shown more precisely.

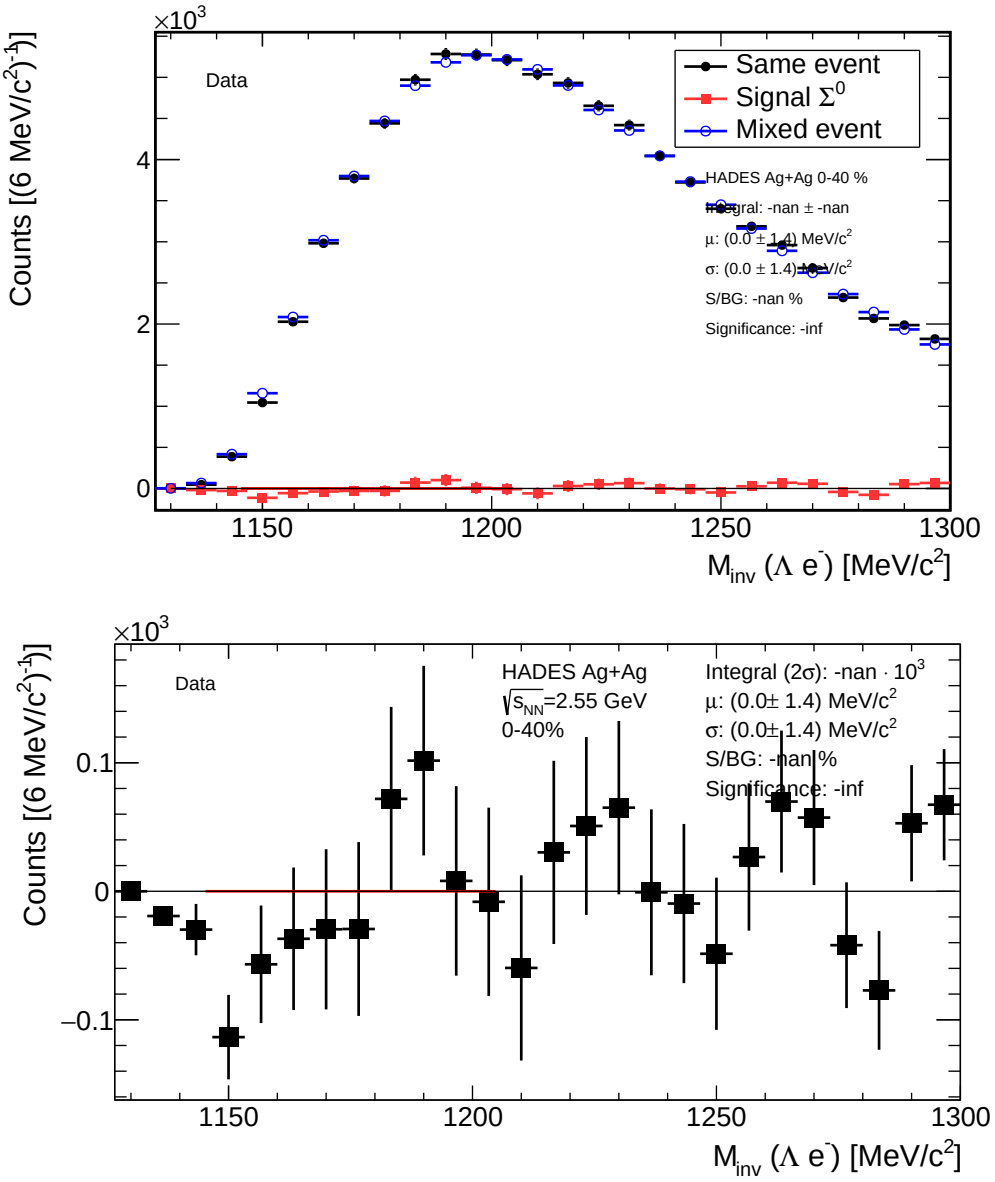

Figure A.13: The upper plot shows the invariant mass of all Λe^- pairs as described in chapter 6.2 for experimental data from the same events in black, the mixed events in blue and the remaining signal spectrum after subtracting the background. Mixed events were scaled to the same events using the sideband method. In the lower plot, the remaining signal spectrum is shown more precisely.

A.11 Conversion Method - Lepton Charge Dependent Spectra After Cut Optimization

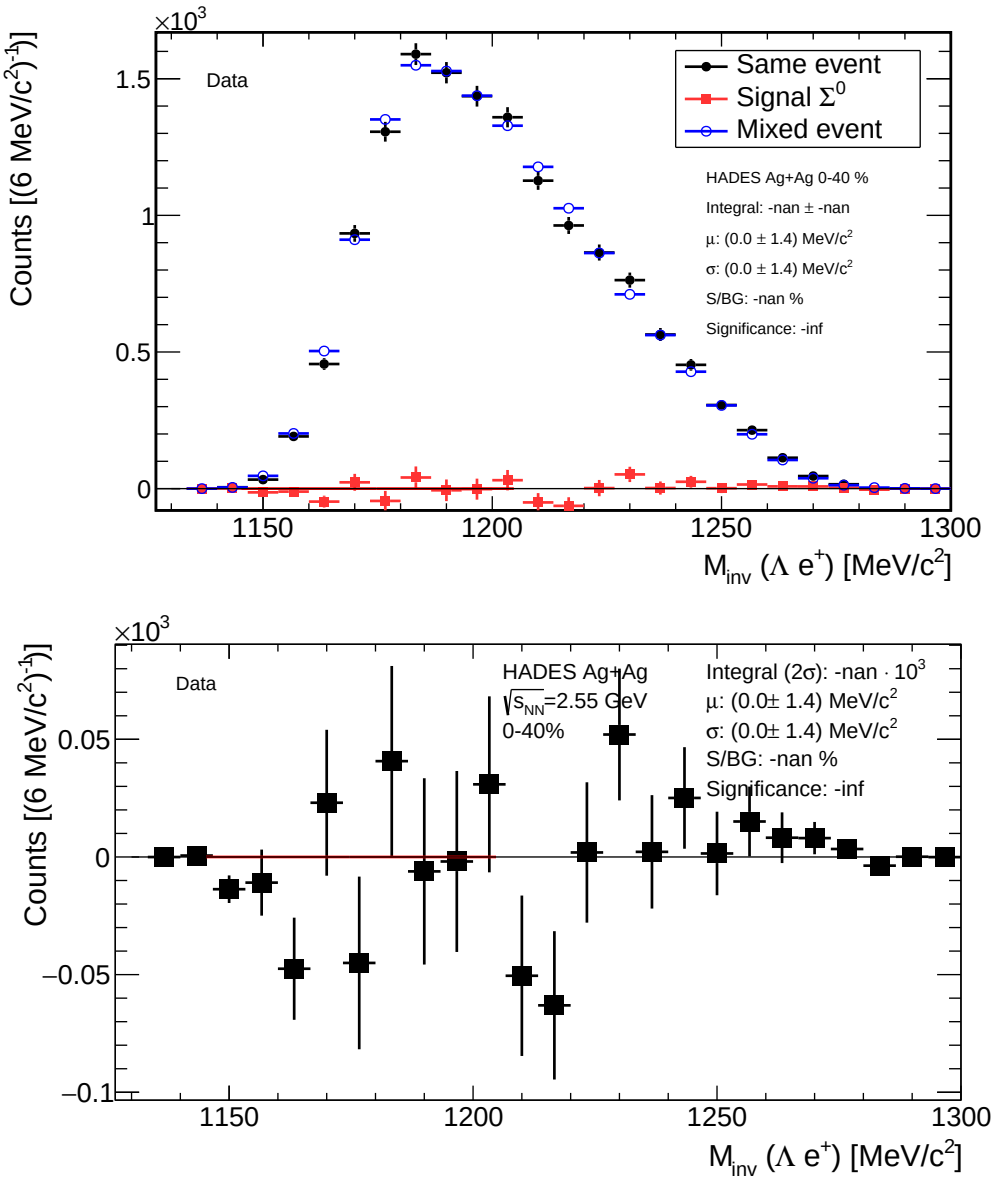

Figure A.14: The upper plot shows the invariant mass of all Λe^+ pairs as described in chapter 6.2 for experimental data from the same events in black, the mixed events in blue and the remaining signal spectrum after subtracting the background. Mixed events were scaled to the same events using the sideband method. In the lower plot, the remaining signal spectrum is shown more precisely.

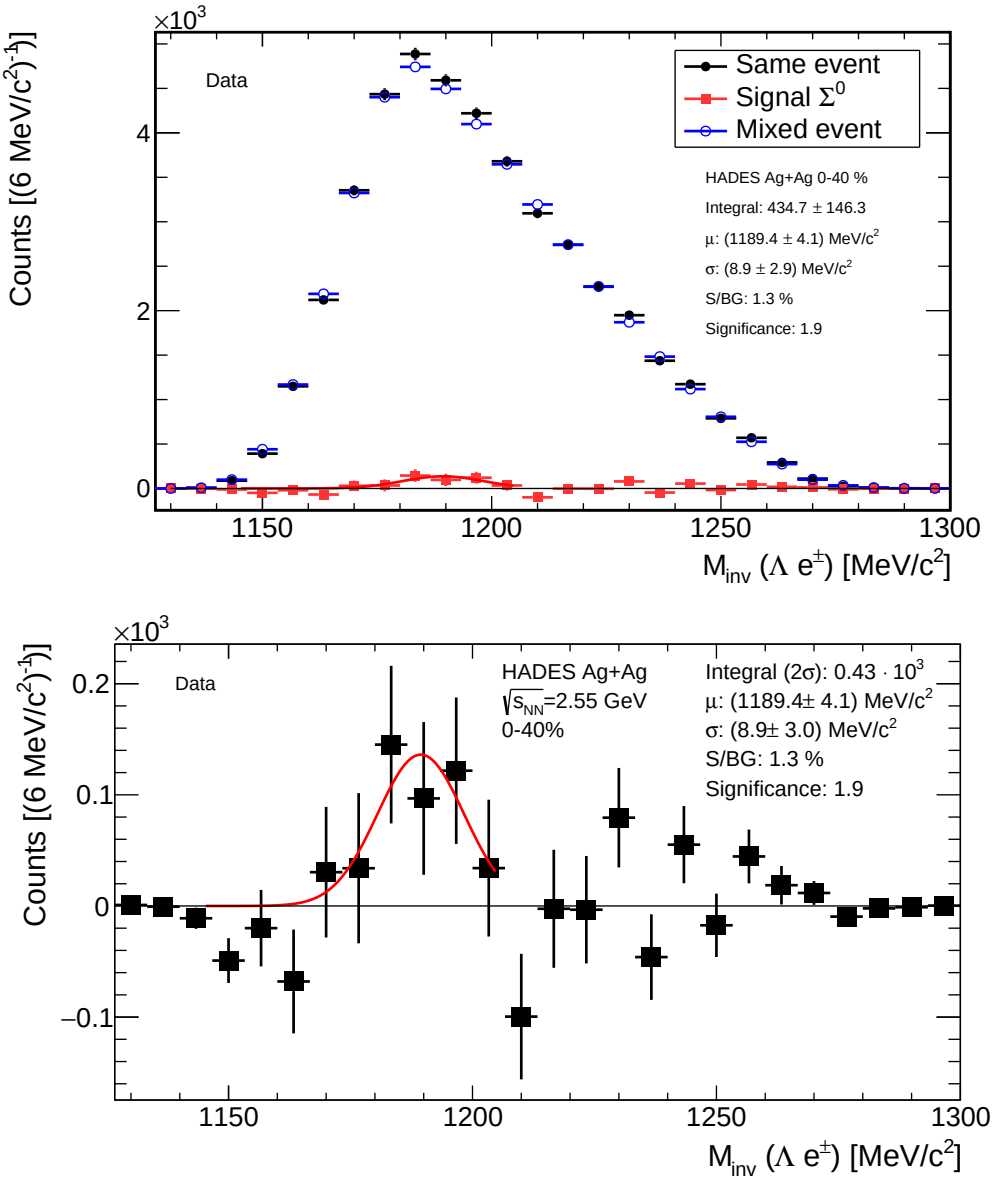

Figure A.15: The upper plot shows the invariant mass of all Λe^- and Λe^+ pairs as described in chapter 6.2 for experimental data from the same events in black, the mixed events in blue and the remaining signal spectrum after subtracting the background. Mixed events were scaled to the same events using the sideband method. In the lower plot, the remaining signal spectrum is shown more precisely.

A.12 Conversion Method - Influence of a Strict Cut on Cherenkov Photons

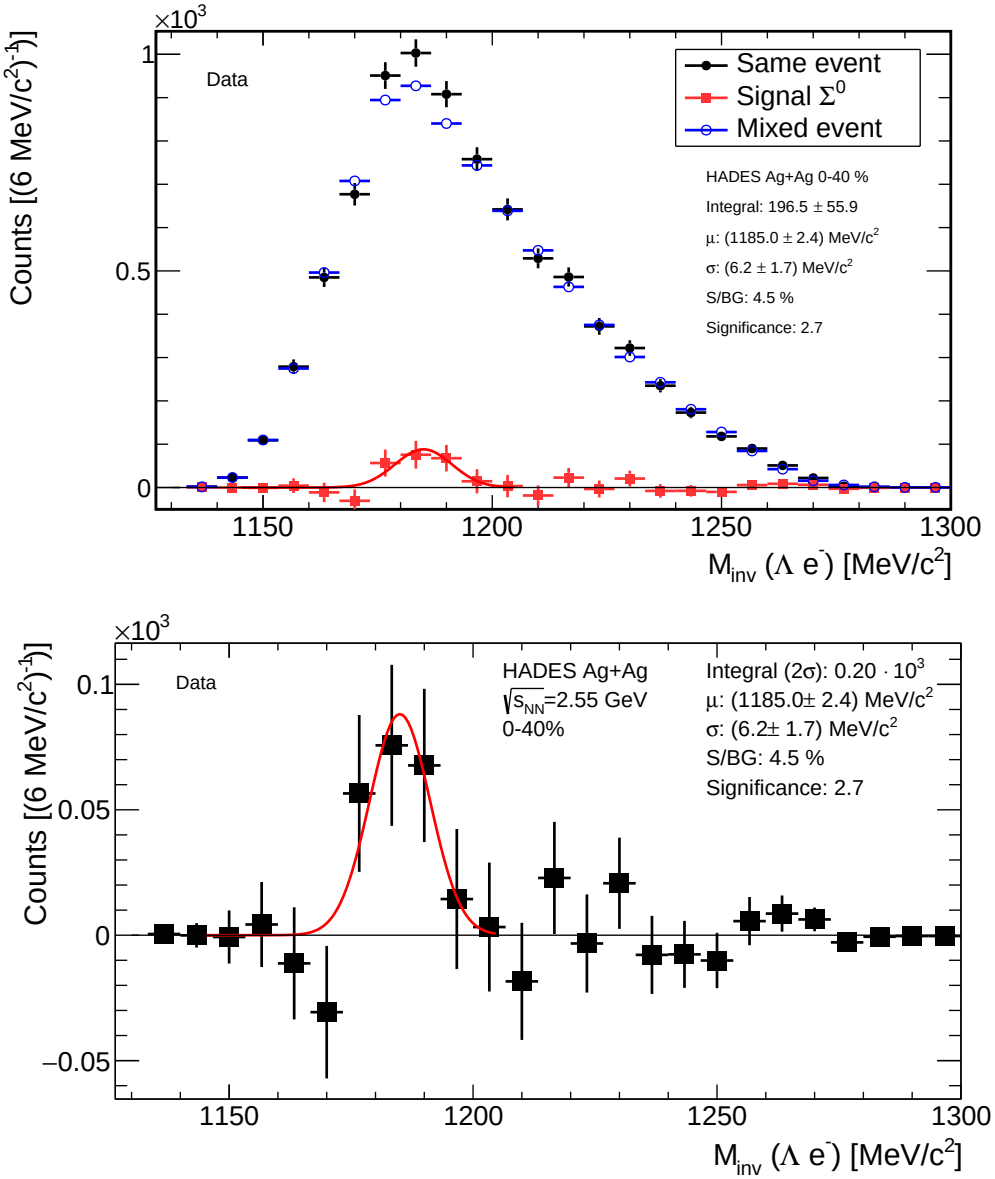

Figure A.16: The upper plot shows the invariant mass of all Λe^- pairs as described in chapter 6.2 for experimental data from the same events in black, the mixed events in blue and the remaining signal spectrum after subtracting the background. Mixed events were scaled to the same events using the sideband method. In the lower plot, the remaining signal spectrum is shown more precisely.

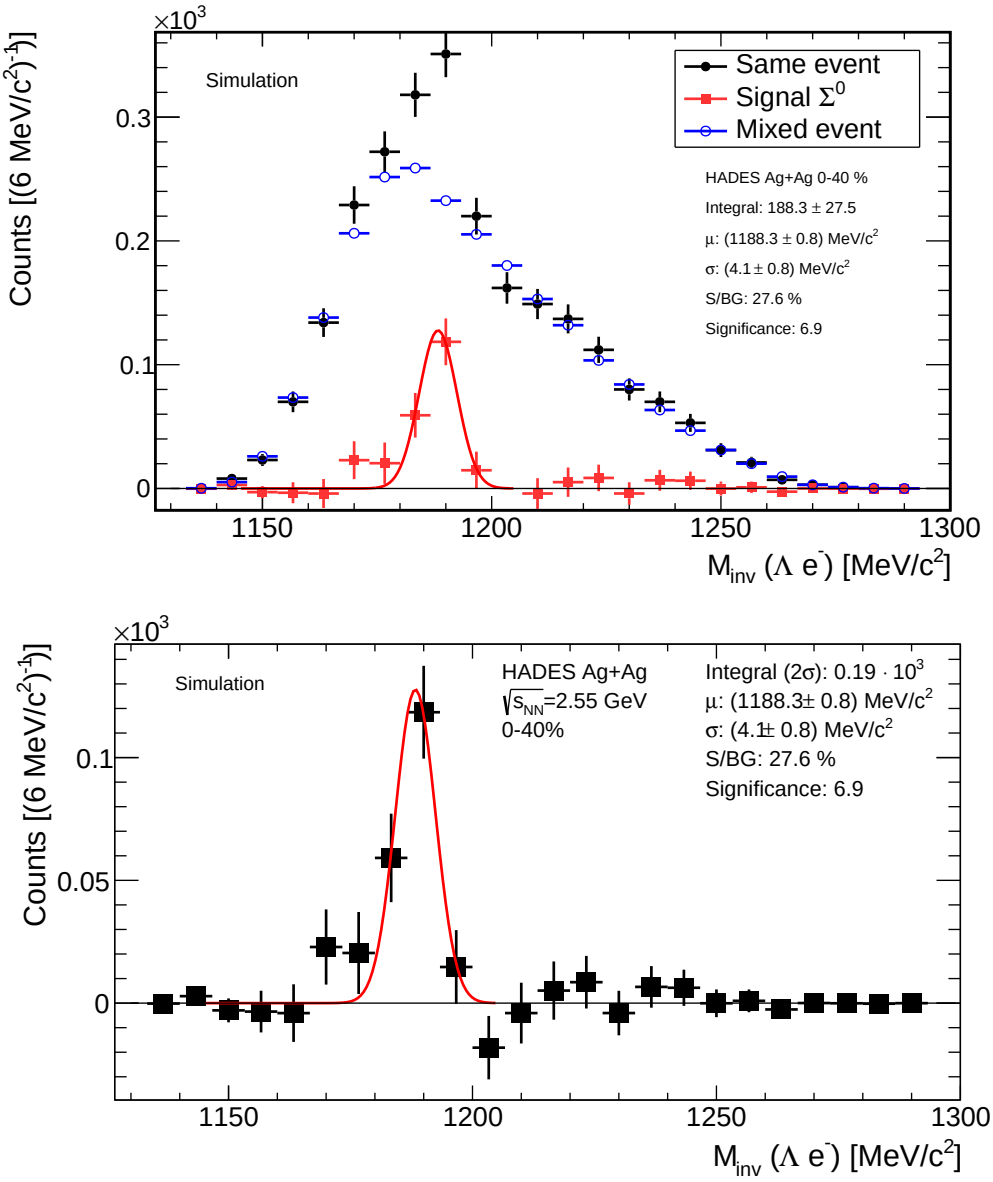

Figure A.17: The upper plot shows the invariant mass of all Λe^- pairs as described in chapter 6.2 for simulations from the same events in black, the mixed events in blue and the remaining signal spectrum after subtracting the background. Mixed events were scaled to the same events using the sideband method. In the lower plot, the signal is shown more precisely.

A.13 Side Band Variation

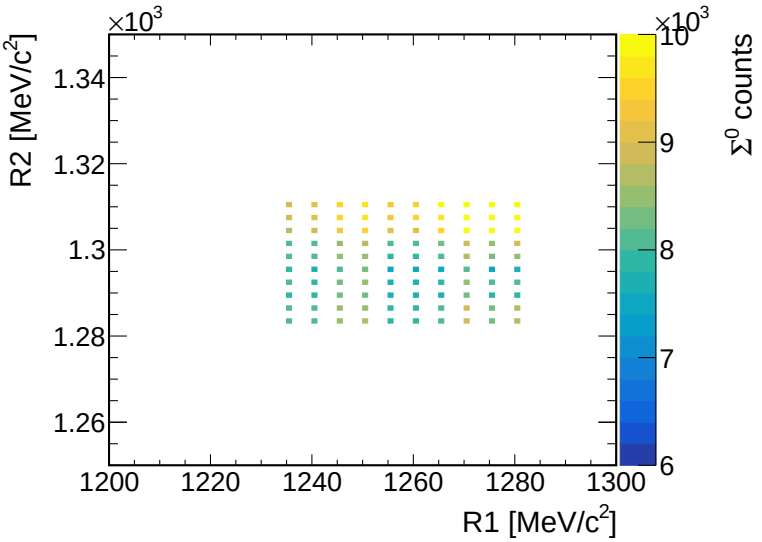

Figure A.18: Variation of the side band ranges of the right side band, where the left and the right border are varied simultaneously.

The more detailed version of the side band variation is displayed in figure A.18 where the borders of the right side band are simultaneously varied. Also here many fluctuations are seen, but as soon as the right border exceeds values above $M_{inv}(\Lambda\gamma) = 1300\,\mathrm{MeV/c^2}$, the signal is systematically growing due to the undershooting structure. Nevertheless, the standard choice of sidebands is centered within a plateau region, where the systematic deviations are covered from the analysis in section 6.3.

A.14 Particle Yield Collection

Particle	Multiplicity	Uncertainty	Reference
N_{part}	161	13	[213]
p	54.3	4.3	[214]
π^0	11.85	1.1	[195]
π^+	9.6	0.7	[215]
π^-	13.9	1.3	[215]
Λ	0.12	0.0041	this work
η	0.253	0.08062	[195]
K^+	0.086	0.014	[216]
K^-	0.00137	0.0001533	[216]
K_s^0	0.045	0.0015	[214]
Φ	0.000382	9.3e-05	[216]
Ξ	6e-5	2.5e-5	[214]
Σ^0	0.028	0.006	this work
d	15.23	1.35	[215]
H^3	2.97	0.39	[215]
He^3	2.0	0.3	[215]

Table A.2: Hadron multiplicities from the 0-10% most central HADES Ag+Ag collisions including light nuclei.

The table of this appendix A.14 contains all particle multiplicities which were used for producing the statistical hadronization model fits with Thermal-FIST when considering the light nuclei d,H^3,He^3 instead of up-scaling the amount of protons for the unmeasured amount of protons which are bound in these light nuclei.

A.15 Statistical Model Fits with Inclusion of K^-

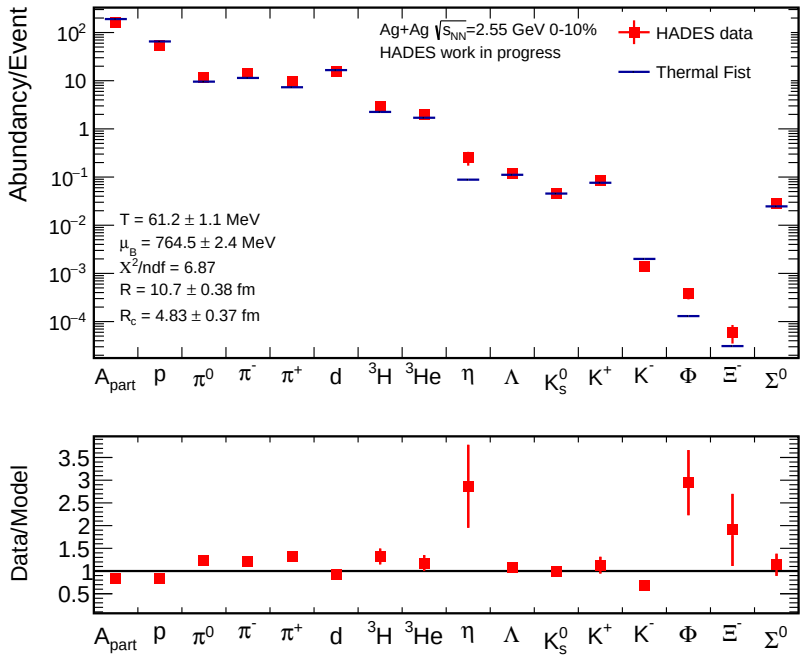

Figure A.19: Fit with Thermal-Fist of the combined HADES data for the 0-10% most central events of the Ag+Ag collisions in the upper plot and the resulting ratio of experimental data to the model predictions below, where the K^- is included in the fitting procedure with light nuclei.

The inclusion of the K^- to the statistical model fits, leads to significantly increased χ^2/n and especially for the case with light nuclei, neither strangeness containing particle, nor non-strange hadron yields are described satisfyingly, even when the estimation for temperature and baryochemical potential are the same within errors.

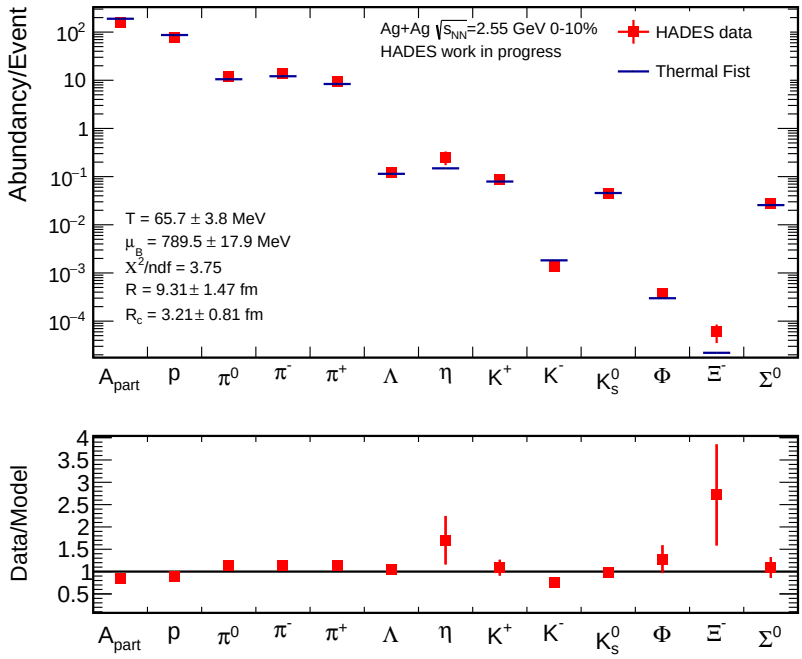

Figure A.20: Fit with Thermal-Fist of the combined HADES data for the 0-10% most central events of the Ag+Ag collisions in the upper plot and the resulting ratio of experimental data to the model predictions below, where the K^- is included in the fitting procedure without light nuclei.

APPENDIX B

Electromagnetic Calorimeter

B.1 Photon Cluster Properties

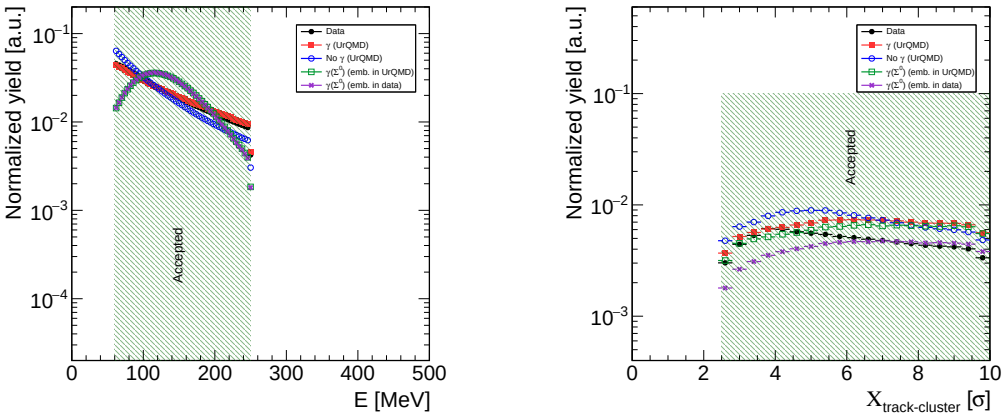

(a) Cluster energy

(c) Cluster-track matching quality

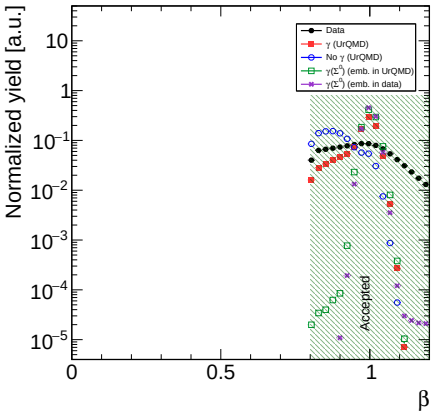

(b) Cluster velocity

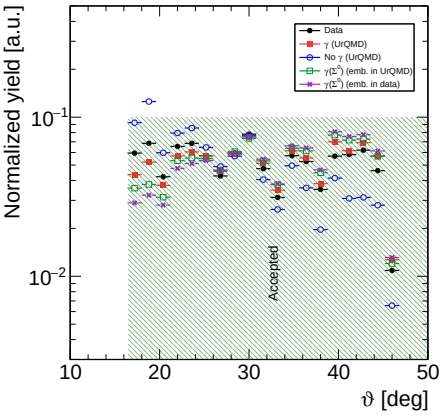

(d) Cluster polar angle

Figure B.1: Distribution of observables of the electromagnetic calorimeter after application of all cuts which were discussed in chapter 4.7.

B.2 Deactivation of ECal Cells with Reduced Quality

During the calibration of the electromagnetic calorimeter, few cells showed reduced quality compared the expected performance, achieved by the remaining cells.

Cell number (sec 2)	Cell number (sec 4)
6	10
9	43
10	72
80	178
195	179
	180
	182
	183
	184

Table B.1: Cell numbers in the electromagnetic calorimeter which were neglected in all analysis steps in data as well as in simulation due to reduced quality of the response in the experimentally measured data.

B.3 Photon Energy in Simulation

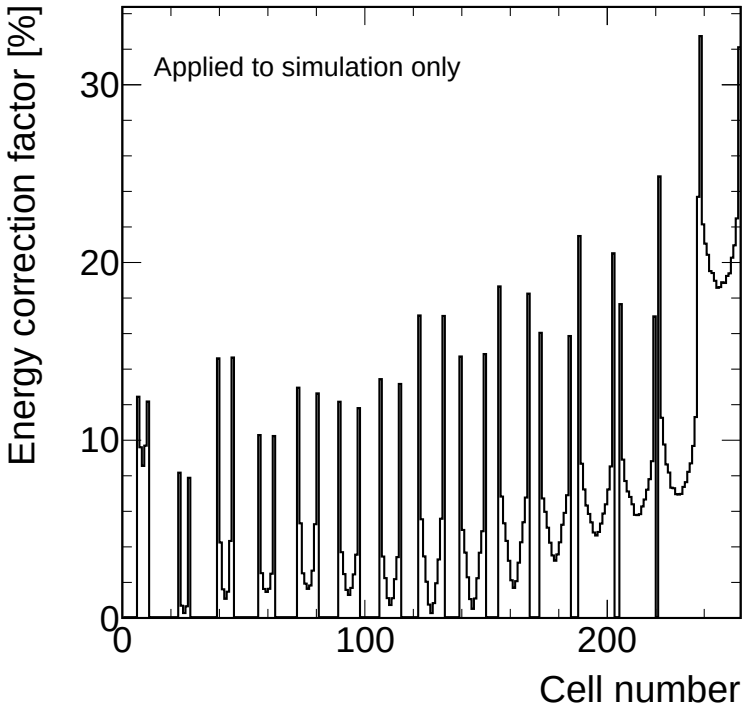

Figure B.2: Additional energy correction applied only in simulation.

Standard correction map for the energy of clusters in the ECal. This correction factor is applied cell wise and is directly correlated to the different distances from the cell to the target area.

B.4 Photon Efficiency

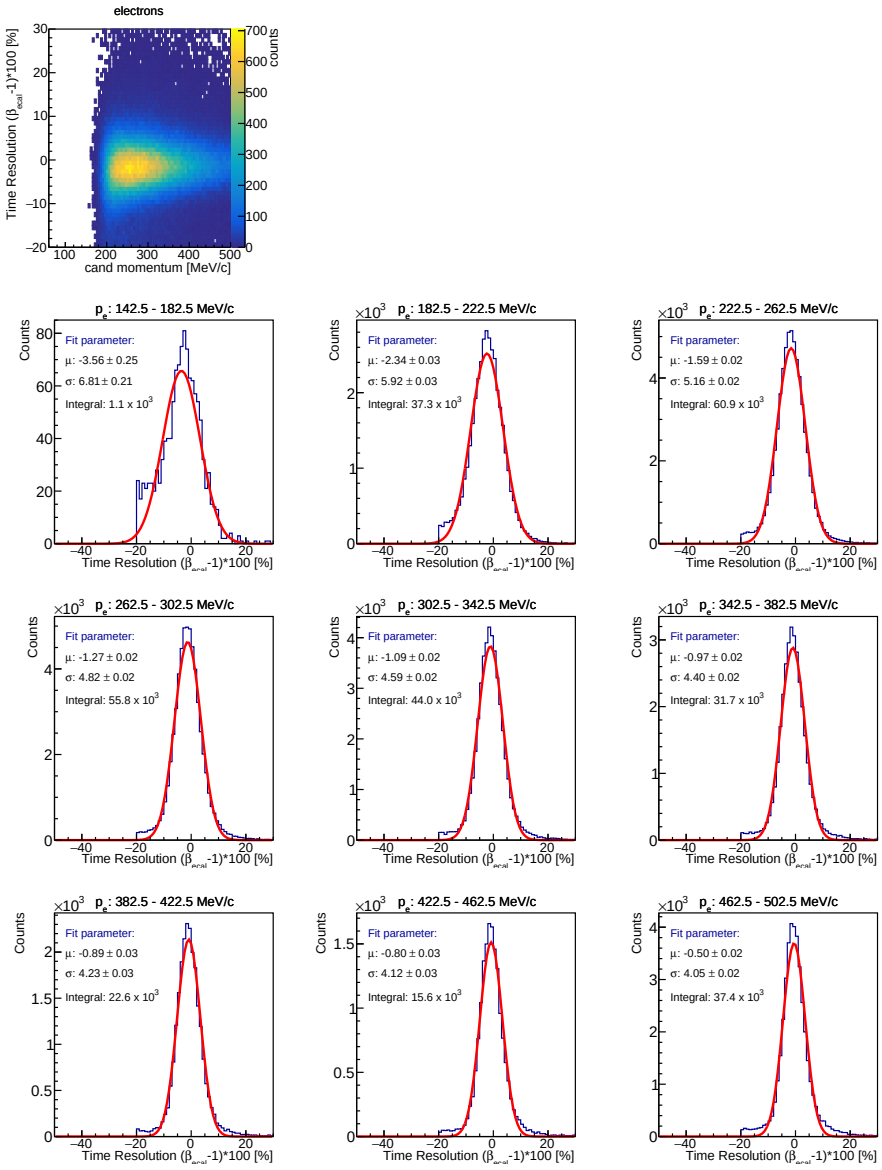

Figure B.3: Fitted electrons and their momentum dependent timing resolution in the ECal.

Projections of the electrons and their velocity resolution extraction within the electromagnetic calorimeter. The selection of the electrons is the same like for the positrons which are shown in chapter 7 where the comparability of electrons and positrons is discussed.

B.5 Cluster-Track Matching

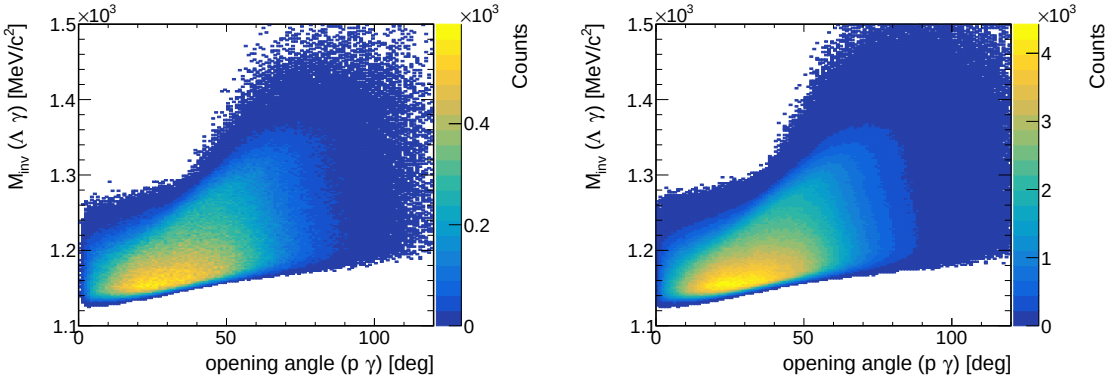

(a) p-track cluster matching, same event **(b)** p-track cluster matching, mixed event

Figure B.4: Representation of the track-cluster matching for protons terms of the distance approximation parameter, here denoted as opening angle, and the $\Lambda\gamma$ invariant mass.

In figure B.4, the invariant mass of the $\Lambda\gamma$ pair is shown in dependence on the matching of the extrapolated proton from the Λ decay to the ECal cluster associated to the γ. By eye same-event distribution on the left looks identical to the distribution extracted from the event mixing, shown on the right. Nevertheless, it elucidates the statistical distribution of the $\Lambda\gamma$ pairs and highlights the comparably small opening angle in the range 15-50 $^\circ$ in most cases which is determined by the HADES geometry.

B.6 Time Calibration Improvement

As shown in chapter 7, there is still some remaining time walk visible, which differs for electrons, positrons and photons. Since they all have to have the same ECal response from physical argumentation, the path length from interaction point within the target to the corresponding ECal cell is the remaining difference. While for the photons, the straight line approach is correct, the track length of electrons and positrons differ by the orientation with respect to the magnetic field lines in between the inner and outer MDCs. The overall track length up to the META detector is calculated by the Runge-Kutta algorithm and stored in each track candidate. While the distance from RPC and ECal was estimated to be a constant of 156 mm, those information can be recalculated by the parameter file, which obtains the geometry. This method is tested in simulated data and provides the correct timing information by including the correct path length between RPC and ECal which is assumed to be be a straight line, since the ECal is far behind the magnetic field region.

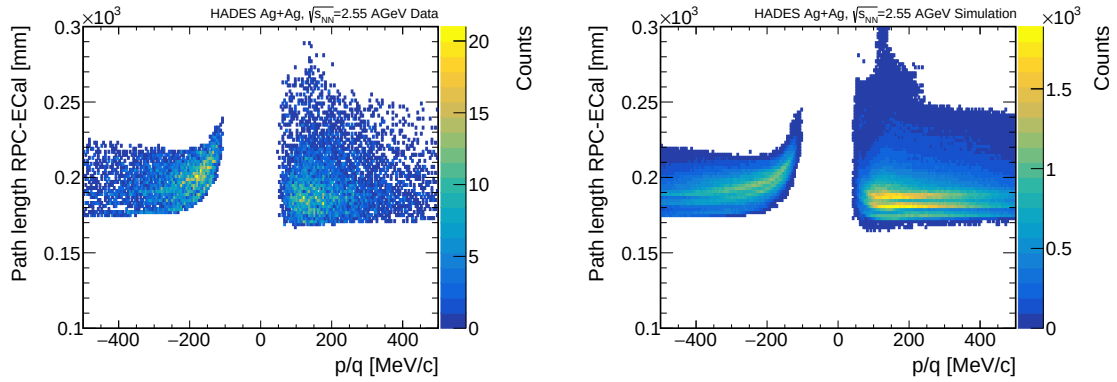

(a) Experimental data (b) White lepton simulation

Figure B.5: Comparison of path length as function of the electromagnetic charge and momentum from real data and simulation.

The path length of leptons from the RPC to the ECal is displayed in figures B.5 and B.6 where the left side shows the lepton sample from experimental data while the right side is extracted from simulation. The length behaves in the same manner, which is expected due to the dependency of only the Runge-Kutta algorithm and the detector geometry.

Besides the acceptance difference for the different electromagnetic charges, the electrons are already centered around $\beta = 1$ for low momenta, without correcting for the additional path length which arises from the bending of the magnetic field in real data, while the simulation describes the correct behaviour, where the influence of the bending is visible for both charges. Already this plot shows the imperfection of the state of calibration of the timing of the ECal in the Ag+Ag data set. Applying the correction of the individual path length addition

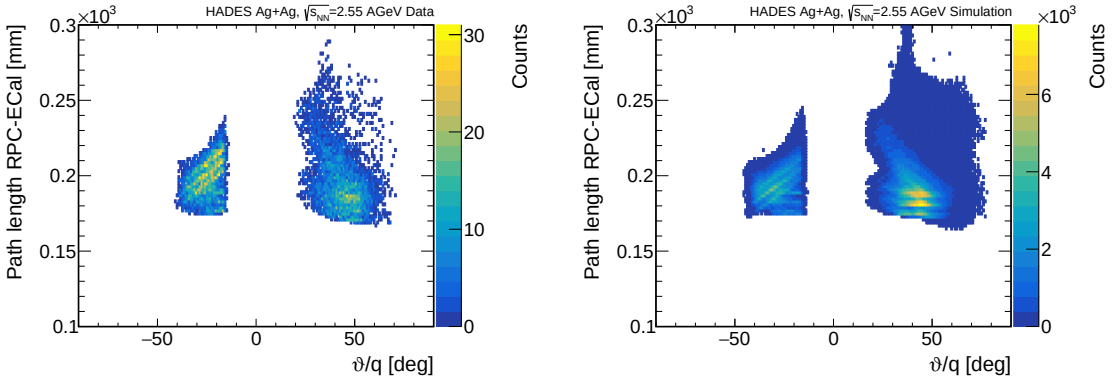

(a) Experimental data (b) White lepton simulation

Figure B.6: Comparison of path length as function of the electromagnetic charge and polar angle from real data and simulation.

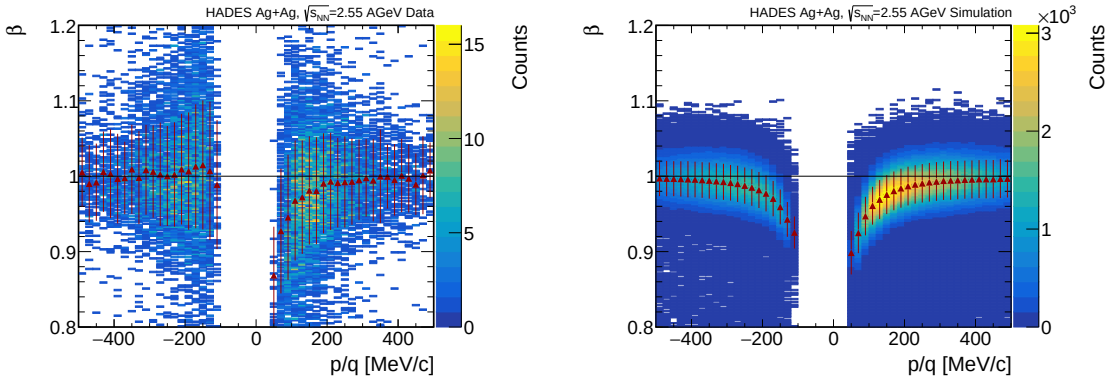

(a) Experimental data (b) White lepton simulation

Figure B.7: Comparison of calculated velocity from ECal information as function of the electromagnetic charge and momentum from real data and simulation.

lead to an overall nice description of the particle velocity estimation of the ECal which is displayed in figure B.8 for the simulation.

The application of the path length correction overshoots the calculated electron velocity for small momenta dramatically, which is also expected since the uncorrected spectrum was centered around $\beta = 1$ already. These assumptions will improve the ECal calibration in further beam times.

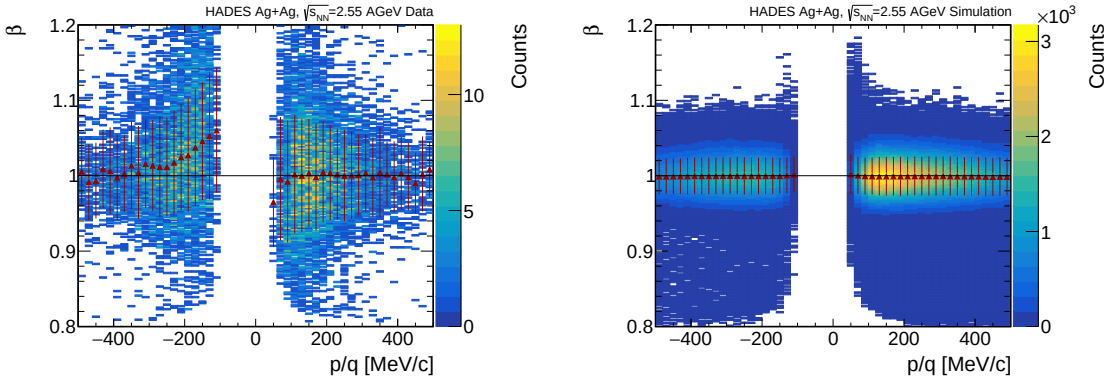

(a) Experimental data (b) White lepton simulation

Figure B.8: Comparison of calculated velocity from ECal information which is corrected by the additional path length of the track bending as function of the electromagnetic charge and momentum from real data and simulation.

B.7 List of Selection Criteria for the Analysis

Observable	Unit	Lower value	Upper value
χ_{track}		-	800.
m_p	MeV/c^2	0.8·m_p^{pdg}	1.2·m_p^{pdg}
m_{π^-}	MeV/c^2	0.7·$m_{\pi^-}^{pdg}$	1.3·$m_{\pi^-}^{pdg}$
$(dE/dx)_p^{MDC}$	MeV cm^2/g	$0.3(dE/dx)_p^{MDC}$(theo)	-

Table B.2: Summary of the values which were used for the hadron selection, used for π^- and proton candidate selection from the Λ decay.

Observable	Unit	Lower value	Upper value
$E\gamma$	MeV	60.	250.
β_{pre}		0.8	1.3
β_{exact}		-1σ	+1σ
ϑ	$^\circ$	16.5	-
Sector		2 and 4	2 and 4
χ_{track}		2.5σ	-
$Size_{\text{Cluster}}$		1	1

Table B.3: Summary of the values which were used for the γ reconstruction.

Observable	Unit	Lower value	Upper value
m_{rec}	MeV/c^2	-	97.7
p_{pre}	MeV/c	-	250.
$\chi_{\text{ring-track}}$	$^\circ$	-	1.5
Ring radius	mm	18.	30.
Ring N_{cals}		8	32

Table B.4: Summary of the values which were used for the lepton reconstruction.

Observable	Unit	Lower value	Upper value
NN_{out}		0.95	-
f_S		1.4	1.4
M_Λ	MeV/c^2	1110.	1120.

Table B.5: Summary of the values which were used for the Λ reconstruction in the double differential Λ multiplicity determination.

Observable	Unit	Lower value	Upper value
NN_{out}		0.98	-
f_S		1.4	1.4
M_Λ	MeV/c^2	1105.	1125.

Table B.6: Summary of the values which were used for the Λ reconstruction, in the $\Lambda\gamma$ as well as the Λe reconstruction for the Σ^0 signal extraction.

Observable	Unit	Lower value	Upper value
$OA_{\gamma-p}$	°	2.5	-
$OA_{\gamma-\pi^-}$	°	2.5	-

Table B.7: Summary of the values which were used for the $\Lambda\gamma$ pair formation reconstruction.

Observable	Unit	Lower value	Upper value
p_e	MeV/c	100.	-
N_{Cals_A}		-	40
$OA_{e-\Lambda}$	°	-	40.
OA_{e-p}	°	2.5	-
$OA_{e-\pi^-}$	°	2.5	-
Charge	e	-1	-1

Table B.8: Summary of the values which were used for the Λe pair formation reconstruction.

Acknowledgements

Zu guter Letzt möchte ich mich bei allen Personen bedanken, die mich während der Promotion unterstützt haben und das Vorhaben somit überhaupt erst ermöglicht haben.

Ein besonderer Dank gilt selbstverständlich Frau Prof. Dr. Claudia Höhne für Ihre Vorlesung der experimentellen Kern- und Teilchenphysik, die mir den ersten Einblick in die faszinierende subatomare Welt ermöglicht hat. Folglich bedanke ich mich für die Aufnahme in Ihre Arbeitsgruppe und die vielen darauf folgenden wissenschaftlichen Tipps und Tricks, aber vor allem auch für den sehr angenehmen menschlichen Umgang in Ihrer gesamten Arbeitsgruppe.

Ich danke allen meinen Büro-Partnern und Arbeitskollegen Cornelius, Martin und Karina für ein freundschaftliches miteinander. Dabei möchte ich besonders Jan-Hendrik Otto und Adrian Weber als Büro-Partner und Freunde besonders hervorheben, die mir mit ihrer Expertise die Arbeit unzählige Male erleichtert haben und mit denen die wissenschaftlichen Diskussionen nie langweilig wurden – auch wenn manchmal die ursprüngliche Fragestellung manchmal in den Hintergrund trat. Vielen Dank auch an Adrian für die Erlaubnis, seine optische Gestaltung der Thesis als Grundlage verwenden zu dürfen. Mein Dank gilt auch allen derzeitigen und ehemaligen Mitgliedern der Arbeitsgruppe für die gemeinsame Zeit.

Natürlich möchte ich auch Evi und Anita dafür danken, dass sie immer gut gelaunt eine Antwort auf jede organisatorische Frage parat hatten.

Weiterhin möchte ich mich bei Jörg Foertsch, Mateusz Grunwald, Marvin Kohls und Simon Spies für die zahlreichen Diskussionen aller Art, vor allem in den Kaffeepausen der jeweiligen Konferenzen sowie unzähligen Remote-Sessions, bedanken. Dadurch konnten viele technische und physikalische Unklarheiten überdacht und ausgeräumt werden. Natürlich möchte ich Dr. Jürgen Friese ganz herzlich für seine Ratschläge und Analysevorschläge danken, gerade weil sie so oft zu kontroversen Diskussionen geführt haben.

Ein weiterer Dank geht an Prof. Dr. Joachim Stroth, Prof. Dr. Tetyana Galatyuk, PD Dr. Manuel Lorenz, apl. Professor Jens Sören Lange und Dr. Kai Gallmeister, die mich alle in unterschiedlichen Phasen meines Studiums unterstützt und wissenschaftlich sehr gefördert haben.

Mein größter Dank gilt meiner Familie, meiner Freundin und allen Freunden, die mich in den letzten Jahren bedingungslos unterstützt haben. Vor allem danke ich ihnen für die Rücksichtnahme, meine physikalischen Überlegungen in den verschiedensten – manchmal unpassenden – Momenten zu tolerieren.

Bibliography

[1] J. J. Thomson. “Cathode Rays”. In: *Philosophical Magazine* 44 (1897), pp. 293–316.

[2] E. Rutherford. “The scattering of α and β particles by matter and the structure of the atom ”. In: *The London, Edinburgh, and Dublin Philosophical Magazine and Journal of Science* 21.125 (1911), pp. 669–688. DOI: 10.1080/14786440508637080. URL: https://doi.org/10.1080/14786440508637080.

[3] J. Chadwick. “The existence of a neutron”. In: *Proceedings of The Royal Society A: Mathematical, Physical and Engineering Sciences* 136 (1932), pp. 692–708. URL: https://api.semanticscholar.org/CorpusID:91182340.

[4] I. Estermann, O. C. Simpson, and O. Stern. “The Magnetic Moment of the Proton”. In: *Phys. Rev.* 52 (6 Sept. 1937), pp. 535–545. DOI: 10.1103/PhysRev.52.535. URL: https://link.aps.org/doi/10.1103/PhysRev.52.535.

[5] M. Gell-Mann. “The Eightfold Way: A Theory Of Strong Interaction Symmetry”. In: (Mar. 1961). DOI: 10.2172/4008239. URL: https://www.osti.gov/biblio/4008239.

[6] G. Zweig. “An SU(3) model for strong interaction symmetry and its breaking. Version 2”. In: *Developments In The Quark Theory Of Hadrons. Vol. 1. 1964 - 1978*. Feb. 1964, pp. 22–101.

[7] G. Zweig. “Origins of the Quark Model”. In: *Proceedings of the Fourth International Conference on Baryon Resonances* (Jan. 1980).

[8] E. Fermi and C. N. Yang. “Are Mesons Elementary Particles?” In: *Phys. Rev.* 76 (12 Dec. 1949), pp. 1739–1743. DOI: 10.1103/PhysRev.76.1739. URL: https://link.aps.org/doi/10.1103/PhysRev.76.1739.

[9] E. D. Bloom et al. “High-Energy Inelastic e-p Scattering at 6 degree and 10 degree”. In: *PRL* 23.16 (Oct. 1969), pp. 930–934. DOI: 10.1103/PhysRevLett.23.930.

[10] M. Breidenbach et al. “Observed Behavior of Highly Inelastic Electron-Proton Scattering”. In: *PRL* 23.16 (Oct. 1969), pp. 935–939. DOI: 10.1103/PhysRevLett.23.935.

[11] D. Galbraith and C. Burgard. “Standard Model of the Standard Model”. CERN Webfest https://texample.net/model-physics/. 2012.

[12] D. J. Gross and F. Wilczek. "Asymptotically Free Gauge Theories. I". In: *Phys. Rev. D* 8 (10 Nov. 1973), pp. 3633–3652. DOI: 10.1103/PhysRevD.8.3633. URL: https://link.aps.org/doi/10.1103/PhysRevD.8.3633.

[13] D. J. Gross and F. Wilczek. "Ultraviolet Behavior of Non-Abelian Gauge Theories". In: *Phys. Rev. Lett.* 30 (26 June 1973), pp. 1343–1346. DOI: 10.1103/PhysRevLett.30.1343. URL: https://link.aps.org/doi/10.1103/PhysRevLett.30.1343.

[14] G. Münster. *Von der Quantenfeldtheorie zum Standardmodell*. Berlin, Boston: De Gruyter, 2019. ISBN: 9783110638547. DOI: doi:10.1515/9783110638547. URL: https://doi.org/10.1515/9783110638547.

[15] R. L. Workman et al. "Review of Particle Physics". In: *PTEP* 2022 (2022), p. 083C01. DOI: 10.1093/ptep/ptac097.

[16] J. C. Collins and M. J. Perry. "Superdense Matter: Neutrons or Asymptotically Free Quarks?" In: *Phys. Rev. Lett.* 34 (21 May 1975), pp. 1353–1356. DOI: 10.1103/PhysRevLett.34.1353. URL: https://link.aps.org/doi/10.1103/PhysRevLett.34.1353.

[17] S. Navas et al. "Review of Particle Physics". In: *Phys. Rev. D* 110 (3 Aug. 2024), p. 030001. DOI: 10.1103/PhysRevD.110.030001. URL: https://link.aps.org/doi/10.1103/PhysRevD.110.030001.

[18] Daisuke Jido et al. "η' meson under partial restoration of chiral symmetry in nuclear medium". In: *EPJ Web of Conferences* 37 (2012). Ed. by A. Wrońska et al., p. 09019. ISSN: 2100-014X. DOI: 10.1051/epjconf/20123709019. URL: http://dx.doi.org/10.1051/epjconf/20123709019.

[19] K. Ackerstaff et al. "Measurement of the strong coupling constant α_s and the vector and axial-vector spectral functions in hadronic tau decays". In: *The European Physical Journal C* 7.4 (Mar. 1999), pp. 571–593. ISSN: 1434-6052. DOI: 10.1007/s100529901061. URL: http://dx.doi.org/10.1007/s100529901061.

[20] J. C. Maxwell. *A Treatise on Electricity and Magnetism*. Vol. 1. Cambridge Library Collection - Physical Sciences. Cambridge University Press, 2010. DOI: 10.1017/CBO9780511709333.

[21] M. Born, W. Heisenberg, and P. Jordan. "Zur Quantenmechanik. II." In: *Z. Phys.* 35.8-9 (1926), pp. 557–615. DOI: 10.1007/BF01379806.

[22] S. Weinberg. *The quantum theory of fields. Vol. 2: Modern applications*. Cambridge, UK: Univ. Pr. (1996) 489 p. 1996. URL: http://www.slac.stanford.edu/spires/find/hep/www?key=3763846.

[23] F. Englert and R. Brout. "Broken Symmetry and the Mass of Gauge Vector Mesons". In: *Phys. Rev. Lett.* 13 (9 Aug. 1964), pp. 321–323. DOI: 10.1103/PhysRevLett.13.321. URL: https://link.aps.org/doi/10.1103/PhysRevLett.13.321.

[24] P.W. Higgs. “Broken symmetries, massless particles and gauge fields”. In: *Physics Letters* 12.2 (1964), pp. 132–133. ISSN: 0031-9163. DOI: https://doi.org/10.1016/0031-9163(64)91136-9. URL: https://www.sciencedirect.com/science/article/pii/0031916364911369.

[25] C. Bloechingerand others. *Physics Opportunities at mu+mu- Higgs Factories*. 2002. arXiv: hep-ph/0202199 [hep-ph]. URL: https://arxiv.org/abs/hep-ph/0202199.

[26] G. Aad et al. “Observation of a new particle in the search for the Standard Model Higgs boson with the ATLAS detector at the LHC”. In: *Physics Letters B* 716.1 (Sept. 2012), pp. 1–29. DOI: 10.1016/j.physletb.2012.08.020. URL: https://doi.org/10.1016%2Fj.physletb.2012.08.020.

[27] S. Chatrchyan et al. “Observation of a new boson at a mass of 125 GeV with the CMS experiment at the LHC”. In: *Physics Letters B* 716.1 (Sept. 2012), pp. 30–61. DOI: 10.1016/j.physletb.2012.08.021. URL: https://doi.org/10.1016%2Fj.physletb.2012.08.021.

[28] S. Chatrchyan et al. “Observation of a New Boson with Mass Near 125 GeV in pp Collisions at $\sqrt{s}$ = 7 and 8 TeV”. In: *JHEP* 06 (2013), p. 081. DOI: 10.1007/JHEP06(2013)081. arXiv: 1303.4571 [hep-ex].

[29] Martin Reuter and Frank Saueressig. *Quantum Gravity and the Functional Renormalization Group: The Road towards Asymptotic Safety*. Cambridge Monographs on Mathematical Physics. Cambridge University Press, 2019.

[30] Nima Arkani–Hamed, Savas Dimopoulos, and Gia Dvali. “The hierarchy problem and new dimensions at a millimeter”. In: *Physics Letters B* 429.3–4 (June 1998), pp. 263–272. ISSN: 0370-2693. DOI: 10.1016/s0370-2693(98)00466-3. URL: http://dx.doi.org/10.1016/S0370-2693(98)00466-3.

[31] G. W. Bennett et al. “Final Report of the Muon E821 Anomalous Magnetic Moment Measurement at BNL”. In: *Phys. Rev. D* 73 (2006), p. 072003. DOI: 10.1103/PhysRevD.73.072003. arXiv: hep-ex/0602035.

[32] D. P. Aguillard et al. “Measurement of the Positive Muon Anomalous Magnetic Moment to 0.20 ppm”. In: *Phys. Rev. Lett.* 131 (16 Oct. 2023), p. 161802. DOI: 10.1103/PhysRevLett.131.161802. URL: https://link.aps.org/doi/10.1103/PhysRevLett.131.161802.

[33] R. Aliberti et al. *The anomalous magnetic moment of the muon in the Standard Model: an update*. 2025. arXiv: 2505.21476 [hep-ph]. URL: https://arxiv.org/abs/2505.21476.

[34] R. Aaij et al. “Test of lepton universality in beauty-quark decays”. In: *Nature Physics* 18.3 (Mar. 2022), pp. 277–282. ISSN: 1745-2481. DOI: 10.1038/s41567-021-01478-8. URL: http://dx.doi.org/10.1038/s41567-021-01478-8.

[35] A. Arbey and F. Mahmoudi. “Dark matter and the early Universe: A review”. In: *Progress in Particle and Nuclear Physics* 119 (July 2021), p. 103865. ISSN: 0146-6410. DOI: 10.1016/j.ppnp.2021.103865. URL: http://dx.doi.org/10.1016/j.ppnp.2021.103865.

[36] M. Persic, P. Salucci, and F. Stel. “The universal rotation curve of spiral galaxies — I. The dark matter connection”. In: *Monthly Notices of the Royal Astronomical Society* 281.1 (July 1996), pp. 27–47. ISSN: 0035-8711. DOI: 10.1093/mnras/278.1.27. eprint: https://academic.oup.com/mnras/article-pdf/281/1/27/30383982/281-1-27.pdf. URL: https://doi.org/10.1093/mnras/278.1.27.

[37] A Lewis and A Challinor. “Weak gravitational lensing of the CMB”. In: *Physics Reports* 429.1 (June 2006), pp. 1–65. ISSN: 0370-1573. DOI: 10.1016/j.physrep.2006.03.002. URL: http://dx.doi.org/10.1016/j.physrep.2006.03.002.

[38] T. Mannel. “Theory and Phenomenology of CP Violation”. In: *Nuclear Physics B - Proceedings Supplements* 167 (2007). Proceedings of the 7th International Conference on Hyperons, Charm and Beauty Hadrons, pp. 170–174. ISSN: 0920-5632. DOI: https://doi.org/10.1016/j.nuclphysbps.2006.12.083. URL: https://www.sciencedirect.com/science/article/pii/S0920563206010711.

[39] H. Georgi and S. L. Glashow. “Unity of All Elementary-Particle Forces”. In: *PRL* 32.8 (Feb. 1974), pp. 438–441. DOI: 10.1103/PhysRevLett.32.438.

[40] G. L. Kane and M. Shifman. *Introduction to The Supersymmetric World: The Beginnings of The Theory*. 2001. arXiv: hep-ph/0102298 [hep-ph]. URL: https://arxiv.org/abs/hep-ph/0102298.

[41] Howard E. Haber and Laurel Stephenson Haskins. “Supersymmetric Theory and Models”. In: *Anticipating the Next Discoveries in Particle Physics*. WORLD SCIENTIFIC, May 2018, pp. 355–499. DOI: 10.1142/9789813233348_0006. URL: http://dx.doi.org/10.1142/9789813233348_0006.

[42] Y. Aoki et al. “The order of the quantum chromodynamics transition predicted by the standard model of particle physics”. In: *Nature* 443.7112 (Oct. 2006), pp. 675–678. DOI: 10.1038/nature05120. URL: https://doi.org/10.1038%2Fnature05120.

[43] P. Steinbrecher. “The QCD crossover at zero and non-zero baryon densities from Lattice QCD”. In: *Nuclear Physics A* 982 (Feb. 2019), pp. 847–850. ISSN: 0375-9474. DOI: 10.1016/j.nuclphysa.2018.08.025. URL: http://dx.doi.org/10.1016/j.nuclphysa.2018.08.025.

[44] M. Floris. “Hadron yields and the phase diagram of strongly interacting matter”. In: *Nuclear Physics A* 931 (Nov. 2014), pp. 103–112. ISSN: 0375-9474. DOI: 10.1016/j.nuclphysa.2014.09.002. URL: http://dx.doi.org/10.1016/j.nuclphysa.2014.09.002.

[45] Hades Collaboration, Adamczewski-Musch, et al. “Probing dense baryon-rich matter with virtual photons”. In: *Nature Physics* 15.10 (July 2019), pp. 1040–1045. DOI: 10.1038/s41567-019-0583-8.

[46] Wei-jie Fu, Jan M. Pawlowski, and Fabian Rennecke. “QCD phase structure at finite temperature and density”. In: *Phys. Rev. D* 101 (5 Mar. 2020), p. 054032. DOI: 10.1103/PhysRevD.101.054032. URL: https://link.aps.org/doi/10.1103/PhysRevD.101.054032.

[47] P. J. Gunkel and C. S. Fischer. “Locating the critical endpoint of QCD: Mesonic backcoupling effects”. In: *Phys. Rev. D* 104 (5 Sept. 2021), p. 054022. DOI: 10.1103/PhysRevD.104.054022. URL: https://link.aps.org/doi/10.1103/PhysRevD.104.054022.

[48] M. G. Alford et al. “Color superconductivity in dense quark matter”. In: *Reviews of Modern Physics* 80.4 (Nov. 2008), pp. 1455–1515. ISSN: 1539-0756. DOI: 10.1103/revmodphys.80.1455. URL: http://dx.doi.org/10.1103/RevModPhys.80.1455.

[49] L. Tolos and L. Fabbietti. “Strangeness in Nuclei and Neutron Stars”. In: *Prog. Part. Nucl. Phys.* 112 (2020), p. 103770. DOI: 10.1016/j.ppnp.2020.103770. arXiv: 2002.09223 [nucl-ex].

[50] E. R. Most et al. “Probing neutron-star matter in the lab: Similarities and differences between binary mergers and heavy-ion collisions”. In: *Phys. Rev. D* 107 (4 Feb. 2023), p. 043034. DOI: 10.1103/PhysRevD.107.043034. URL: https://link.aps.org/doi/10.1103/PhysRevD.107.043034.

[51] I. Bombaci. “The Hyperon Puzzle in Neutron Stars”. In: *Proceedings of the 12th International Conference on Hypernuclear and Strange Particle Physics (HYP2015)*. Journal of the Physical Society of Japan, July 2017. DOI: 10.7566/jpscp.17.101002. URL: http://dx.doi.org/10.7566/JPSCP.17.101002.

[52] D. Rischke. “The quark–gluon plasma in equilibrium”. In: *Progress in Particle and Nuclear Physics* 52.1 (Mar. 2004), pp. 197–296. ISSN: 0146-6410. DOI: 10.1016/j.ppnp.2003.09.002. URL: http://dx.doi.org/10.1016/j.ppnp.2003.09.002.

[53] D. B. Blaschke et al. *Accessibility of color superconducting quark matter phases in heavy-ion collisions*. 2010. arXiv: 1004.4375 [hep-ph]. URL: https://arxiv.org/abs/1004.4375.

[54] T. Nishimura et al. “Enhanced Dilepton production near the color superconducting phase and the QCD critical point”. In: *The European Physical Journal A* 60.4 (Apr. 2024), p. 82. ISSN: 1434-601X. DOI: 10.1140/epja/s10050-024-01273-y. URL: https://doi.org/10.1140/epja/s10050-024-01273-y.

[55] U. Heinz and G. Kestin. "Jozsó's Legacy: Chemical and kinetic freeze-out in heavy-ion collisions". In: *The European Physical Journal Special Topics* 155.1 (Mar. 2008), pp. 75–87. ISSN: 1951-6401. DOI: 10.1140/epjst/e2008-00591-4. URL: http://dx.doi.org/10.1140/epjst/e2008-00591-4.

[56] J.E. Bernhard. *Bayesian parameter estimation for relativistic heavy-ion collisions*. 2018. arXiv: 1804.06469 [nucl-th]. URL: https://arxiv.org/abs/1804.06469.

[57] ATLAS Collaboration. *Charged-hadron production in pp, p+Pb, Pb+Pb, and Xe+Xe collisions at $\sqrt{s_{NN}} = 5$ TeV with the ATLAS detector at the LHC*. 2023. arXiv: 2211.15257 [hep-ex]. URL: https://arxiv.org/abs/2211.15257.

[58] K. Aamodt et al. "Charged-Particle Multiplicity Density at Midrapidity in Central Pb-Pb Collisions at $\sqrt{s_{NN}} = 2.76$ TeV". In: *Phys. Rev. Lett.* 105 (25 Dec. 2010), p. 252301. DOI: 10.1103/PhysRevLett.105.252301. URL: https://link.aps.org/doi/10.1103/PhysRevLett.105.252301.

[59] L. Adamczyk et al. "Measurements of dielectron production in Au + Au collisions at $\sqrt{s_{NN}} = 200$ GeV from the STAR experiment". In: *Physical Review C* 92.2 (Aug. 2015). ISSN: 1089-490X. DOI: 10.1103/physrevc.92.024912. URL: http://dx.doi.org/10.1103/PhysRevC.92.024912.

[60] D. Neff. *Recent Highlights from STAR BES Phase II*. 2024. arXiv: 2405.20928 [nucl-ex]. URL: https://arxiv.org/abs/2405.20928.

[61] N. Abgrall et al. "NA61/SHINE facility at the CERN SPS: beams and detector system". In: *Journal of Instrumentation* 9.06 (June 2014), P06005–P06005. ISSN: 1748-0221. DOI: 10.1088/1748-0221/9/06/p06005. URL: http://dx.doi.org/10.1088/1748-0221/9/06/P06005.

[62] L. Turko. *NA61/SHINE experiment - programme beyond 2020*. 2018. arXiv: 1811.05522 [nucl-ex]. URL: https://arxiv.org/abs/1811.05522.

[63] Y. Mori. "The 50-GeV proton synchrotron and proposed pulsed proton beam facility in J-PARC project". In: *Nuclear Instruments and Methods in Physics Research Section A: Accelerators, Spectrometers, Detectors and Associated Equipment* 532.1 (2004). International Workshop on Beam Cooling and Related Topics, pp. 184–195. ISSN: 0168-9002. DOI: https://doi.org/10.1016/j.nima.2004.06.114. URL: https://www.sciencedirect.com/science/article/pii/S0168900204012732.

[64] V.D. Kekelidze. "NICA project at JINR: status and prospects". In: *Journal of Instrumentation* 12.06 (June 2017), p. C06012. DOI: 10.1088/1748-0221/12/06/C06012. URL: https://dx.doi.org/10.1088/1748-0221/12/06/C06012.

[65] S. Z. Belenkij and L. D. Landau. "Hydrodynamic theory of multiple production of particles". In: *Usp. Fiz. Nauk* 56 (1955), p. 309. DOI: 10.1007/BF02745507.

[66] W. Scheid, H. Müller, and W. Greiner. “Nuclear Shock Waves in Heavy-Ion Collisions”. In: *Phys. Rev. Lett.* 32 (13 Apr. 1974), pp. 741–745. DOI: 10.1103/PhysRevLett.32.741. URL: https://link.aps.org/doi/10.1103/PhysRevLett.32.741.

[67] N. Herrmann, J. P. Wessels, and T. Wienold. “Collective Flow in Heavy-Ion Collisions”. In: *Annual Review of Nuclear and Particle Science* 49.1 (1999), pp. 581–632. DOI: 10.1146/annurev.nucl.49.1.581. eprint: https://doi.org/10.1146/annurev.nucl.49.1.581. URL: https://doi.org/10.1146/annurev.nucl.49.1.581.

[68] S. Voloshin and Y. Zhang. “Flow study in relativistic nuclear collisions by Fourier expansion of azimuthal particle distributions”. In: *Zeitschrift fuer Physik C Particles and Fields* 70.4 (May 1996), pp. 665–671. ISSN: 1431-5858. DOI: 10.1007/s002880050141. URL: http://dx.doi.org/10.1007/s002880050141.

[69] A. M. Poskanzer and S. A. Voloshin. “Methods for analyzing anisotropic flow in relativistic nuclear collisions”. In: *Phys. Rev. C* 58 (1998), pp. 1671–1678. DOI: 10.1103/PhysRevC.58.1671. arXiv: nucl-ex/9805001.

[70] B. Kardan. “Collective flow and correlation measurements with HADES in Au+Au collisions at 1.23 AGeV”. Hirschegg, International Workshop XLVII on Gross Properties of Nuclei and Nuclear Excitations. 2019. URL: https://theory.gsi.de/hirschegg/2019/talks/Thu/Kardan.pdf.

[71] K. H. Ackermann et al. “Elliptic Flow in Au+Au Collisions at 130 GeV”. In: *Physical Review Letters* 86.3 (Jan. 2001), pp. 402–407. ISSN: 1079-7114. DOI: 10.1103/physrevlett.86.402. URL: http://dx.doi.org/10.1103/PhysRevLett.86.402.

[72] J. Adamczewski-Musch et al. “Proton, deuteron and triton flow measurements in Au+Au collisions at $\sqrt{s_{\mathrm{NN}}} = 2.4$ GeV”. In: *Eur. Phys. J. A* 59.4 (2023), p. 80. DOI: 10.1140/epja/s10050-023-00936-6. arXiv: 2208.02740 [nucl-ex].

[73] R. Rapp and H. van Hees. “Thermal dileptons as fireball thermometer and chronometer”. In: *Physics Letters B* 753 (Feb. 2016), pp. 586–590. ISSN: 0370-2693. DOI: 10.1016/j.physletb.2015.12.065. URL: http://dx.doi.org/10.1016/j.physletb.2015.12.065.

[74] A. Drees et al. “First results of the CERES electron pair spectrometer from p + Be, P + Au and S + Au collisions”. In: *Nucl. Phys. A* 566 (1994). Ed. by E. Stenlund et al., pp. 87C–94C. DOI: 10.1016/0375-9474(94)90612-2.

[75] A. Yegneswaran et al. “The dilepton spectrometer”. In: *Nuclear Instruments and Methods in Physics Research Section A: Accelerators, Spectrometers, Detectors and Associated Equipment* 290.1 (1990), pp. 61–75. ISSN: 0168-9002. DOI: https://doi.org/10.1016/0168-9002(90)90345-7. URL: https://www.sciencedirect.com/science/article/pii/0168900290903457.

[76] D. Adamová et al. “Enhanced Production of Low-Mass Electron-Positron Pairs in 40-AGeV Pb-Au Collisions at the CERN SPS”. In: *Phys. Rev. Lett.* 91 (4 July 2003), p. 042301. DOI: 10.1103/PhysRevLett.91.042301. URL: https://link.aps.org/doi/10.1103/PhysRevLett.91.042301.

[77] G. Agakichiev et al. “The high-acceptance dielectron spectrometer HADES”. In: *The European Physical Journal A* 41.2 (July 2009), pp. 243–277. DOI: 10.1140/epja/i2009-10807-5. URL: https://doi.org/10.1140%2Fepja%2Fi2009-10807-5.

[78] R. Arnaldi et al. “NA60 results on thermal dimuons”. In: *The European Physical Journal C* 61.4 (Feb. 2009), pp. 711–720. ISSN: 1434-6052. DOI: 10.1140/epjc/s10052-009-0878-5. URL: http://dx.doi.org/10.1140/epjc/s10052-009-0878-5.

[79] K. Adcox et al. “Formation of dense partonic matter in relativistic nucleus-nucleus collisions at RHIC: Experimental evaluation by the PHENIX collaboration”. In: *Nucl. Phys. A* 757 (2005), pp. 184–283. DOI: 10.1016/j.nuclphysa.2005.03.086. arXiv: nucl-ex/0410003.

[80] K. Aamodt et al. “The ALICE experiment at the CERN LHC”. In: *JINST* 3 (2008), S08002. DOI: 10.1088/1748-0221/3/08/S08002.

[81] K. H. Ackermann et al. “STAR detector overview”. In: *Nucl. Instrum. Meth. A* 499 (2003), pp. 624–632. DOI: 10.1016/S0168-9002(02)01960-5.

[82] T. Ablyazimov et al. “Challenges in QCD matter physics –The scientific programme of the Compressed Baryonic Matter experiment at FAIR”. In: *Eur. Phys. J. A* 53.3 (2017), p. 60. DOI: 10.1140/epja/i2017-12248-y. arXiv: 1607.01487 [nucl-ex].

[83] S. Acharya et al. “Dielectron production in proton-proton collisions at $\sqrt{s} = 7$ TeV”. In: *Journal of High Energy Physics* 2018.9 (Sept. 2018). ISSN: 1029-8479. DOI: 10.1007/jhep09(2018)064. URL: http://dx.doi.org/10.1007/JHEP09(2018)064.

[84] L. Adamczyk et al. “Energy dependence of acceptance-corrected dielectron excess mass spectrum at mid-rapidity in Au+Au collisions at $\sqrt{s_{NN}}$=19.6 and 200 GeV”. In: *Physics Letters B* 750 (Nov. 2015), pp. 64–71. ISSN: 0370-2693. DOI: 10.1016/j.physletb.2015.08.044. URL: http://dx.doi.org/10.1016/j.physletb.2015.08.044.

[85] M. Stephanov, K. Rajagopal, and E. Shuryak. “Event-by-event fluctuations in heavy ion collisions and the QCD critical point”. In: *Physical Review D* 60.11 (Nov. 1999). ISSN: 1089-4918. DOI: 10.1103/physrevd.60.114028. URL: http://dx.doi.org/10.1103/PhysRevD.60.114028.

[86] V. Koch, A. Majumder, and J. Randrup. “Baryon-Strangeness Correlations: A Diagnostic of Strongly Interacting Matter”. In: *Phys. Rev. Lett.* 95 (18 Oct. 2005), p. 182301. DOI: 10.1103/PhysRevLett.95.182301. URL: https://link.aps.org/doi/10.1103/PhysRevLett.95.182301.

[87] B. Friman et al. “Fluctuations as probe of the QCD phase transition and freeze-out in heavy ion collisions at LHC and RHIC”. In: *The European Physical Journal C* 71.7 (July 2011). ISSN: 1434-6052. DOI: 10.1140/epjc/s10052-011-1694-2. URL: http://dx.doi.org/10.1140/epjc/s10052-011-1694-2.

[88] M. Asakawa et al. “Third moments of conserved charges as probes of QCD phase structure”. In: *Phys. Rev. Lett.* 103 (2009), p. 262301. DOI: 10.1103/PhysRevLett.103.262301. arXiv: 0904.2089 [nucl-th].

[89] J. Adam et al. “Nonmonotonic Energy Dependence of Net-Proton Number Fluctuations”. In: *Phys. Rev. Lett.* 126 (9 Mar. 2021), p. 092301. DOI: 10.1103/PhysRevLett.126.092301. URL: https://link.aps.org/doi/10.1103/PhysRevLett.126.092301.

[90] M. A. Stephanov. “Non-Gaussian Fluctuations near the QCD Critical Point”. In: *Physical Review Letters* 102.3 (Jan. 2009). ISSN: 1079-7114. DOI: 10.1103/physrevlett.102.032301. URL: http://dx.doi.org/10.1103/PhysRevLett.102.032301.

[91] The STAR Collaboration. *Precision Measurement of (Net-)proton Number Fluctuations in Au+Au Collisions at RHIC*. 2025. arXiv: 2504.00817 [nucl-ex]. URL: https://arxiv.org/abs/2504.00817.

[92] J. Rafelski and B. Müller. “Strangeness Production in the Quark-Gluon Plasma”. In: *Phys. Rev. Lett.* 48 (16 Apr. 1982), pp. 1066–1069. DOI: 10.1103/PhysRevLett.48.1066. URL: https://link.aps.org/doi/10.1103/PhysRevLett.48.1066.

[93] J. W. Harris et al. “Λ Production near Threshold in Central Nucleus-Nucleus Collisions”. In: *Phys. Rev. Lett.* 47 (4 July 1981), pp. 229–232. DOI: 10.1103/PhysRevLett.47.229. URL: https://link.aps.org/doi/10.1103/PhysRevLett.47.229.

[94] J. Rafelski and J. Letessier. “Strangeness and statistical hadronization: How to study quark gluon plasma”. In: *Acta Phys. Polon. B* 34 (2003). Ed. by M. Praszalowicz, pp. 5791–5824. arXiv: hep-ph/0309030.

[95] J. Adam et al. “Enhanced production of multi-strange hadrons in high-multiplicity proton–proton collisions”. In: *Nature Physics* 13.6 (Apr. 2017), pp. 535–539. DOI: 10.1038/nphys4111. URL: https://doi.org/10.1038%2Fnphys4111.

[96] A. Foerster et al. “Production of K^+ and of K^- mesons in heavy-ion collisions from 0.6A to 2.0A GeV incident energy”. In: *Phys. Rev. C* 75 (2 Feb. 2007), p. 024906. DOI: 10.1103/PhysRevC.75.024906. URL: https://link.aps.org/doi/10.1103/PhysRevC.75.024906.

[97] G. Agakishiev et al. “Deep Subthreshold Ξ^- Production in $\mathrm{Ar} + \mathrm{KCl}$ Reactions at $1.76A$ GeV”. In: *Phys. Rev. Lett.* 103 (13 Sept. 2009), p. 132301. DOI: 10.1103/PhysRevLett.103.132301. URL: https://link.aps.org/doi/10.1103/PhysRevLett.103.132301.

[98] J. Weil et al. “Particle production and equilibrium properties within a new hadron transport approach for heavy-ion collisions”. In: *Phys. Rev. C* 94 (5 Nov. 2016), p. 054905. DOI: 10.1103/PhysRevC.94.054905. URL: https://link.aps.org/doi/10.1103/PhysRevC.94.054905.

[99] H. Christoph et al. “Strangeness production close to the threshold in proton–nucleus and heavy-ion collisions”. In: *Physics Reports* 510.4 (2012), pp. 119–200. ISSN: 0370-1573. DOI: https://doi.org/10.1016/j.physrep.2011.08.004. URL: https://www.sciencedirect.com/science/article/pii/S037015731100247X.

[100] R. Bellwied, H. Caines, and T. J. Humanic. “Time dependence of strange baryon freeze-out in relativistic heavy ion collisions”. In: *Physical Review C* 62.5 (Oct. 2000). ISSN: 1089-490X. DOI: 10.1103/physrevc.62.054906. URL: http://dx.doi.org/10.1103/PhysRevC.62.054906.

[101] T. Scheib. “Λ and K^0_s Production in Au+Au Collisions at 1.23A GeV”. PhD thesis. Frankfurt U., 2022. DOI: 10.21248/gups.68651.

[102] I. G. Bearden et al. “Charged Meson Rapidity Distributions in Central $\mathrm{Au}+\mathrm{Au}$ Collisions at $\sqrt{s_{NN}} = 200\ \mathrm{GeV}$”. In: *Phys. Rev. Lett.* 94 (16 Apr. 2005), p. 162301. DOI: 10.1103/PhysRevLett.94.162301. URL: https://link.aps.org/doi/10.1103/PhysRevLett.94.162301.

[103] C. Alt et al. “Ω^- and $\overline{\Omega}^+$ Production in Central $\mathrm{Pb}+\mathrm{Pb}$ collisions at 40 and $158A\ \mathrm{GeV}$”. In: *Phys. Rev. Lett.* 94 (19 May 2005), p. 192301. DOI: 10.1103/PhysRevLett.94.192301. URL: https://link.aps.org/doi/10.1103/PhysRevLett.94.192301.

[104] C. Alt et al. “Energy dependence of ϕ meson production in central $\mathrm{Pb}+\mathrm{Pb}$ collisions at $\sqrt{s_{NN}} = 6$ to 17 GeV”. In: *Phys. Rev. C* 78 (4 Oct. 2008), p. 044907. DOI: 10.1103/PhysRevC.78.044907. URL: https://link.aps.org/doi/10.1103/PhysRevC.78.044907.

[105] C. Alt et al. “Energy dependence of Λ and Ξ production in central $\mathrm{Pb}+\mathrm{Pb}$ collisions at $20A, 30A, 40A, 80A$, and $158A$ GeV measured at the CERN Super Proton Synchrotron”. In: *Phys. Rev. C* 78 (3 Sept. 2008), p. 034918. DOI: 10.1103/PhysRevC.78.034918. URL: https://link.aps.org/doi/10.1103/PhysRevC.78.034918.

[106] S. V. Afanasiev et al. “Energy dependence of pion and kaon production in central Pb+Pb collisions”. In: *Phys. Rev. C* 66 (5 Nov. 2002), p. 054902. DOI: 10.1103/PhysRevC.66.054902. URL: https://link.aps.org/doi/10.1103/PhysRevC.66.054902.

[107] P. Chung et al. “Near-Threshold Production of the Multistrange Ξ^- Hyperon”. In: *Phys. Rev. Lett.* 91 (20 Nov. 2003), p. 202301. DOI: 10.1103/PhysRevLett.91.202301. URL: https://link.aps.org/doi/10.1103/PhysRevLett.91.202301.

[108] B. B. Back et al. “Production of ϕ mesons in Au + Au collisions at $11.7A\mathrm{GeV}/c$”. In: *Phys. Rev. C* 69 (5 May 2004), p. 054901. DOI: 10.1103/PhysRevC.69.054901. URL: https://link.aps.org/doi/10.1103/PhysRevC.69.054901.

[109] L. Ahle et al. “Kaon production in Au+Au collisions at $11.6A\mathrm{GeV}/c$”. In: *Phys. Rev. C* 58 (6 Dec. 1998), pp. 3523–3538. DOI: 10.1103/PhysRevC.58.3523. URL: https://link.aps.org/doi/10.1103/PhysRevC.58.3523.

[110] L Ahle et al. “An Excitation function of K- and K+ production in Au + Au reactions at the AGS”. In: *Phys. Lett. B* 490 (2000), pp. 53–60. DOI: 10.1016/S0370-2693(00)00916-3. arXiv: nucl-ex/0008010.

[111] L. Ahle et al. “Particle production at high baryon density in central Au+Au reactions at 11.6A GeV/c”. In: *Phys. Rev. C* 57.2 (1998), R466–R470. DOI: 10.1103/PhysRevC.57.R466.

[112] J. L. Klay et al. “Charged pion production in $2A$ to $8A$ GeV central Au + Au Collisions”. In: *Phys. Rev. C* 68 (5 Nov. 2003), p. 054905. DOI: 10.1103/PhysRevC.68.054905. URL: https://link.aps.org/doi/10.1103/PhysRevC.68.054905.

[113] G. Agakishiev et al. “Hyperon production in Ar+KCl collisions at 1.76A GeV”. In: *Eur. Phys. J. A* 47 (2011), p. 21. DOI: 10.1140/epja/i2011-11021-8. arXiv: 1010.1675 [nucl-ex].

[114] C. Alt et al. “Pion and Kaon production in central $\mathrm{Pb}+\mathrm{Pb}$ collisions at $20A$ and $30A$ GeV: Evidence for the onset of deconfinement”. In: *Phys. Rev. C* 77 (2 Feb. 2008), p. 024903. DOI: 10.1103/PhysRevC.77.024903. URL: https://link.aps.org/doi/10.1103/PhysRevC.77.024903.

[115] L. Adamczyk et al. “Bulk properties of the medium produced in relativistic heavy-ion collisions from the beam energy scan program”. In: *Physical Review C* 96.4 (Oct. 2017). ISSN: 2469-9993. DOI: 10.1103/physrevc.96.044904. URL: http://dx.doi.org/10.1103/PhysRevC.96.044904.

[116] J. Cleymans et al. “The thermal model and the transition from baryonic to mesonic freeze-out”. In: *The European Physical Journal A* 29.1 (July 2006), pp. 119–121. ISSN: 1434-601X. DOI: 10.1140/epja/i2005-10309-6. URL: http://dx.doi.org/10.1140/epja/i2005-10309-6.

[117] B. Povh et al. *Particles and nuclei: an introduction to the physical concepts; 4th ed.* Berlin: Springer, 2004. DOI: 10.1007/978-3-662-05432-1. URL: https://cds.cern.ch/record/706817.

[118] L. Liu and C. S. Fischer. “Space-like electromagnetic form factors of lambda- and sigma-baryons from quark-diquark Faddeev equations”. In: *The European Physical Journal A* 60.4 (Apr. 2024). ISSN: 1434-601X. DOI: 10.1140/epja/s10050-024-01283-w. URL: http://dx.doi.org/10.1140/epja/s10050-024-01283-w.

[119] Particle Data Group, P A Zyla, et al. “Review of Particle Physics”. In: *Progress of Theoretical and Experimental Physics* 2020.8 (Aug. 2020), p. 083C01. ISSN: 2050-3911. DOI: 10.1093/ptep/ptaa104. eprint: https://academic.oup.com/ptep/article-pdf/2020/8/083C01/34673722/ptaa104.pdf. URL: https://doi.org/10.1093/ptep/ptaa104.

[120] J. Haidenbauer, U.-G. Meißner, and A. Nogga. “Hyperon–nucleon interaction within chiral effective field theory revisited”. In: *The European Physical Journal A* 56.3 (Mar. 2020). ISSN: 1434-601X. DOI: 10.1140/epja/s10050-020-00100-4. URL: http://dx.doi.org/10.1140/epja/s10050-020-00100-4.

[121] T. Kunz. “Sigma0-Produktion in p+Nb-Reaktionen bei E = 3,5 GeV”. de. PhD thesis. Technische Universität München, 2017, p. 143. URL: https://mediatum.ub.tum.de/1364265.

[122] R. Abou Yassine et al. “Investigation of the Σ^0 Production Mechanism in p(3.5 GeV)+p Collisions”. In: *The European Physical Journal A* 60.1 (Jan. 2024), p. 18. ISSN: 1434-601X. DOI: 10.1140/epja/s10050-023-01214-1. URL: https://doi.org/10.1140/epja/s10050-023-01214-1.

[123] A. Borissov. “Production of Σ^0 Hyperons at LHC with ALICE”. In: *EPJ Web Conf.* 222 (2019). DOI: 10.1051/epjconf/201922202002. URL: https://doi.org/10.1051/epjconf/201922202002.

[124] P. Kowina et al. “Energy dependence of the Lambda / Sigma0 production cross-section ratio in p p interactions”. In: *Eur. Phys. J. A* 22 (2004), pp. 293–299. DOI: 10.1140/epja/i2003-10236-6. arXiv: nucl-ex/0402008.

[125] A. Sibirtsev et al. “Phenomenology of the Λ/Σ^0 production ratio in pp collisions”. In: *The European Physical Journal A - Hadrons and Nuclei* 29.3 (Sept. 2006), pp. 363–367. ISSN: 1434-601X. DOI: 10.1140/epja/i2006-10097-5. URL: https://doi.org/10.1140/epja/i2006-10097-5.

[126] G. Van Buren et al. “The Σ^0/Λ ratio in high energy nuclear collisions”. In: *Journal of Physics G: Nuclear and Particle Physics* 31.6 (May 2005), S1127. DOI: 10.1088/0954-3899/31/6/072. URL: https://dx.doi.org/10.1088/0954-3899/31/6/072.

[127] H. Wolter et al. “Transport model comparison studies of intermediate-energy heavy-ion collisions”. In: *Progress in Particle and Nuclear Physics* 125 (July 2022), p. 103962. ISSN: 0146-6410. DOI: 10.1016/j.ppnp.2022.103962. URL: http://dx.doi.org/10.1016/j.ppnp.2022.103962.

[128] A. Andronic, P. Braun-Munzinger, and J. Stachel. “Hadron production in central nucleus-nucleus collisions at chemical freeze-out”. In: *Nucl. Phys. A* 772 (2006), pp. 167–199. DOI: 10.1016/j.nuclphysa.2006.03.012. arXiv: nucl-th/0511071.

[129] A. Andronic et al. “Decoding the phase structure of QCD via particle production at high energy”. In: *Nature* 561.7723 (2018), pp. 321–330. DOI: 10.1038/s41586-018-0491-6. arXiv: 1710.09425 [nucl-th].

[130] J. Stachel et al. “Confronting LHC data with the statistical hadronization model”. In: *J. Phys. Conf. Ser.* 509 (2014). Ed. by David Evans et al., p. 012019. DOI: 10.1088/1742-6596/509/1/012019. arXiv: 1311.4662 [nucl-th].

[131] P. Alba et al. “Influence of hadronic resonances on the chemical freeze-out in heavy-ion collisions”. In: *Phys. Rev. C* 101 (5 May 2020), p. 054905. DOI: 10.1103/PhysRevC.101.054905. URL: https://link.aps.org/doi/10.1103/PhysRevC.101.054905.

[132] V. Vovchenko and H. Stoecker. “Thermal-FIST: A package for heavy-ion collisions and hadronic equation of state”. In: *Computer Physics Communications* 244 (Nov. 2019), pp. 295–310. ISSN: 0010-4655. DOI: 10.1016/j.cpc.2019.06.024. URL: http://dx.doi.org/10.1016/j.cpc.2019.06.024.

[133] S. Bass et al. “Microscopic models for ultrarelativistic heavy ion collisions”. In: *Progress in Particle and Nuclear Physics* 41 (1998), pp. 255–369. ISSN: 0146-6410. DOI: 10.1016/s0146-6410(98)00058-1. URL: http://dx.doi.org/10.1016/S0146-6410(98)00058-1.

[134] J. Gerhard et al. “Stability of transport models under changes of resonance parameters: A study with the ultrarelativistic quantum molecular dynamics model”. In: *Phys. Rev. C* 85 (4 Apr. 2012), p. 044912. DOI: 10.1103/PhysRevC.85.044912. URL: https://link.aps.org/doi/10.1103/PhysRevC.85.044912.

[135] M. Bleicher et al. “Relativistic hadron-hadron collisions in the ultra-relativistic quantum molecular dynamics model”. In: *Journal of Physics G: Nuclear and Particle Physics* 25.9 (Sept. 1999), pp. 1859–1896. DOI: 10.1088/0954-3899/25/9/308. URL: https://doi.org/10.1088%2F0954-3899%2F25%2F9%2F308.

[136] H. Petersen et al. “Fully integrated transport approach to heavy ion reactions with an intermediate hydrodynamic stage”. In: *Phys. Rev. C* 78 (4 Oct. 2008), p. 044901. DOI: 10.1103/PhysRevC.78.044901. URL: https://link.aps.org/doi/10.1103/PhysRevC.78.044901.

[137] G. Graef et al. “Deep sub-threshold Xi and Lambda production in nuclear collisions with the UrQMD transport model”. In: *Physical Review C* 90.6 (Dec. 2014). ISSN: 1089-490X. DOI: 10.1103/physrevc.90.064909. URL: http://dx.doi.org/10.1103/PhysRevC.90.064909.

[138] T. Reichert et al. “Comparison of heavy ion transport simulations: Ag + Ag collisions at Elab = 1.58A GeV”. In: *Journal of Physics G: Nuclear and Particle Physics* 49.5 (Apr. 2022), p. 055108. DOI: 10.1088/1361-6471/ac5dfe. URL: https://dx.doi.org/10.1088/1361-6471/ac5dfe.

[139] U. Mosel and Gallmeister K. “GiBUU - a general introduction”. Modeling neutrino-nucleus interactions, Trento. 2018.

[140] O. Buss et al. “Transport-theoretical Description of Nuclear Reactions”. In: *Phys. Rept.* 512 (2012), pp. 1–124. DOI: 10.1016/j.physrep.2011.12.001. arXiv: 1106.1344 [hep-ph].

[141] J. Weil et al. “Particle production and equilibrium properties within a new hadron transport approach for heavy-ion collisions”. In: *Phys. Rev. C* 94.5 (2016), p. 054905. DOI: 10.1103/PhysRevC.94.054905. arXiv: 1606.06642 [nucl-th].

[142] W. Cassing and E. L. Bratkovskaya. “Parton transport and hadronization from the dynamical quasiparticle point of view”. In: *Phys. Rev. C* 78 (2008), p. 034919. DOI: 10.1103/PhysRevC.78.034919. arXiv: 0808.0022 [hep-ph].

[143] J. Weil. “Vector mesons in medium in a transport approach”. en. PhD thesis. Justus Liebig University Giessen, 2013. DOI: 10.22029/JLUPUB-9613. URL: https://jlupub.ub.uni-giessen.de//handle/jlupub/10229.

[144] K. Tsushima, A. Sibirtsev, and A.W. Thomas. “Resonance model study of strangeness production in pp collisions”. In: *Physics Letters B* 390.1–4 (Jan. 1997), pp. 29–35. ISSN: 0370-2693. DOI: 10.1016/s0370-2693(96)01391-3. URL: http://dx.doi.org/10.1016/S0370-2693(96)01391-3.

[145] V. Steinberg et al. “Strangeness production via resonances in heavy-ion collisions at energies available at the GSI Schwerionensynchrotron”. In: *Physical Review C* 99.6 (June 2019). ISSN: 2469-9985. DOI: 10.1103/physrevc.99.064908. URL: https://www.osti.gov/biblio/1564047.

[146] R. Münzer et al. “Determination of N* amplitudes from associated strangeness production in p+p collisions”. In: *Physics Letters B* 785 (Oct. 2018), pp. 574–580. ISSN: 0370-2693. DOI: 10.1016/j.physletb.2018.08.068. URL: http://dx.doi.org/10.1016/j.physletb.2018.08.068.

[147] J. Aichelin. ““Quantum” molecular dynamics—a dynamical microscopic n-body approach to investigate fragment formation and the nuclear equation of state in heavy ion collisions”. In: *Physics Reports* 202.5 (1991), pp. 233–360. ISSN: 0370-1573. DOI: https://doi.org/10.1016/0370-1573(91)90094-3. URL: https://www.sciencedirect.com/science/article/pii/0370157391900943.

[148] P. Kramer and M. Saraceno. “Geometry of the time-dependent variational principle in quantum mechanics”. In: *Group Theoretical Methods in Physics: Proceedings of the IX International Colloquium Held at Cocoyoc, México, June 23–27, 1980*. Springer. 2005, pp. 112–121.

[149] B. Franzke. “The Heavy Ion Storage and Cooler Ring Project ESR at GSI”. In: *Nucl. Instrum. Meth.* B24/25 (1987), pp. 18–25. DOI: 10.1016/0168-583X(87)90583-0.

[150] G. Münzenberg et al. “The velocity filter ship, a separator of unslowed heavy ion fusion products”. In: *Nuclear Instruments and Methods* 161.1 (1979), pp. 65–82. ISSN: 0029-554X. DOI: https://doi.org/10.1016/0029-554X(79)90362-8. URL: https://www.sciencedirect.com/science/article/pii/0029554X79903628.

[151] A. Semchenkov et al. “The TransActinide Separator and Chemistry Apparatus (TASCA) at GSI – Optimization of ion-optical structures and magnet designs”. In: *Nuclear Instruments and Methods in Physics Research Section B: Beam Interactions with Materials and Atoms* 266.19 (2008). Proceedings of the XVth International Conference on Electromagnetic Isotope Separators and Techniques Related to their Applications, pp. 4153–4161. ISSN: 0168-583X. DOI: https://doi.org/10.1016/j.nimb.2008.05.132. URL: https://www.sciencedirect.com/science/article/pii/S0168583X08006964.

[152] P. Senger et al. “The kaon spectrometer at SIS”. In: *Nuclear Instruments and Methods in Physics Research Section A: Accelerators, Spectrometers, Detectors and Associated Equipment* 327.2 (1993), pp. 393–411. ISSN: 0168-9002. DOI: https://doi.org/10.1016/0168-9002(93)90706-N. URL: https://www.sciencedirect.com/science/article/pii/016890029390706N.

[153] A. Gobbi et al. “A highly-segmented Δ E-time-of-flight wall as forward detector of the 4π-system for charged particles at the SIS/ESR accelerator”. In: *Nuclear Instruments and Methods in Physics Research Section A: Accelerators, Spectrometers, Detectors and Associated Equipment* 324.1 (1993), pp. 156–176. ISSN: 0168-9002. DOI: https://doi.org/10.1016/0168-9002(93)90974-M. URL: https://www.sciencedirect.com/science/article/pii/016890029390974M.

[154] GSI website. "https://www.gsi.de/en/work/research" [Date of access: 27.03.2023].

[155] GSI website. https://www.gsi.de/en/researchaccelerators/accelerator_facility [Date of access: 27.03.2023].

[156] H. Vormann et al. “High intensity heavy ion beam optimization at GSI UNILAC”. In: *Journals of Accelerator Conferences Website* (2021). DOI: DOI:10.18429/JACoW-LINAC2022.

[157] Rahul Singh. “Tune Measurement at GSI SIS-18: Methods and Applications”. en. PhD thesis. Darmstadt: Technische Universität Darmstadt, 2014. URL: http://tuprints.ulb.tu-darmstadt.de/3976/.

[158] A. A. Weber. “Development of readout electronics for the RICH detector in the HADES and CBM experiments”. Justus-Liebig-University Giessen, 2021.

[159] R Tapper. “Diamond detectors in particle physics”. In: *Reports on Progress in Physics* 63 (July 2000), p. 1273. DOI: 10.1088/0034-4885/63/8/203.

[160] A. Rost et al. “Performance of the CVD Diamond Based Beam Quality Monitoring System in the HADES Experiment at GSI*”. In: *10th International Particle Accelerator Conference*. 2019, WEPGW019. DOI: 10.18429/JACoW-IPAC2019-WEPGW019.

[161] J. Pietraszko. “T0 setup for Ag beam in 2018/2019”. https://hades-wiki.gsi.de/pub/RICH/StartVeto/T0Setup_2018.pdf. 2019.

[162] HADES Collaboration. *Proposals for experiments at SIS18 during FAIR Phase-0*. GSI Helmholtzzentrum fuer Schwerionenforschung, GSI, Darmstadt, 2017.

[163] J. V. Jelley. "Cerenkov radiation and its applications". In: *British Journal of Applied Physics* 6.7 (July 1955), p. 227. DOI: 10.1088/0508-3443/6/7/301. URL: https://dx.doi.org/10.1088/0508-3443/6/7/301.

[164] I. Frank and I. Tamm. "Coherent visible radiation from fast electrons passing through matter". In: *C. R. Acad. Sci. USSR* 14 (1937), pp. 109–114. URL: http://cds.cern.ch/record/485596.

[165] R. Mansmann et al. "Detector calibration and measurement issues in multi-color time-resolved laser-induced incandescence". In: *Applied Physics B* 125 (June 2019), p. 126. DOI: 10.1007/s00340-019-7235-7.

[166] J. Foertsch. "Upgrade of the HADES RICH photon detector and first performance analyses". doctoralthesis. Bergische Universität Wuppertal, 2021. DOI: https://doi.org/10.25926/69gp-b484.

[167] C. Pauly. "Upgrade of the HADES RICH photon detector with H12700 MAPMTs". In: *"Nuclear Instruments and Methods in Physics Research Section A: Accelerators, Spectrometers, Detectors and Associated Equipment"* 876 (2017). The 9th international workshop on Ring Imaging Cherenkov Detectors (RICH2016), pp. 164–167. ISSN: 0168-9002. DOI: https://doi.org/10.1016/j.nima.2017.02.067.

[168] M. Becker et al. "Performance of the new hadron blind HADES RICH in heavy ion collisions". In: *Nuclear Instruments and Methods in Physics Research Section A: Accelerators, Spectrometers, Detectors and Associated Equipment* 1056 (Sept. 2023), p. 168697. DOI: 10.1016/j.nima.2023.168697.

[169] T. Bretz. "Magnetfeldeigenschaften des Spektrometers HADES". 1999.

[170] R. Veenhof. "GARFIELD, Simulation of gaseous detectors". http://garfield.web.cern.ch/garfield. 1984.

[171] HADES Collaboration. "https://hades-wiki.gsi.de/MDC/Materials". Date of access: 11.04.2023.

[172] C. Wendisch. *Recovery of HADES drift chambers suffering from Malter-like effects*. oral presentation, 3rd Conference on Detector Stability and Aging Phenomena in gaseous detectors. 2023.

[173] J. Markert. "Untersuchung zum Ansprechverhalten der Vieldraht-Driftkammern niedriger Massenbelegung des HADES Experimentes". doctoralthesis. 2005.

[174] D. Belver et al. “The HADES RPC inner TOF wall”. In: *Nuclear Instruments and Methods in Physics Research Section A: Accelerators, Spectrometers, Detectors and Associated Equipment* 602.3 (2009). Proceedings of the 9th International Workshop on Resistive Plate Chambers and Related Detectors, pp. 687–690. ISSN: 0168-9002. DOI: https://doi.org/10.1016/j.nima.2008.12.090. URL: https://www.sciencedirect.com/science/article/pii/S0168900208019633.

[175] G. Kornakov. “New advances and developments on the RPC TOF wall of the HADES experiment at GSI”. doctoralthesis. 2012.

[176] C. Behnke. “Reconstruction of π^0 and η mesons via conversion in 197Au+197Au at 1.23 GeV/u with the HADES Spectrometer”. doctoralthesis. Universitätsbibliothek Johann Christian Senckenberg, 2017, p. 152.

[177] W. Czyzycki et al. *Electromagnetic Calorimeter for HADES*. 2011. arXiv: 1109.5550 [nucl-ex].

[178] T. Galatyuket et al. *Tests of the Electromagnetic Calorimeter for HADES Experiment at GSI*. 2018. DOI: DOI10.18502/ken.v3i1.1739.

[179] Christian W. Fabjan and F. Gianotti. “Calorimetry for particle physics”. In: *Rev. Mod. Phys.* 75 (4 Oct. 2003), pp. 1243–1286. DOI: 10.1103/RevModPhys.75.1243. URL: https://link.aps.org/doi/10.1103/RevModPhys.75.1243.

[180] C. Grupen and B. Shwartz. *Particle Detectors*. 2nd ed. Cambridge Monographs on Particle Physics, Nuclear Physics and Cosmology. Cambridge University Press, 2008. DOI: 10.1017/CBO9780511534966.

[181] O.V. Andreeva et al. “Forward scintillation hodoscope for nuclear fragment detection at the high acceptance dielectron spectrometer (HADES) setup”. In: *Instruments and Experimental Techniques* 2014 (Apr. 2014), pp. 103–119. DOI: 10.1134/S0020441214020146.

[182] J. Michel. “Development and Implementation of a New Trigger and Data Acquisition System for the HADES Detector”. 2012.

[183] The HADES collaboration. “HADES Oracle database”. March 2019 beamtime. 2019.

[184] J. Michel. “DAQ 2020 planned upgrades and whishlist”. HADES collaboration meeting. 2019.

[185] Hades software group. *HYDRA2 manual*. GSI: HADES collaboration, Oct. 2011. URL: https://docplayer.net/77065564-Hydra2-manual-hades-software-group.html.

[186] R. Brun and F. Rademakers. *ROOT - An Object Oriented Data Analysis Framework*. Lausanne: Proceedings AIHENP’96 Workshop, 1996.

[187] I. Fröhlich et al. “Pluto: A Monte Carlo Simulation Tool for Hadronic Physics”. In: *PoS* ACAT (2007), p. 076. DOI: 10.22323/1.050.0076. arXiv: 0708.2382 [nucl-ex].

[188] R. Brun et al. *GEANT 3: user's guide Geant 3.10, Geant 3.11; rev. version*. Geneva: CERN, 1987. URL: https://cds.cern.ch/record/1119728.

[189] B. Betz. "Jet Propagation and Mach-Cone Formation in (3+1)-dimensional Ideal Hydrodynamics". PhD thesis. Frankfurt U., 2009.

[190] Roy J. Glauber. "Quantum Optics and Heavy Ion Physics". In: *Nuclear Physics A* 774 (Aug. 2006), pp. 3–13. ISSN: 0375-9474. DOI: 10.1016/j.nuclphysa.2006.06.009. URL: http://dx.doi.org/10.1016/j.nuclphysa.2006.06.009.

[191] J. Adamczewski-Musch et al. "Centrality determination of Au + Au collisions at 1.23A GeV with HADES". In: *Eur. Phys. J. A* 54.5 (2018), p. 85. DOI: 10.1140/epja/i2018-12513-7. arXiv: 1712.07993 [nucl-ex].

[192] B. Kardan for the HADES Collaboration. *Centrality determination in Ag + Ag collisions at 1.58A GeV*. Work in progress, https://hades-wiki.gsi.de/foswiki/bin/view/Physics/AgagEventChara. 2022.

[193] M. Parschau. "KFParticle - update on latest progress". HADES collaboration meeting. 2023.

[194] R. L. Workman et al. "Review of Particle Physics". In: *PTEP* 2022 (2022), p. 083C01. DOI: 10.1093/ptep/ptac097. URL: https://pdg.lbl.gov/2022/reviews/rpp2022-rev-passage-particles-matter.pdf.

[195] J.-H. Otto. "Dielectron reconstruction in Ag+Ag collisions at $\sqrt{s_{NN}}$=2.55 GeV with HADES". PhD thesis. Justus-Liebig-University Giessen, 2022.

[196] A. Prozorov. "π^0 flow in Ag+Ag collisions at 1.58 AGeV". HADES collaboration meeting. 2022. URL: https://indico.gsi.de/event/14582/contributions/64410/attachments/40278/55195/ProzorovPi0Flow.pdf.

[197] A. Prozorov. "Neutral Meson Production in Ag+Ag Collisions at 1.58 A GeV with HADES Electromagnetic Calorimeter". Dissertation, Univerzita Karlova, 2023. Dissertation. Univerzita Karlova, 2023. URL: https://repository.gsi.de/record/348497.

[198] R. L. Workman et al. "Review of Particle Physics". In: *PTEP* 2022 (2022). DOI: 10.1093/ptep/ptac097. URL: https://pdg.lbl.gov/2022/listings/contents_listings.html.

[199] M. Becker. "Search for the Σ^0 in Ag+Ag collisions at 1.58 AGeV via photon conversion method". HADES collaboration meeting XLI. 2021.

[200] S. Spies. "Rekonstruktion schwacher Zerfälle in Au+Au Kollisionen bei 1,23A GeV". MA thesis. Frankfurt University, 2018.

[201] A. Hoecker et al. *TMVA - Toolkit for Multivariate Data Analysis*. 2007. DOI: 10.48550/ARXIV.PHYSICS/0703039. URL: https://arxiv.org/abs/physics/0703039.

[202] F. Rosenblatt. "Principles of Neurodynamics: Perceptions and the Theory of Brain Mechanisms". In: *American Journal of Psychology* 76 (1963), p. 705.

[203] G. I. Kopylov. “Like particle correlations as a tool to study the multiple production mechanism”. In: *Physics Letters B* 50.4 (1974), pp. 472–474. ISSN: 0370-2693. DOI: https://doi.org/10.1016/0370-2693(74)90263-9. URL: https://www.sciencedirect.com/science/article/pii/0370269374902639.

[204] R. L. Workman et al. “Review of Particle Physics”. In: *PTEP* 2022 (2022). DOI: 10.1093/ptep/ptac097. URL: https://pdg.lbl.gov/2023/web/viewer.html?file=../listings/rpp2023-list-sigma-1385.pdf.

[205] R. L. Workman et al. “Review of Particle Physics”. In: *PTEP* 2022 (2022). DOI: 10.1093/ptep/ptac097. URL: https://pdg.lbl.gov/2023/web/viewer.html?file=../listings/rpp2023-list-xi-zero.pdf.

[206] J. T. Rieger. “The Chances of Hyperon Dalitz Decays in pp at 4.5 AGeV”. HADES collaboration meeting XLIV. 2023. URL: https://indico.gsi.de/event/15741/contributions/70515/attachments/43186/60487/hyperon_dalitz_chances.pdf.

[207] M. Becker. “Search for the Σ^0 in Ag+Ag collisions at 1.58 AGeV ”. HADES collaboration meeting XLIII. 2022.

[208] S. Wheaton, J. Cleymans, and M. Hauer. “THERMUS—A thermal model package for ROOT”. In: *Computer Physics Communications* 180.1 (Jan. 2009), pp. 84–106. ISSN: 0010-4655. DOI: 10.1016/j.cpc.2008.08.001. URL: http://dx.doi.org/10.1016/j.cpc.2008.08.001.

[209] K. Redlich and A. Tounsi. “Strangeness enhancement and energy dependence in heavy ion collisions”. In: *The European Physical Journal C* 24.4 (Aug. 2002), pp. 589–594. DOI: 10.1007/s10052-002-0983-1. URL: https://doi.org/10.1007%2Fs10052-002-0983-1.

[210] P. Castorina, S. Plumari, and H. Satz. “Strangeness production and color deconfinement”. In: *International Journal of Modern Physics E* 26.12 (Dec. 2017), p. 1750081. ISSN: 1793-6608. DOI: 10.1142/s0218301317500811. URL: http://dx.doi.org/10.1142/S0218301317500811.

[211] Volodymyr Vovchenko, Mark I. Gorenstein, and Horst Stoecker. “Finite resonance widths influence the thermal-model description of hadron yields”. In: *Physical Review C* 98.3 (Sept. 2018). ISSN: 2469-9993. DOI: 10.1103/physrevc.98.034906. URL: http://dx.doi.org/10.1103/PhysRevC.98.034906.

[212] M. Kohls. “Strange Hadron Production”. HADES analysis meeting. 2023. URL: https://indico.gsi.de/event/17507/contributions/72726/attachments/44285/62418/mkohls_HADES_PhiK%2BK-_AM_July2023.pdf.

[213] M. Lorenz. private communication, 28.11.2022. 2022.

[214] S. Spies. “Strange hadron production in Ag+Ag collisions at 1.58A GeV”. PhD thesis. Johann Wolfgang Goethe-Universität, Frankfurt, 2022. DOI: 10.21248/gups.68651.

[215] M. Nabroth. private communication, 17.08.2023. 2023.

[216] M. Kohls. "Production of $K^{\pm}$ and ϕ-Mesons in Ag+Ag-Collisions at 1.58 A GeV". PhD thesis. Goethe University Frankfurt, Frankfurt U., 2023.

[217] M. Nabroth. "Emission patterns of charged pions from Ag+Ag collisions at 1.58A GeV". Johann Wolfgang Goethe-Universität Frankfurt, 2022.

[218] H. Schuldes. "Charged kaon and Φ reconstruction in Au+Au collisions at 1.23 AGeV". doctoralthesis. Universitätsbibliothek Johann Christian Senckenberg, 2016, p. 223.

[219] A. Wroblewski. "On the strange quark suppression factor in high-energy collisions". In: *Acta Phys. Polon. B* 16 (1985), pp. 379–392.

[220] J. Cleymans, H. Oeschler, and K. Redlich. "Influence of impact parameter on thermal description of relativistic heavy ion collisions at $(1-2)A\mathrm{GeV}$". In: *Phys. Rev. C* 59 (3 Mar. 1999), pp. 1663–1673. DOI: 10.1103/PhysRevC.59.1663. URL: https://link.aps.org/doi/10.1103/PhysRevC.59.1663.

[221] H. Satz. "Strangeness Suppression and Color Deconfinement". In: *EPJ Web Conf.* 171 (2018). Ed. by A. Mischke and P. Kuijer, p. 02005. DOI: 10.1051/epjconf/201817102005.

[222] H. Elfner. "SMASH: Status and Results". On-line seminar, https://indico.ihep.ac.cn/event/12476/. 2020.

[223] T. Rozek et al. "Threshold hyperon production in proton-proton collisions at COSY-11". In: *Phys. Lett. B* 643 (2006), pp. 251–256. DOI: 10.1016/j.physletb.2006.07.066. arXiv: nucl-ex/0607034.

[224] S. Sewerin et al. "Comparison of Λ and Σ^0 Production near Threshold in Proton-Proton Collisions". In: *Phys. Rev. Lett.* 83 (4 July 1999), pp. 682–685. DOI: 10.1103/PhysRevLett.83.682. URL: https://link.aps.org/doi/10.1103/PhysRevLett.83.682.

[225] H Schopper. *Total cross-sections for reactions of high energy particles: (including elastic, topological, inclusive and exclusive reactions)*. Landolt-Börnstein. New series. Group 1 Nuclear and particle physics. Berlin: Springer, 1988. DOI: 10.1007/b35211. URL: https://cds.cern.ch/record/214138.

[226] G. Kornakov. "Sub-threshold strangeness production measured with HADES". In: *Nuclear Physics A* 982 (2019). The 27th International Conference on Ultrarelativistic Nucleus-Nucleus Collisions: Quark Matter 2018, pp. 803–806. ISSN: 0375-9474. DOI: https://doi.org/10.1016/j.nuclphysa.2018.10.073. URL: https://www.sciencedirect.com/science/article/pii/S0375947418303543.

[227] G. Agakishiev et al. "Subthreshold Ξ^- Production in Collisions of $\mathrm{p}(3.5\,\mathrm{GeV}) + \mathrm{Nb}$". In: *Phys. Rev. Lett.* 114 (21 May 2015), p. 212301. DOI: 10.1103/PhysRevLett.114.212301. URL: https://link.aps.org/doi/10.1103/PhysRevLett.114.212301.

[228] J. Cleymans et al. “Comparison of chemical freeze-out criteria in heavy-ion collisions”. In: *Physical Review C* 73.3 (Mar. 2006). ISSN: 1089-490X. DOI: 10.1103/physrevc.73.034905. URL: http://dx.doi.org/10.1103/PhysRevC.73.034905.

[229] G. Agakishiev et al. *Statistical model analysis of hadron yields in proton-nucleus and heavy-ion collisions at SIS 18 energies*. 2015. arXiv: 1512.07070 [nucl-ex]. URL: https://arxiv.org/abs/1512.07070.

[230] M. Becker for the HADES collaboration. Σ^0 *reconstruction in Ag+Ag collisions at 1.58 AGeV with HADES*. oral presentation, Quark Matter Conference. 2023.

[231] R. Lalik and the HADES Collaboration. “Status and perspectives of hyperon production and electromagnetic decays with HADES at FAIR”. In: *Journal of Physics: Conference Series* 1137.1 (Jan. 2019), p. 012057. DOI: 10.1088/1742-6596/1137/1/012057. URL: https://dx.doi.org/10.1088/1742-6596/1137/1/012057.